TIP VORTICES–
SINGLE PHASE AND
CAVITATING FLOW PHENOMENA

Thesis by

Sheldon I. Green

In Partial Fulfillment of the Requirements
for the degree of
Doctor of Philosophy

California Institute of Technology
Pasadena, California
1988
(submitted May 16, 1988)

ACKNOWLEDGEMENTS

The author would first and foremost like to express his gratitude for the guidance and support of his advisor, Professor A. J. Acosta. Without the perspicacity and pertinacity of Professor Acosta, the author would still doubtless be performing experiments. The research was funded by the ONR under contract number N000167-85-K-0165. The financial support of Caltech (including Cole and Powell Fellowships) is acknowledged.

Caltech being the open institution that it is, the author was able to consult with many faculty members over the course of his stay. A partial list includes Professors: A. Leonard, C. Brennen, A. Roshko, M. Billet (Penn State), E. Hauptmann (UBC), and J. Katz (Johns Hopkins). The author also owes a great debt to his professors at the University of Toronto, and to L. Pollock (Tulane) for her insightful suggestions about the thesis text.

Many students have also helped the author. Thai Pham and Raza Akbar each spent a summer "SURFing" under the author's guidance. The author's immediate predecessor, Tim O'Hern, was instrumental in the crucial LTWT and holocamera familiarization period. Luca d'Agostino, Steve Ceccio, Norbert Arndt, Ron Franz, Hojin Ahn, Agnes Allard, and Regina Rieves have all served as sounding boards for ideas. A host of other friends made Caltech more enjoyable.

The author is appreciative of the technical assistance given him by Joe Fontana and Rich Eastvedt of the Keck Hydraulics Laboratory, and by George Lundgren and other members of the Aero shop. Cecilia Lin drew many of the thesis figures.

The numerical simulation conducted at NASA Ames could not have been done without the encouragement and aid of Dr. Dochan Kwak, Dr. Terri Holst, and Stuart Rogers.

Finally, the author wishes to express (but cannot in words alone) his deepest thanks to his family, who have bolstered his morale when it flagged, and served as an anchor in the stormy academic arena.

ABSTRACT

Tip vortices occur wherever a lifting surface terminates in a fluid. An understanding of tip vortices is salient to the solution of many engineering problems, including lift induced drag tip inefficiency, the overturning of small planes flown into the tip wake of larger aircraft, and marine propellor tip cavitation.

The tip vortex shed by several rectangular planform wings, fitted with three different tips, was studied in a water tunnel. Four techniques were employed to examine the tip vortex:

(i) Surface flow visualization to reveal the early stages of vortex rollup.

(ii) Double pulsed holography of buoyant, Lagrangian particle tracers for detailed tangential and axial velocity data around the vortex core. Holograms were also a source of instantaneous core structure information.

(iii) Single pulse holography of air bubbles, of uniform, measured, original size. The size of the bubbles is related to the instantaneous local static pressure. The bubbles are driven by the centripetal pressure gradient forces into the vortex core, providing a means of measuring the average and transient vortex core pressure non-intrusively.

(iv) Direct observation of vortex cavitation. These measurements are useful in their own right because of the considerable technological significance of tip vortex cavitation. In addition, many single phase tip flow characteristics have cavitating flow counterparts.

The present study has shown that one chord downstream of the wing trailing edge virtually all the foil bound vorticity has rolled up into the trailing vortex. Armed with this knowledge one may *a priori* evaluate, in the near field, the tangential velocity distribution, the core axial velocity excess, and the core mean pressure. These predictions are in agreement with the experimental measurements. Three aspects of the core flow, first observed in the present study, remain analytically inexplicable:

(i) The trend towards a Reynolds number dependent, axial velocity deficit with downstream distance.

(ii) The unsteady core velocity, particularly immediately downstream of the foil.

(iii) The vortex kinking which is coincident with highly unsteady axial core flow.

As a first approximation, cavitation inception occurs when the core pressure is reduced to the vapour pressure. The large measured fluctuating core pressure explains the occurrence of inception at core pressures somewhat above p_v, and the dependence of σ_i on the dissolved air content.

Modifying the tip geometry profoundly affects the trailing vortex. Installation of a ring wing tip can reduce the inception index relative to that of a normal rounded tip foil by a factor of three. The reduction was caused primarily by the redistribution, in the Trefftz plane, of the shed vorticity about a line and circle. Fortuitously, this redistribution caused most of the wing bound vorticity to be shed from the ring, decreasing the tip effect lift loss over the foil body.

TABLE OF CONTENTS

NOMENCLATURE

A	=	bubble surface area [m^2]
AR	=	aspect ratio = 2s/c [1]
c	=	foil chord [m]
c_D	=	drag coefficient of 2D wing [1]
c_L	=	lift coefficient [1]
c_p	=	specific heat at constant pressure [$m^2/K\text{-}s^2$]
c_v	=	specific heat at constant volume [$m^2/K\text{-}s^2$]
$d\Gamma/dy$	=	rate of change of bound circulation with y [m/s]
DAC	=	dissolved air content [ppm]
F	=	force [$kg\text{-}m/s^2$]
g	=	gravitational acceleration [m/s^2]
h	=	heat transfer coefficient [$kg/K\text{-}s^3$]
i.d.	=	internal diameter [m]
k	=	$(U_\theta)_{max}/U_\infty$ for a Rankine vortex [1]
l	=	spanwise unit length [m]
L	=	wing lift [$kg\text{-}m/s^2$]
L_L	=	lost wing lift due to tip downwash [$kg\text{-}m/s^2$]
LTWT	=	Low Turbulence Water Tunnel
n	=	polytropic exponent (=1:isothermal; =γ:adiabatic) [1]
N	=	number of data points, or computational grid points [1]
p	=	pressure [$kg/m\text{-}s^2$]
p_v	=	vapour pressure [$kg/m\text{-}s^2$]
p^*	=	$(p_\infty - p)/(0.5\rho U_\infty^2)$ [1]
$\overline{(p_c')^*}$	=	$(1/\sqrt{N})[\sum_1^N (p - \bar{p})^2/(0.5\rho U_\infty^2)]^{0.5}$ [1]
r	=	radius [m]
R	=	radius [m]
Re	=	Reynolds number [1]
s	=	semispan of foil [m]
S	=	surface tension [kg/s^2]

SFV	=	Surface Flow Visualization
t	=	time [s]
u	=	flow velocity in x-direction (computations) [m/s]
U	=	flow velocity in x-direction (freestream direction) [m/s]
U_L	=	freestream velocity above plate in Figure V.6 [m/s]
$\overline{U_{xc}}$	=	$(1/N)\sum_1^N U_{xc}$ [m/s]
U_θ	=	tangential velocity around vortex core [m/s]
U_∞	=	local freestream velocity [m/s]
		note that U_∞ varies slightly from the test section to the foil
v	=	flow velocity in y-direction (computations) [m/s]
V	=	flow velocity in y-direction (spanwise direction) [m/s]
w	=	flow velocity in z-direction [m/s]
x	=	distance from leading edge along chord line [m]
x	=	distance in freestream direction from leading edge [m]
y	=	spanwise distance from reflection plane mount [m]
z	=	distance orthogonal to x-y plane [m]
α	=	angle of attack [degrees]
α_o	=	zero lift angle of attack of 2D foil [degrees]
β	=	pseudocompressibility used in numerical simulation [kg/m-s^2]
γ	=	c_p/c_v [1]
Γ	=	vorticity [m^2/s]
Γ_B	=	bound circulation on the foil [m^2/s]
Γ_v	=	circulation around the trailing vortex [m^2/s]
Γ^*	=	$(d\Gamma/dy)[1/U_\infty(\alpha - \alpha_o)]$ [1]
Δt	=	change in time [s]
ϵ'	=	downwash angle at the tip [degrees]
ϵ^*	=	$\epsilon'/(\alpha - \alpha_o)$=normalized downwash angle [1]
κ	=	constant [1]
μ	=	fluid dynamic viscosity [kg/m-s]
ν	=	fluid kinematic viscosity [m^2/s]

ϕ = bubble diameter [m]

ϕ = inboard flow angle (refer to Figure IV.1) [degrees]

ρ = fluid density [kg/m^3]

σ_i = $[(p_\infty)_i - p_v]/0.5\rho(U_\infty)_i^2$ = cavitation inception index [1]

σ_d = $[(p_\infty)_d - p_v]/0.5\rho(U_\infty)_d^2$ = desinent cavitation index [1]

τ = bubble thermal response time [s]

Subscripts

1 = location '1'

B = bubble

c = core

d = desinence condition

D = drag

g = gas

i = inception condition

le = leading edge

max = maximum

min = minimum

o = reference location

p = pressure

rs = radial slip

tv = tip vortex

∞ = farfield

Superscripts

* = non-dimensionalized quantity

$\dot{}$ = derivative with respect to time

$'$ = fluctuating quantity = (instantaneous - mean)

$\bar{}$ = time averaged quantity

Note: British spelling and punctuation are employed throughout the thesis

LIST OF FIGURE CAPTIONS

LIST OF TABLE CAPTIONS

Chapter I–INTRODUCTION

Tip vortices form wherever a lifting surface terminates in a fluid moving relative to it. Two classic examples of tip vortex formation are the tip vortices generated by aircraft wings (which may occasionally be seen in the motion of the white airplane contrails formed by engine exhaust water vapour), and propellor tip vortices (which may be made visible by cavitation of fluid in their cores).

As a form of preface, the question "Why?"–"Why do tip vortices exist?" will be answered in part 1 of this introductory chapter. The follow up question "How?"–"How are tip vortices relevant to engineering?" will be considered in part 2. The third and final portions of this introduction concern the question "What?"–"What aspects of tip vortices are already understood, and in what ways does this thesis extend our knowledge?"

I.1 Nature of Tip Vortex Formation

Three different interpretations of why tip vortices occur will be outlined. The first mode of understanding tip vortices is in terms of pressure fields. A lifting surface (hereinafter referred to as a 'wing' or 'foil' for simplicity) moving through a fluid generates lift by hydrodynamically producing larger static pressures below the wing than above it. Since fluid accelerates in the direction of a favourable pressure gradient, fluid tends to flow from the pressure surface to the suction surface around the tip, and thus produces a tip vortex (refer to Figure I.1).

A second explanation of tip vortex flows is in terms of a shear layer. Figure I.2 is an inboard view of a wing terminating in a fluid. The parallel lines in the direction of U_∞ represent the undisturbed flow at some spanwise distance away from the wing, and the arrows parallel to the wing represent the in-plane flow inboard of the tip. The non-parallelism of the two implies vorticity oriented between the two directions. This explication allows for two tip vortices of opposite sign behind a symmetric airfoil at $\alpha = 0°$ (which has been observed through the use of SFV).

The third explication of trailing vortices involves Helmholtz Vortex Laws. Consider a finite length wing impulsively started from rest. The difference in velocity between the pressure and suction surfaces implies a net circulation around the wing (the "bound vortex"). Helmholtz vortex laws demand that this circulation be matched by an equal and opposite circulation shed by the wing (the "starting vortex"), and since vortex lines never end in the fluid, these two vortices must be connected by tip vortices (refer to Figure I.3).

I.2 Importance of Tip Vortices

Tip vortices are surprisingly important in engineering applications. Problems associated with tip vortices may be conveniently grouped into three categories: vortex-structure interactions, "vortex-fluid" interactions, and the tip vortex as an inefficiency.

The interaction of vortices with structures is an active topic. For example, each helicopter main rotor blade sheds vortices which may interact with following blades (Martin et al. 1984, Summa 1982, Mosher and Peterson 1983, Lewy and Caplot 1982, Widnall and Wolf 1980) and the tail rotor blades (Schreier 1982), producing undesirable noise, and fatigue inducing-vibration of the impinged-on structure. If one airplane accidentally flies into the tip wake of another, the following craft may experience a dangerous rolling moment (Donaldson 1971, Kantha et al. 1971, Snedeker 1972, Barber et al. 1975). Chigier (1974) reported that "accidents involving loss of life or serious injury [due to encounters with vortex wake turbulence] have now exceeded 100." This has prompted the FAA to impose a minimum time of several minutes between successive controlled aircraft landings at a runway. Concern about this problem resulted in a workshop held specifically to address it (Vortex 1980). Finally, vortex breakdown of F-18 Hornet wingstrake-generated vortices causes instantaneous accelerations of up to 1500g at the back fin of the aircraft (Brown 1988), which is undesirable in terms of both structural integrity and fighter maneuverability.

Tip vortices may "interact" with the fluid in the sense that tip vortices are the dominant feature of aircraft wakes, producing, among other things, a non-uniform dispersion of agricultural aerial sprays (Hackett 1981 and Wickens 1980). Furthermore, the pressure in the core of a tip vortex may be sufficiently low to trigger cavitation, which is important in turbomachinery impellers (Gostelow and Wong 1985) and inducers (Arndt 1987), and in marine propulsion (Huang 1987, Sponagle and Leggat 1984, Noordzij 1977, Kuiper 1981). In both these applications the cavitation may cause undesirable noise, structural vibration, and cavitation erosion. Tip vortices tend to be unsteady and hence strong noise sources. This is particularly problematic in helicopters (George et al. 1980) where the noise source is close to the passengers, and airplanes (McInerny et al. 1986, Brooks and Marcoloni 1984; refer to Hanson 1986 for a study of propfan tip noise).

In every application tip vortices act as lifting surface inefficiencies by decreasing the lift per unit length of the wing (because the flow downwash angle decreases the effective incidence angle of the wing near the tip). Tip vortex inefficiency is particularly consequential when the wing aspect ratio is small, as is often the case for military aircraft, small planes, and ship propellors. Tip clearance flow in axial flow fans (Ruden 1947) and compressors (Raines 1954) decrease their efficiency. An understanding of the tip vortex flow is also salient to the design of propfan blades (Vaczy and McCormick 1987). Even commercial aircraft may benefit from a "total drag reduction [of] ... 3-6%" when the tip vortex is alleviated (Webber and Dansby 1983)– adequate explanation of the active research into tip vortex modification (refer to Chapter IV). In fact, tip flow even plays an important role in the design of America's Cup yacht keels (Devoss 1986).

A final *raison d'être* of tip vortex research is the existence of regions of concentrated vorticity in many different engineering flows (e.g. wakes, meteorological flows, jets, some combustion processes, etc.). A reasonable expectation is that furthering our understanding of tip vortex flows will provide insight into other vortical flows.

I.3 Review of Pertinent Tip Vortex Research

A complete review of the tip vortex literature is impossible here–over 1000 papers have been published on the topic. Rather, this brief section outlines some of the more outstanding contributions to the field. Fairly complete reviews of the literature may be found in Donaldson and Bilanin (1975), Platzer and Sounders (1979), and Hoeijmakers (1983).

Tip vortices are a very well established field. Prandtl (1920 a,b) developed lifting surface theory, which describes the two dimensional flow over a finite aspect ratio wing. An analytical description of the inviscid rollup† process was formulated in the 1930's (Betz 1933).

The presence of axial flow in the trailing vortex affects the trailing vortex stability, including the possible occurrence of vortex breakdown (Hall 1972), and thus is worthy of study. Consider a streamline in the vortex core which originates upstream of a wing. If viscous and unsteady effects are neglected, the application of Bernoulli's equation from upstream of the wing where the pressure and velocity are p_∞ and U_∞, to the core where the pressure is $p < p_\infty$ (to maintain the centripetal acceleration) requires $U_c > U_\infty$. Batchelor (1964), who made this analysis, showed that a Rankine vortex with maximum tangential velocity $U_\theta = kU_\infty$ has $(U_c)_{max} = U_\infty\sqrt{1+2k^2}$. Batchelor also demonstrated through the use of an asymptotic analysis that viscous diffusion of the trailing vortex, which causes the core pressure to rise with downstream distance and hence imposes an adverse pressure gradient on the core fluid, decelerates the core fluid such that its velocity varies as $x^{-1}\log x$.

On the grounds that Batchelor's analysis is only valid hundreds of chords downstream of the foil (roughly 200-2000c for the experimental work done in this thesis),

† In recent aerodynamics papers the expression "roll-up" has become increasingly prevalent. The author is here merely carrying the language evolution to its logical next step.

a small perturbation study was undertaken by Moore and Saffman (1973) on the effect of core viscosity. They showed that either an axial velocity excess or deficit may exist in the core, depending on the tip loading, Reynolds number, and downstream distance. In view of their mathematical requirement that $|U_{xc} - U_\infty| \ll U_\infty$ and that the flow be steady and laminar (c.f. Chapter IV), one suspects their results have only limited applicability.

Numerical simulations of the rollup were done crudely at first (Westwater 1935), and then with progressively more care (Takami 1964 and Moore 1974). Moore in particular found that the trailing vortex (of an elliptical lift distribution wing) is elliptical in cross-section after substantial rollup. Many more recent numerical simulations have been performed. A summary of several of these is given in Chapter VI. Although a marked improvement in the quality of these simulations with time is evident, none of the simulations has provided as detailed a picture of the trailing vortex as that measured experimentally.

Attempts have been made to measure the tangential and axial velocity distributions around trailing vortices using LDV (Orloff and Grant 1973, Baker et al. 1974, Higuchi et al. 1986a), hot wire anemometry (Corsiglia et al. 1973, Chigier and Corsiglia 1972, Zalay 1976), and five-hole probes (McCormick 1968, Logan 1971). Although these techniques have the fairly severe limitations discussed in Chapter III, several characteristics of trailing vortices are known:

(i) The maximum tangential velocity around the vortex core at x/c=5 is on the order of $0.8U_\infty$ for $\alpha = 10°$.

(ii) The vortex core is not axisymmetric, and meanders in time–presumably due to freestream turbulence in the tunnel.

(iii) The core radius increases and $(U_\theta)_{max}$ decreases as x/c increases.

(iv) Well downstream of the foil an axial velocity deficit exists in the core.

Tip vortex cavitation is even less well understood than single phase tip flow, primarily because freestream (Arndt 1981, Gates and Acosta 1978) and surface (Holl

1968, Kuiper 1985) nuclei are additional parameters in the problem, and because two-phase effects are important when the cavitation number is reduced much below σ_i (for example, this explains why cavitation desinence occurs at $\sigma > \sigma_i$, and why vapour-filled trailing vortices are more stable than single phase vortices).

McCormick (1962) found experimentally that:

(i) σ_i increases weakly with Re ($\approx$ as $Re^{0.35}$).

(ii) σ_i increases as α increases.

(iii) σ_i is virtually independent of the aspect ratio when $AR > 1.5$.

Perhaps his most important finding was that roughening the pressure surface of a wing near its tip reduced the inception index, σ_i. No similar effect was seen for suction surface roughening. From this behaviour he inferred that, since σ_i is dependent on the vortex core size, the core size is substantially dependent on the pressure side boundary layer thickness. It is interesting to note that roughening the suction surface of a marine propellor (Arndt 1976) decreases σ_i, which suggests that centrifugal effects in propellor flow cause suction surface fluid to be incorporated in the trailing vortex. Readers interested in a discussion of propellor tip cavitation may refer to the recent study by Kuiper (1981).

Recently Katz (1984) and Arakeri and Acosta (1979) have demonstrated the importance of laminar separation on cavitation. Elliptical planform hydrofoils experience separation at low attack angles; it has been shown for these hydrofoils that the tip vortex inception behaviour can be partially understood by allowing for the effect of laminar separation (Arakeri et al. 1986, Arndt et al. 1985). Rectangular planform foils do not have separated flow regions at normal α (Green 1987), and consequently their inception characteristics cannot be explained in the same way.

I.4 Scope of the Present Work

Although tip vortices have been studied for many years, surprisingly much remains unknown about them. For example, *the transient static pressure inside a tip vortex core* has not been measured previously. The mean static pressure has only been measured using intrusive probes. An understanding of both of these quantities is clearly necessary to determine when cavitation may occur. The *fluctuating velocity of the tip vortex* has similarly never been measured prior to the present work. Knowledge thereof is certainly germane to an understanding of tip vortex cavitation, vortex breakdown, and vortex-structure interactions. This thesis is the first systematic treatise on *tip vortex flow Reynolds number effects.* As discussed in Chapter IV, many different proposals have been made for tip vortex alleviation devices, though few have found practical application. A *novel ring wing tip vortex modification device* which has potential for both marine propellor cavitation avoidance and aircraft wing efficiency improvement is described in Chapter IV. These are the main contributions of this thesis to scientific knowledge.

Chapter II is devoted to a description of the apparatus used during the experimental phase. Chapter III sets forth the techniques used to examine the tip vortex. Chapter IV is a presentation of most of the results of the present research, and a discussion of these results is given in Chapter V. Finally, Chapter VI recounts an unsuccessful attempt to simulate the flow numerically, and a summary and conclusions are the topics of Chapter VII.

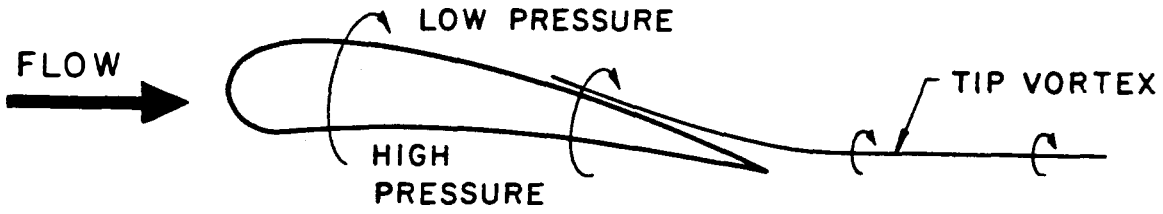

Figure I.1 Pressure Field Interpretation of Tip Vortices.

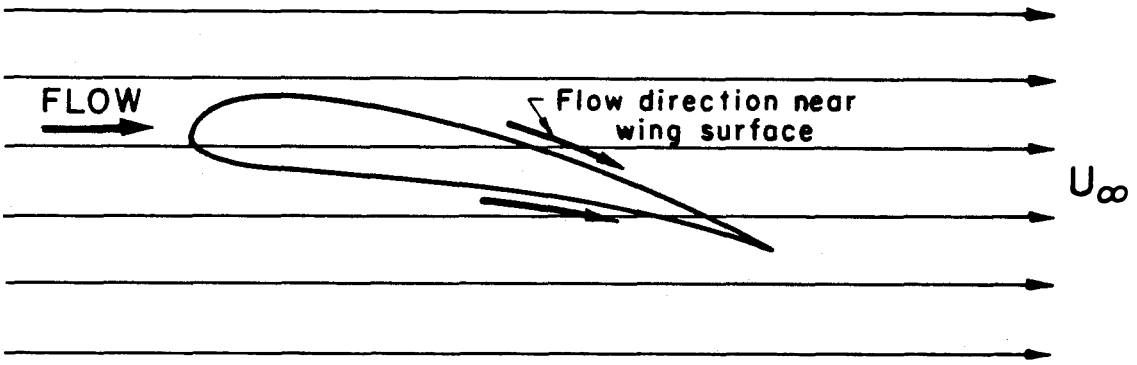

Figure I.2 Shear Layer Intrepretation of Tip Vortices.

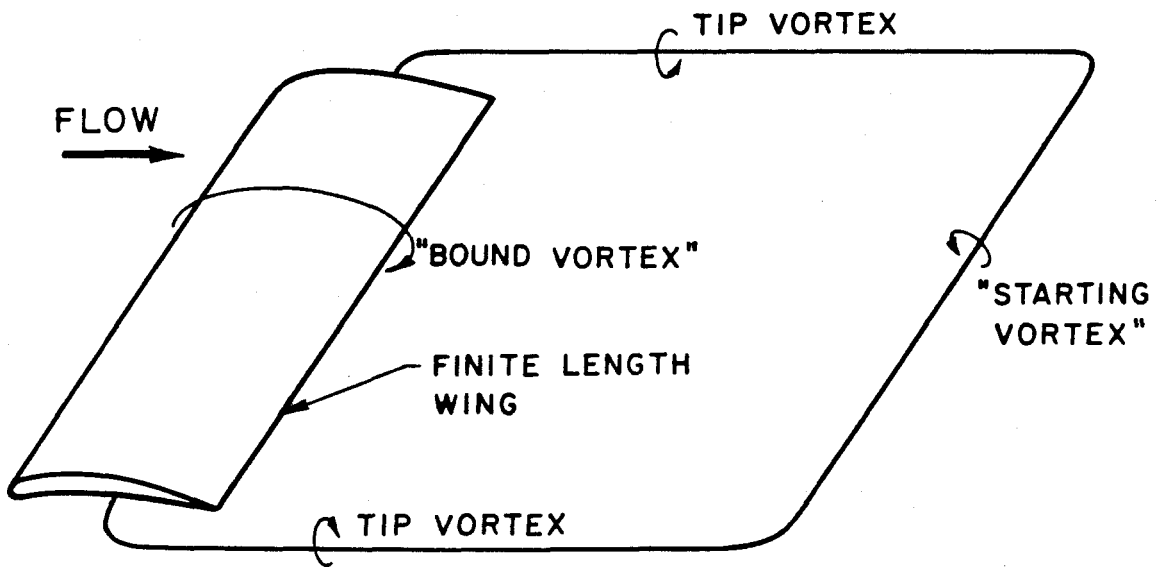

Figure I.3 Helmholtz Vortex Laws Interpretation of Tip Vortices.

Chapter II–EXPERIMENTAL APPARATUS

This chapter describes the three main components of the experimental apparutus: the Low Turbulence Water Tunnel (LTWT), the different hydrofoils and the hydrofoil mount, and the holocamera and bubble injection system which was used in much of the experimentation. Equipment used only during limited tests is documented in Chapter III.

II.1 Low Turbulence Water Tunnel

Gates (1977) has described in detail the LTWT– only a short overview is given here. The LTWT, a schematic of which is given as Figure II.1, possesses the following characteristics:

A/ Test Section Velocity

A mixed flow pump driven by a 30 HP DC motor pushes water around guide vanes at the tunnel bends, through two honeycombs and three screens, and then through a 14.5:1 contraction ratio nozzle prior to entry into the test section. These measures ensure that the freestream turbulence level in the test section does not exceed 0.04% (Gates 1977). The test section, 2.5m long, expands from a 0.3m$\times$0.3m cross-section at the inlet to a 0.3m $\times$ 0.36m high cross-section at the outlet. The test section velocity is variable in the range 0-10 m/s, and may be measured using a $Hg - H_2O$ manometer, or a pressure transducer connected to the manometer.

B/ Test Section Pressure

The test section pressure may be adjusted by using the vacuum pump to apply a partial vacuum to the pressure vessel. Test section pressures of from 20-120 kPa are attainable; both a $Hg - H_2O$ manometer and an attached pressure transducer may be used for its measurement.

C/ Water Quality

The dissolved air content of the tunnel water may be reduced from 15 ppm (saturation) to 3 ppm using the deaeration system. Because the tunnel contains

no resorber, the 30 second recirculation time of the tunnel (at maximum velocity) is an important restriction in view of the effect of freestream nuclei on cavitation. The dissolved air content is measured using a van Slyke Blood Gas Analyzer. Particulates suspended in the water during operation are filtered out using a diatomaceous earth filter. Several different metals are simultaneously present in the tunnel, which necessitates the use of dilute concentrations of Na_2CrO_4 (700 ppm) and KOH (pH=9–10) for corrosion control. These chemicals are not believed to affect the water's physical properties.

II.2 Hydrofoils and Mount

Four different hydrofoils were used over the course of the experimental work. Most testing was carried out on two foils: a NACA 66-209 hydrofoil with c=0.152m, s=0.175m; and a NACA 64-309 hydrofoil with c=0.152m, s=0.178m. Both foils have a design attack angle of 7.1°. The former foil was aluminum coated with smooth epoxy paint to preclude corrosion, and the latter was a smooth stainless steel foil with a flap (set at 0°) at x/c = 0.75. The other two foils were a symmetric brass Joukowski 12% thick foil with c=0.102m, s=0.190m (a portion of the foil was removable to give b=0.111m), and an epoxy-painted steel 0.0032m-thick, flat plate foil (having semicircular leading and trailing edges) with c=0.152m, s=0.169m. These foils were mounted by means of a long spindle passing through a false floor and the tunnel floor, which permitted attack angle adjustment with the test section filled. The attack angle could be measured with an error of ±0.1°. The 0.032m-thick false floor was necessary to accommodate the 0.019m-thick disk in which the hydrofoils were potted, and also served to both disrupt the test section floor boundary layer, and, more significantly, reduce the attainable cavitation number in the tunnel.

II.3 Holocamera and Bubble Injection System

The holographic system has been described in considerable detail previously

(O'Hern 1987, Katz et al. 1984, Katz 1979); only basic attributes will be described herein.

Figure II.2 is a schematic of the holocamera system. Triggering the flashlamp at high voltage causes it to emit intense light for $\approx$ 1500μs. If the Pockels cell is removed from the optical cavity, this light pulse will cause continuous lasing to occur roughly 200$-$700μs after triggering. The Pockels cell allows for Q-switching of the laser to produce either one (single pulse lasing for pressure measurements only) or two (double pulsed lasing for both pressure and velocity measurement) pulses of very short duration– typically 20ns–50ns – which are brief enough to freeze the motion of bubbles in the sample volume. A pulse spacing of 150μs was used while double pulsed lasing. These light pulses pass through the front mirror and neutral density filters (for hologram exposure control), and a small percentage of the light is directed by a beamsplitter onto a photodiode to obtain a crude record of the light intensity. The majority of the light is spatially filtered and then collimated before passage through the sample volume. Some of the light is diffracted by bubbles in the sample volume prior to reaching the recording medium. The interference formed by the interaction of the diffracted light ("the subject beam") with the majority, undiffracted light ("the reference beam"), is recorded on holographic film (Agfa-Gevaert 10E75 roll film) as a Fraunhofer, or "in-line," hologram. A photograph of the holographic system in position near the tunnel is labelled as Figure II. 3. After development of the film the hologram is reconstructed by illuminating it with collimated He-Ne laser light (refer to Figure II. 4). Measurements were made on a highly magnified portion of the real reconstructed image. The difference in the wavelenth of He-Ne (633nm) and ruby (694nm) laser light causes distances normal to the hologram plane to be contracted on reconstruction, an effect which is allowed for in the data manipulation.

The holographic system was used for recording bubbles, and, in a limited set of runs, heptane droplets, injected into the tunnel. For accurate pressure measurement it was crucial that the injected bubbles be of uniform size. It was also necessary that the concentration be low enough to avoid bubble interactions but high enough

to clearly define the trailing vortex core. After considerable effort a good solution was found– when uniform bubbles were required, bubble injection was done in the settling chamber just upstream of the LTWT nozzle†; when this was not a constraint, injection was carried out 0.25m upstream of the foil in the LTWT test section (the latter injection site chosen because the injector's tendency to clog made a readily accessible site useful). The bubble injector consisted of a 0.0064m o.d. stainless steel tube to which was silver-soldered a 0.0032m o.d. tube with a small machined brass tip. Glass nozzles consisting of 0.0016m o.d. glass capillary tubes pulled to a sharp point and then broken to yield an opening of $\approx 20\mu$m i.d. were installed on this brass tip, and sealed using 0.0016m i.d. Tygon tubing and wire (refer to Figure II.5). The injector was held in the settling tank in a relatively unintrusive H-frame; a pitot probe holder held the injector in the test section. Pressurized filtered dry air at 100-200kPa absolute, controllable by a regulator, was forced through the glass tip to produce bubbles. The flow rate was adjusted with a needle valve.

---

† It is thought that bubbles injected in the test section were not sufficiently uniform for pressure measurement because of the unsteady wake generated by the bubbles themselves at the local Reynolds number in the test section. The factor of 15 lower velocities that exist in the settling chamber are one explanation for the uniform bubbles produced by an injector located there. Injecting bubbles in the settling tank has a significant shortcoming. Number continuity implies the test section bubbles will be spaced 15 times farther apart than bubbles injected in the test section. Intuitively, it is reasonable to anticipate that 150μm bubbles can be spaced no closer than 200μm apart at the injection site. These bubbles would be 3mm apart in the test section. Since the holographic sample length is only 45mm, a maximum of 15 bubbles would be recorded in each hologram– a severe limitation in the data-taking rate.

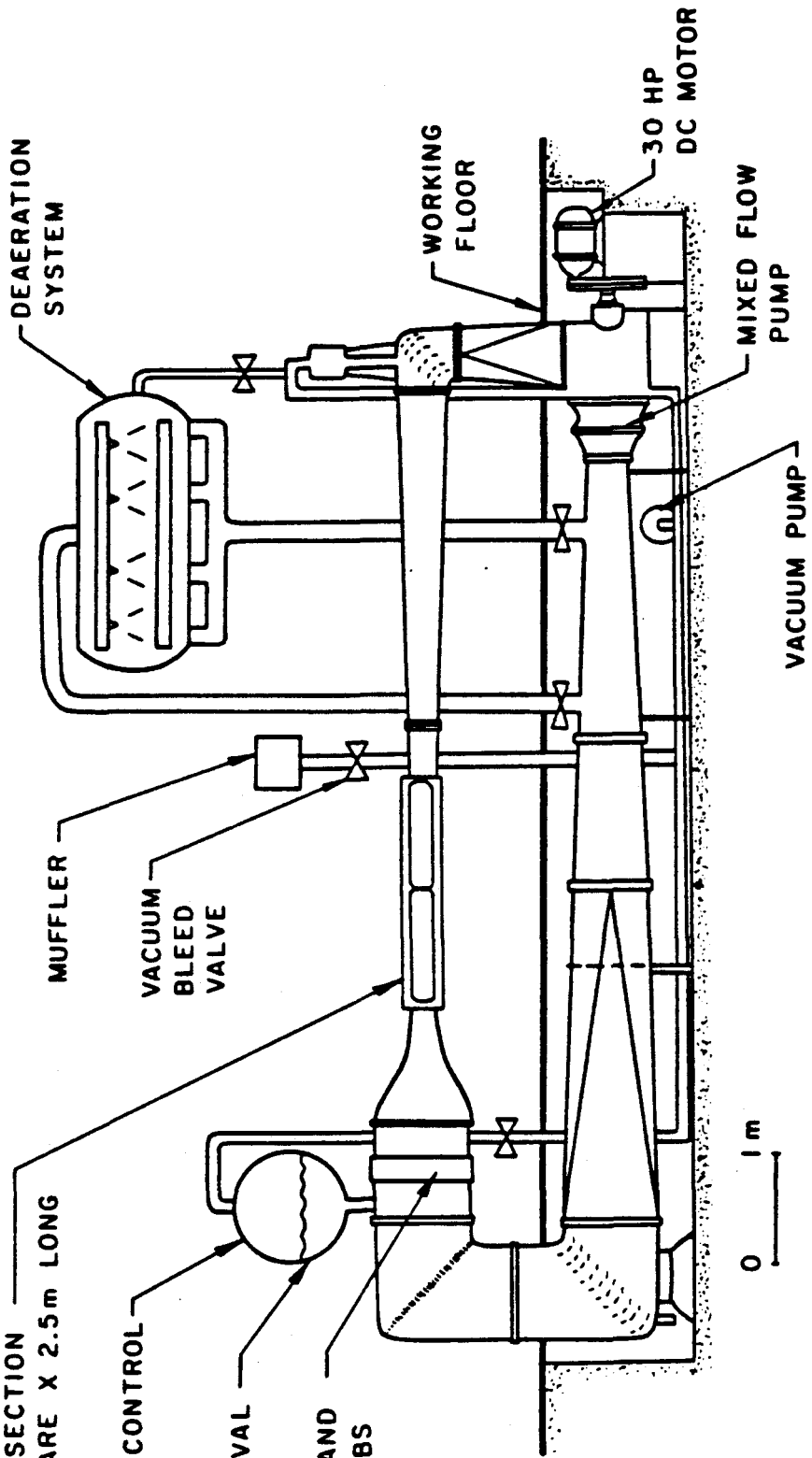

Figure II.1 Low Turbulence Water Tunnel – schematic.

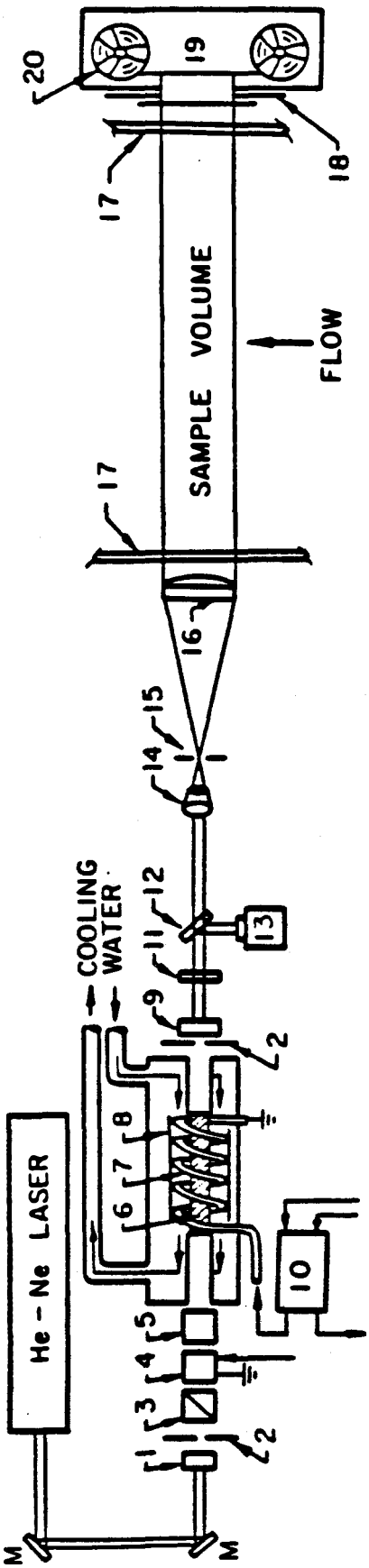

1. BACK MIRROR
2. IRIS APERTURE
3. POLARIZER
4. POCKELS CELL
5. POLARIZER
6. RUBY ROD
7. XENON FLASH LAMP
8. REFLECTOR
9. FRONT MIRROR-SAPPHIRE ETALON
10. TRIGGER TRANSFORMER
11. NEUTRAL DENSITY FILTER
12. BEAM SPLITTER (4% REFLECTIVITY)
13. PIN DIODE
M. MIRROR
14. MICROSCOPE OBJECTIVE
15. SPATIAL FILTER-10μ PIN HOLE
16. COLLIMATING LENS
17. GLASS WINDOWS OF THE TUNNEL
18. SHUTTER
19. AUTOMATIC FILM DRIVE
20. HOLOGRAPHIC FILM

Figure II.2 In-line Holographic System.

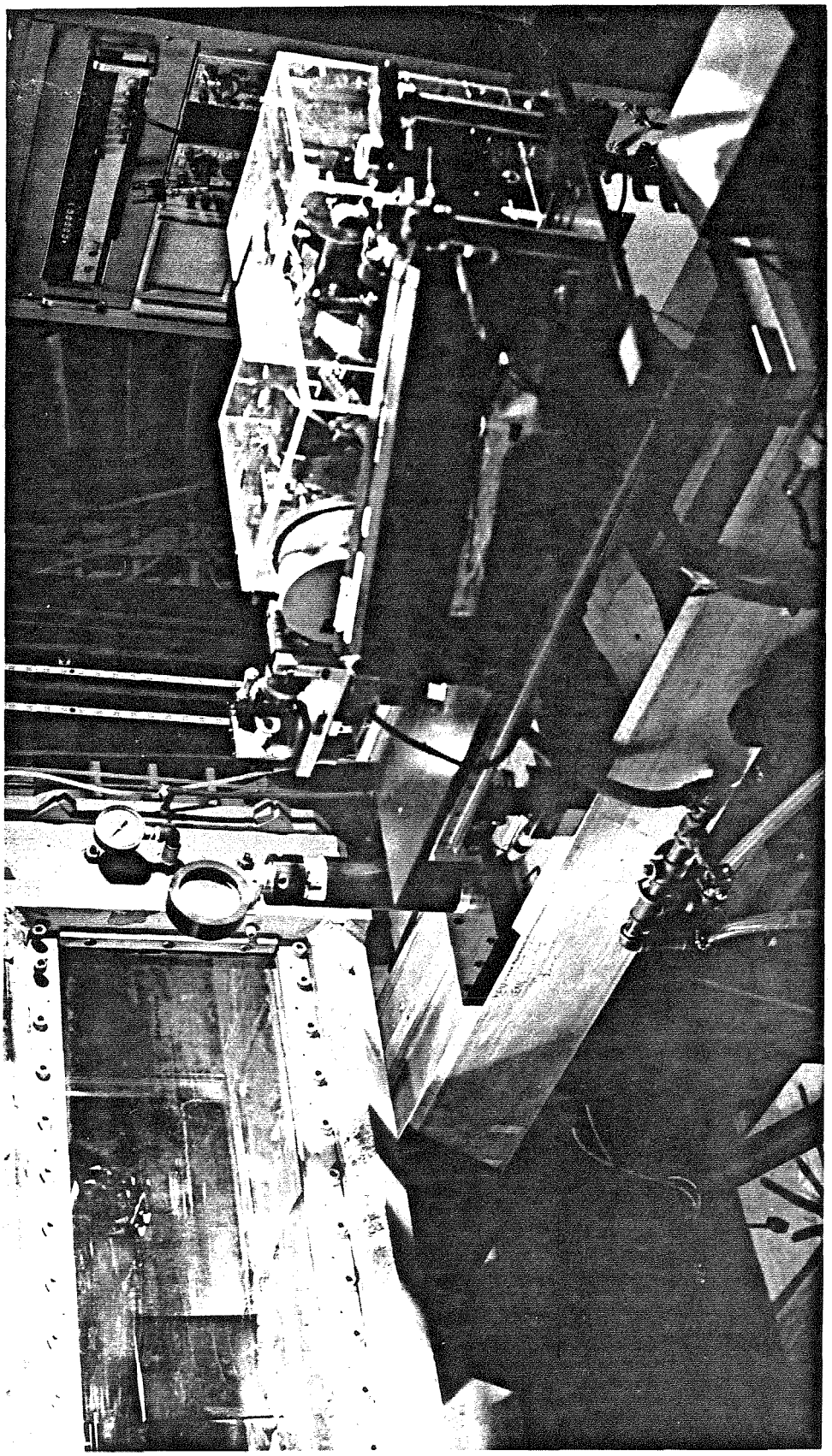

Figure II.3 Installation of the Holographic System near the LTWT (the hydrofoil is visible in the test section).

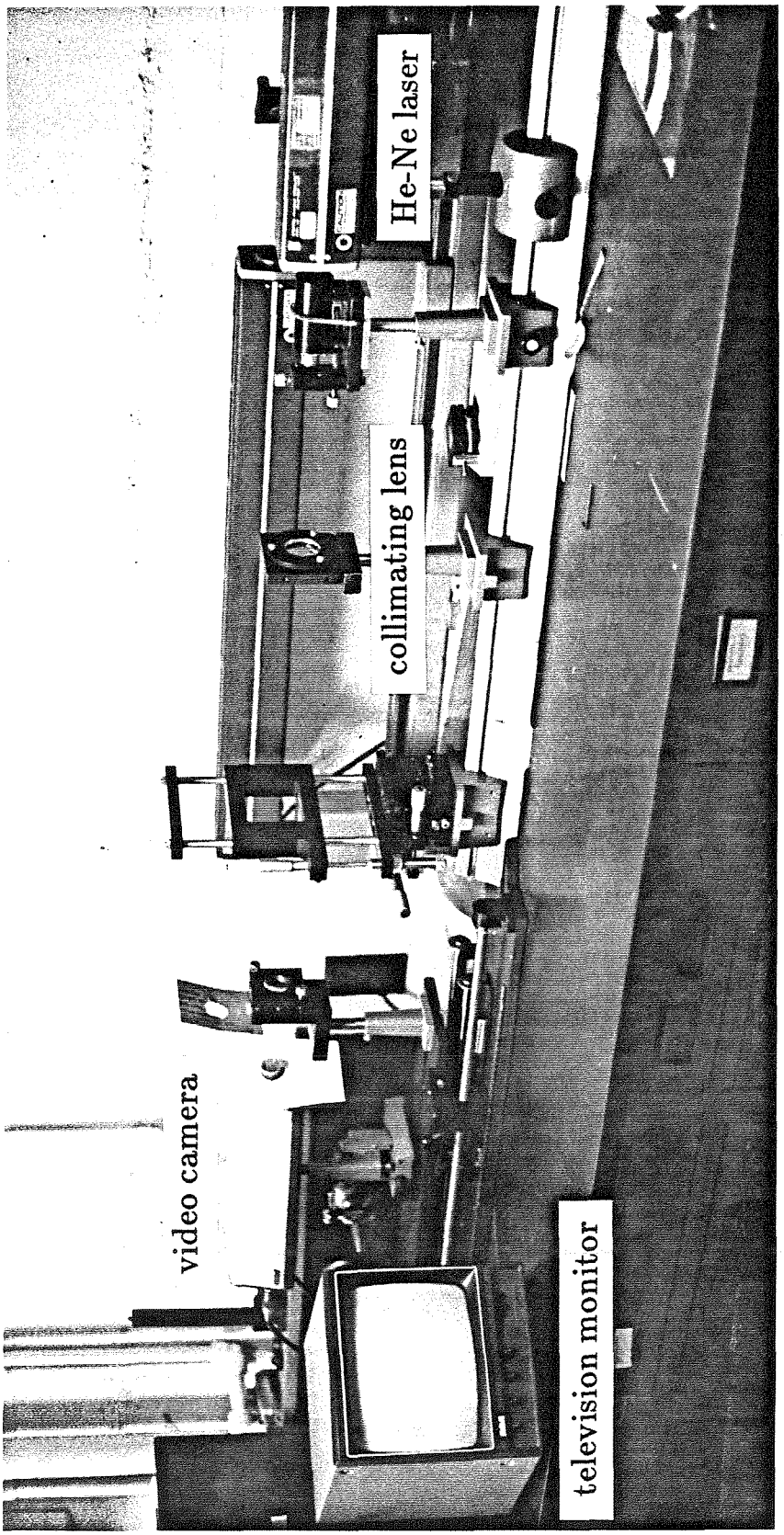

Figure II.4 Holographic Reconstruction System.

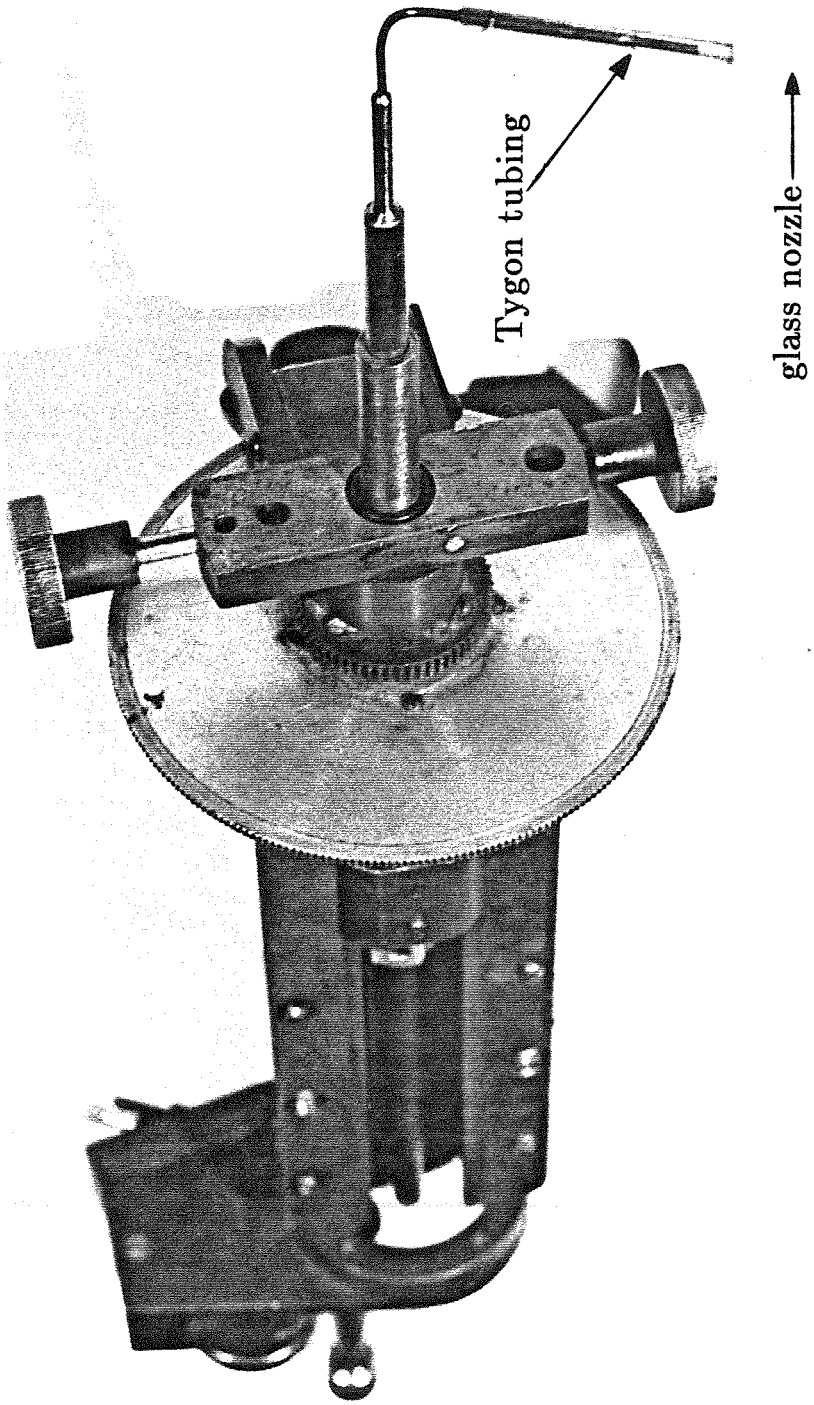

Figure II.5 The Bubble Injector.

Chapter III–EXPERIMENTAL TECHNIQUES

Several different experimental techniques were used to examine the trailing vortices. A qualitative impression of the vortex rollup process was gleaned from surface flow visualization photographs. Double pulsed holograms provided detailed quantitative information about the velocity field around the trailing vortex. Pressure field information was obtained from single pulse holograms of initially uniform bubbles. Photographs of the tip vortex cavitation and cavitation inception measurement round out the experimental techniques listing.

Before delving into a detailed discussion of the different techniques, some characteristics of trailing vortices which dictate the choice of measurement method will be described.

It has been known for many years (Holl et al. 1972, Holman and Moore 1961) that vortices are sensitive to even very small intrusive probes. Consequently, only non-intrusive techniques (holography, LDV, speckle photography, etc.) yield consistently reliable data. Measurements taken by previous investigators using 5-hole probes (e.g. Snedeker 1972, Logan 1971, McCormick et al. 1968), vortex meters (Zalay 1976, Jarvinen 1973), and hot wire probes (e.g. Corsiglia et al. 1973, Chigier and Corsiglia 1972, Chigier and Corsiglia 1971. Possibly acceptable when the vortex is not near breakdown.) are subject to doubt on these grounds.

Vortex meandering, the tendency for vortices to chaotically move about some mean location, was also observed long ago (e.g. Baker et al. 1974, Corsiglia et al. 1973). The meandering, which is thought to be due to freestream turbulence, causes the trailing vortex to move randomly across a fixed probe (or LDV "probe volume"). This means that at one instant in time the probe may reside in the vortex core while at subsequent times it may lie in the irrotational flow surrounding the core. The author has observed, for example, that in the low turbulence facility used in this study trailing vortices meander laterally by 0.01m or 0.02m (roughly 2-4 R_c) about a mean location for $x/c > 3$. The meander is smaller for $x/c < 3$. When hot wire, pressure probe, or LDV data is temporally averaged at a fixed location, the result is

equivalent to spatially averaging over several R_c. Baker et al. (1974) attempted to allow for this meandering analytically, but with questionable effect (they measured maximum tangential velocities of $\approx 0.22U_\infty$ at x/c=10 for a foil at $\alpha = 10°$, which is wrong by at least a factor of 3). Two reasonable methodologies exist for coping with the vortex meandering problem – scanning across the approximate vortex location very rapidly and discarding all scans which do not pass through the vortex center (Corsiglia et al. 1973), or accurately recording the exact vortex location whenever data is acquired (the tack taken in this study).

Three other characteristics of trailing vortices have only been discovered recently (Green 1988) – strong unsteadiness of the core flow, very small core dimension ($O(10^{-3}c)$), and vortex core structure. The poor spatial resolution, susceptibility to vortex meander, and the fact that they are only point – not global – measurements all mitigated against the detection of these phenomena by the above techniques.

III.1 Surface Flow Visualization

The first step in surface flow visualization (SFV) was the removal of the hydrofoil from the tunnel. A grid was drawn on the foil, and a viscous oil-based paint/linseed oil mixture was dotted on the grid markings. Dot uniformity was adequate for the purposes of this study. The precise linseed oil concentration required to produce good results was dependent on the flow velocity, angle of attack, foil surface finish, and oil-based paint used. Typically 1 part oil in 8 parts Pictor oil-based white paint was appropriate. The paint mixture was found to be highly non-Newtonian, not deforming substantially until a high shearing stress was applied. The foil thus dotted (see Figure III.1) was returned to the tunnel, the 0° attack angle was remeasured, and the desired attack angle chosen. After tunnel refilling excess air was bled off and the tunnel water was rapidly accelerated up to a set speed. Due to the highly thixotropic behaviour of the dot mixture, and its slow motion, virtually all dot movement occurred at very nearly the set tunnel velocity. The foil with its smeared dots was subsequently removed from the tunnel and

photographed. Photographic enlargements were used to measure flow downwash angles.

SFV is a useful technique because it is non-intrusive and a good source of global flow information. Squires (in Maltby 1962) has analytically demonstrated that the paint flow direction matches the local boundary layer flow direction, except near points of small skin friction (e.g. near separation). The smear line length is a very rough measure of the local shearing stress magnitude (the length depends, in addition, on the flow history, the paint viscosity, and the foil surface condition).

III.2 Double Pulsed Holographic Measurement of Instantaneous Velocity

Consider injecting microbubbles, or any other buoyant particles such as oil drops, upstream of a hydrofoil mounted in a water tunnel. In this research phase the injector was located 0.25m upstream of the foil. The bubbles (70μm-400μm in diameter for this study) act principally as Lagrangian flow markers, but, because a net centripetal force (due to the imposed pressure field) slowly drives some of the bubbles into the vortex core, they very accurately define the instantaneous vortex core location. Double pulsed in-line holograms – two holograms of a specified volume taken in quick (150μs time separation) succession – were recorded on holographic film. On reconstruction of the holograms the displacement of each bubble between the two instants in time was measured (refer to Figure III.2), from which the in-plane velocity could be inferred. This velocimetry technique was validated by determining the velocity distribution near the leading edge of the NACA 66-209 foil (refer to Figure III.3). Theoretically, one should be able to obtain complete three-dimensional particle location information from a hologram. However, even on the best holograms out-of-plane displacements could be measured to only $\pm$130μm, which is not surprising given the typical bubble size and the Fraunhofer holography method used. This shortcoming limited the data to accurate in-plane (2D) velocities located accurately in 3D space. The 2D velocity, in conjunction with precise knowledge of the instantaneous location of the vortex core, yielded the radial and axial velocity of each bubble about the core (and the radial distance of the bubble

from the core). Figure III.4 illustrates this process. Only values of θ near 0° or 180° will produce accurate tangential velocity measurements; small errors in U_y are greatly magnified by the secθ factor when $|\theta \pm \pi/2|$ is small. The author has found that restricting tangential velocity data to $|\theta \pm \pi/2| > \pi/6$ gives sufficiently accurate results. Limiting the data in this fashion also reduces the small contribution of the radial velocity to the measured U_y (and hence to the inferred U_θ). An estimate of the maximum radial velocity relative to the water, which is a measure of how closely the bubbles behave as Lagrangian tracers, is given in Appendix B.

III.3 Single Pulse Holography Determination of Instantaneous Pressure

Ooi (1981) introduced the use of air bubbles as Lagrangian static pressure sensors. Consider a spherically symmetric (for all time) bubble exposed to a far field pressure $p_\infty(t)$. The bubble responds to the pressure field by changing its radius as:

$$\rho R\ddot{R} + \frac{3}{2}\rho\dot{R}^2 = p_g - p_\infty + p_v - \frac{2S}{R} - \frac{4\nu\dot{R}}{R} \qquad \text{(III.3.1)}$$

If the bubble response time is small compared with typical pressure fluctuation times, then the bubble responds quasistatically to the external pressure as:

$$p_\infty(t) = p_g + p_v - \frac{2S}{R} \qquad \text{(III.3.2)}$$

where p_g is the internal gas pressure and p_v is the vapour pressure. Provided that the bubble deformation is not too large, the appropriate response time is approximately 1/(bubble natural frequency) (Ooi and Acosta 1983), which for a 100μm radius bubble is about 100μs. Smaller bubbles respond more quickly; the response time varies as $R^{1.5}$ (Arndt and George 1979).

If the bubble undergoes a polytropic expansion from an initial radius R_o and external pressure p_o, to a final radius R_1 (at the location '1'), then p_g may be expressed as:

$$p_g = \left(p_o + \frac{2S}{R_o}\right)\left(\frac{R_o}{R_1}\right)^{3n} \qquad \text{(III.3.3)}$$

This equation is predicated on the assumption that none of the gas passes into solution. Holl (1970) has invoked the theoretical results of Epstein and Plesset (1950) to show that the time for a 100μm radius bubble to be reduced to 50μm by dissolution is 5000 s. Clearly the bubble radius reduction in the up to 0.4 s (for x/c=10, U_∞ = 5m/s) between the time when measurements of p_o and p_1 are made, is negligible.

The injected air bubbles are essentially dry, and very little evaporation of water into the bubbles occurs over the short time between injection and measurement, so the contribution of p_v may be neglected. Then, III.3.2 and III.3.3 together imply:

$$p_1 = \left(p_o + \frac{2S}{R_o}\right)\left(\frac{R_o}{R_1}\right)^{3n} - \frac{2S}{R_1} \qquad \text{(III.3.4)}$$

which means that if at a reference location (the test section entrance) p_o and R_o are measured, a measurement of the bubble radius, R_1, at a second location is implicitly a measure of the local static pressure, p_1, there. It remains to determine the value of n. If the time from when the bubble was last in thermal equilibrium to the present is large relative to the bubble thermal response time, then the bubble gas behaves isothermally. We may crudely calculate the bubble thermal response time as:

$$\tau = \frac{\rho c_v R}{3h} \qquad \text{(III.3.5)}$$

Since the speed of the gas within the bubble is small, a reasonable guess of the heat transfer coefficient is h=10W/m^{2}K. Using properties for a 100μm radius bubble, this gives $\tau \approx 3 \times 10^{-3}$s. Apparently, the bubbles respond isothermally to the generally lower mean pressure in the trailing vortex core, but cannot be assumed to have an isothermal response to the very brief pressure transients that occur in the core (refer to Chapter IV). To summarize, then, n=1 will be assumed when analyzing the results, but it is recognized that an error will be incurred in this approximation when the core pressure is quickly varying.

Rather than follow the motion of an individual bubble downstream as suggested by Equation III.3.4, bubbles of uniform size were continuously injected upstream of

the test section. Measurements of their radii, R_1, in the region of interest, and the uniform radius R_o (determined by taking several holograms of the bubbles at the test section entrance and averaging their measured sizes) and p_o, determined the local pressures p_1 (refer to Figure III.5). The difficulty with this approach is that bubble uniformity is crucial. Much effort was expended before a final acceptable injection site in the settling tank upstream of the tunnel nozzle was found. Figure III.6 is evidence that uniform bubbles were attained – 95% of the bubbles had radii within 3% of the mean value.

No previous author has calculated the error involved in measuring static pressures using this technique. Such a calculation is, if not invaluable, certainly instructive. For a typical injected 150μm diameter bubble, the surface tension term may be neglected relative to the external pressure term in Equation III.3.4, whence it may be rewritten as:

$$p_1 = p_o \left(\frac{R_o}{R_1} \right)^{3n} \qquad \text{(III.3.6)}$$

The finite resolution of the holographic system limits the accuracy of measurements of bubble diameter to $\pm 5\mu$m (O'Hern 1987) (this corresponds with $\pm$1mm on the monitor at normal magnification), so the error in R_1 is $\approx 3\%$. Similarly, the error in R_o is $\approx 3\%$ (if not higher, due to the initial slight non-uniformity in the bubble sizes). If isothermal bubble growth is assumed, then the error in p_1 is 7%. If adiabatic bubble growth is assumed, and a slightly higher error in $R_o \approx 5\%$ is postulated, then the error in p_1 is a substantial 12%. Consider measuring $p_o = 100$ kPa, and R_o and R_1 such that $p_1 = 90$ kPa. The error in p_1 (6 or 11 kPa depending on the scheme) is so large that the quantity of interest, $p_o - p_1 = 10 \pm (6 \text{ or } 11)$kPa is meaningless. To clarify this point, what we wish to measure is the difference between two large quantities, one of which is known precisely and the other of which is subject to considerable error. Performing the subtraction amplifies the relative error.

This problem may be addressed in two ways (the bubble radius is fixed by the aforementioned bubble response time limitations). By increasing U_∞ , $p_o - p_1$ is

increased, which reduces the relative error (e.g. $p_o = 100$ kPa, $p_1 = 30$ kPa implies $p_o - p_1 = 70 \pm$ (2 or 4)kPa). A related but subtly different approach is to reduce p_o so that p_1 is very small, which also reduces the relative error (e.g. $p_o = 20$ kPa, $p_1 = 4$ kPa implies $p_o - p_1 = 16 \pm$ (0.3 or 0.5)kPa). Both schemes were utilized to yield the results of Chapter IV.

III.4 Cavitation Measurements

With the foil in the tunnel, gradually U_∞ was increased and p_∞ decreased. At the moment of cavitation inception (as evidenced by the sudden appearance of at least one macroscopic bubble per second in the trailing vortex core under stroboscopic illumination) U_∞ and p_∞ were measured. The LTWT water was circulated for at least 5 minutes at high pressure and low velocity between measurements to return the freestream nuclei concentration to its steady state value (see Katz 1984). This procedure is necessary due to the lack of a tunnel resorber.

The range over which tunnel pressure may be changed is nowhere near sufficient to reduce σ by the factor of 5 necessary to cover the "cavitation bucket" extremes. Consequently, the tunnel velocity was also altered between different measurements. The Reynolds number at which σ_i was measured varies by as much as a factor of 1.5 over each plot in Chapter IV. However, at this Reynolds number McCormick (1962) has found that σ_i is not a strong function of Re, and is certainly much more strongly dependent on α and the dissolved air content.

Flash and time exposure photographs of both inception and more developed cavitation were taken for reference purposes.

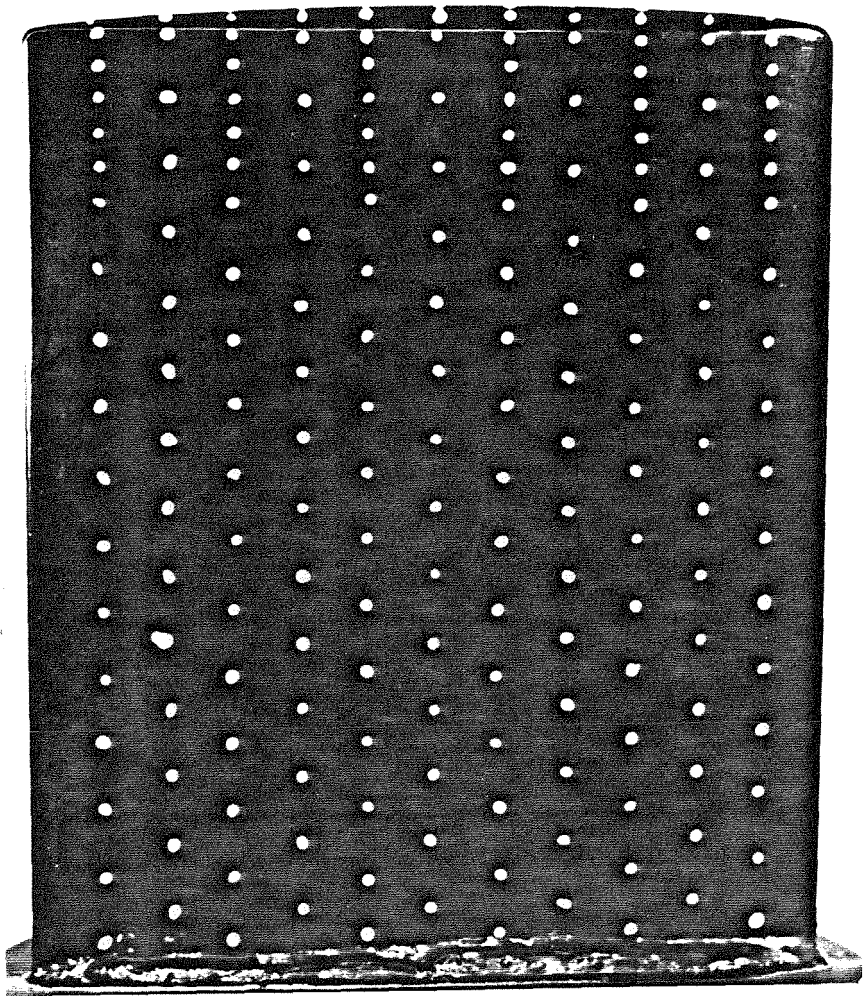

Figure III.1 Hydrofoil Dotted for SFV in the LTWT.

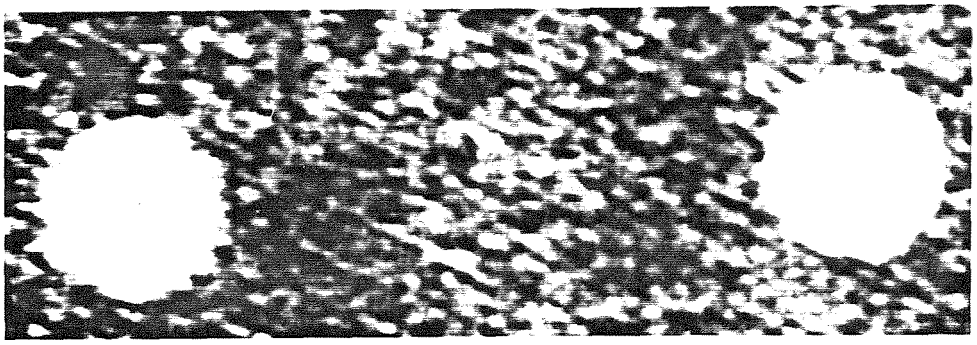

Figure III.2 A Typical Double Pulsed Hologram Pair.

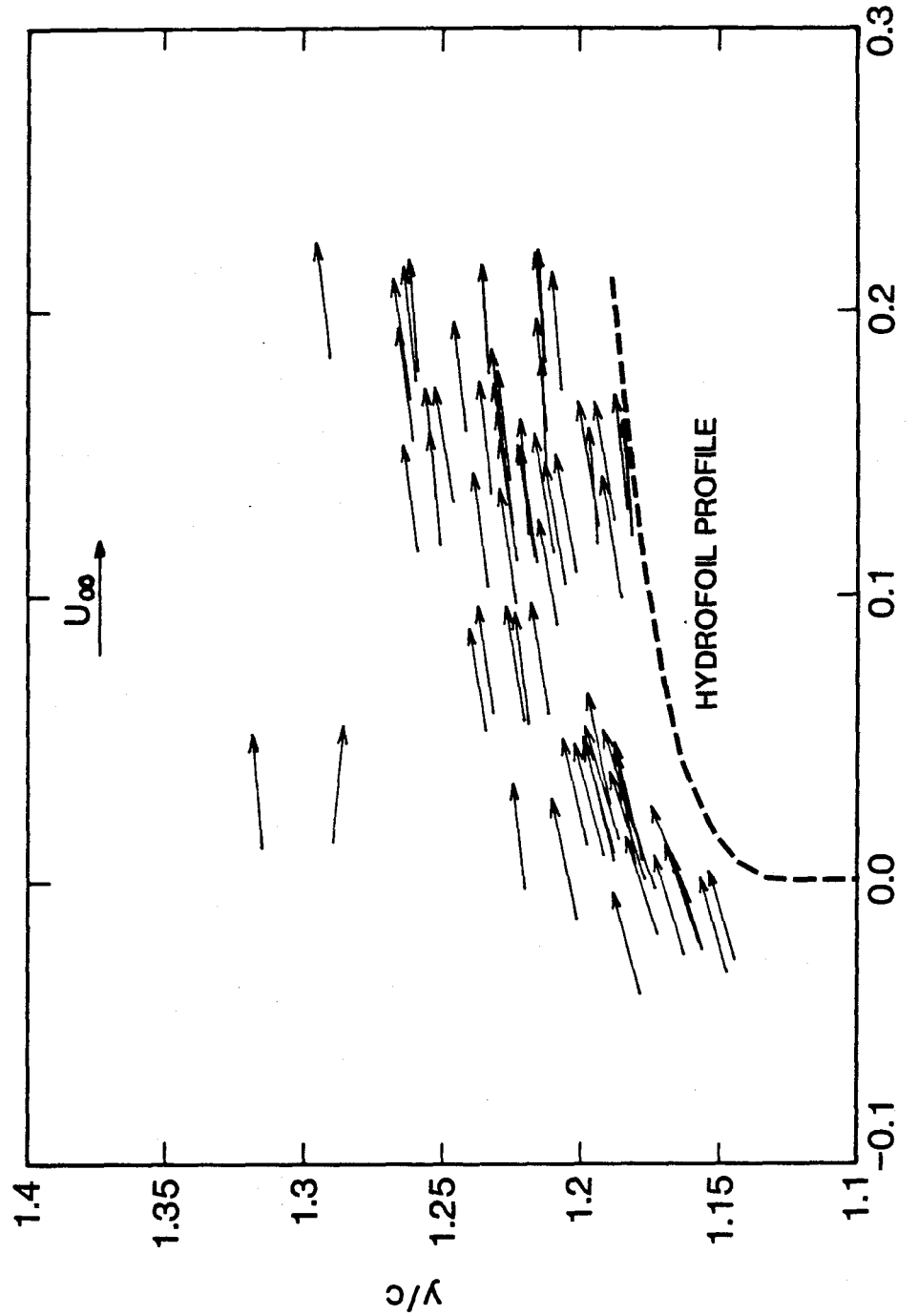

Figure III.3 Validating the Double Pulsed Holography Technique. In plane velocity vectors near the foil leading edge. U_∞ was measured manometrically.

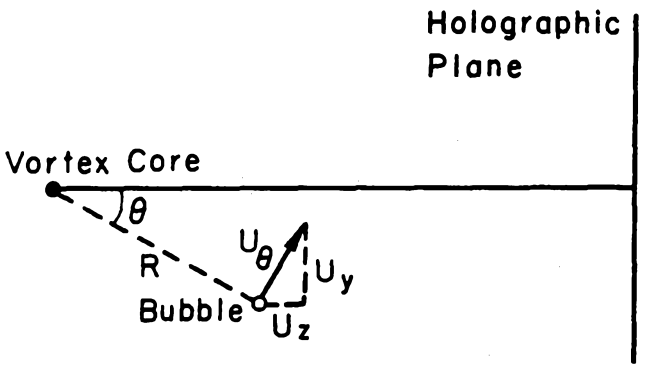

$$U_\theta = U_y \sec\theta$$

Figure III.4 Geometry of Tangential Velocity Measurement.

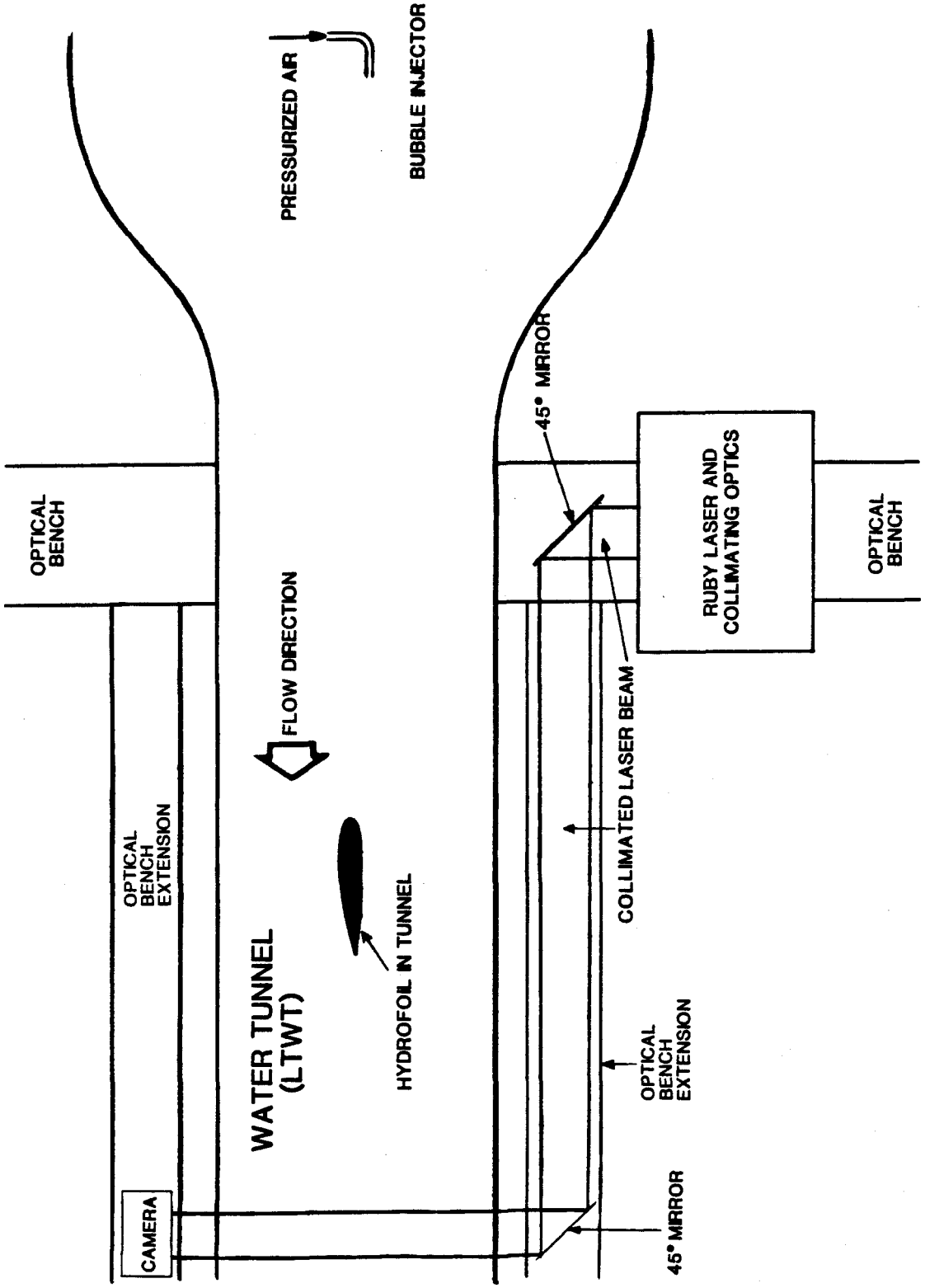

Figure III.5 Single Pulse Holographic System for Pressure Measurement.

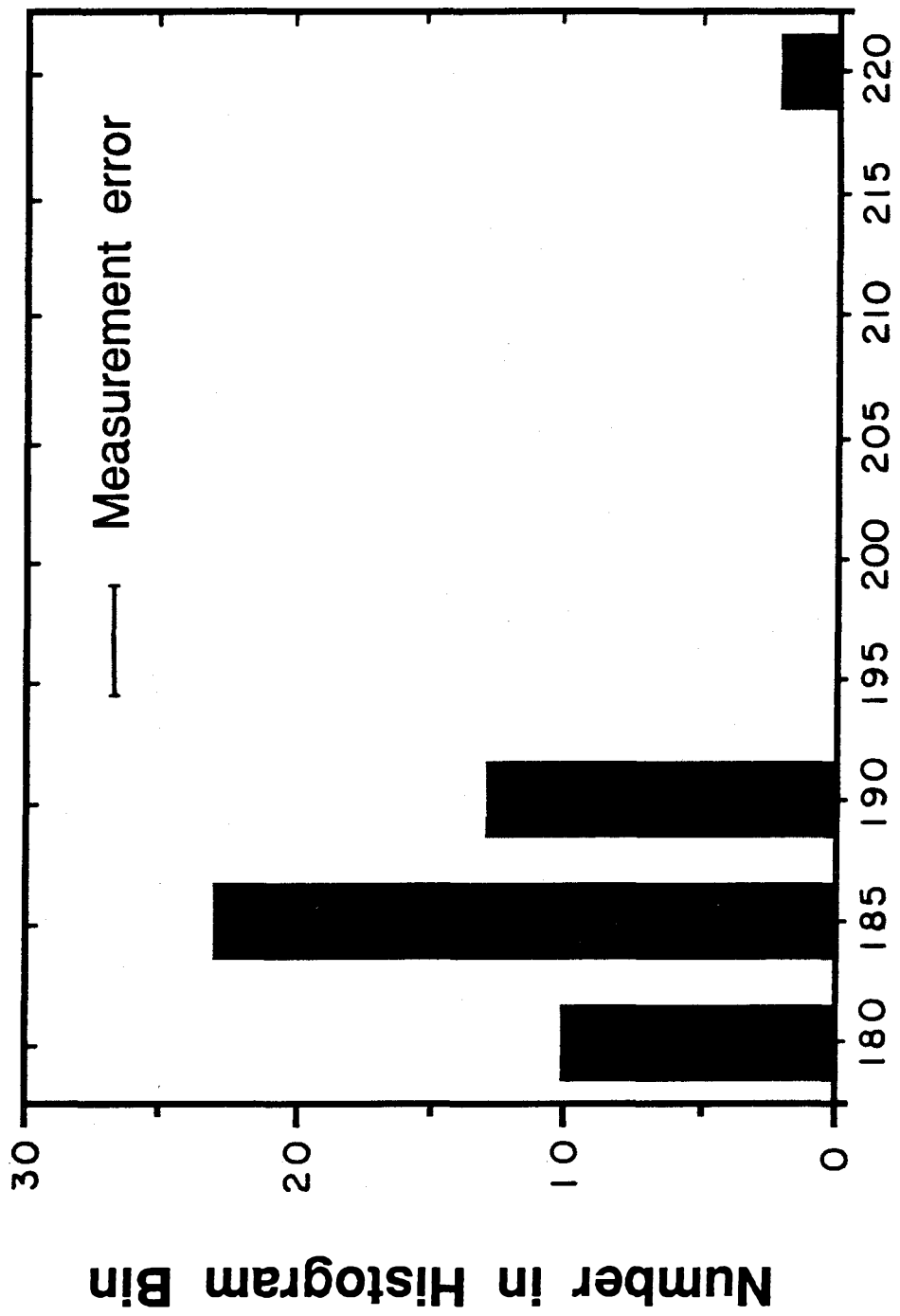

Figure III.6 Injected Bubble Size Distribution in the Tunnel Test Section.

Chapter IV–RESULTS

This chapter is devoted to a presentation of the experimental results. The first section of this chapter displays the results of SFV (described in III.1) carried out on two basic wings – the 66-209 wing with a rounded tip, and the 64-309 rounded tip wing. An exposition of the double pulsed holography results (refer to III.2) for the 66-209 wing is given in section two, and of the single pulse holography results (refer to III.3) in section three. Section four contains the cavitation inception results, and section five is the repository of wing tip modification results.

IV.1 Vortex Rollup

Surface flow visualization is a particularly graphic technique for revealing the the flow pattern near the foil surface. SFV photographs thus prove helpful in qualitatively understanding early stages of the vortex rollup process. A surprising amount of hard data may also be gleaned from these pictures.

All of the SFV photos (with the sole exception of Figure IV.8) were taken at Reynolds numbers of $1.2 - 1.5 \times 10^6$. For all cases the flow is right to left on the pressure side, left to right on the suction side, and right to left on the inboard view. Additional SFV photographs are included in Chapter IV.5 and Appendix A.

Figure IV.1(a,b,c) is a series of SFV photographs of the 64-309 foil at $\alpha = 7°$, the design angle of attack. A wing/wall interaction on the suction side is apparent in the region $x/c > 0.5$, $y/s < 0.2$, which precedes the wake formation occurring at higher α (refer to Figure IV.4). No equivalent interaction is seen on the pressure surface. Substantially different shearing stress magnitudes on the suction surface exist at y/s=0.5 and x/c=0.1 (small), x/c=0.3 (large), and x/c=0.7 (moderate) – in qualitative agreement with two-dimensional potential flow predictions. The pressure surface shearing stress magnitude is low near the leading edge and much higher for $x/c > 0.3$.

Strong indications of the initial vortex core rollup are apparent at y/s=0.95, x/c=0.5; an observation that will be referred to in Chapter V. A physical interpreta-

tion of the smear lines in the vicinity of the tip (Figure A.2.1 is particularly graphic in this respect) is presented as Figure IV.2. Significant inboard and outboard flow due to the tip is apparent in the photographs. The flow angles are quantified in Figure IV.3(a) (refer to Figure IV.1 for the definition of ϕ). It is evident that whereas the pressure side displays the strong tip loading one would anticipate from a rectangular planform wing, the suction side has a much less pronounced tip effect, even in regions where the tip vortex rollup influence is slight. The reason for this load distribution is not understood, though it does agree fairly well with the X-wire measurements of Francis and Kennedy (1979).

The downwash angle at the tip is the angle made by the smear lines with respect to the chordline, measured on the chordline at the tip. This angle (Figure IV.3(b)) is on the order of 40°, and increases along the chord length. The measured large downwash angles are interesting because they imply tangential velocities around the trailing vortex up to $2U_\infty$.

Figure IV.4 reflects the surface flow pattern at $\alpha = 12°$. All of the features present in Figure IV.1 are enhanced here: the wing/wall interaction is stronger, with some signs of unsteady wake formation, and the vortex rollup is more pronounced and has moved upstream on the wing to x/c=0.3. Francis and Kennedy (1979) speculated on the upstream motion of the vortex rollup position – "one would expect vortex spillover with increasing incidence," and cite the higher tip lift increment measured experimentally (Pearson 1937) and confirmed computationally (Maskew 1976) as support. This is the first time this behaviour has been directly observed. A very small unsteady separated flow region is indicated by the upstream motion of some of the dots near $y/s < 0.3$, x/c=0.08.

The surface flow at $\alpha = 3°$ is documented in Figure IV.5. Relative to $\alpha = 7°$ the vortex rollup location is farther back on the foil (near x/c=0.7), and all of the downwash and inboard flow angles are much smaller than for $\alpha = 7°$ as a result of the smaller total lift.

A sequence of SFV images of the NACA 66-209 round tip foil at increasing α

are to be found in Figures IV.6 – IV.10. A comparison of Figures IV.7 and IV.8 reveals that Reynolds number effects on the rollup process ($5\times10^5 \leq Re \leq 1.5\times10^6$) are slight. This observation is borne out by a quantitative comparison of downwash angles at the tip (Figure IV.11). The similarities between the surface flow patterns on the 66-209 and 64-209 foils are manifest. One difference is the 66-209 foil does not show suction surface leading edge separation below $\alpha = 13°$, in contrast with the 64-309 separated flow occurring at $\alpha = 12°$.

The downwash angle (unrelated to the lifting line theory "downwash angle") at the tip (Figure IV.12) scales as $\alpha - \alpha_o$ for $x/c < 0.6$, but at larger values of x/c, ϵ' no longer does so (Figure IV.13). The former observation is in accord with linear wing theory, whereas the latter observation is thought to disagree with linear theory because of tip vortex rollup.

In summary, examination of various surface flow visualization photographs has shown:

1. a strong wing/wall interaction for $y/s < 0.2$, particularly for higher α.
2. highly three dimensional flow near the tip. When $\alpha \geq 8°$ the flow is significantly three dimensional everywhere on the span.
3. rollup is only weakly dependent on Re.
4. the load distribution on the suction side is qualitatively not as concentrated near the tip as one might expect from experience with lifting line computations.
5. the location of vortex rollup moves forward (to smaller x/c) as α increases.
6. the downwash angle at the tip, for $x/c < 0.6$, is proportional to the wing lift angle.

IV.2 Trailing Vortex Velocity Distribution

This section is divided into two major parts – the first devoted to justifying the air bubble injection/double pulsed holography technique for velocity measurement, and the second to presenting the multitudinous data acquired around the NACA

66-209 rounded tip foil vortex core.

IV.2.1 Validating the Air Bubble Injection/Holography Technique

Typical air bubble injection velocity results are displayed in Figure IV.14. Different symbols in the figure represent data acquired from 5 holograms taken over a span of two hours. The excellent correspondence of the data implies both that the gross flow behaviour (e.g. $\overline{U_{xc}}$, $\overline{U_\theta(R)}$, $\overline{U'_{xc}}$, etc.) is invariant with time, and that the velocity distribution of the bubbles may be accurately inferred from holograms.

A natural question arises– Is the velocity distribution of the bubbles equivalent to that of the single phase fluid around the core? Three different phenomena might reasonably be expected to cause the bubble motion to differ from that of the single phase vortex – bubble/vortex interactions causing gross overall changes in the flow pattern, bubble/flow field interactions producing a bubble velocity which differs from that of the surrounding fluid, and bubble/bubble interactions which have the same effect.

It is highly unlikely that bubble/vortex interactions could produce overall changes in the flow pattern because outside the vortex core the bubble void fraction was on the order of 10^{-6}, a level well below that at which the flow would exhibit significant two phase behaviour. The bubble density in the core is typically much larger than in the surrounding fluid. However, all of the unusual core behaviour described in this section has been observed at inter-bubble spacings of from $3R_B$ to 20 or more R_B, which strongly suggests that gross interactions of bubbles with the vortex do not play a role in the core either.

The second possible cause of bubble velocity error is now considered. Bubbles may have a relative velocity with respect to the surrounding fluid if a pressure gradient exists within the fluid. As discussed in Appendix B, this relative (or "slip") velocity increases as R_B increases (it varies roughly as $(R_B)^2$). Thus, if relative motion of the bubbles were a factor in the results, the observed velocity of large bubbles would be significantly different from that of smaller bubbles. Figure

IV.15, which includes data from bubbles of 40μm to 200μm in radius, shows the slip velocity is inconsequential to within experimental error.

"Bubble/bubble interactions" refers to the possibility that oscillations of one bubble may cause nearby bubbles to move relative to the fluid. It is highly improbable that these interactions are important because the inter-bubble spacing is fairly large (the intensity of these interactions falls off approximately as the square of the distance between the bubbles), and the bubble oscillations are themselves relatively weak.

In order to dispel any lingering doubts that the bubbles are not representative of the surrounding fluid motion, different buoyant fluid droplets – a heptane/azobenzene mixture – were used as Lagrangian flow markers. Heptane was chosen for this study because it is substantially less dense than water (specific gravity =0.66) and hence adequately marks the vortex core. Heptane is also insoluble in water. Azobenzene, which is soluble in heptane but not in water was used to dye the heptane deep orange, making it more visible both during the experiment and in holograms. Since this mixture is a liquid, the possibility of two-phase effects no longer exists. Furthermore, the smaller density difference between the mixture and the water (than between air and water) produces comparatively less relative motion of the droplets. Finally, the interfacial tension existing at the heptane/water interface is less than that between air and water, which causes small droplets to form at the nozzle (R_B as small as 20μm). As discussed previously, these smaller markers move slowly relative to the surrounding fluid, thus providing a more accurate measure of the local velocity.*

Figure IV.16 is a comparison of the results of air bubble and heptane injection. These figures demonstrate that, as anticipated, the type of injected particle has no effect on the measured velocity.

It bears mention that the radial and axial pressure gradients in the flow corresponding with Figures IV.14-IV.16 are the largest encountered in any of the ex-

* Heptane was not used for all measurements because it contaminates the LTWT.

periments. They are, therefore, a severe test of the no relative-motion assumption. Consequently, by establishing that the air bubbles are in fact good indicators of the local single phase flow velocity for this particular flow, one may infer that the bubbles are at least equally good markers for all the flows studied.

Before beginning a detailed presentation of the results, certain very basic features of the velocity distributions must be described. The most glaring attribute of the axial velocity distribution is the substantial difference in mean axial velocity between the vortex centerline and the freestream. Associated with this axial velocity difference (for this flow an excess, in other cases a velocity deficit) is a significant axial velocity unsteadiness. Some of the flow unsteadiness manifests itself outside the core. The out-of-core unsteadiness is almost certainly being driven by in-core unsteadiness rather than the opposite causal relation, as a comparison of the magnitude of the fluctuations makes clear. There is no unequivocal evidence of tangential velocity unsteadiness.

Indisputable photographic evidence of both axial core velocity excesses and deficits is displayed in Figures IV.17 and IV.18. These are photographs of reconstructed double pulsed holograms. In Figure IV.17 the bubble pair in focus lies in the core and has an axial velocity of $1.52U_\infty$, whereas the out of focus bubble pair to the left represents a bubble 2.8cm out of the core travelling at $0.95U_\infty$. The in focus bubble pair in Figure IV.18 lies in the vortex core and has an axial velocity of $0.64U_\infty$; the out of focus bubble is 3.0cm from the core and is travelling at $1.05U_\infty$.

The tangential velocity distribution around the vortex consists of two basic regions – a solid body rotation region ("the core") in the vicinity of the vortex axis (in this case for $R \leq 0.5$cm*, though the precise value is not readily discernible on the plot), and a monotonically decreasing tangential velocity region away from the core. The decaying tangential velocity region is well described numerically by a $1/R$ distribution outside a specific radius (R=2.5cm for this case). The implication is most of the axial vorticity is confined within $R \leq 2.5$cm, leaving an external, near

* i.e. $R_c/s \approx 0.03$, in rough agreement with Orloff and Grant (1973).

potential, flow. These features of the trailing vortex will be mentioned repeatedly in this section.

Three different parameters were varied in this study of trailing vortex velocity: downstream distance (x/c), Reynolds number (Re), and attack angle (α). It is helpful to present the data organized first by downstream distance and then further differentiated by attack angle and Reynolds number. Data taken at x/c=10† comprises the "farfield" section. The "transition region" data (x/c=2,4) may be found in the subsection that follows it. "Near field" (x/c=1) data is grouped in the last subsection.

IV.2.2 The Far Field Trailing Vortex

The finite length of the LTWT test section precluded measurements beyond x/c=10. Moore (1974) has shown numerically that 85% of the elliptical lift distribution bound vorticity is rolled up into the trailing vortex at this distance. An even higher percentage rollup should exist at the same distance behind a rectangular planform wing because such a wing concentrates the shedding of its bound vorticity near the tip. In addition, Spreiter and Sacks (1951) write: "(for) low-aspect-ratio wings, the trailing vortex sheet may become essentially rolled up into two trailing vortex cores within a chordlength of the trailing edge." Consequently, it seems reasonable to refer to this portion of the flow as "far field".

At an attack angle of 5° Reynolds number effects are examined by comparing three different Re flows against a basic flow (Re=4.31×10^5). In each of plots IV.19-IV.21 the basic flow is denoted by an open box. Note in Figure IV.19(a) that reducing Re (to Re=1.79×10^5) has reduced the mean core velocity (from $\overline{U_{xc}} = 0.773U_\infty$ to $\overline{U_{xc}} = 0.595U_\infty$). Figure IV.20(a) shows that increasing Re to 7.61×10^5 has only a small effect on the mean core velocity. By way of contrast,

† When a location is referred to as "x/c=10," this means the center of the hologram lay at x/c=10. Data were taken over a range of ±2cm around the hologram center; in this case $9.87 \leq x/c \leq 10.13$.

further increases in Re (to Re= 1.04×10^6, see Figure IV.21(a)) very substantially decrease the mean core velocity (to $\overline{U_{xc}} = 0.462$). Two conclusions may be drawn from these comparisons:

1. The core flow is strongly Re dependent
2. The Re effect is not monotonic

It is interesting to compare these results with the LDV measurement of Orloff and Grant (1973) that $\overline{U_{xc}} \approx U_\infty$ for a similar wing at $\alpha = 11.1°$, Re $= 7.5 \times 10^5$, x/c = 7.0. In the vortex shed by a comparable wing at x/c=27 and 83, for Re= 2.78×10^5, and $\alpha = 8°$, Corsiglia et al. (1973) measured $\overline{U_{xc}} = 0.8U_\infty$.

The corresponding tangential velocity distribution data (Figures IV.19(b)-IV.21(b)) are now considered. No change in the tangential velocity distribution between the four Reynolds numbers in Figures IV.19 – IV.21 is apparent. Thus, one concludes that the variation in $\overline{U_{xc}}$ is *not* related to the local tangential velocity distribution. As mentioned previously, one may deduce the trailing vortex circulation by fitting the tangential velocity distribution with a curve: $U_\theta = \Gamma/2\pi R$, for R> 2.5cm. The calculated values of Γ are displayed in Table IV.1.

The next few paragraphs repeat the presentation just completed of results at $\alpha = 5°$, but now the focus is on $\alpha = 10°$.

At Re=1.44×10^5 (Figure IV.22) a distinct axial velocity *deficit* exists within the core ($\overline{U_{xc}} = 0.818U_\infty$). If the Reynolds number is increased to 4.31×10^5 (Figure IV.23), the deficit becomes an axial velocity *excess* ($\overline{U_{xc}} = 1.14U_\infty$). Further increasing Re to 7.76×10^5 increases the core velocity excess to $\overline{U_{xc}} = 1.23U_\infty$ (Figure IV.24). The increased core axial velocity has associated with it an increased core unsteadiness. In particular, $\overline{U'_{xc}}$ increases from 0.03 to 0.13 as $\overline{U_{xc}}$ changes from 0.82 to 1.23. Figure IV.24 contains sufficient data to make a histogram of U_{xc} meaningful (Figure IV.25). U_{xc}/U_∞ has a nearly Poissonian distribution, biased heavily towards U_{xc}/U_∞ =1. Similar histograms exist for many of the Re and x/c values studied. Normalized tangential velocity distributions are again Reynolds number independent.

IV.2.3 The Transition Region Trailing Vortex

The data acquired at x/c=2 and 4 will be discussed together in this subsection. Two underlying reasons exist for delineating this region – cavitation inception typically occurs here, and (without intending to be flippant) something must bridge the gap between the near and far fields.

Consider Figures IV.26-IV.28, which display the results at x/c=4, $\alpha = 5°$ for increasing Re. The most important observation to be made is that for these x/c and α values the $\overline{U_{xc}}$ dependence on Reynolds number is again not monotonic; first increasing with Re, and then decreasing ($Re = 2.14 \times 10^5 : \overline{U_{xc}}/U_\infty = 0.78; Re = 8.19 \times 10^5 : \overline{U_{xc}}/U_\infty = 1.16; Re = 1.08 \times 10^6 : \overline{U_{xc}}/U_\infty = 0.69$). The normalized tangential velocity distribution is Re independent, and, in accord with the behaviour at x/c=10, $\overline{U'_{xc}}/U_\infty$ is largest when an axial velocity excess exists within the core.

Velocity distributions at x/c=2, $\alpha = 5°$ for three Reynolds numbers are presented as Figure IV.29. Neither the axial nor the tangential velocity distributions displays a Re dependence.

Figure IV.30 exhibits the velocity distributions at three Reynolds numbers, at x/c=2 and $\alpha = 10°$. Once again, the axial and tangential velocity data display no Re dependence. The tangential velocity reaches a maximum of at least $0.8U_\infty$, somewhat higher than $(U_\theta)_{max} \approx 0.6U_\infty$ for $\alpha = 5°$.

At x/c=2, for both $\alpha = 5°$ and $\alpha = 10°$, and for all of the Reynolds numbers tested, $\overline{U_{xc}}/U_\infty > 1$. Associated with this high core velocity is a great deal of axial velocity unsteadiness (e.g. for x/c=2, $\alpha = 10°, Re = 5.16 \times 10^5 : \overline{U'_{xc}}/U_\infty = 0.17$). A physical feature observable in all of these high axial velocity flows has been given the name "vortex kink" by the author. Photographs of two vortex kinks are labelled as Figure IV.31. Two photos have been included to substantiate the author's claim that this kinking is not caused by bubble-bubble interactions. Figure 32 is a vortex kink schematic. A second global flow instability – which has been tentatively

labelled "vortex stutter" – has also been photographed (refer to Figure IV.33, a reconstructed double pulsed hologram). This phenomenon consists of fairly unsteady, non-axial motion in the core, bounded up and downstream by regions of relatively steady motion – similar to some forms of macroscopic vortex breakdown.* Macroscopic vortex breakdown was never observed experimentally. "Vortex stutter" is thought to be associated with vortex kinking (refer to Chapter V). The kinking and stutter account for much of the high core axial velocity unsteadiness.

A necessary requirement for the core axial velocity to be unsteady is that core fluid accelerations and decelerations occur. The double pulsed hologram reconstruction in Figure IV.34 is a graphic example of strong local deceleration of the core fluid. Each first exposure of a bubble in the core is labelled with a number and the second exposure is labelled with the same number primed. Between 1 and 1' the bubble average velocity is 8.6 m/s. Between 3 and 3' the bubble average velocity is 5.3 m/s. Assuming that the deceleration is approximately fixed in Eulerian space (relative to the axial velocity of the core), this observation implies that fluid between positions 1 and 3 decelerates by 3.3m/s in 330μs, or a remarkable 1000g! This rough calculation is corroborated by the severely deformed (285μm height normal to the flow direction; 160μm length parallel to the flow direction) appearance of bubble 2', and the low velocity of bubble 4. These axial decelerations are comparable in magnitude to the maximum centripetal acceleration of fluid around the core $= (U_\theta)^2_{max}/R = 340g$.

IV.2.4 The Near Field Trailing Vortex

The "near field" of a trailing vortex consists of the highly three dimensional portion of the flow immediately downstream of the foil. The three dimensionality

* N.B. This vortex breakdown is not necessarily in any way related to macroscopic vortex breakdown. The author was tempted to use the expression "vortex breakdown" to describe this phenomenon because of the similarities that exist between this structure and structures labelled by other authors (see V.1.7) as "breakdown."

is a manifestation of the wing wake and the rapid movement of vorticity into the core. The near field is a particularly difficult region to study experimentally due to its 3D character; presentation of tangential velocity data is of limited value due to the absence of axial symmetry.

Figure IV.35(a) ($\alpha = 5°$, Re= 1.86×10^5) shows that $\overline{U_{xc}}$ is, like all of the x/c=2 results, elevated above U_∞. An axial velocity excess is also observed both at a higher Reynolds number (Figure IV.36(a)) and at a different angle of attack (Figure IV.37(a) and Figure IV.38(a)). The low axial velocity data points on several of the figures arise from bubbles moving in the wing wake; the extent of the wing wake may be estimated from bubble motions in the holograms. One estimates the viscous (low velocity) wake of the foil ceases to be discernible 0.05 chords downstream of the trailing edge.

The tangential velocity plots are much more abstruse due to the flow three dimensionality. Very large tangential velocities, perhaps as great as U_∞, exist at this location. Large scatter of the results confirms that the flow is not cylindrically symmetric. The data are not sufficiently detailed to allow for more insightful observations.

IV.2.5 Summary of Velocity Results

An attempt to convey a great deal of information has been made in this section. Before beginning a description of the pressure field results, a brief listing of the salient velocity field results is given:

1. The validity of the double pulsed holographic measurements of flow velocities using bubble tracers has been confirmed.
2. U_θ/U_∞ is Re independent.
3. U_θ/U_∞ can be as large as $0.8U_\infty$, or even higher.
4. The mean core axial velocity is much higher than U_∞ for small x/c, and tends towards $\overline{U_{xc}} < U_\infty$ as the downstream distance increases. This is in agreement with the results of Corsiglia et al. (1973) and Chigier and Corsiglia (1972).

5. $\overline{U_{xc}}/U_\infty$ as high as 1.5 and as low as 0.5 has been measured.

6. $\overline{U_{xc}}/U_\infty$ is a non-monotonic, strong function of Re in the far field.

7. Points 2. and 7. together imply that $\overline{U_{xc}}$ is not solely driven by variations in U_θ.

8. For all cases the axial flow in the trailing vortex is unsteady. The unsteadiness increases, generally, as $\overline{U_{xc}}$ increases. $\overline{U'_{xc}}$ can be as large as $0.2U_\infty$ with peak-to-peak variations of U_∞!

9. When the core axial velocity is high and flow unsteadiness is substantial, two physical structures of the core have been observed – "vortex kinking" and "vortex stutter."

10. Maximum fluid decelerations of on the order of 1000g have been inferred from measurements in the trailing vortex core.

11. The readily quantifiable data are tabulated in Table IV.1.

α (deg)	x/c	Re	$\overline{U_{xc}}/U_\infty$	$\overline{U'_{xc}}/U_\infty$	Γ (m^2/s)
5	10	1.79×10^5	0.60	0.04	0.034
5	10	4.31×10^5	0.77	0.08	0.083
5	10	7.61×10^5	0.77	0.04	0.158
5	10	1.04×10^6	0.47	0.05	0.207
10	10	1.44×10^5	0.82	0.03	0.050
10	10	4.31×10^5	1.14	0.11	0.139
10	10	7.76×10^5	1.23	0.13	0.283
5	4	2.14×10^5	0.78	0.07	0.040
5	4	8.19×10^5	1.16	0.12	0.133
5	4	1.08×10^6	0.70	0.08	0.184
5	2	2.88×10^5	1.23	0.11	—
5	2	4.58×10^5	1.26	0.21	—
5	2	5.79×10^5	1.23	0.13	0.110
5	2	7.85×10^5	1.27	0.12	0.140
5	2	1.03×10^6	1.16	0.21	—
10	2	1.54×10^5	1.55	0.07	0.044
10	2	5.16×10^5	1.53	0.17	0.168
10	2	7.72×10^5	1.53	0.09	0.229
5	1	1.86×10^5	1.43	0.09	—
5	1	8.06×10^5	1.68	0.13	—
10	1	1.86×10^5	1.54	—	—
10	1	8.06×10^5	1.31	—	—

Table IV.1 Trailing Vortex Double Pulsed Holography Velocity Results

IV.3 Trailing Vortex Pressure Distribution

As mentioned in Chapter III, the instantaneous core static pressure, at isolated points, can be inferred from measurements of the sizes of bubbles, initially uniform in size, which had been forced into the core. Due to the experimental constraints discussed in Chapter III, very few bubbles were recorded on each hologram; far too few to develop meaningful p(R) information. For this reason, only core results will be presented. Nonetheless, because trailing vortex core static pressures have never been non-intrusively measured prior to this study, even this limited experimental data, acquired in the NACA 66-209 round tip vortex core, is of interest.

Table IV.2 is a summary of the pressure data.* The intrinsic error associated with measuring the static pressure using this tailored bubble technique is approximately 0.4 in p_c^* (refer to the discussion of errors in Chapter III). An additional error incurred experimentally was that bubbles, exposed to low pressure peaks in the fluid, may have cavitated.† Cavitation would cause $\overline{p_c^*}$ and $\overline{(p_c')^*}$ to be overestimated. Conclusions one may reasonably draw from the tabulated data are:

1. $\overline{p_c^*}$ is approximately 3, with no detectable variation with downstream distance.
2. $\overline{p_c^*}$ increases somewhat when α is increased.
3. the core pressure is highly unsteady, with $\overline{(p_c')^*} \approx 1.8$.

Dunham (1979) has proposed a semi-theoretical correlation for the core pressure based in part on the intrusive pressure probe measurements made by a number of researchers (e.g. Mason and Marchman 1972):

$$\frac{p_\infty - p_c}{0.5\rho(U_\theta^2)_{max}} = p_c^* \left(\frac{U_\infty}{(U_\theta)_{max}}\right)^2 = 3.44 \qquad \text{(IV.3.1)}$$

* The author did discard one egregious bubble datum (in the $\alpha = 5°$, x/c=10 results), presumably caused by an injected non-uniform bubble or a freestream bubble which migrated to the core.

† This problem is a hazard of the tailored air bubble technique. One wishes to reduce p_c to near zero in order to decrease the experimental error, but if p_c has a fluctuating component, cavitation may occur.

In the preceding section it was seen that for $\alpha = 5°$, at x/c=2,4 : $U_\infty/(U_\theta)_{max} \approx$ 1.4. Substituting this value into (IV.3.1) gives $p_c^* = 1.7$. The agreement of this correlated value with the measured value (≈ 2.7) is surprising in view of the uncertainty in $U_\infty/(U_\theta)_{max}$ and in the measurement of p_c^*, as well as the questionable accuracy of the data on which Dunham's correlation is based. For $\alpha = 10°$, $(\overline{p_c^*})_{measured} \approx 3.1$; reasonably close to $(p_c^*)_{correlation} \approx 2.5$.

α (deg)	x/c	Re	$\overline{p_c^*}$	$\overline{(p_c^*)'}$	# OF BUBBLES
5	2	7.9×10^5	2.2	1.6	6
10	2	7.9×10^5	2.8	2.1	12
5	4	7.9×10^5	3.3	1.7	9
10	4	7.9×10^5	4.5	1.5	3
5	10	7.9×10^5	3.0	2.0	16
10	10	7.9×10^5	3.3	1.8	21

Table IV.2 Trailing Vortex Single Pulse Holography Pressure Results

IV.4 Cavitation Observation

Tip vortex cavitation inception study is motivated by the observation that operating marine propellors often have vortex core pressures low enough to produce cavitation. Cavitation is the cause of both undesirable cavitation noise and cavitation erosion. Furthermore, once the cavitating trailing vortex becomes sufficiently large it acts as an additional inefficiency, above and beyond that associated with a single phase tip vortex.

Figure IV.39, a plot of cavitation inception index versus attack angle, is a good starting point for this discussion. Each curve on the figure (data from the NACA 66-209 rounded tip foil) forms a "cavitation bucket" with elevated σ_i at large $|\alpha|$,

and much smaller σ_i near $\alpha = 0°$. Point measurements of σ_i have an error of ± 0.2. The elevated leading edge σ_i at large $|\alpha|$ is due to the reduced surface pressures that occur when $|\alpha|$ is increased. Tip vortex σ_i increases with $|\alpha|$ because the increased circulation (refer to Table IV.1) around the vortex core reduces the core pressure and thus increases the inception index. Over the entire operating range of the foil, tip vortex inception occurs before (i.e. at a higher σ_i) than leading edge inception. From a practical, noise avoidance, standpoint this means tip vortex inception must be reduced before the reduction of leading edge σ_i becomes a consideration. A final observation concerns the importance of dissolved air content on both leading edge and trailing vortex inception. At the design angle of attack $(\sigma_i)_{tv}$ is reduced from 3.2 to 1.6 by decreasing the dissolved air content from 15ppm (saturation) to 6.5ppm. The same qualitative behaviour occurs with the NACA 64-309 shape (Figure IV.40). The range of $(\sigma_i)_{tv}$ is comparable with that measured by McCormick (1962) and Billet and Holl (1979) for different rectangular wings. McCormick measured no DAC dependence. Billet and Holl have observed a substantial DAC effect. One must question McCormick's observations in view of the agreement between Billet and Holl's, and the present, study.

Trailing vortex cavitation inception, for all of the attack angles (except $|\alpha - \alpha_o| < 2°$) and dissolved air contents studied, appeared under stroboscopic illumination as intermittent flashes of light. These flashes were caused by the passage under the light of freestream nuclei grown to macroscopic size in the vortex. Inception at low DAC was often accompanied by cavitation noise audible above the din of the LTWT pump fan. The location of inception fluctuated in time over the downstream interval $1.3 < x/c < 3$ for $1° < \alpha < 13°$.

The author has included as figures two high speed flash photographs of cavitation inception and "near" inception. Figure IV.41 shows inception at $\alpha = 3°$ behind the NACA 64-309 foil. The very large, mottled appearance of cavitation is suggestive of the explosive bubble growth that occurs when the water is highly undersaturated. Figure IV.42 is a photograph of tip vortex cavitation for σ slightly less than σ_i behind the Joukowski large aspect ratio, square cut foil. Apart from the

existence of two cavitating vortices, regard the individual bubbles which comprise the cavitating vortex. Observe in addition that a long length of the vortex (literally the whole test section length) cavitates once σ is slightly reduced below σ_i. At lower σ these bubbles combine to form a continuous vapour core.

The above discussion has consistently referred to cavitation inception. A second index, "cavitation desinence," is also widely encountered in the technical literature. Cavitation "desinence" is the value of σ measured by gradually increasing the freestream pressure until a formerly cavitating flow ceases to cavitate. Cavitation "inception," by way of contrast, is σ measured by gradually decreasing the freestream pressure until cavitation occurs. Often desinent cavitation happens at a higher σ than inception, a phenomenon referred to as "cavitation hysteresis." Three reasonable explanations of cavitation hysteresis will be described. Cavitation nuclei generated by cavitation may recirculate around a test facility, making the water more susceptible to cavitation. It is feasible that the propagation of pressure waves from collapsing bubbles through the fluid might cause unstable nuclei in low pressure regions to cavitate. Finally, sufficiently strong cavitation might affect the underlying single phase flow in ways to increase the likelihood of further cavitation.

The first and third explanations have both been supported by experiment. If the tunnel is run for a prolonged time (30s is the approximate recirculation time of the tunnel at top speed) between measurements of σ_i and σ_d, cavitation hysteresis is observed. However, if the tunnel is run non-cavitating at high pressure for several minutes to reduce the freestream bubble concentration, and first cavitation inception, and then quickly thereafter cavitation desinence, are measured, the cavitation hysteresis disappears. This pair of observations confirms the first hypothesis.

A different form of cavitation hysteresis also exists. Reducing σ_i until an attached trailing vortex cavity is produced affects the flow field dramatically. Forcing the trailing vortex to separate from the foil requires a higher σ than that required to cause cavitation attachment. Sometimes the higher σ is above σ_i. This behaviour clearly supports the third hypothesis.

Cavitation inception is not the sole phenomenon of technical interest. The appearance of developed trailing vortex cavitation is important in its own right, and because it provides information about the trailing vortex structure. Figure IV.43 is a long-exposure photograph of developed trailing vortex cavitation. Significant features of this photograph are:

1. the roughly elliptical cross-section of the vortex which becomes circularized for x/c> 2.5.
2. the steady appearance of the cavitating tip vortex near the foil (beyond x/c=3 the vortex meander is considerable).
3. the tip vortex is attached to the foil near x/c=0.8 .
4. leading edge cavitation is heavy away from the tip, but is not visible near the tip, presumably because the tip downwash raises the local pressure above the inception value.
5. the vortex core has a glassy appearance, which indicates that the flow is free of surface instabilities.

At $\alpha = 7°$ tip vortex cavitation appears as in the long exposure photograph of Figure IV.44 . Note that the tip vortex is cavitating strongly while leading edge cavitation is only visible near the false floor. This observation is in agreement with the measured higher $(\sigma_i)_{tv}$ than $(\sigma_i)_{le}$. The tip vortex at this angle, too, is attached to the foil near x/c=0.8 .

For an attack angle of 15°, developed trailing vortex cavitation (Figure IV.45) does not have the smooth appearance of lower α cavitation. This probably indicates that a surface instability has roughened the water/vapour interface. It is also interesting to note that the leading edge cavitation is separated from the surface and highly unsteady over the lower 3/4 of the foil, and attached and fairly steady close to the tip. This behaviour is caused by tip downwash inhibiting flow separation near the tip (surface flow visualization indicated the occurrence of a transition from attached to separated flow in the same location, see Figure A.1.1). Here, too, the tip vortex cavity is attached to the foil near x/c=0.8 .

The above separation phenomenon is one of many cavitation features that can be better understood through a knowledge of the single phase flow. An attempt will be made to relate single phase and cavitating flows in Chapter V.2 .

An interesting phenomenon, only observed when the concentration of air bubbles in the test section is very high, is large-scale two-phase vortex breakdown. A 1/60 second exposure photograph of a typical breakdown (Figure IV.46) has been included.

IV.5 Tip Modifications

The preceding portions of this chapter have been concerned with basic scientific research. This research may ultimately lead to improvements in tip vortex characteristics, but the gap between basic scientific results and technological application would appear to be large. From a pragmatic standpoint, then, one is interested in more direct ways of "improving" the tip vortex. "Improving" here depends on the exact application – for aircraft wings tip vortex improvements would reduce the downwash inefficiency* and diminish the hazard to following aircraft; for submarine propellors both an efficiency increase and a decreased cavitation inception index would be improvements.

IV.5.1 Previous Work on Tip Modifications

Platzer and Sounders (1979) have reviewed much of the literature on tip vortex alleviation for marine applications. A recent vortex wake alleviation workshop (Vortex 1980) included discussion of many vortex reduction techniques appropriate for aircraft. Neither literature review found a panacea for its application.

A few of the plethora of tip vortex alleviation methods expounded in the literature will be briefly mentioned in order to give the reader an impression of the

* Webber and Dansby (1983) state: "At conditions for economical cruise, the lift-dependent drag is typically 35-45% of the total, and thus any modification that can reduce this portion is worthwhile."

amount of effort expended on, and interest in, this field. The papers are cited in chronological order.

Scheiman and Shivers (1971) modified the tip flow with a leading edge disk flow spoiler, a trailing edge disk flow spoiler, a porous wing-span extension, and a tip adjustable air jet-sheet ejector. They acheived "vortex cross-sectional variations ... [but only] at the expense of wing lift and/or drag characteristics."

Kantha et al. (1971, 1972) tried blowing air axially into the tip vortex and concluded that with sufficiently fast blowing the core behaves as a turbulent jet, spreading quickly. The lift and drag penalty of this approach is probably severe, and the applicability of such a scheme to commercial aircraft is dubious. Snedeker (1972) measured the rolling moment on a simulated following aircraft caused by a tip vortex with and without axial injection and found that "maximum flow from the central jet reduces the rolling moment by only 13% [for vortex generating wings at $\alpha = 6°$]. The effect for the case $\alpha = 3°$ is hardly noticeable." He argues that although the peak tangential velocities around the tip vortex are greatly reduced by axial blowing, angular momentum has been merely redistributed farther from the vortex core, where it still profoundly affects following planes.

Hastings et al. (1975) conducted a full scale study of small aircraft encounters with the wake of a large aircraft fitted both with and without "vortex-attenuating splines." These splines consist of large, retractable plates mounted normal to the flow direction, radially around the wing tip. The authors reported that these splines made small aircraft wake interactions controllable, but noted that the splines cause a considerable noise increase and a lift/drag ratio reduction.

One wing tip modification device that has found commercial application is the Whitcomb wing tip (Whitcomb 1976 and Flechner et al. 1976). This wing tip consists of a short ($\approx$ 1/2 chord high) lifting surface mounted almost normal to the wing at the tip. The wing is connected to the suction surface of the wing with a smooth fillet. Among the aircraft that have flown with such a winglet are the MD-11, the Gulfstream III, and the DC-10 (Webber and Dansby 1983 and Devoss

1986). Closely related in concept to the Whitcomb winglet is a series of winglets set at varying angles to the planform plane, which are referred to as "wing tip sails." Spillman (1978) has reported up to a 29% reduction in lift dependent drag in flight tests of (small aspect ratio) aircraft fitted with sails.

IV.5.2 New Tip Modification Results

In view of the immense possible benefits of a superlative tip design, the author tested two different tip geometries – a square cut tip and a novel "ring wing" tip. These tips were compared with the basic rounded tip; the comparison based on both SFV and cavitation behaviour.

The square cut foil was formed by removing the rounded tip from the standard wing, leaving a two dimensional foil with a sharp edge.

SFV performed on this foil (Figures IV.47 - IV.49) shows surface flow on the pressure and suction surfaces is not significantly different from that around the rounded tip foil. The flow separates from the sharp tip edges (Figure IV.47(c)-IV.49(c)), which has important consequences in terms of the foil cavitation behaviour. The inboard flow angles measured at four chordwise positions are displayed in Figure IV.50 . On the pressure surface there is almost no flow angle variation with chordwise distance. This means the flow streamlines are parallel, and consequently the flow velocity is roughly uniform along streamlines near the wing surface. The suction surface near the tip displays some chordwise variation of flow angle, probably due to a combination of vortex rollup and bound vorticity concentration as x/c increases.

Flow separation from the sharp tip of the foil causes the trailing vortex to roll up into several vortices (4 are cavitating in Figure IV.51), rather than the single rounded tip vortex. Multiple tip vortices were also observed (Fig. IV.42) behind the square cut Joukowski foil and the square cut NACA 66-209 foil, so it is reasonable to predict multiple vortices behind most square cut foils. The square cut tip has a lower σ_i than the rounded tip (1.2 versus 1.8 at $\alpha = 7°$) because the single vortex

which results when these vortices wind together is much larger than the rounded tip trailing vortex (Figure IV.52). When α is small, separated flow cavitation from the leading edge tip (where inception now occurs) may elevate $(\sigma_i)_{tv}$ above the rounded tip value. The installation of a square cut tip also reduces the NACA 66-209 $(\sigma_i)_{tv}$ (Figure IV.53).

Patent action has commenced (Acosta and Green 1987) on a novel "ring wing tip" device (Figure IV.54). The basic idea underlying this device is to distribute the bound wing vorticity in the Trefftz plane about a combination of a ring and line, as opposed to the single line which characterizes normal wings. Since the vorticity shed by the ring wing tip is spread over a large area, the resulting trailing vortex has a larger core diameter, and consequently cavitates less readily, than a normal wing tip. In addition, the flow through the ring probably interacts with the flow around the ring on a microscale level, furthering dissipating the trailing vorticity.

The ring wing tipped hydrofoil consisted of the square cut foil, to which was affixed a 0.19c-diameter, 0.67c-long cambered brass pipe. The pipe was attached to the foil using two screws, and the region near the joint was streamlined using body filler and epoxy glue. Some care was taken to optimize the shape of the ring wing tip – in particular to avoid cavitation from the leading edge of the ring – but without question the final configuration could be considerably improved.

The photographic evidence presented in Figure IV.54 is indisputable – most of the shed circulation from the foil, at $\alpha = 12°$, originates at the ring. The photographs taken at $\alpha = 7°$ (Figure IV.55) are quantified in Figure IV.56. The small flow angles in this figure imply a serendipitously larger wing lift than the other tip geometries. A comparison of the flow fields at $\alpha = 3°$ (Figure IV.57), 7°, and 12° suggests deployment of a ring wing tip is most beneficial at high angles of attack.

Cavitation photographs of the trailing vortex (Figure IV.58) reveal more about the inadequate streamlining of the ring leading edge than they do about the trailing vortex structure. Trailing vortex inception occurs, as for the other tip geometries,

in the range $1.3 < x/c < 3$. Figure IV.59 confirms that the ring wing tip has suppressed tip vortex cavitation. $(\sigma_i)_{tv}$ is a factor of 2 below $(\sigma_i)_{le}$ for the design angle of attack. In fact, cavitation nuclei generation at the cavitating leading edge of the ring elevates $(\sigma_i)_{tv}$ above that which would be measured with a better designed ring.

In summary, two different tip geometries were studied using cavitation photography and SFV. The square cut tip has a somewhat lower σ_i than does the rounded tip due to flow separation from the sharp edge. The ring wing tip both augments the lift, and reduces $(\sigma_i)_{tv}$, probably by as much as a factor of 3 below the rounded tip σ_i. It works primarily by distributing the shed vorticity in the Trefftz plane over a circle and trailing edge line.

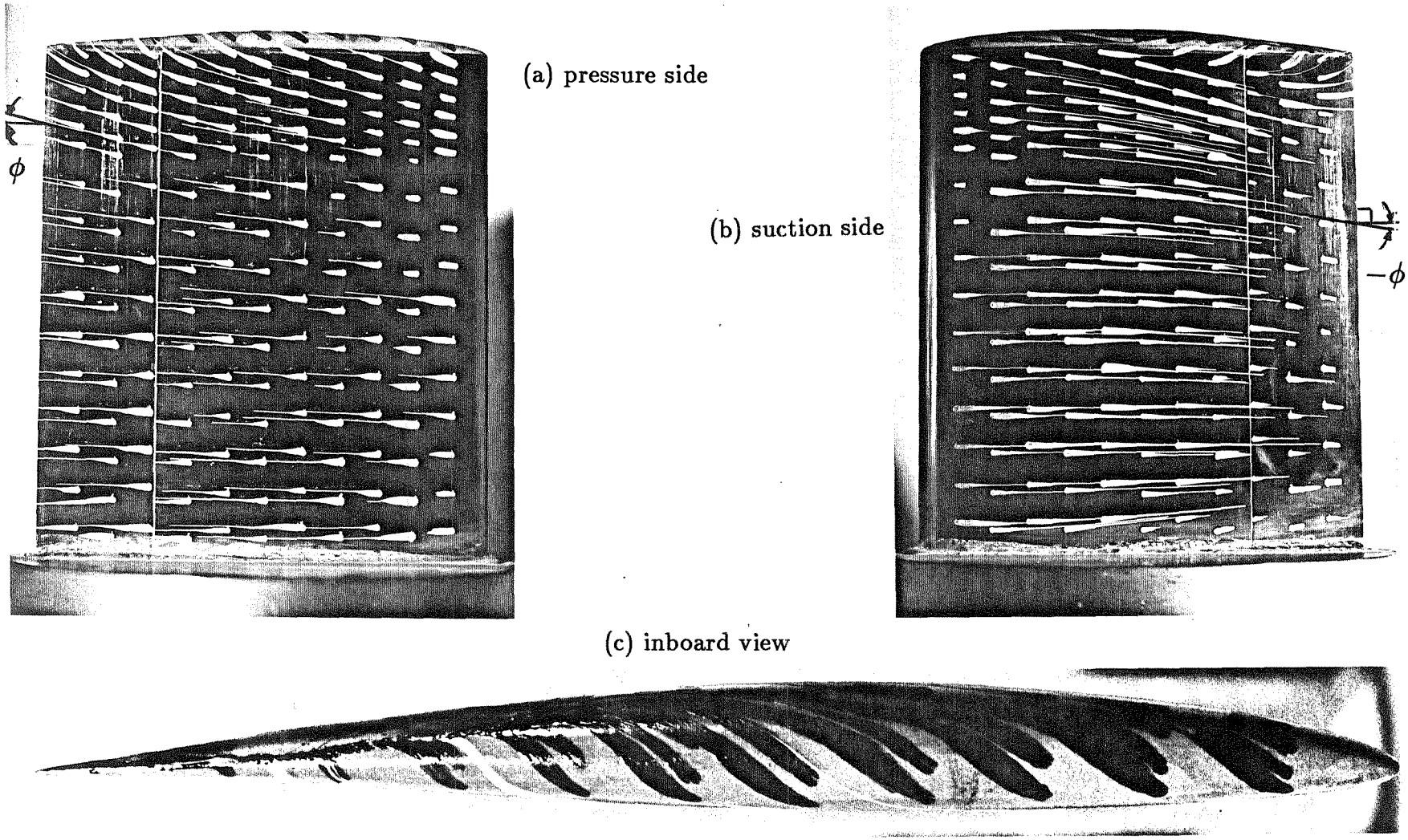

Figure IV.1(a,b,c) SFV of 64-309 round tip foil at $\alpha = 7°, \mathrm{Re} = 1.2 \times 10^6$. Inboard flow angles marked.

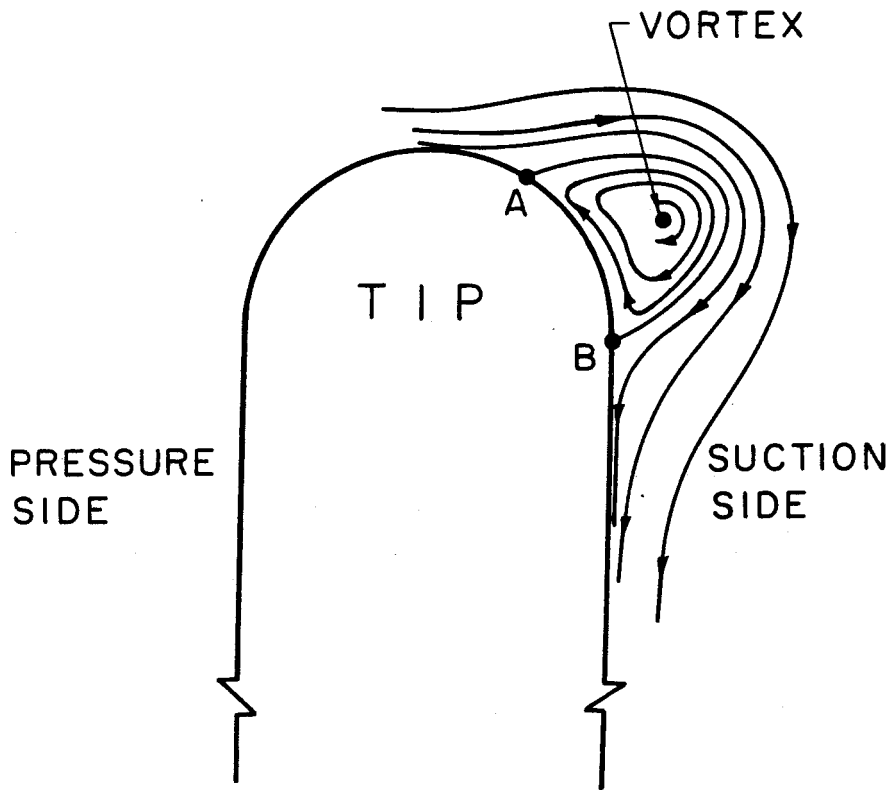

Figure IV.2 Physical Interpretation of Tip Smear Lines
(view in streamwise direction).

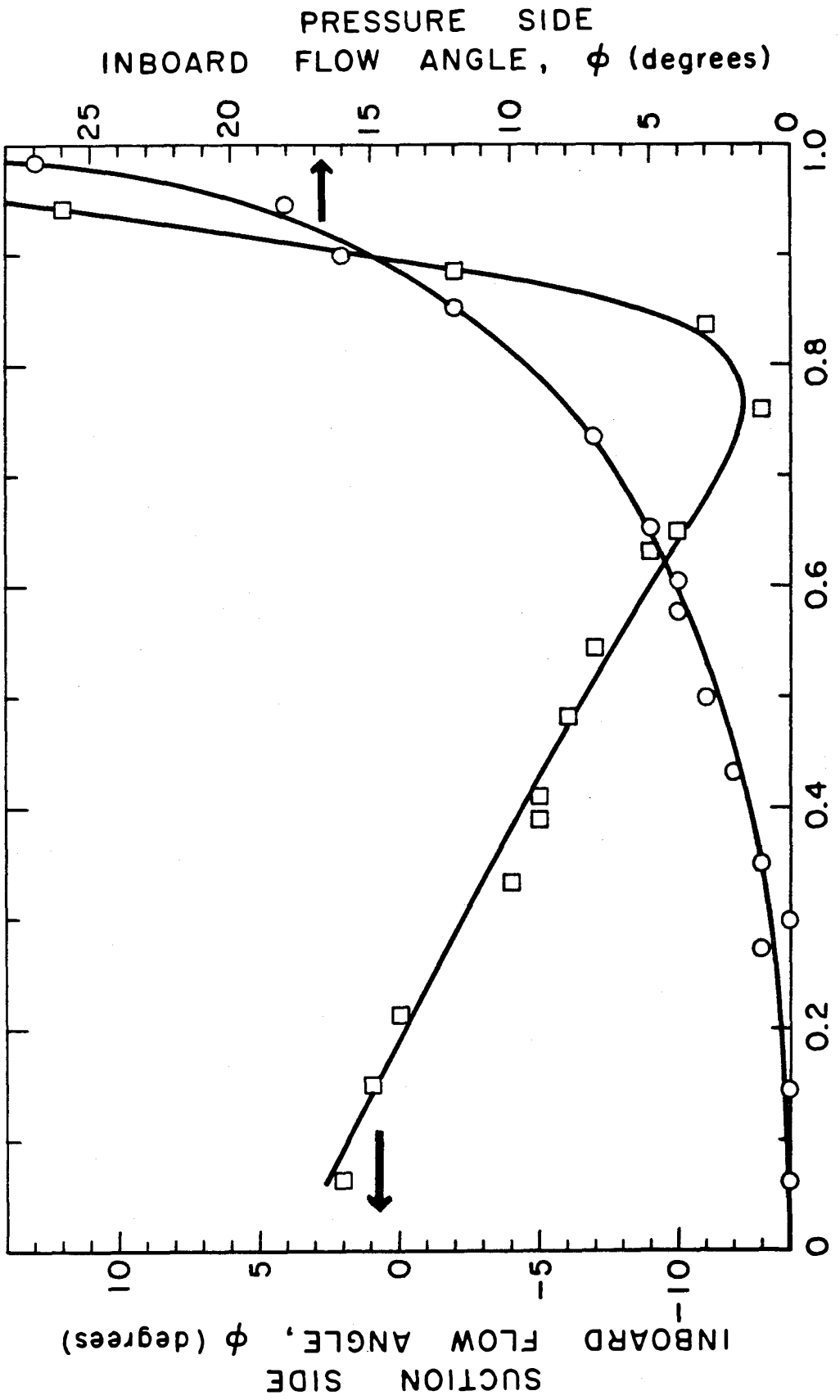

Figure IV.3(a) Inboard Flow Angles at Trailing Edge. NACA 64-309 round tip foil at $\alpha = 7°$.

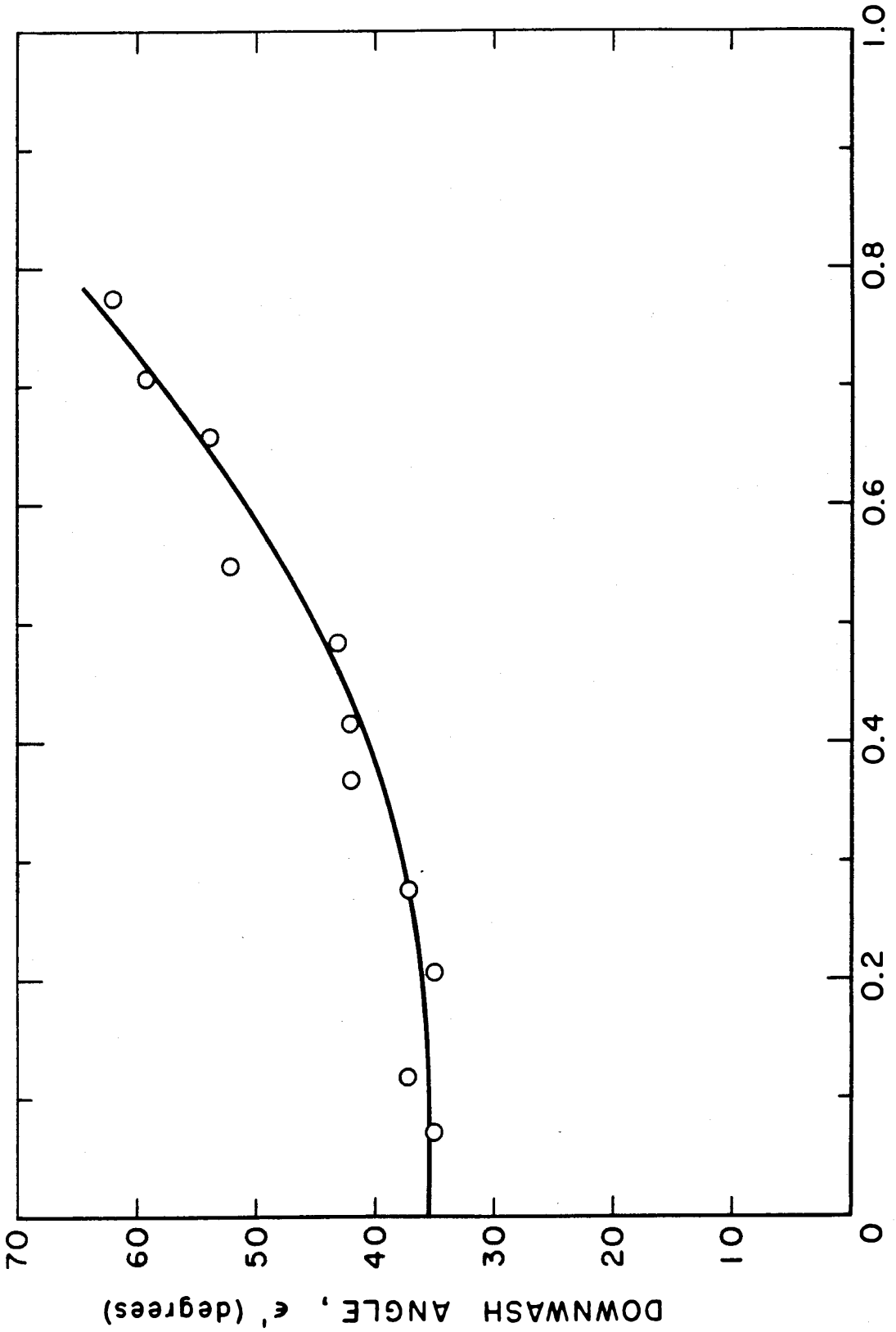

Figure IV.3(b) Downwash Angle at the Tip, 64-309 round tip foil, $\alpha = 7°$.

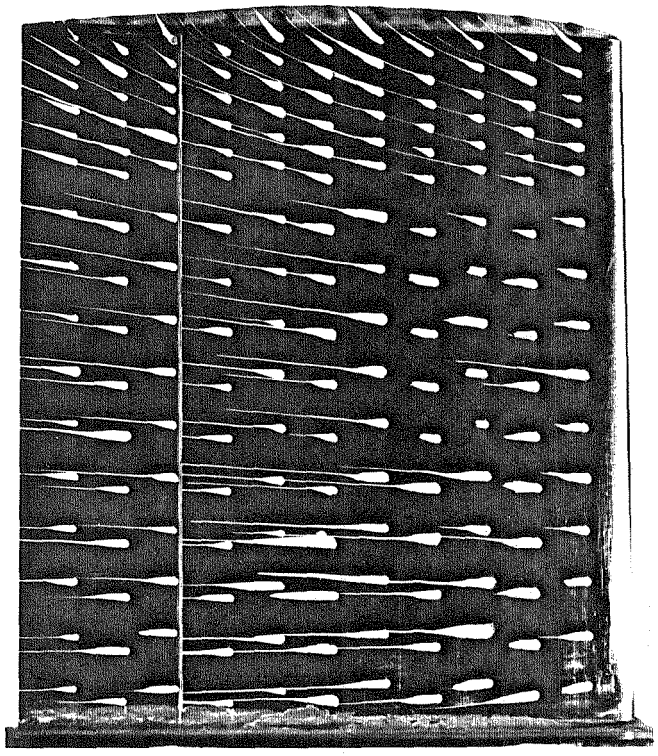

(a) pressure side

(b) suction side

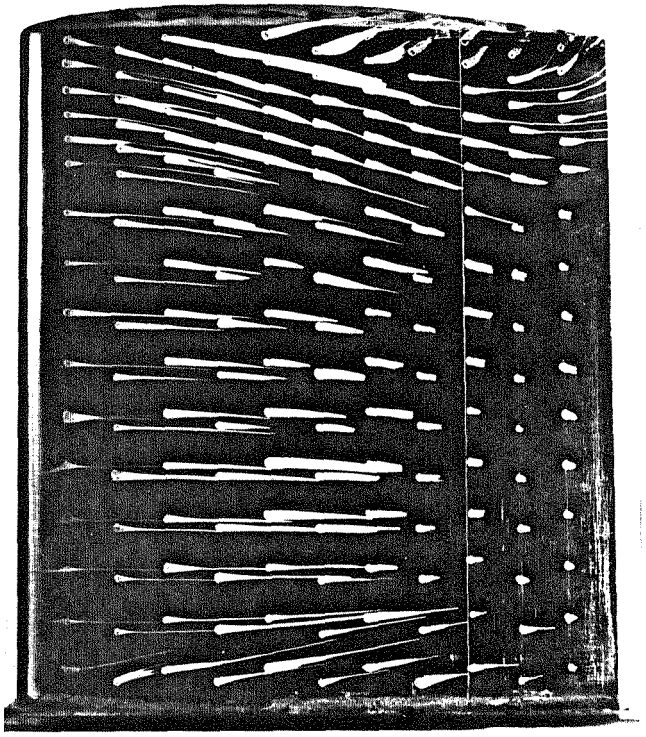

(c) inboard view

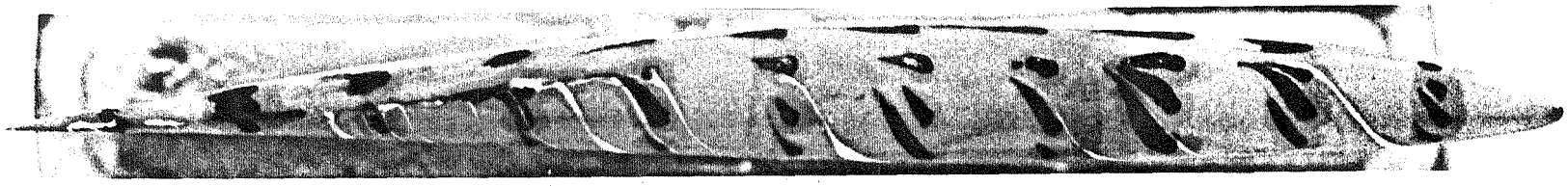

Figure IV.4(a,b,c) SFV of 64-309 round tip foil at $\alpha = 12°, \mathrm{Re} = 1.2 \times 10^6$.

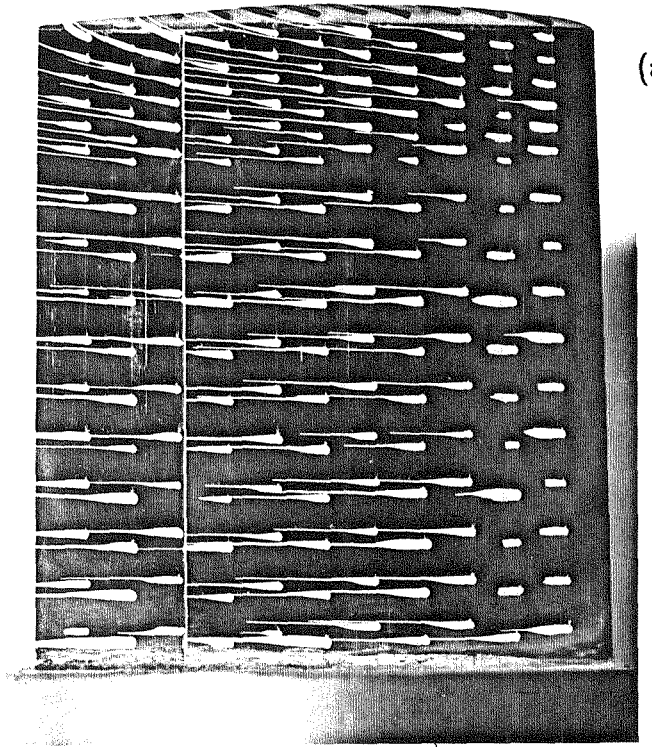

(a) pressure side

(b) suction side

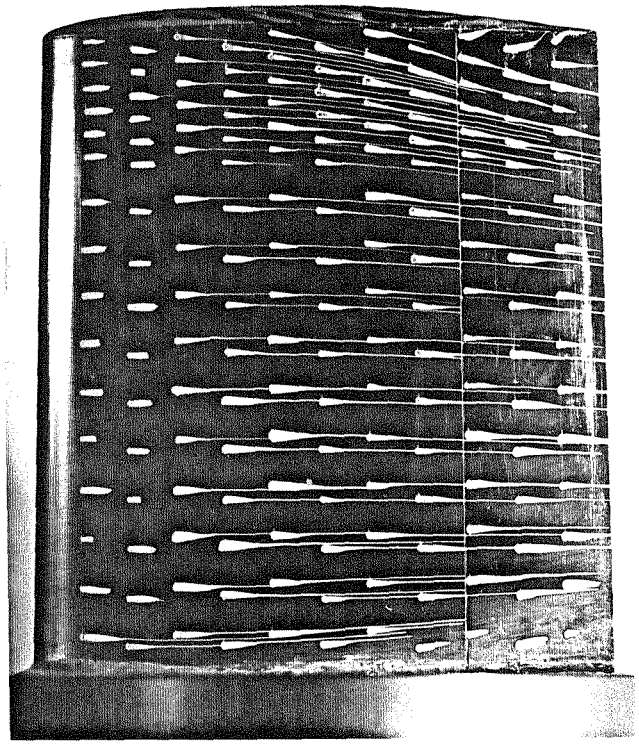

(c) inboard view

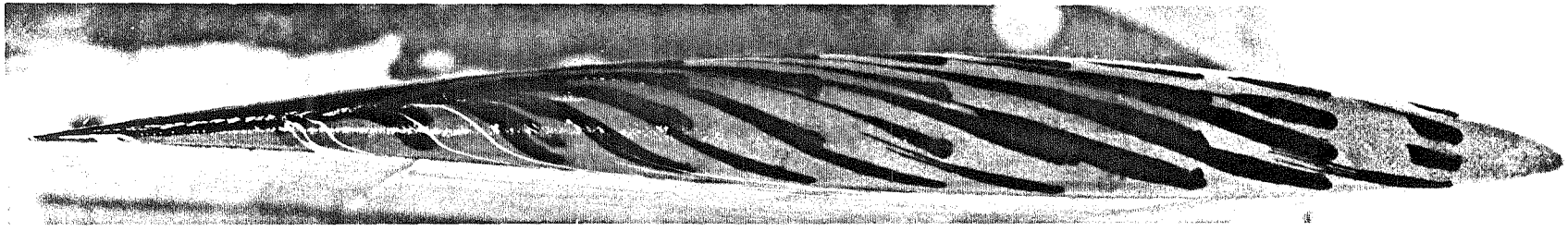

Figure IV.5(a,b,c) SFV of 64-309 round tip foil at $\alpha = 3°, \mathrm{Re} = 1.2 \times 10^6$.

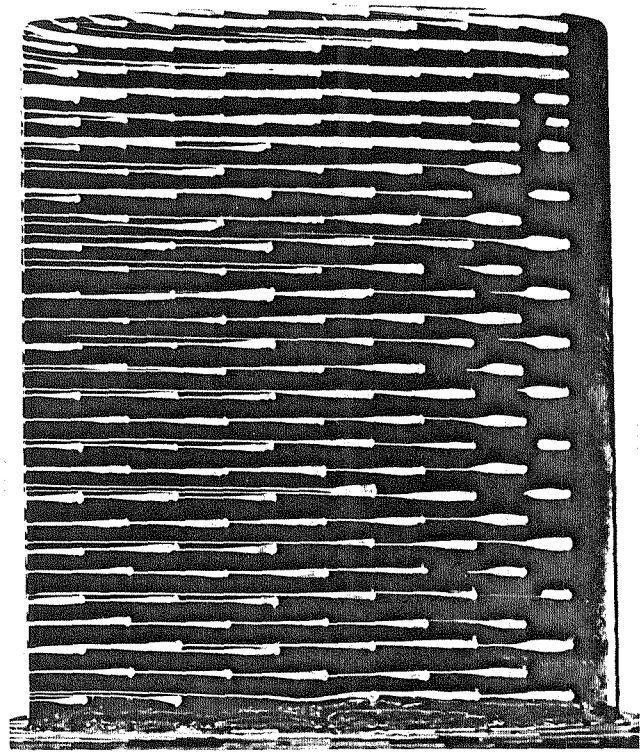

(a) pressure side

(b) suction side

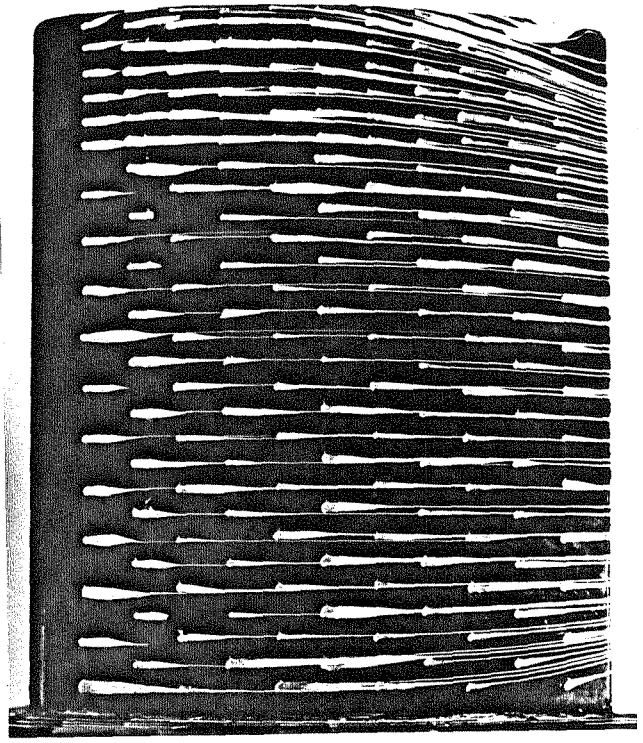

(c) inboard view

Figure IV.6(a,b,c) SFV of 66-209 round tip foil at $\alpha = 0°$, $\mathrm{Re} = 1.5 \times 10^6$.

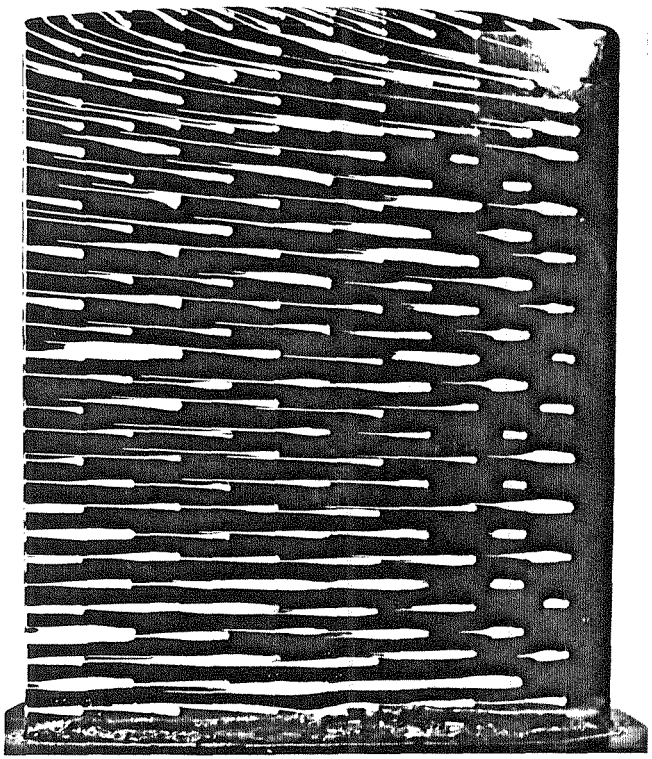

(a) pressure side

(b) suction side

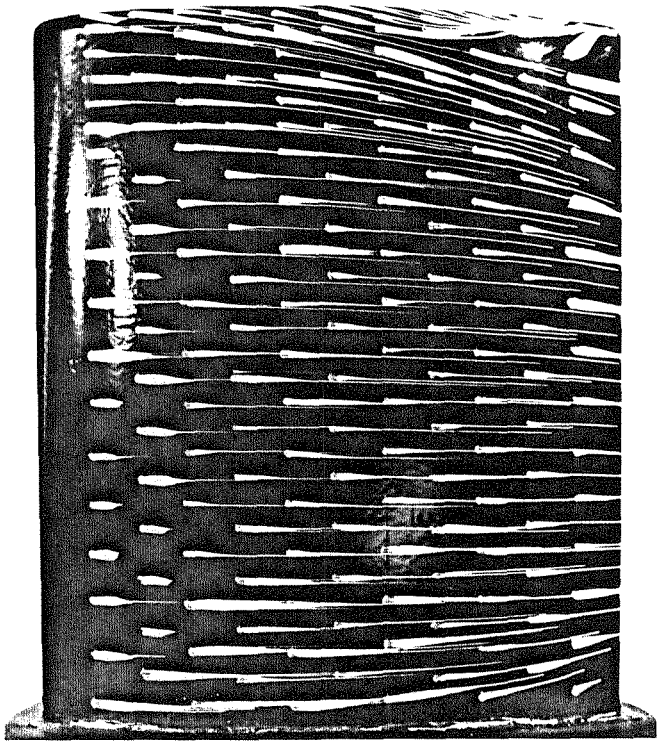

(c) inboard view

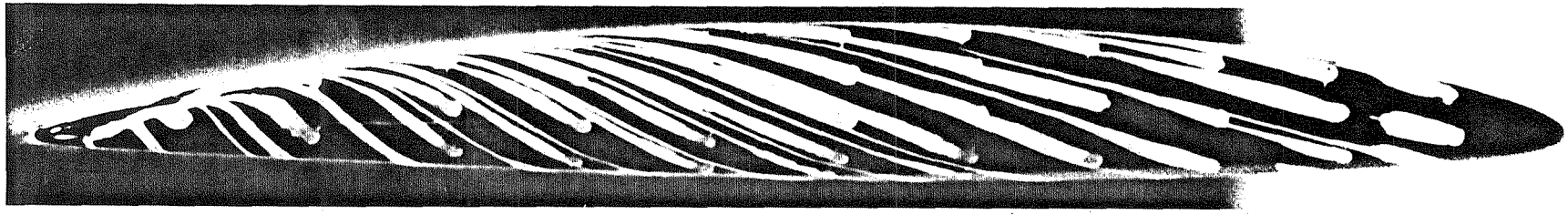

Figure IV.7(a,b,c) SFV of 66-209 round tip foil at $\alpha = 4°$, $\mathrm{Re} = 1.5 \times 10^6$.

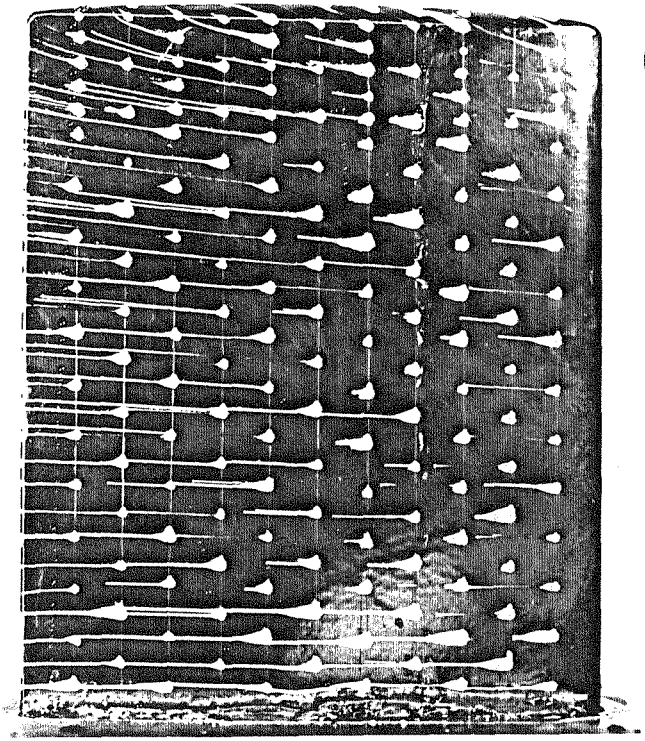

(a) pressure side

(b) suction side

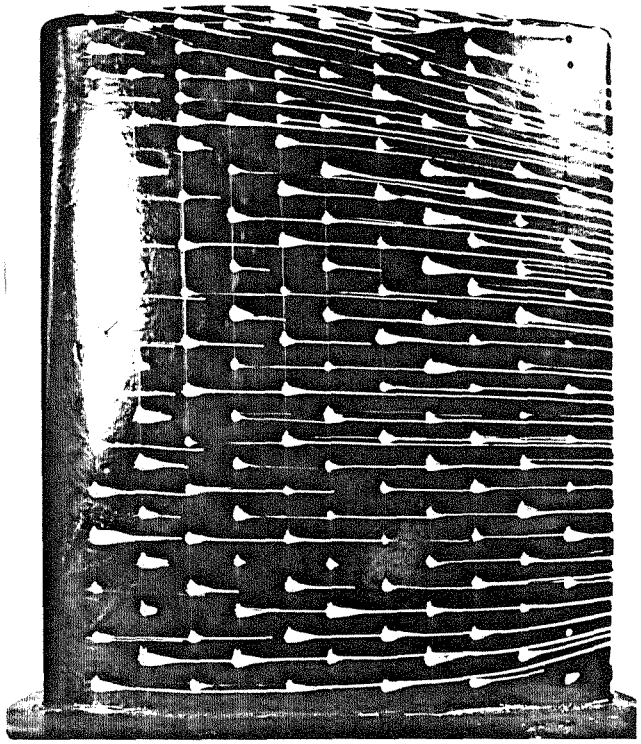

(c) inboard view

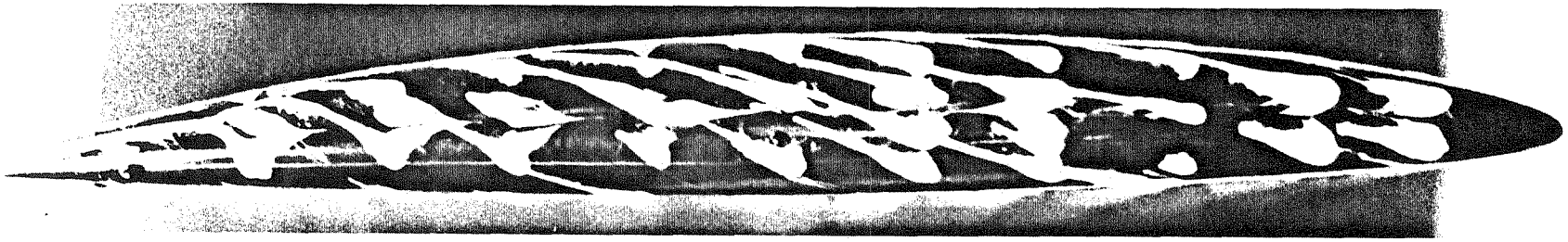

Figure IV.8(a,b,c) SFV of 66-209 round tip foil at $\alpha = 4°, \mathrm{Re} = 0.5 \times 10^6$.

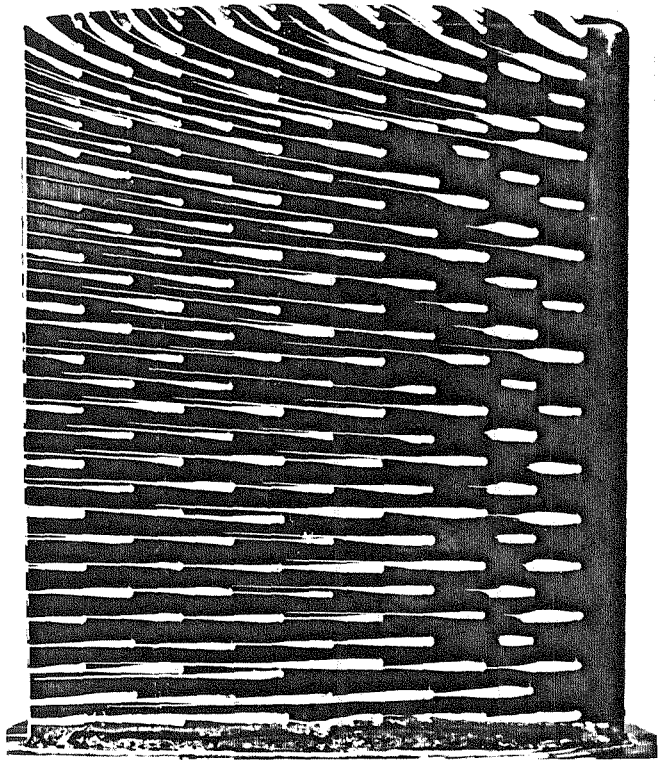

(a) pressure side

(b) suction side

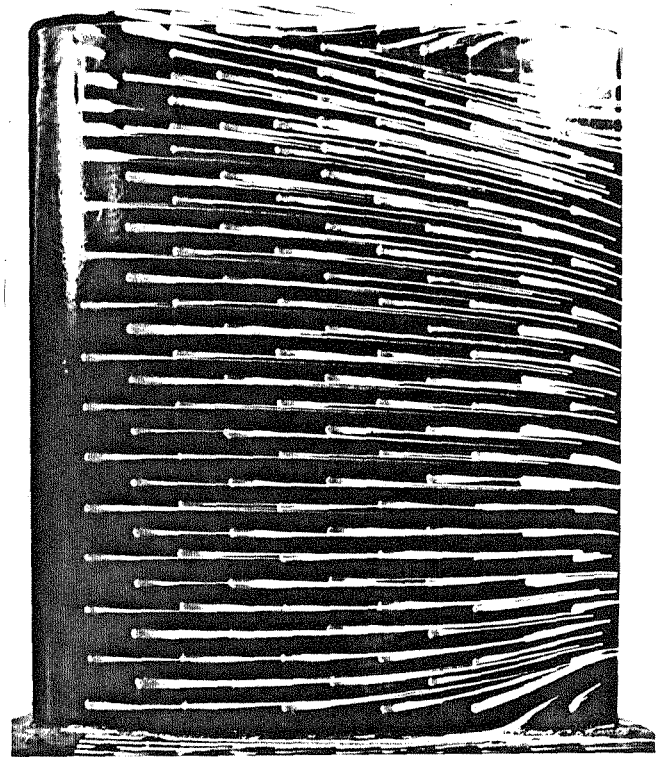

(c) inboard view

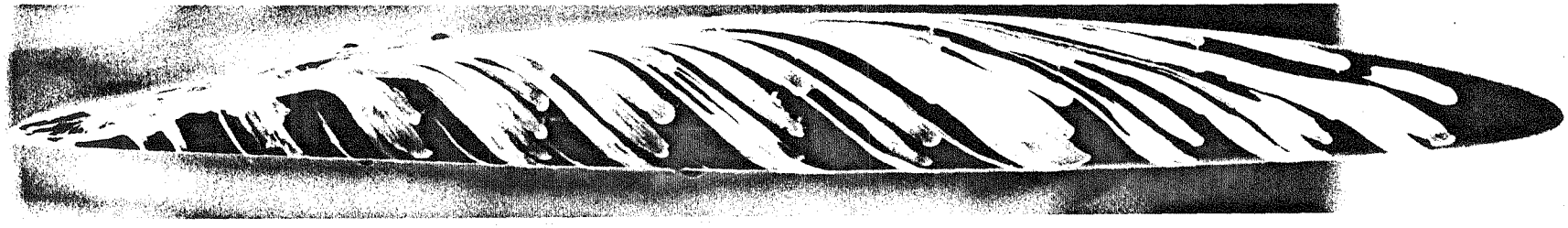

Figure IV.9(a,b,c) SFV of 66-209 round tip foil at $\alpha = 8°, \mathrm{Re} = 1.5 \times 10^6$.

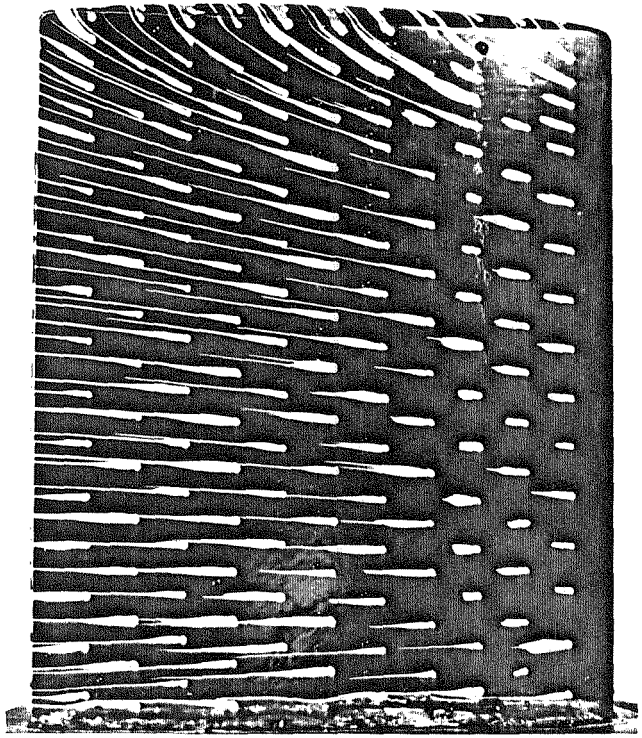

(a) pressure side

(b) suction side

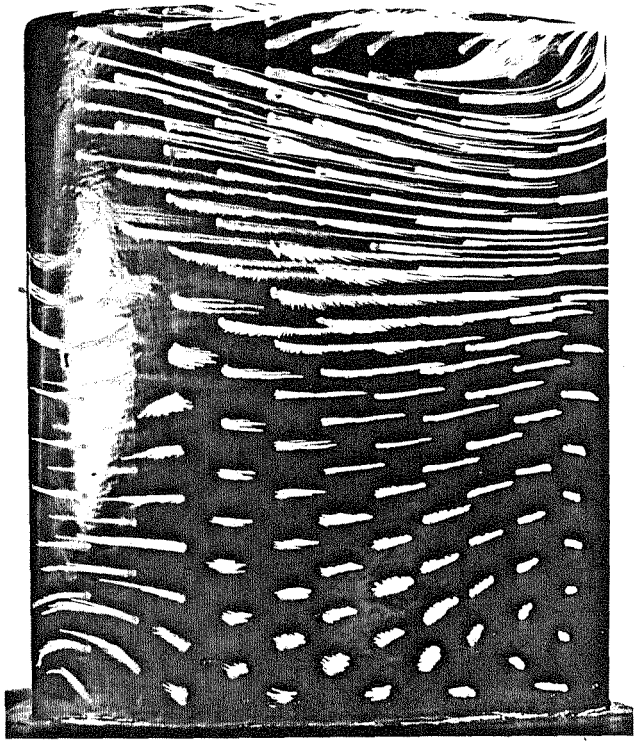

(c) inboard view

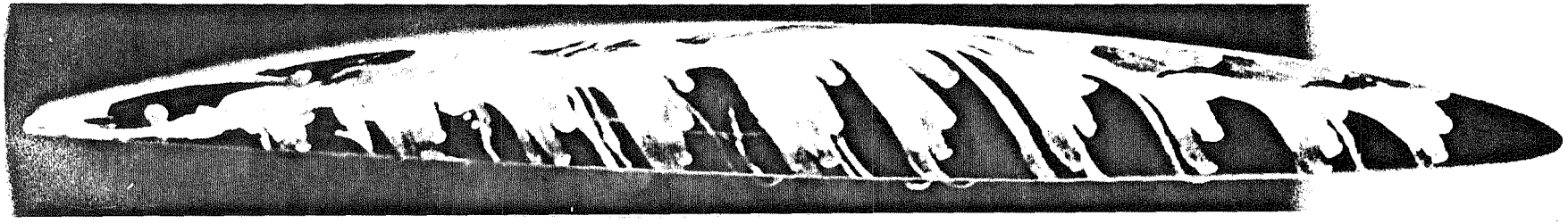

Figure IV.10(a,b,c) SFV of 66-209 round tip foil at $\alpha = 15.1°, \mathrm{Re} = 1.5 \times 10^6$.

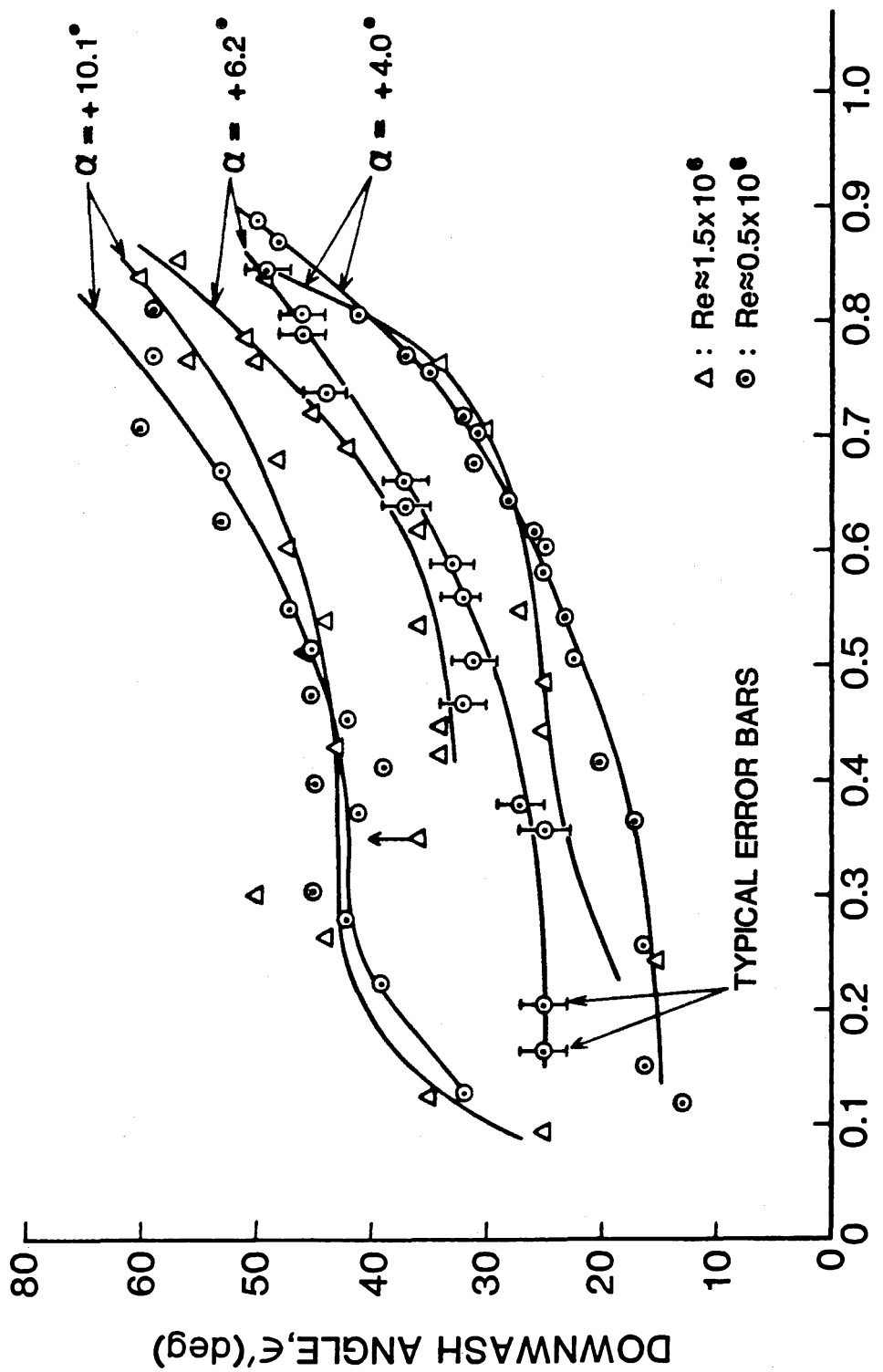

Figure IV.11 The Effect of Reynolds Number on Downwash Angle at the Tip.

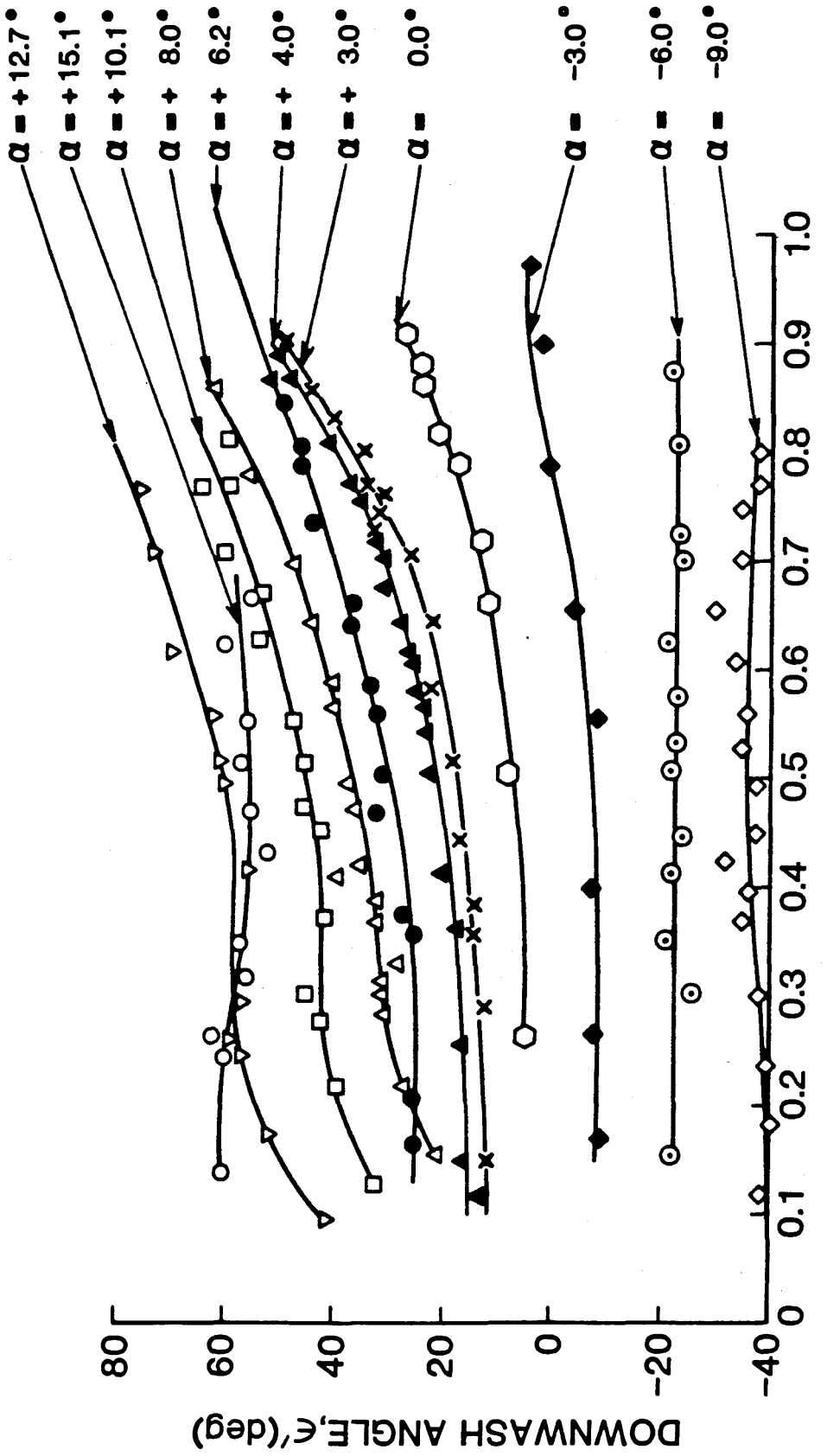

Figure IV.12 The Effect of Attack Angle on Downwash Angle at the Tip.

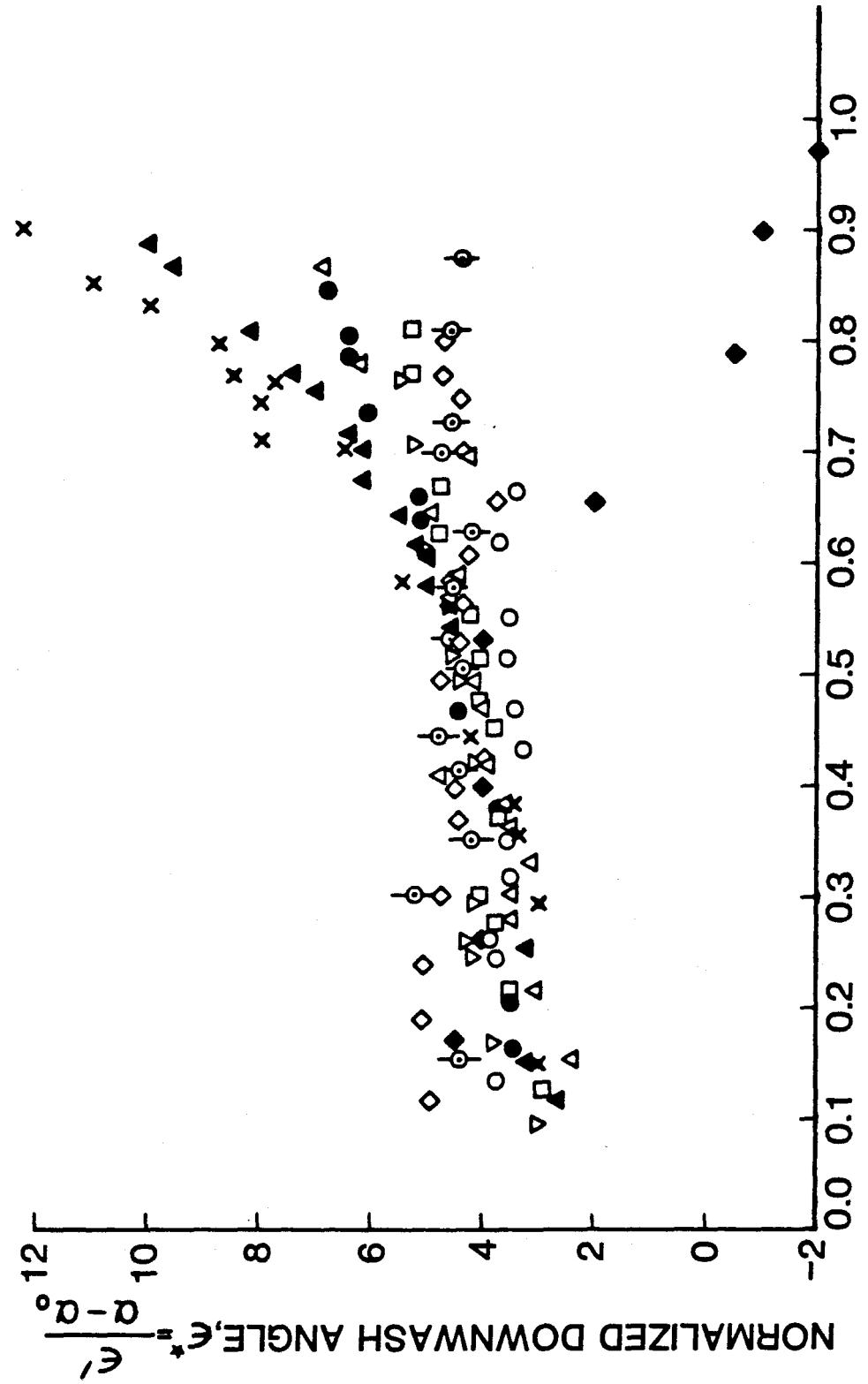

Figure IV.13 Normalized Downwash Angle vs x/c, Illustrating the Influence of Vortex Rollup (same symbols as Figure IV.12).

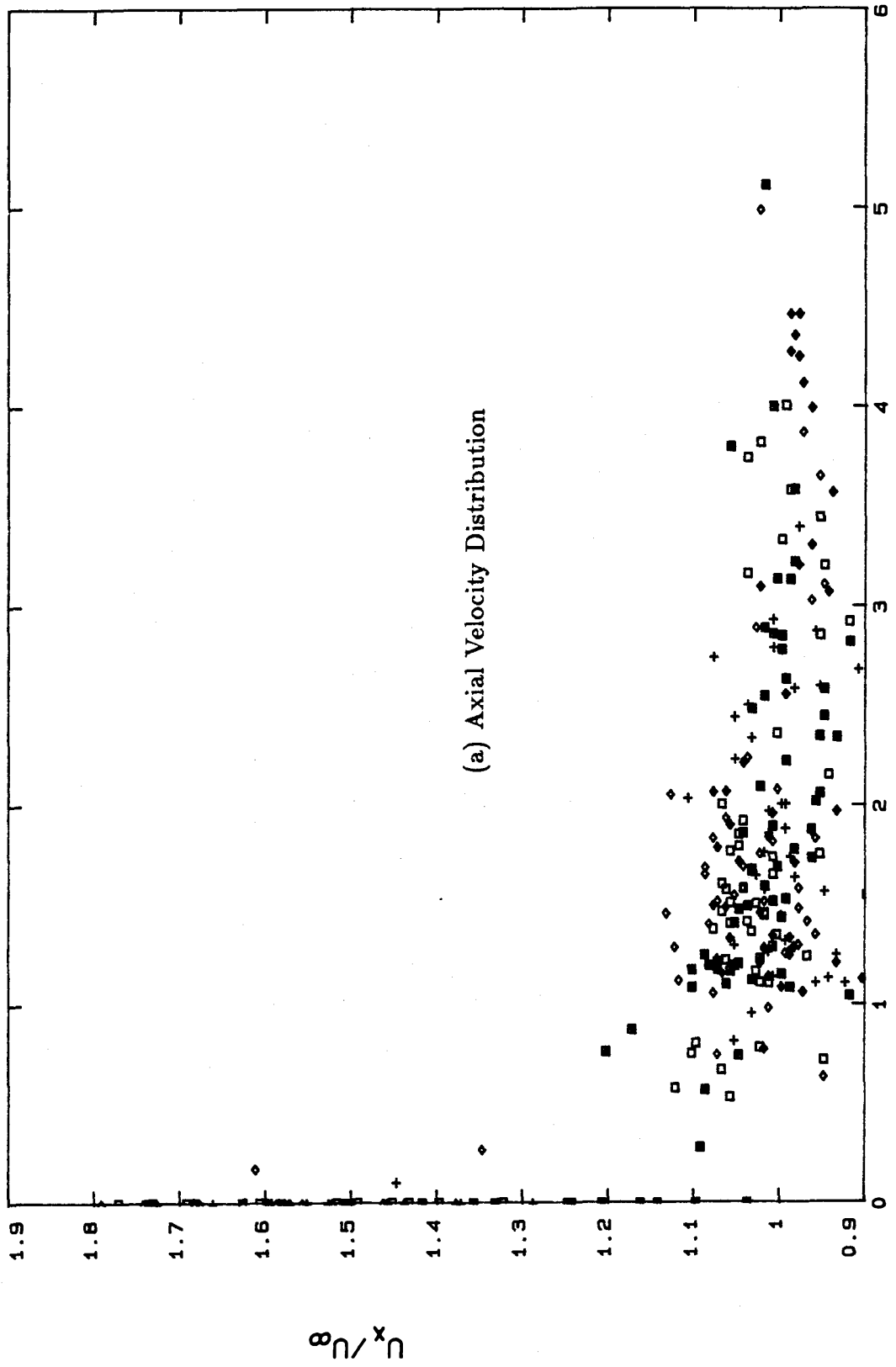

Figure IV.14(a,b) Trailing Vortex Velocity Distribution.
$\alpha = 10°, x/c = 2, Re = 5.2 \times 10^5$.

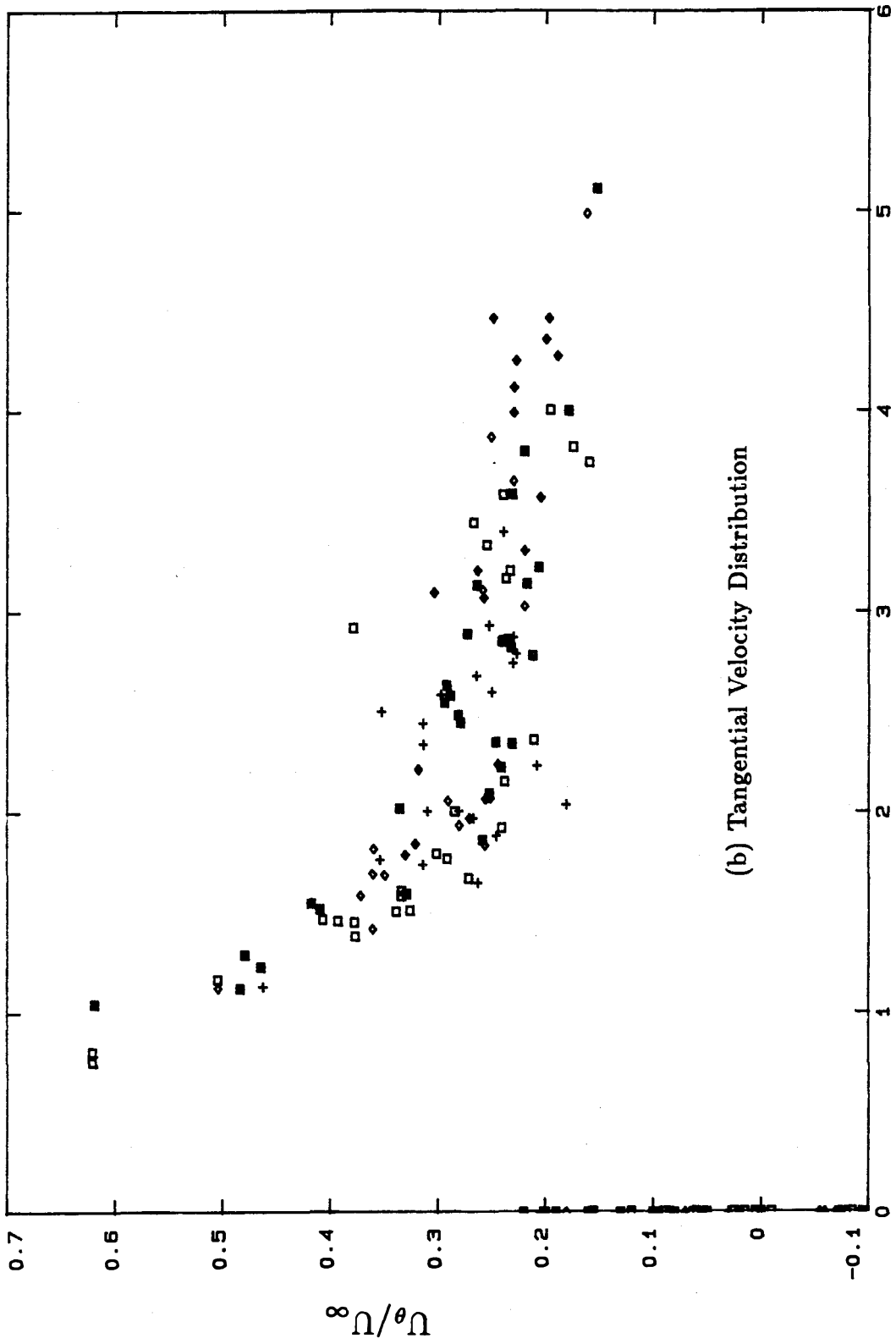

Figure IV.14(a,b) Trailing Vortex Velocity Distribution. $\alpha = 10°, x/c = 2, Re = 5.2 \times 10^5$.

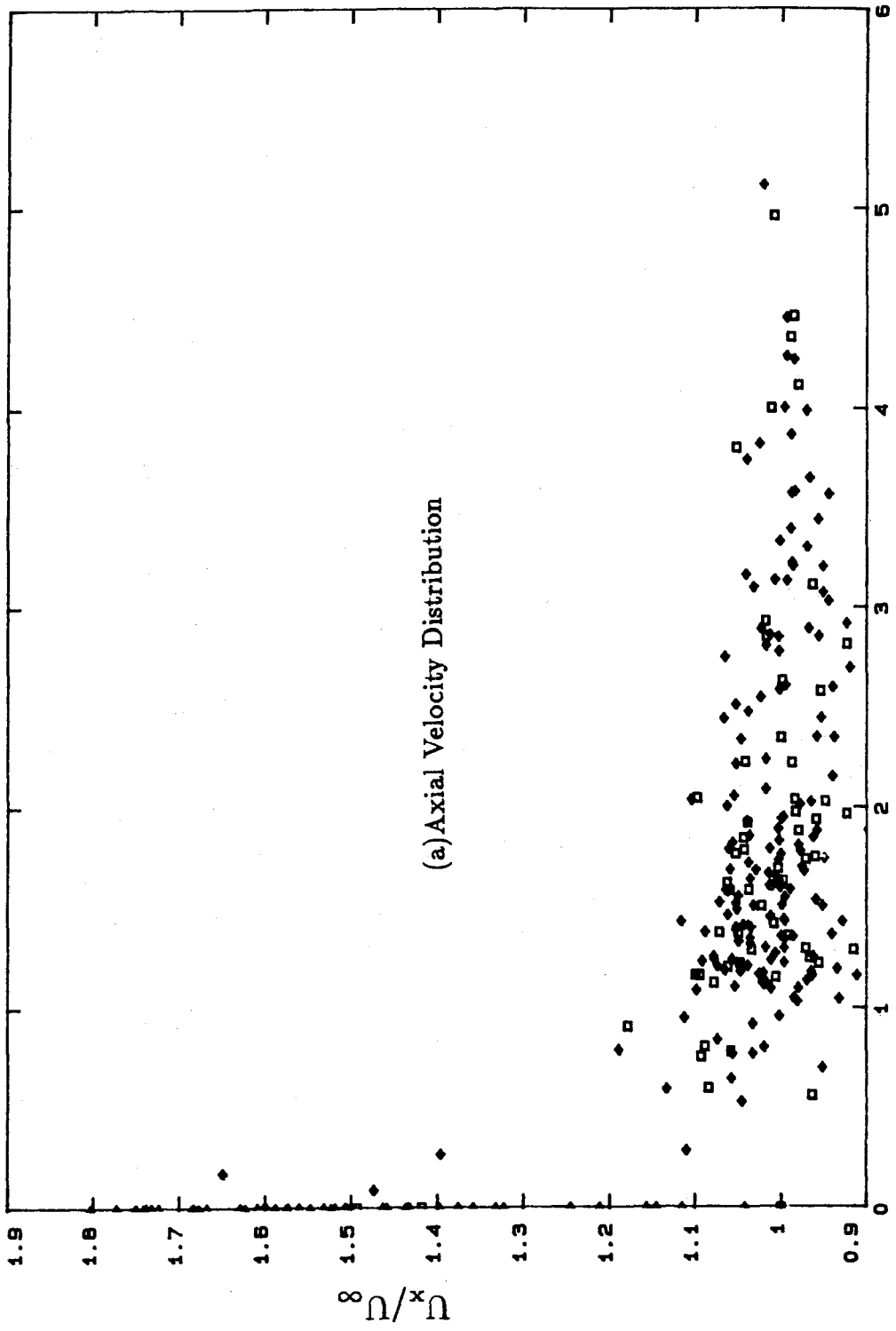

Figure IV.15(a,b) Trailing Vortex Velocity Distribution. Same data as Figure IV.14 replotted with bubble radius as a parameter. (open box:$\phi < 150\mu$m; solid diamond:$150 \leq \phi \leq 250\mu$m; solid box:$\phi > 250\mu$m).

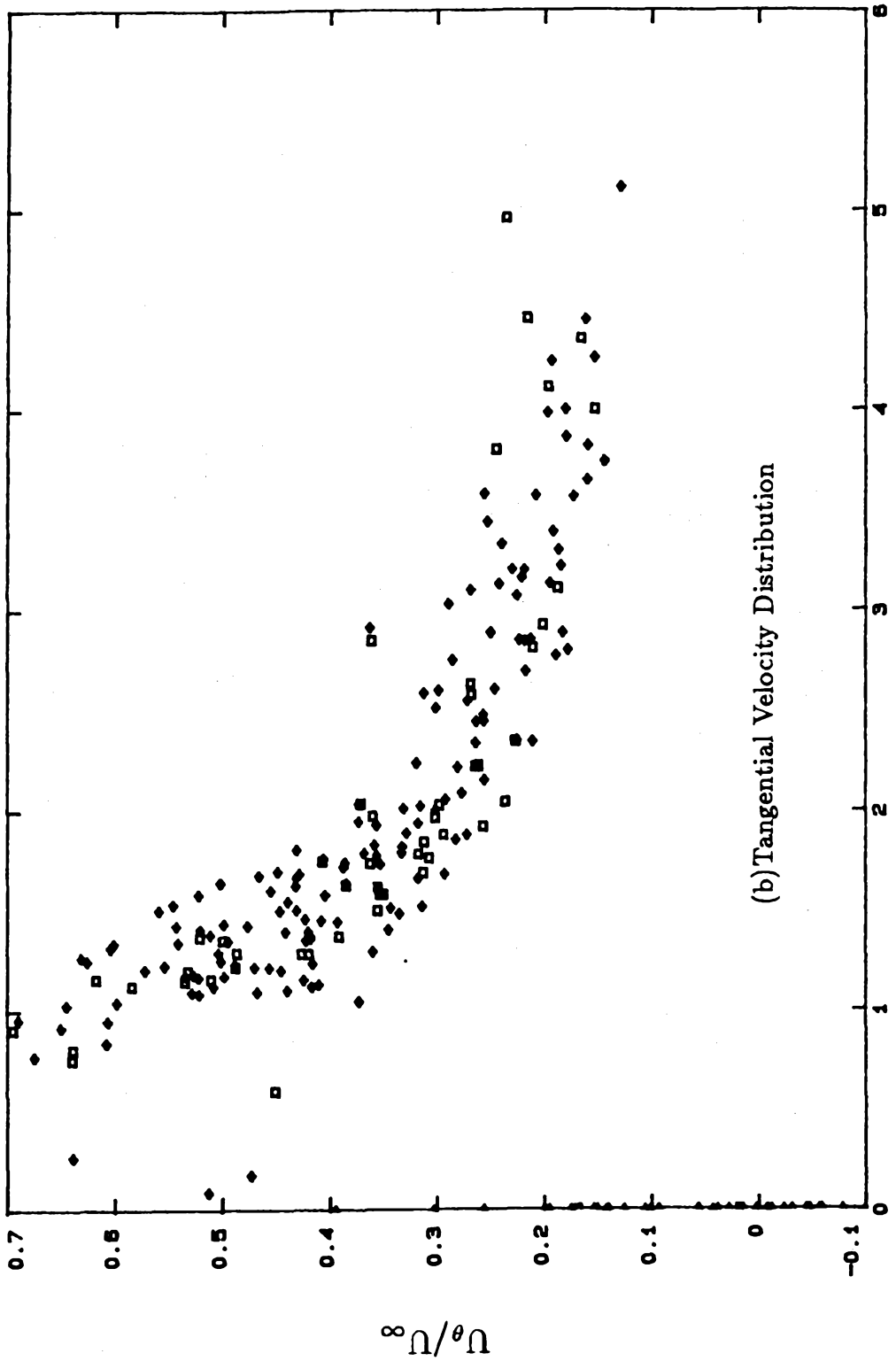

Figure IV.15(a,b) Trailing Vortex Velocity Distribution. Same data as Figure IV.14 replotted with bubble radius as a parameter. (open box:$\phi < 150\mu$m; solid diamond:$150 \leq \phi \leq 250\mu$m; solid box:$\phi > 250\mu$m).

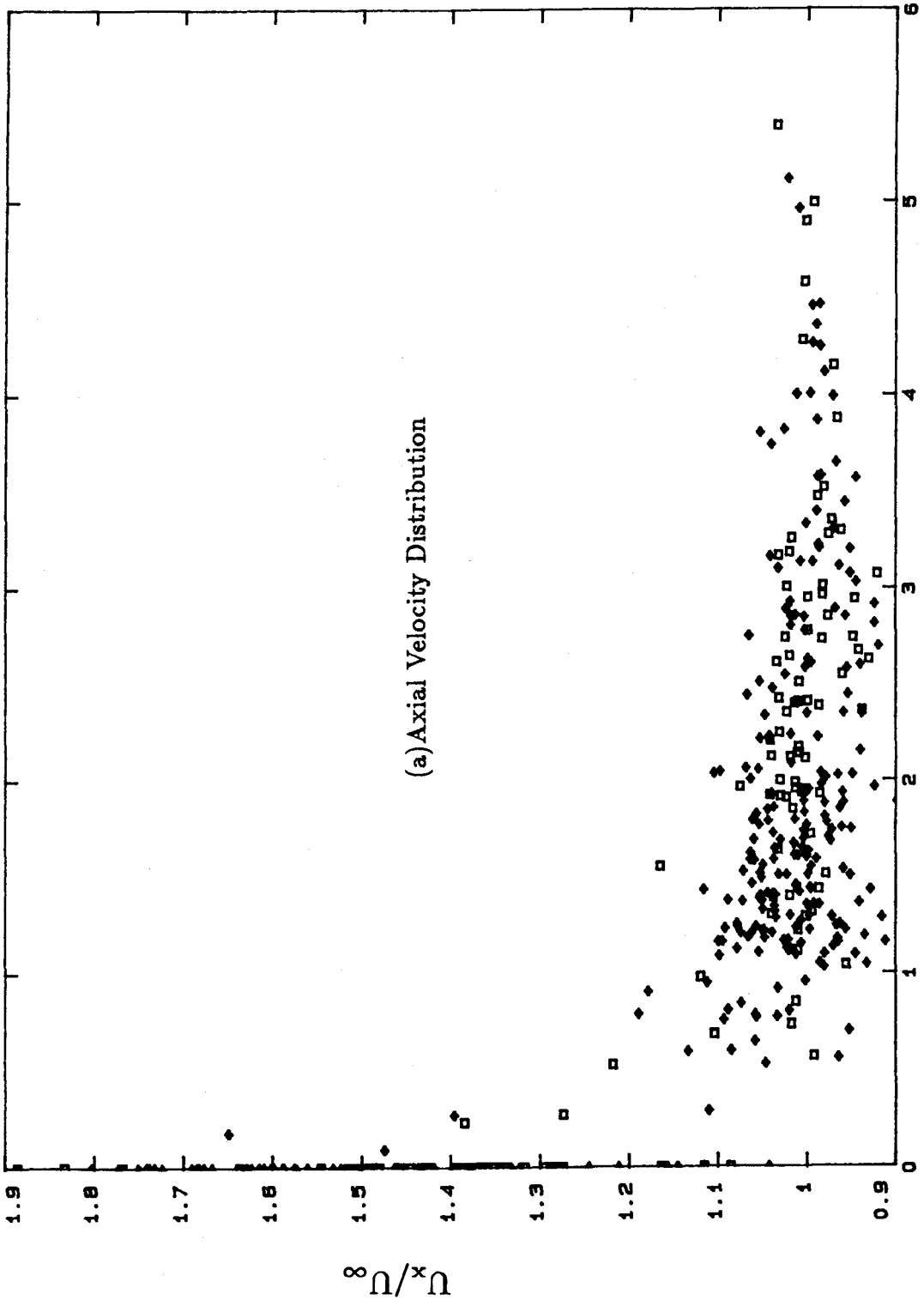

Figure IV.16(a,b) Heptane-Azobenzene Droplet Measurement of Trailing Vortex Velocity Distribution.
Same flow parameters as Figure IV.14 . (open box: heptane; solid diamond: air bubbles).

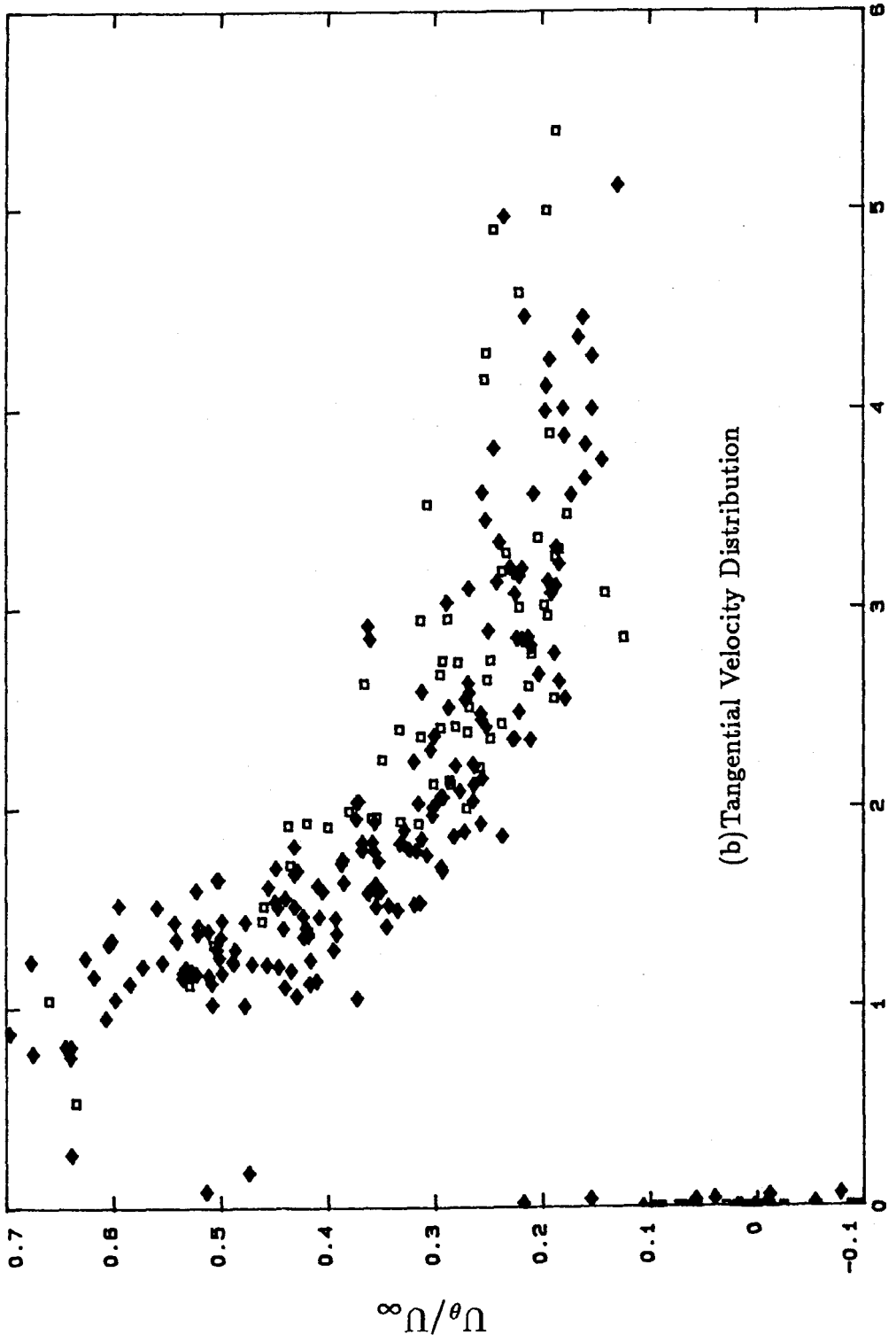

Figure IV.16(a,b) Heptane-Azobenzene Droplet Measurement of Trailing Vortex Velocity Distribution.
Same flow parameters as Figure IV.14 . (open box: heptane; solid diamond: air bubbles).

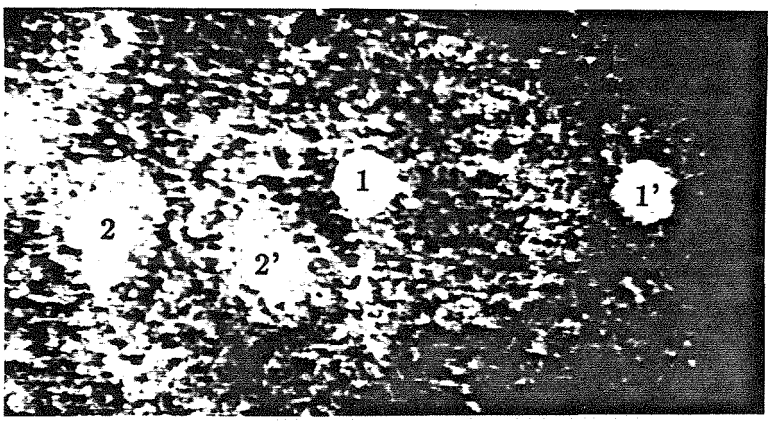

Figure IV.17 Core Axial Velocity Excess. x/c=2, $\alpha = 10°$, Re=5.16×10^5. Each number represents the first image of a bubble, and the number primed is the image 150μs later.

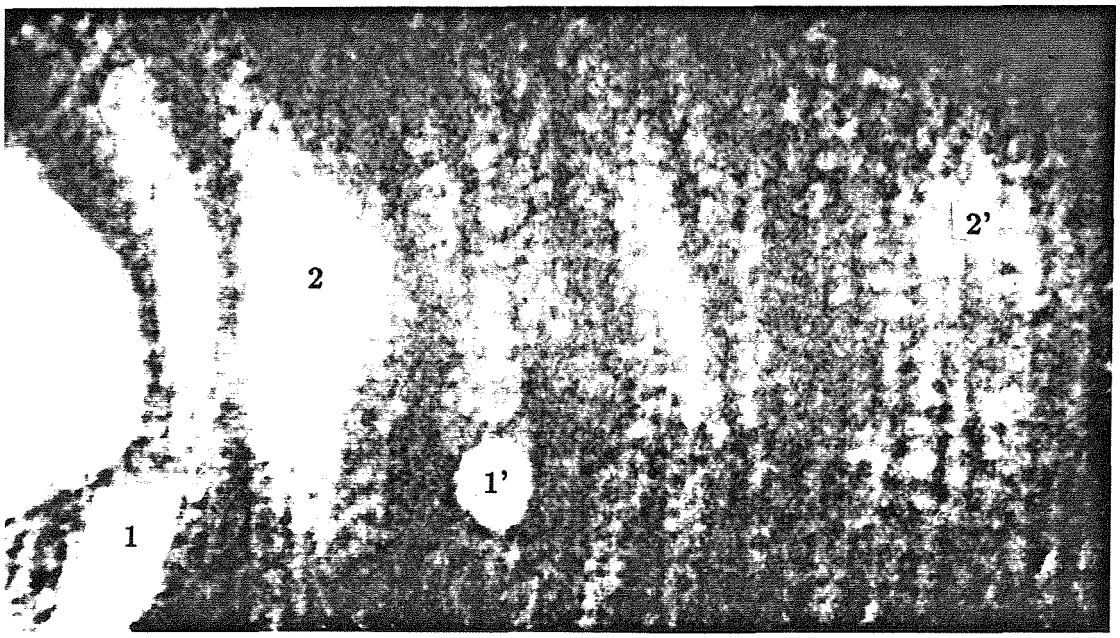

Figure IV.18 Core Axial Velocity Deficit. x/c=10, $\alpha = 5°$, Re=1.04×10^6. Each number represents the first image of a bubble, and the number primed is the image 150μs later.

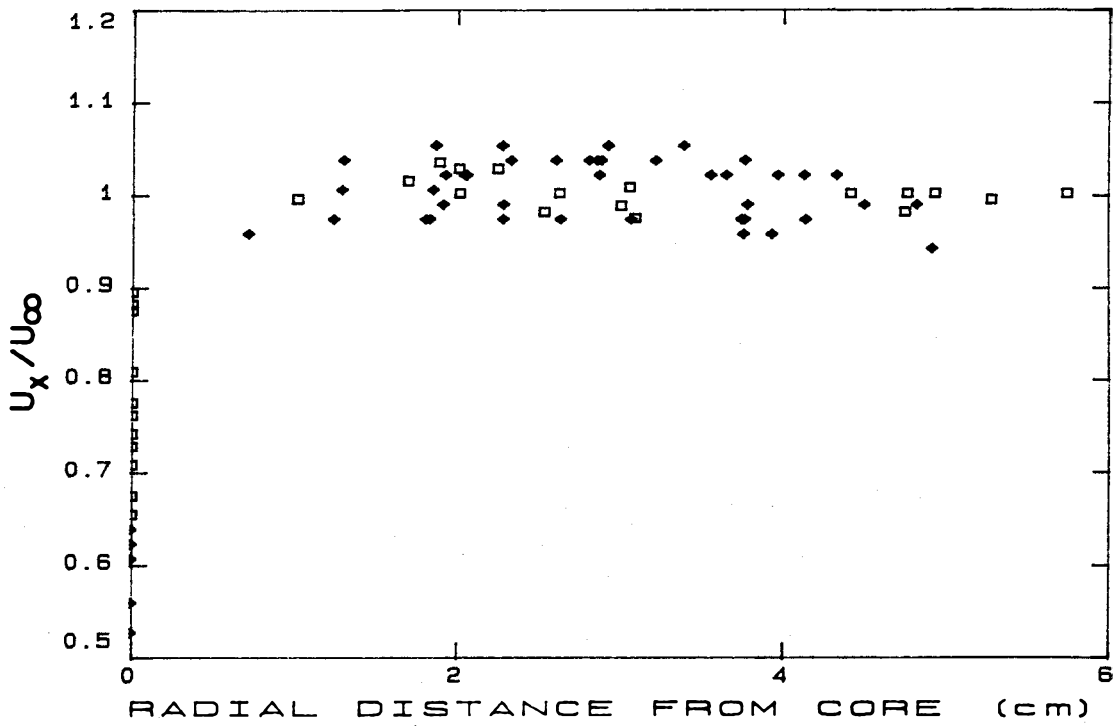

(a) Axial Velocity Distribution

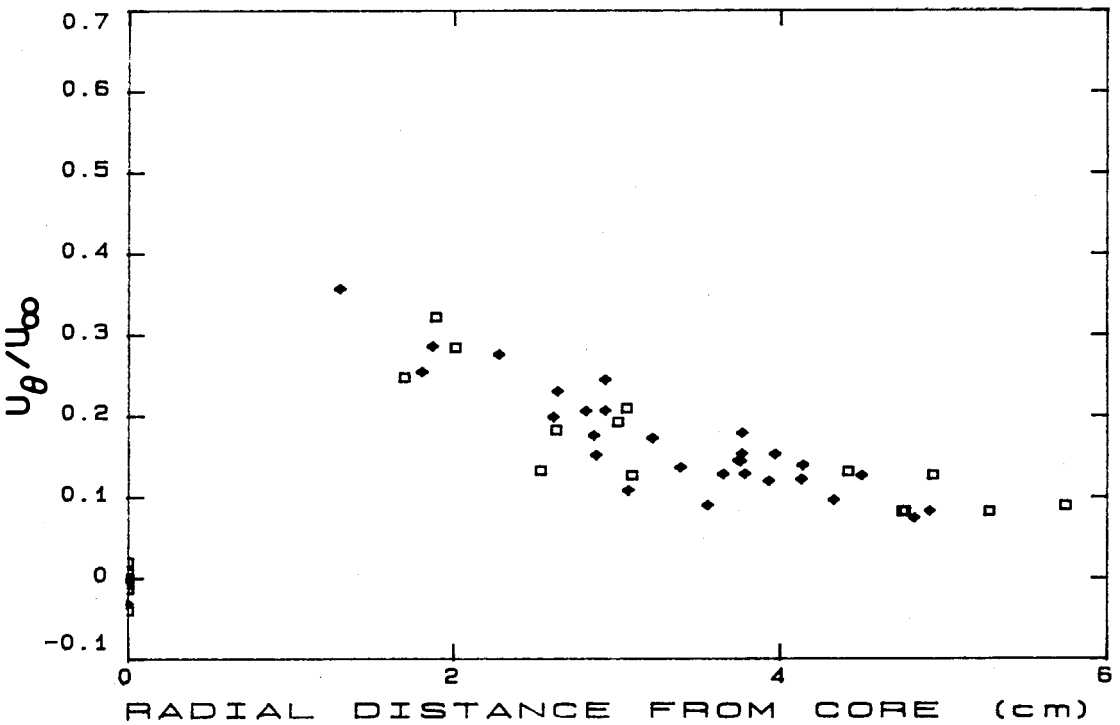

(b) Tangential Velocity Distribution

Figure IV.19(a,b) Trailing Vortex Velocity Distribution. x/c=10, $\alpha = 5°$ (solid diamond: Re=1.79×10^5; open box: Re=4.31×10^5).

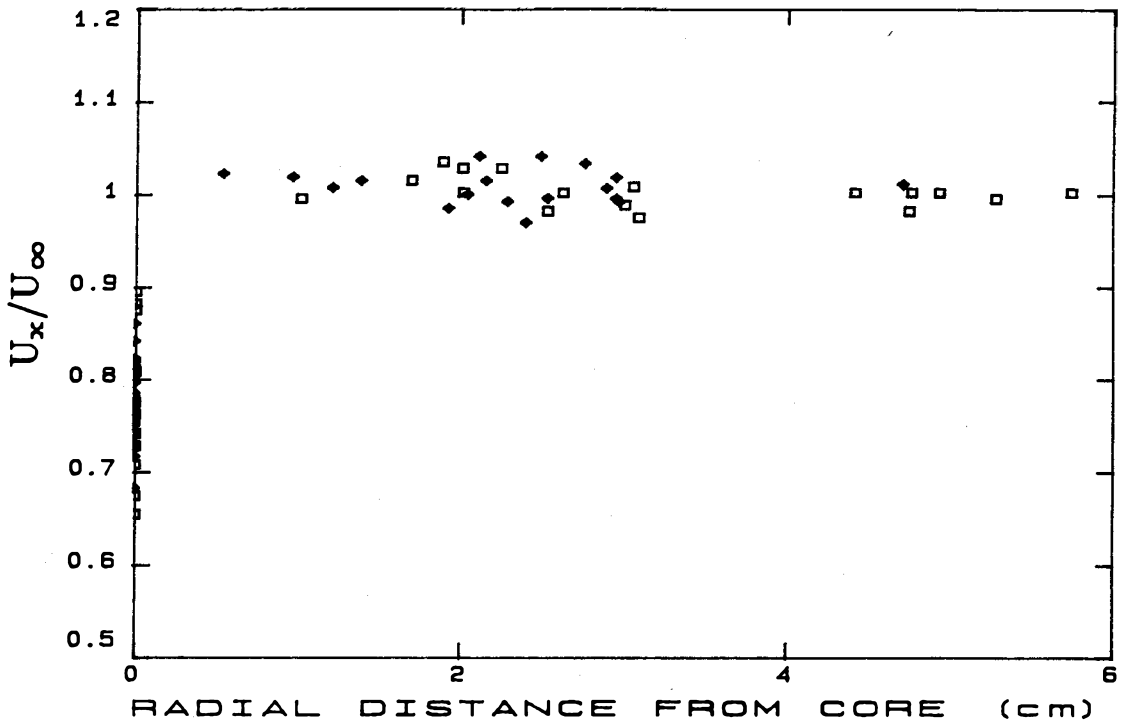

(a) Axial Velocity Distribution

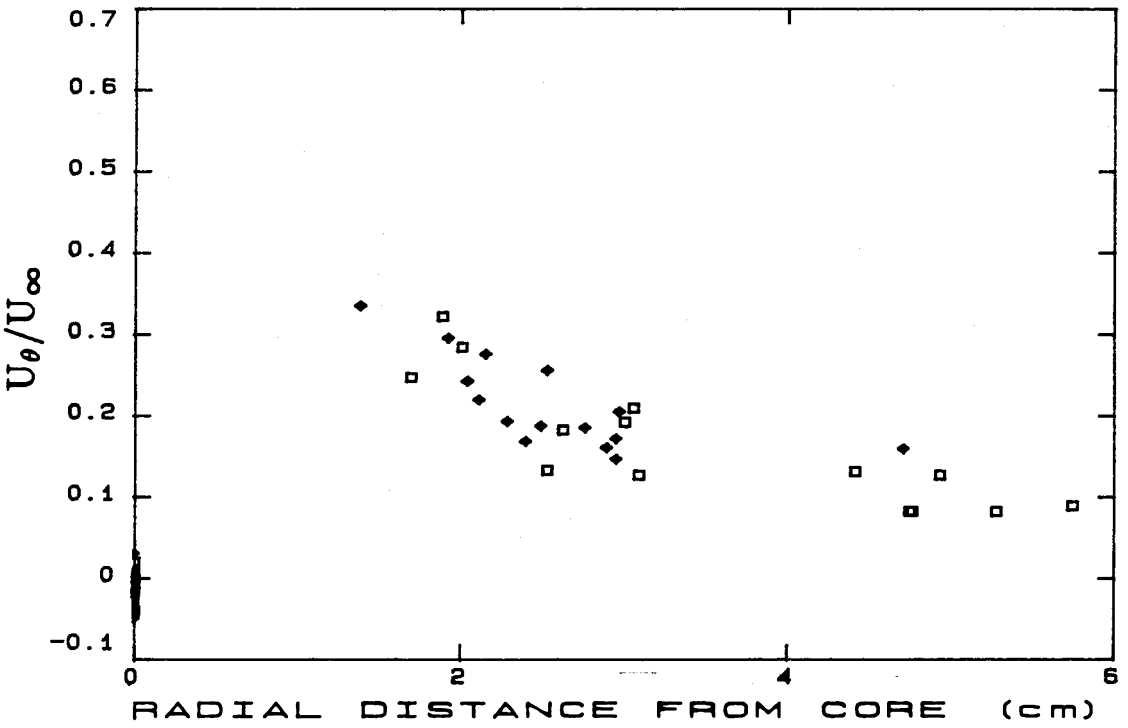

(b) Tangential Velocity Distribution

Figure IV.20(a,b) Trailing Vortex Velocity Distribution. x/c=10, $\alpha = 5°$ (solid diamond: Re=7.61 x 10^5; open box: Re=4.31 x 10^5).

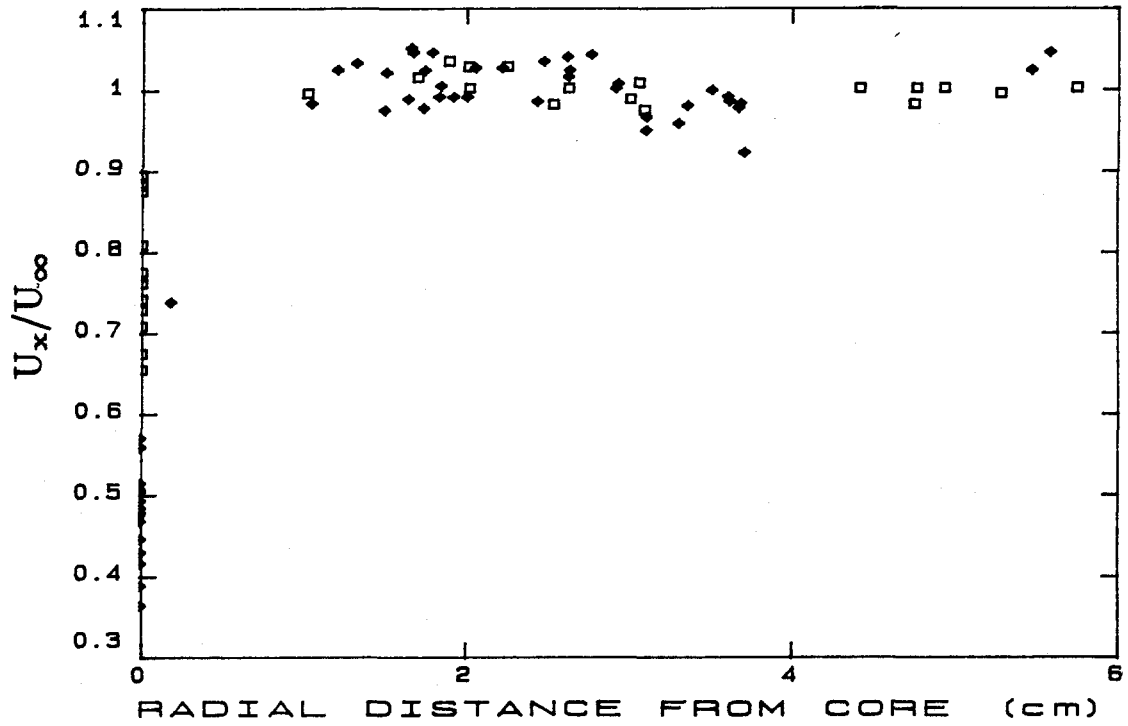

(a)Axial Velocity Distribution

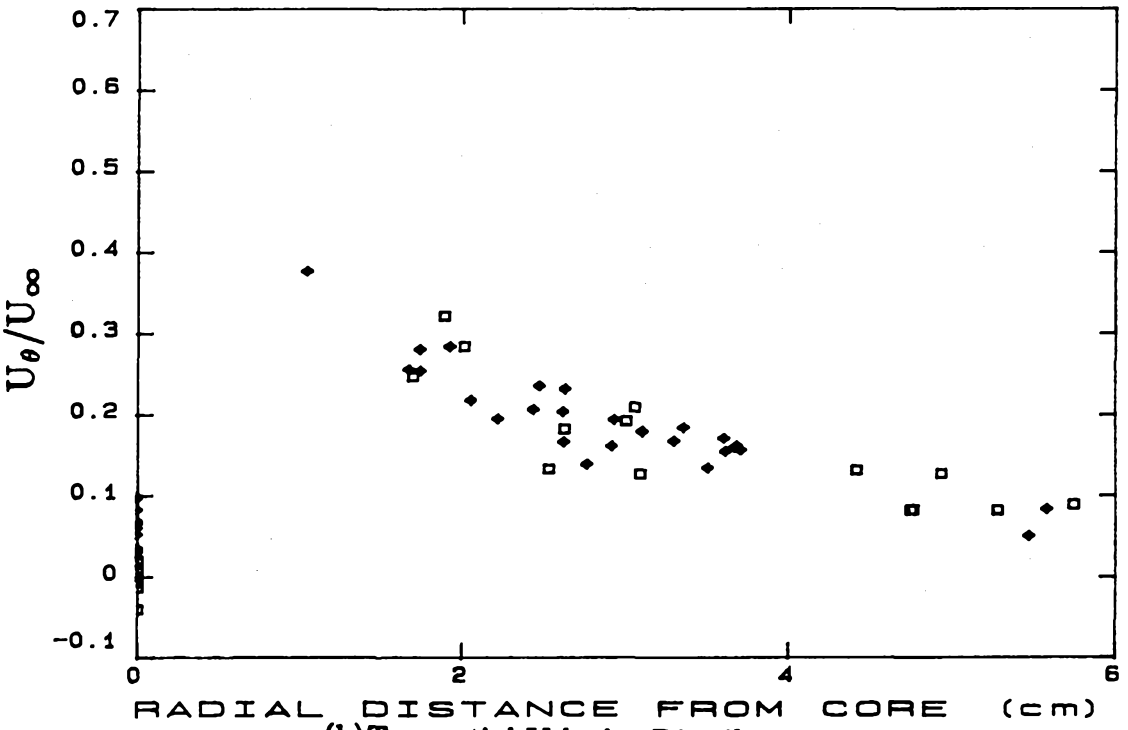

(b)Tangential Velocity Distribution

Figure IV.21(a,b) Trailing Vortex Velocity Distribution. x/c=10, $\alpha = 5°$ (solid diamond: Re=1.04×10^6; open box: Re=4.31×10^5).

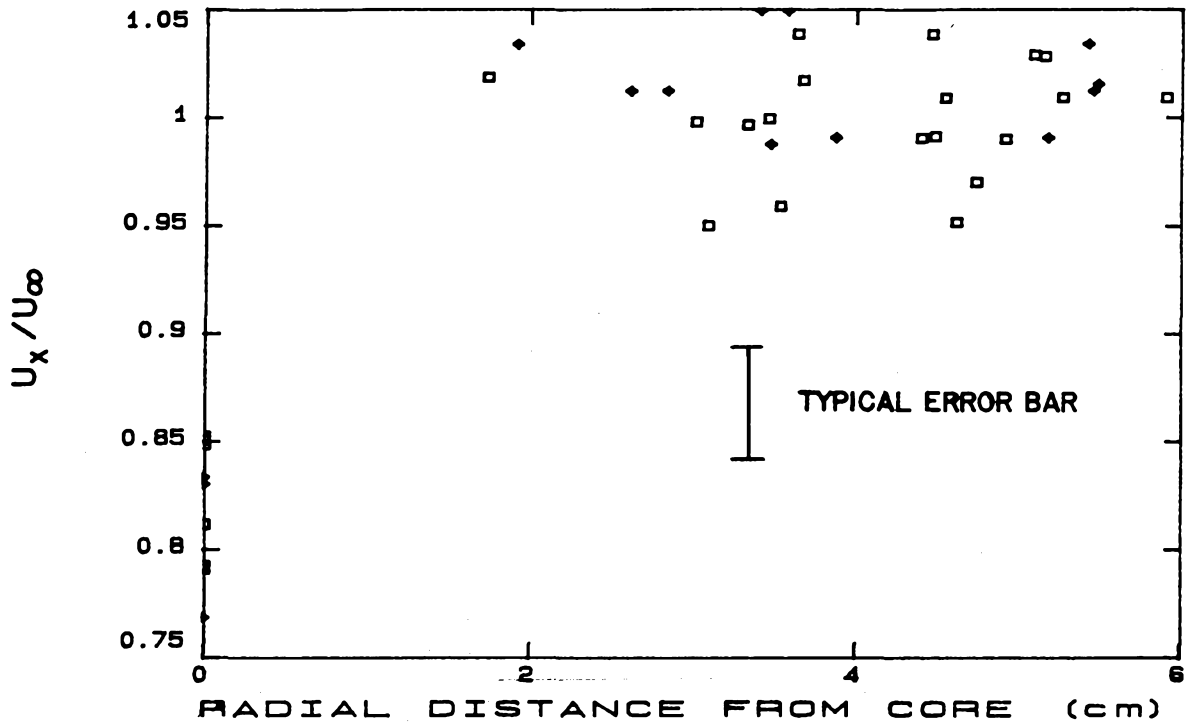

(a) Axial Velocity Distribution

(b) Tangential Velocity Distribution

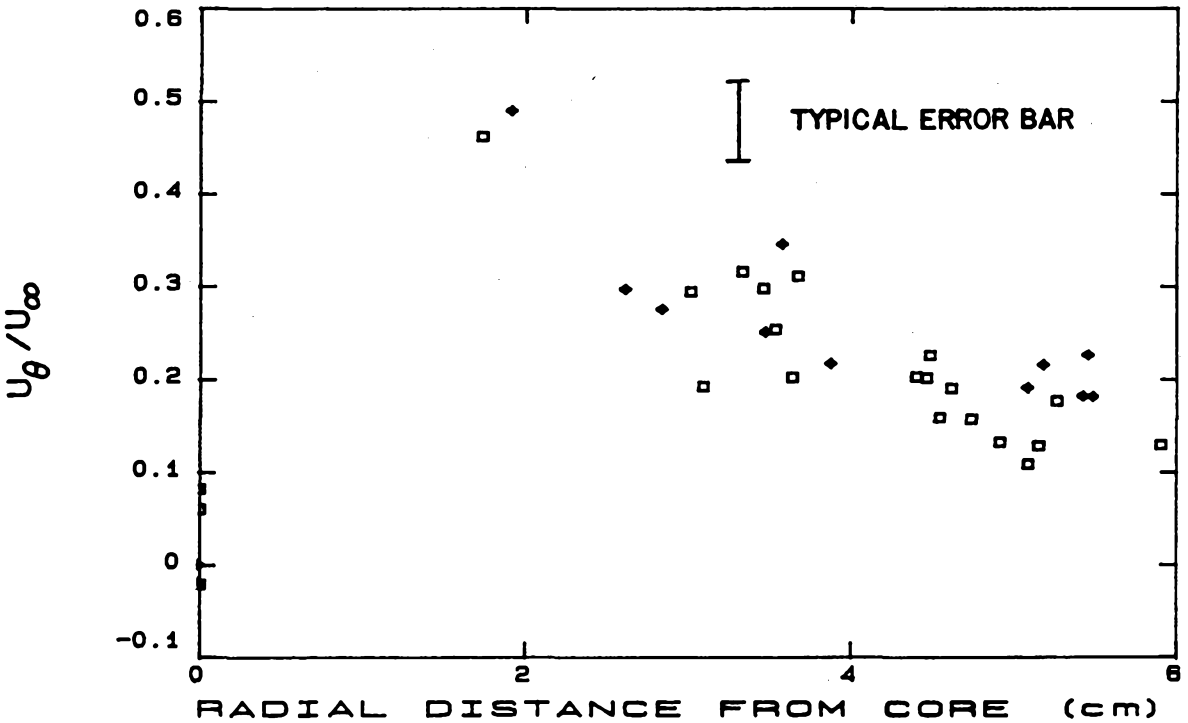

Figure IV.22(a,b) Vortex Velocity Distribution. x/c=10, $\alpha = 5°$, Re=1.44×10^5.

The two symbols represent two different holograms.

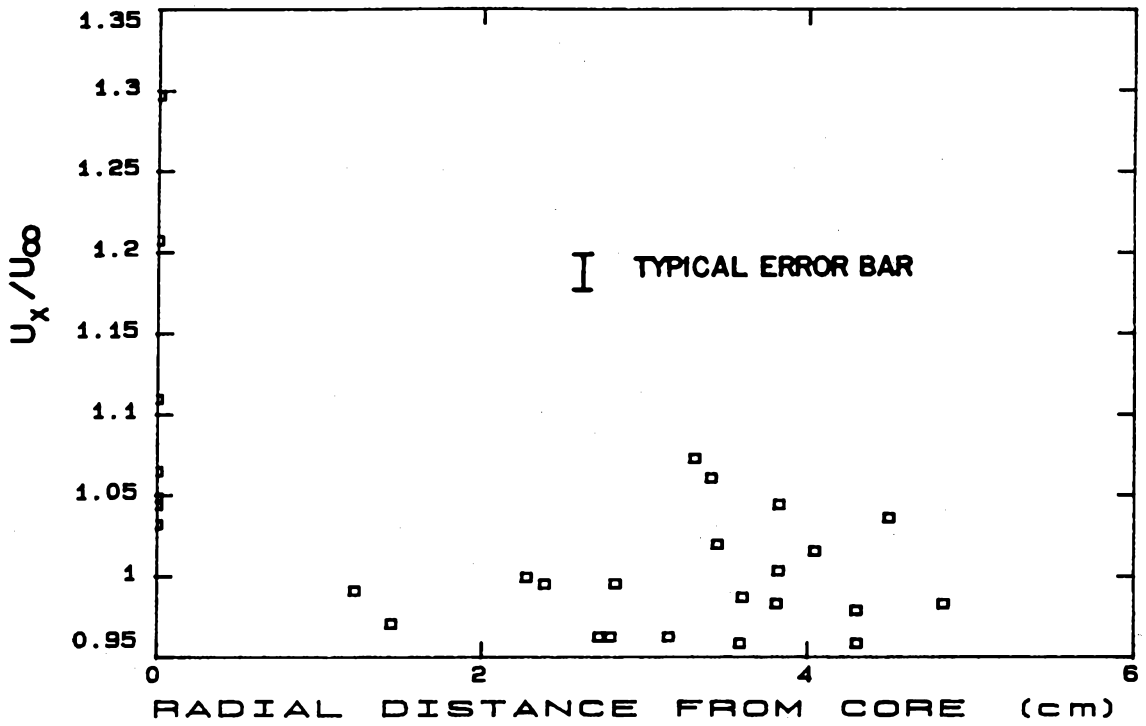

(a) Axial Velocity Distribution

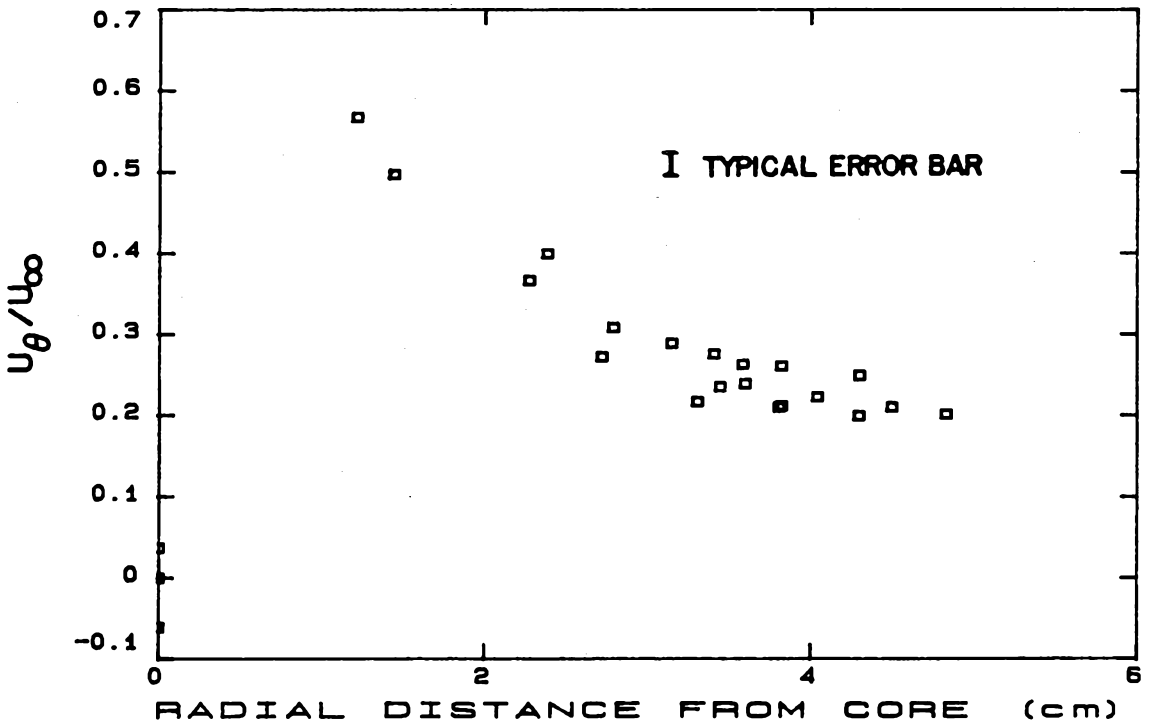

(b) Tangential Velocity Distribution

Figure IV.23(a,b) Vortex Velocity Distribution. x/c=10, $\alpha = 5°$, Re=4.31×10^5.

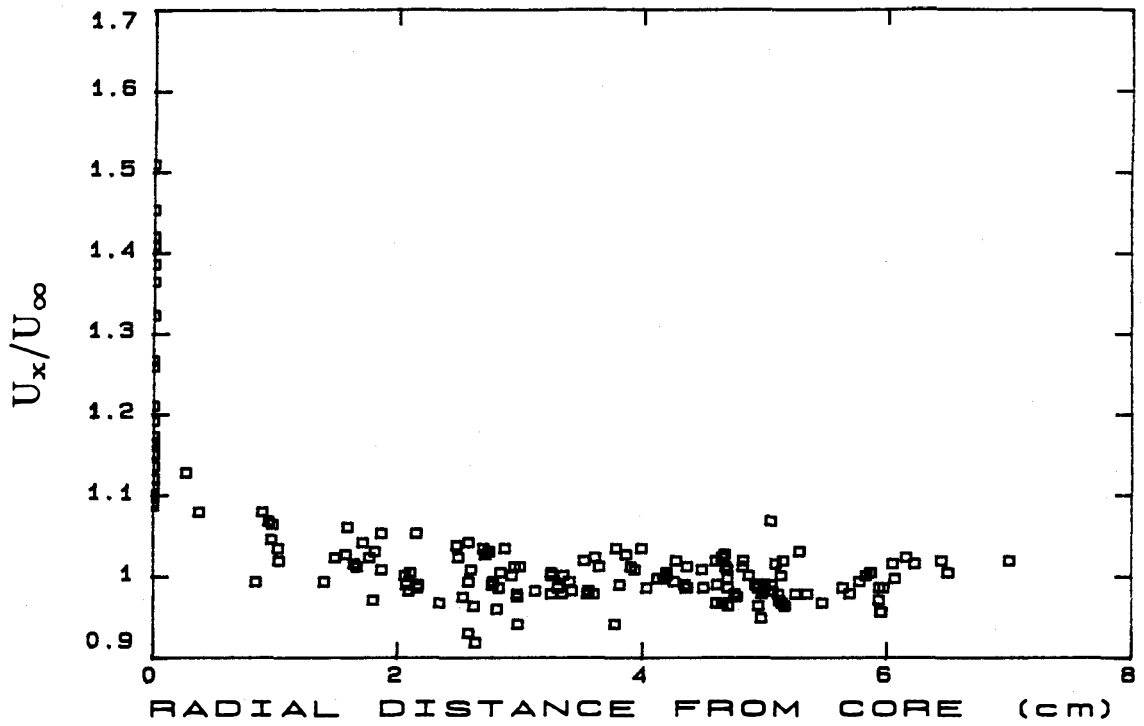

(a) Axial Velocity Distribution

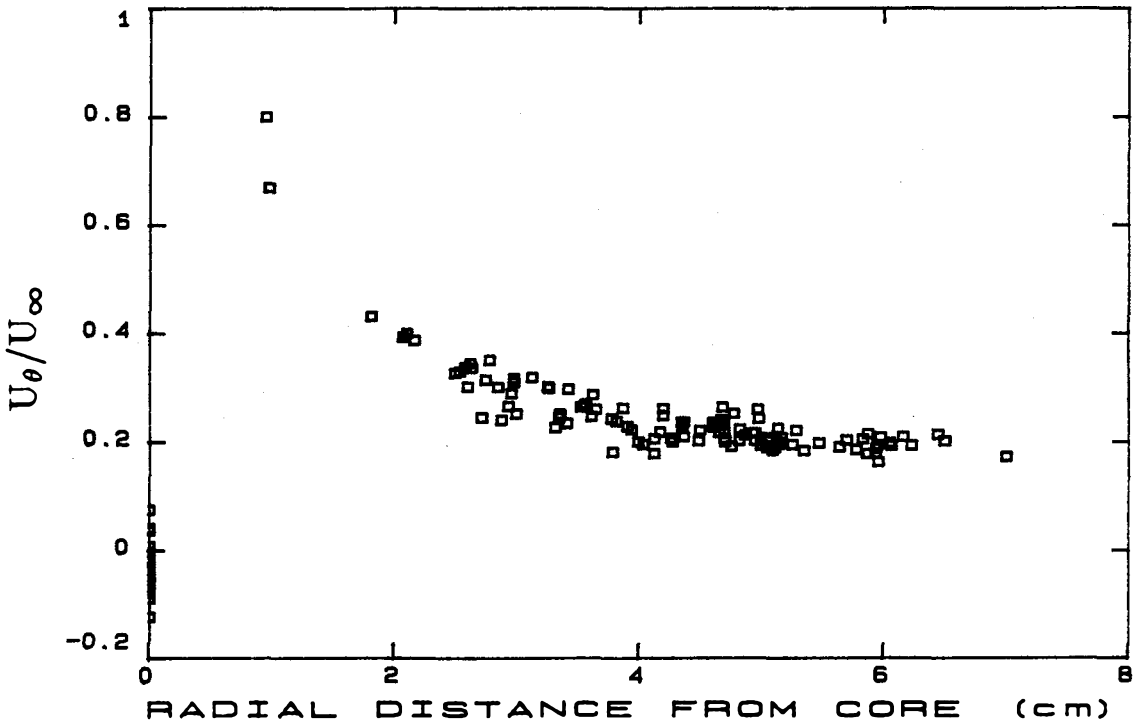

(b) Tangential Velocity Distribution

Figure IV.24(a,b) Vortex Velocity Distribution. x/c=10, $\alpha = 5°$, Re=7.76×10^5.

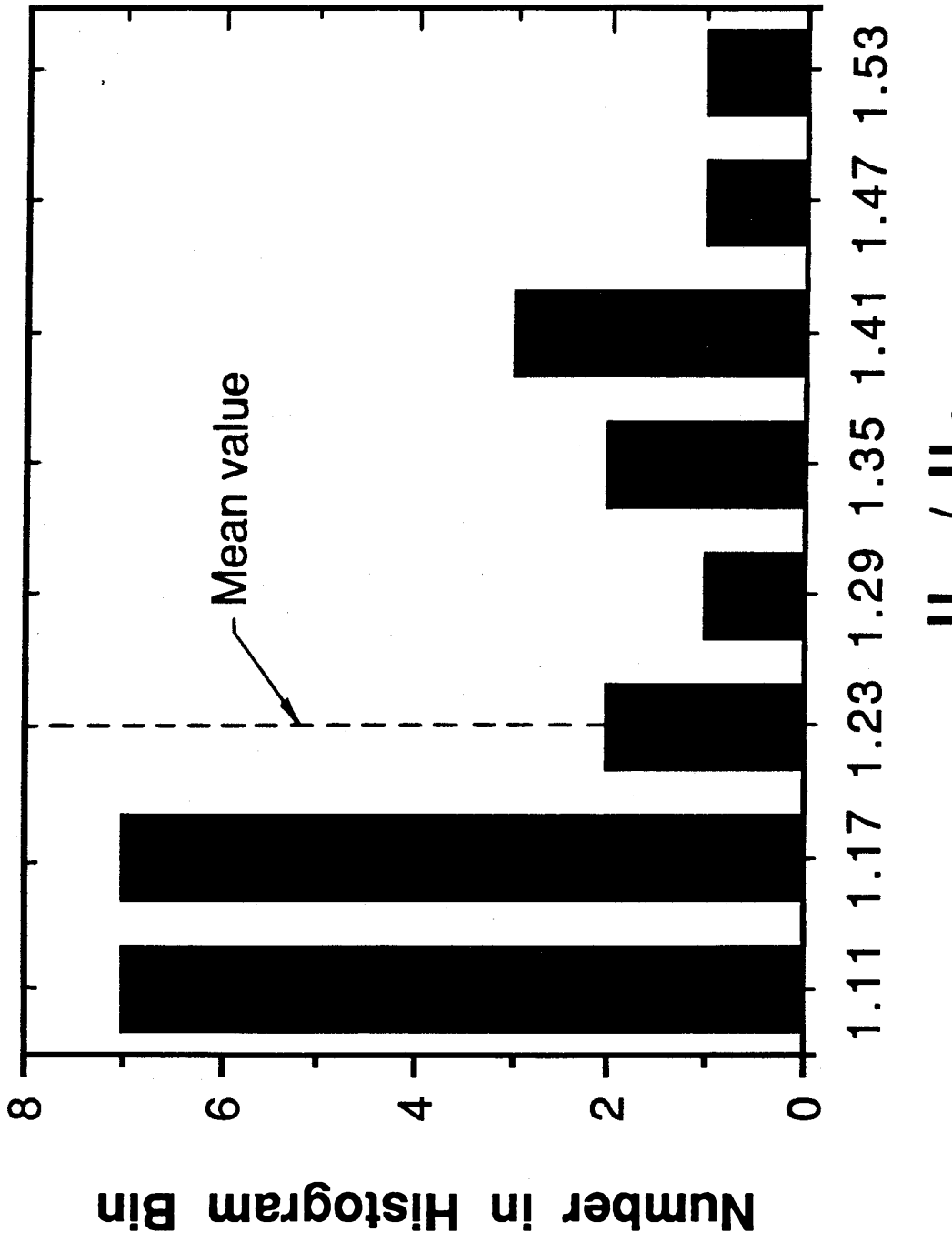

Figure IV.25 Histogram of Core Axial Velocities. x/c=10, $\alpha = 10^0$, Re=7.76×10^5.

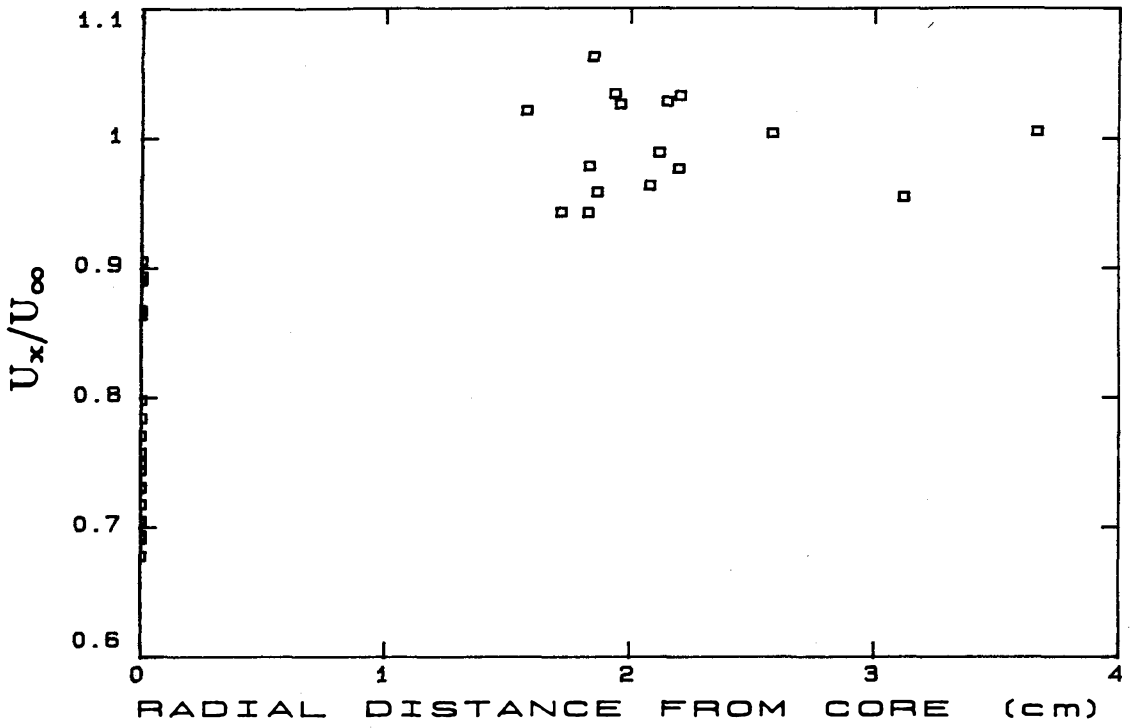

(a) Axial Velocity Distribution

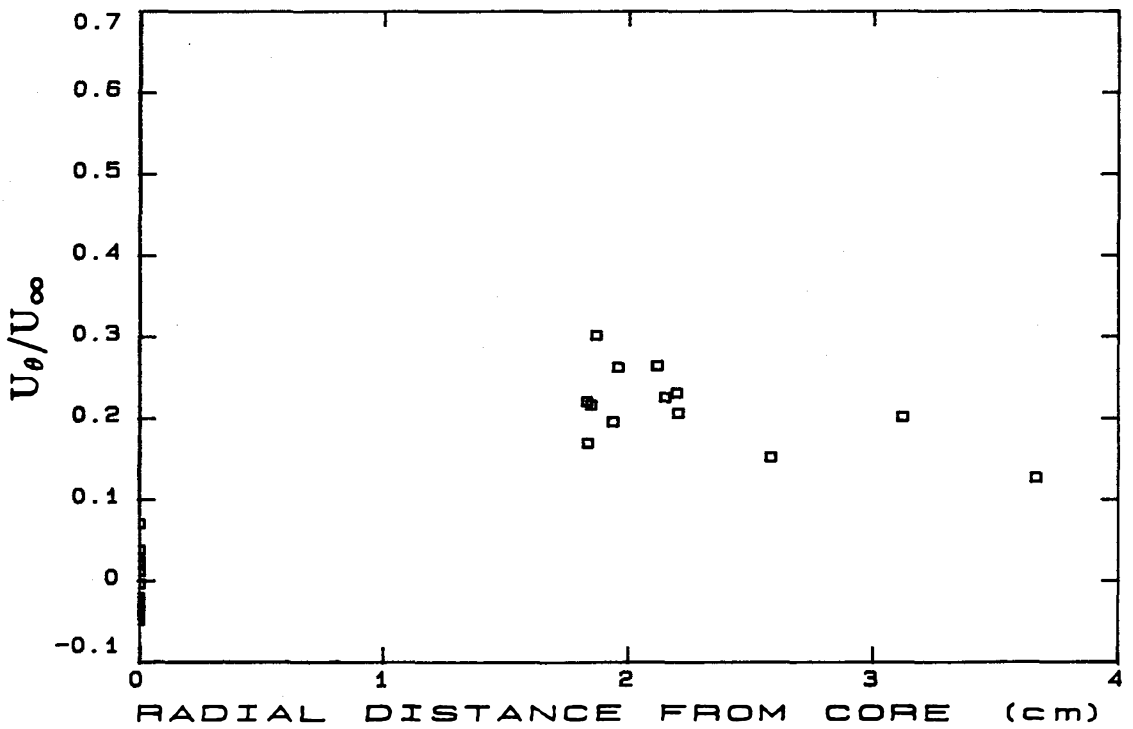

(b) Tangential Velocity Distribution

Figure IV.26(a,b) Vortex Velocity Distribution. x/c=4, $\alpha = 5°$, Re=2.14×10^5.

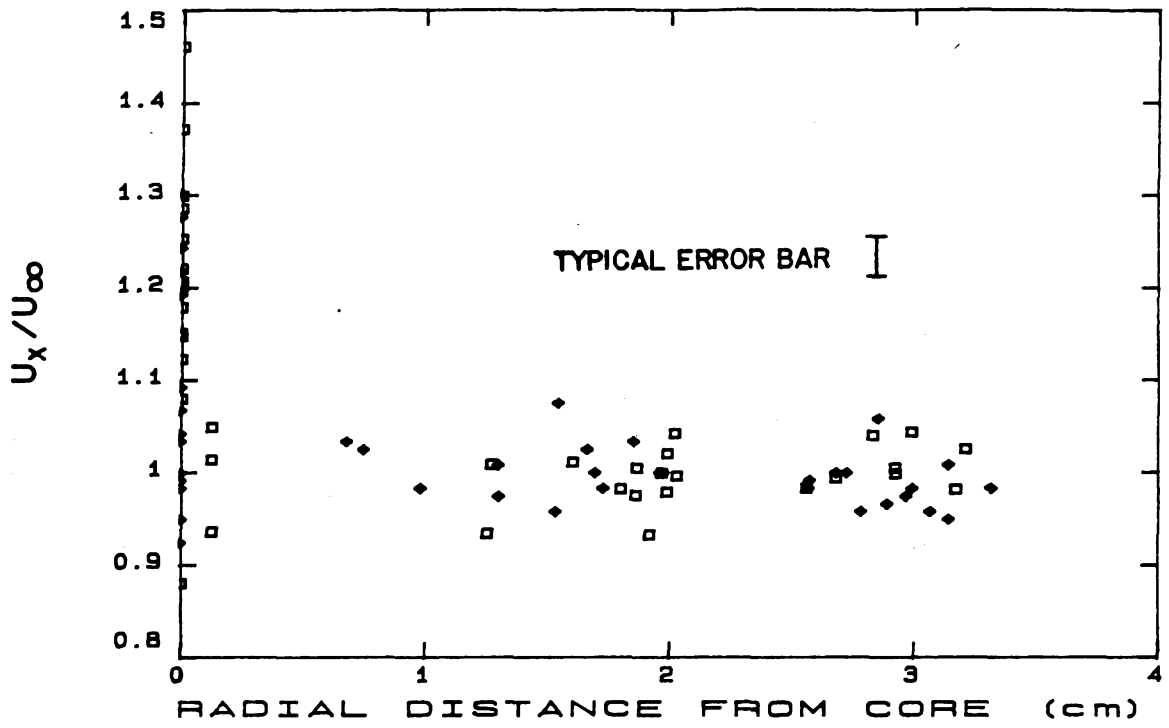

(a) Axial Velocity Distribution

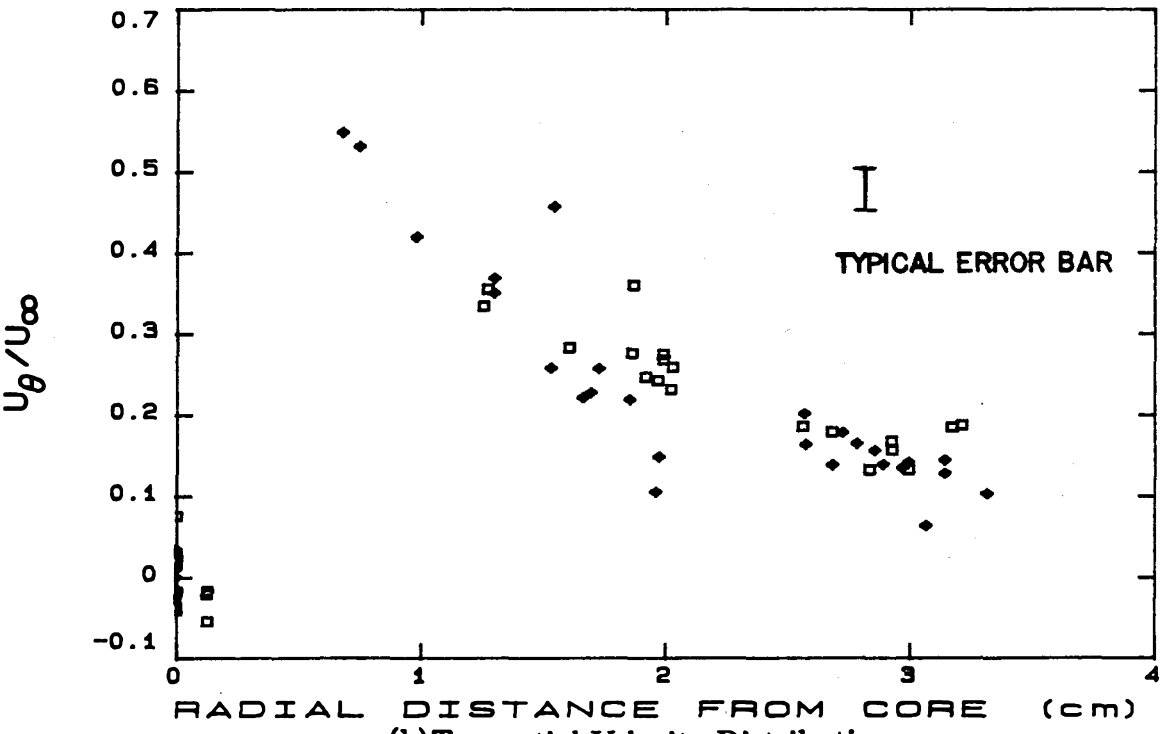

(b)Tangential Velocity Distribution

Figure IV.27(a,b) Vortex Velocity Distribution. x/c=4, $\alpha = 5°$, Re=8.19×10^5.

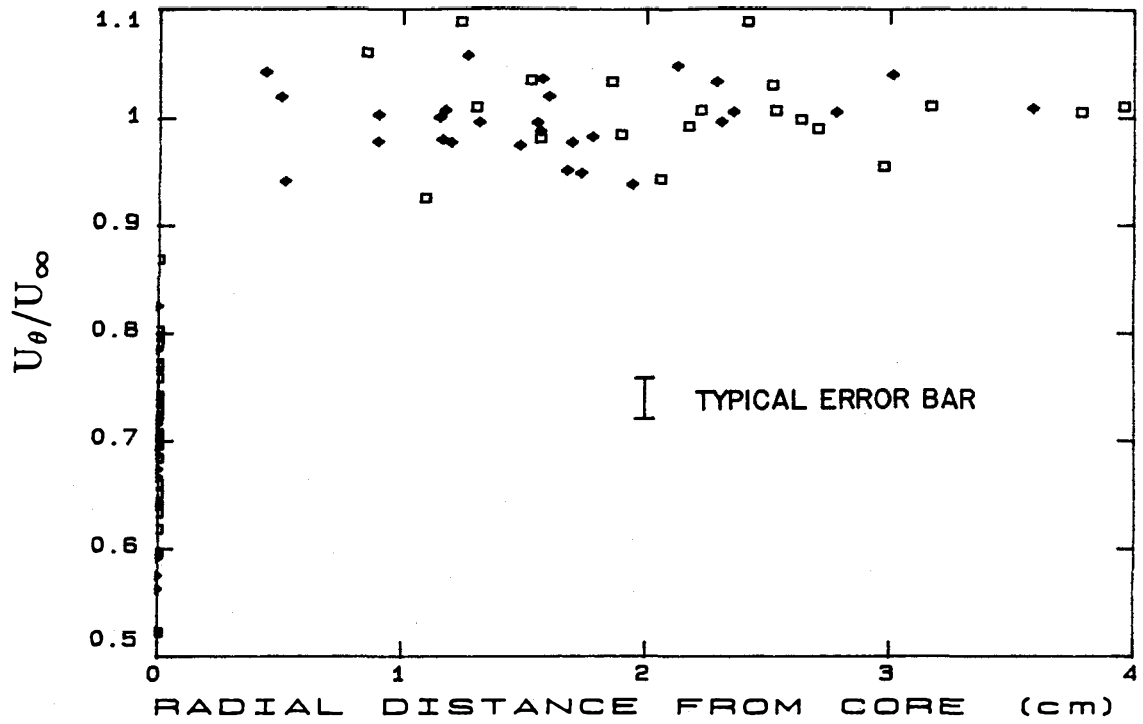

(a)Axial Velocity Distribution

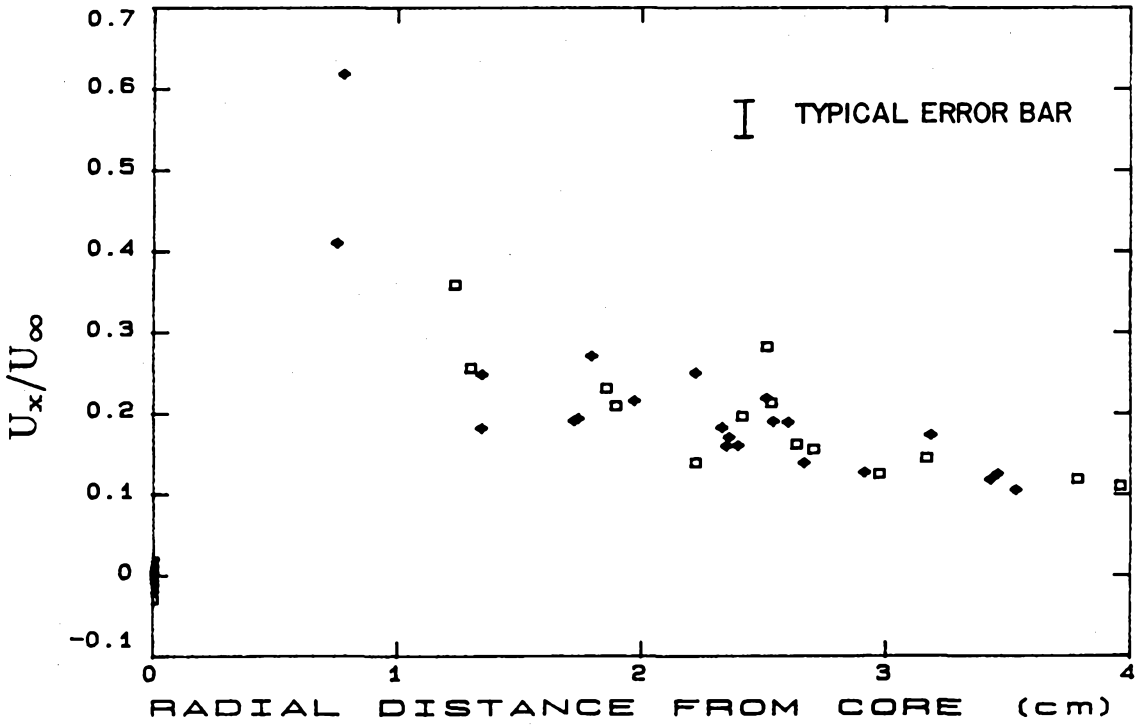

(b)Tangential Velocity Distribution

Figure IV.28(a,b) Vortex Velocity Distribution. x/c=4, $\alpha = 5°$, Re=1.08×10^6.

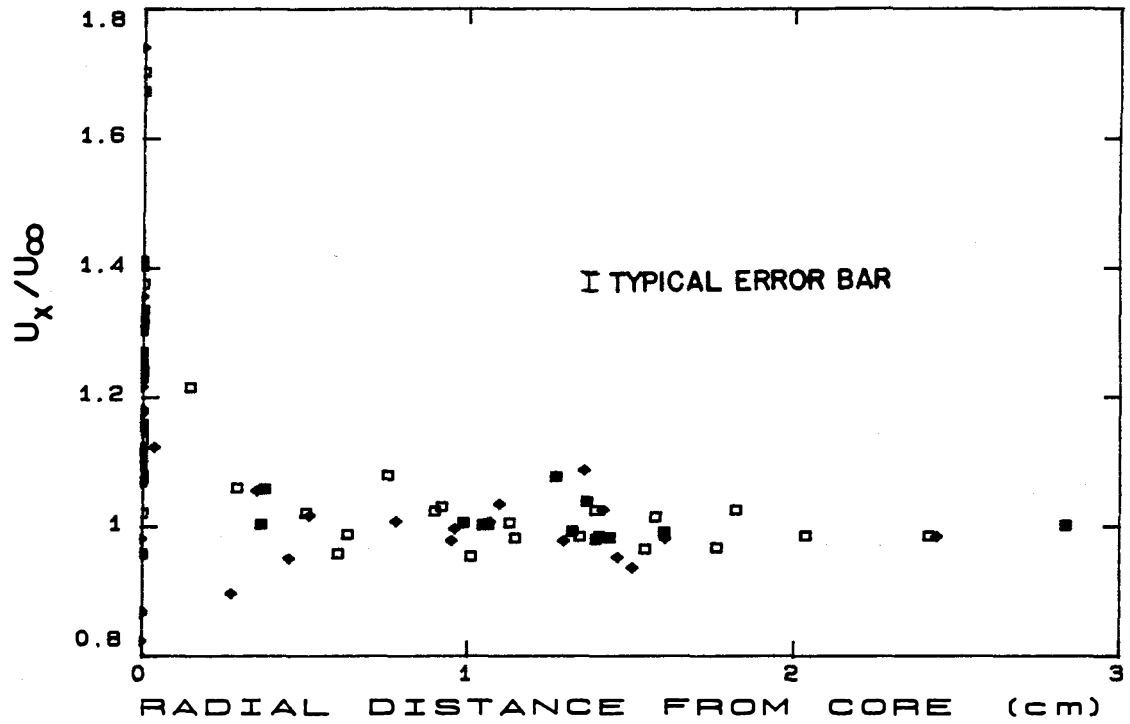

(a) Axial Velocity Distribution

(b) Tangential Velocity Distribution

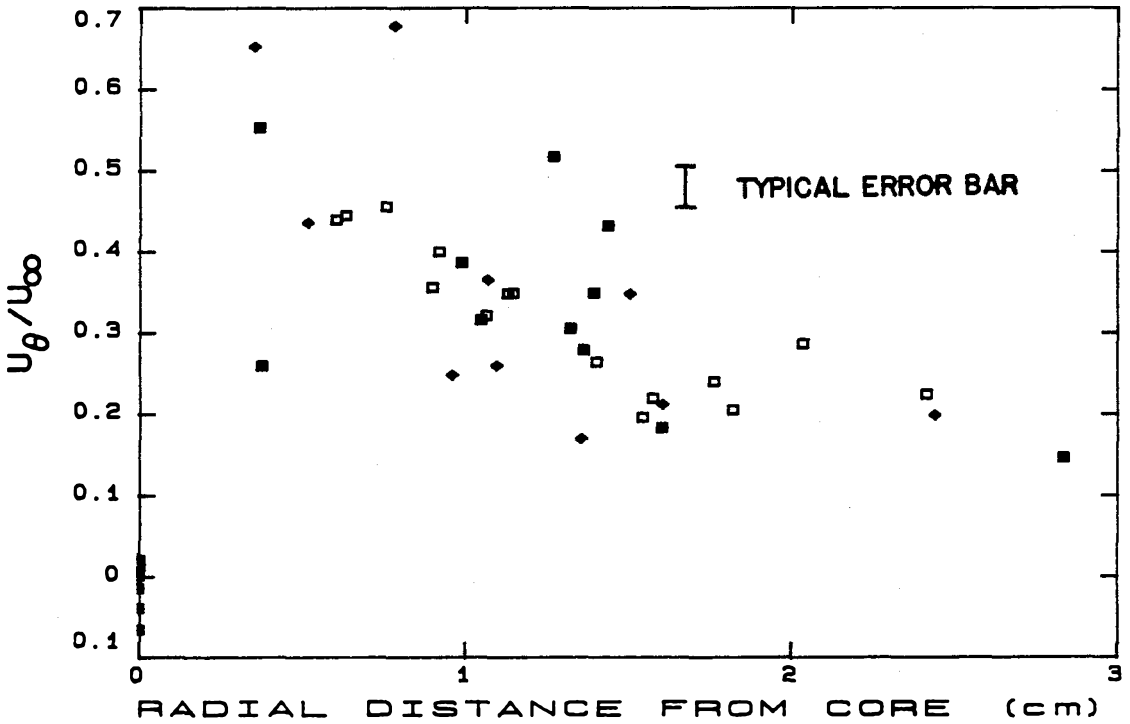

Figure IV.29(a,b) Trailing Vortex Velocity Distribution. x/c=2, $\alpha = 5°$. (solid box: Re=2.88×10^5; open box: Re=4.58×10^5; solid diamond: Re=1.03×10^6).

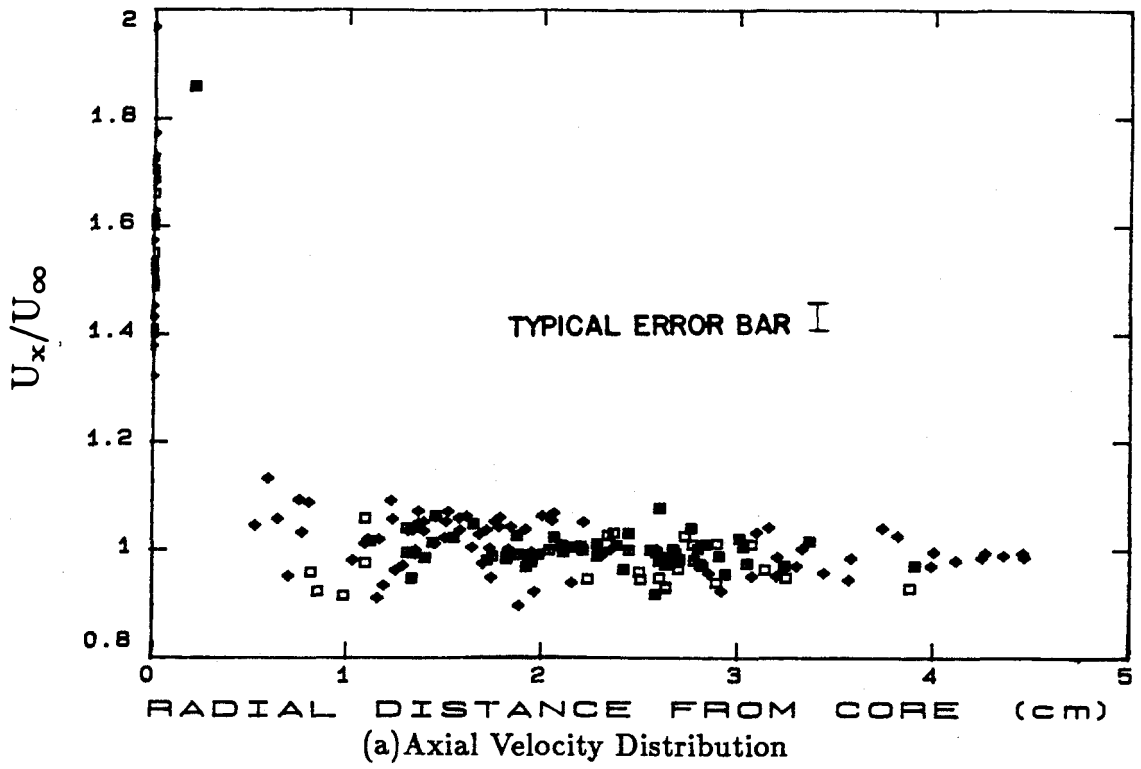

(a)Axial Velocity Distribution

(b)Tangential Velocity Distribution

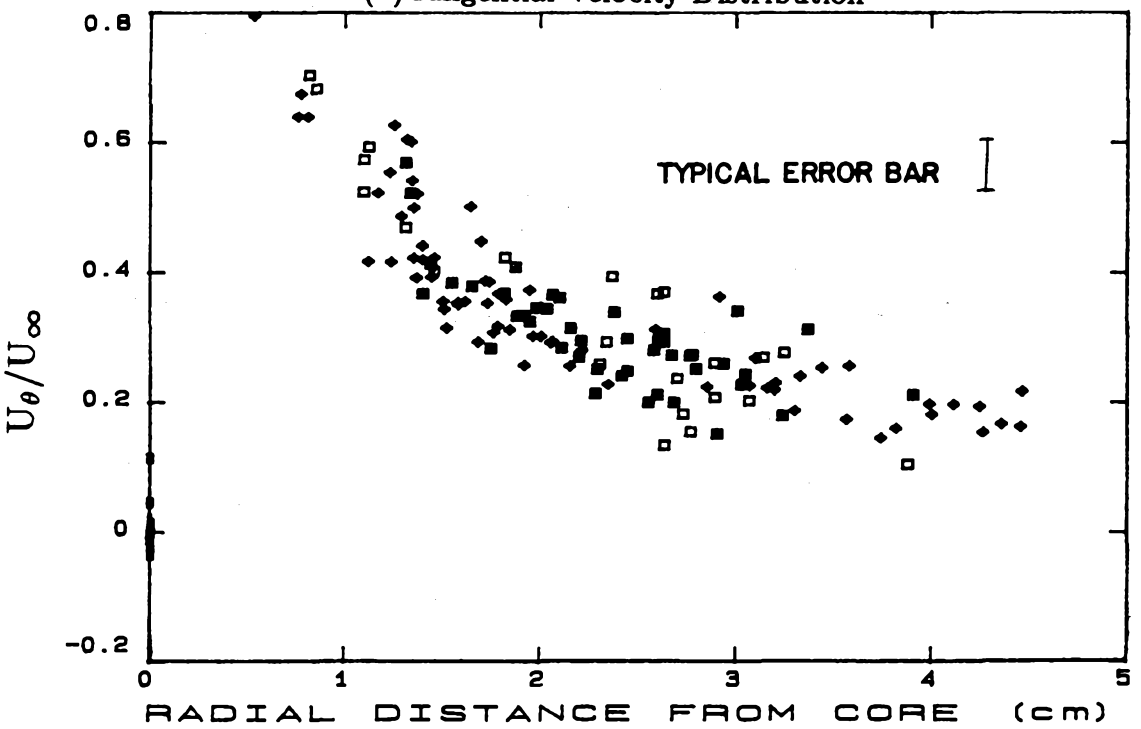

Figure IV.30(a,b) Trailing Vortex Velocity Distribution. x/c=2, $\alpha = 10°$.
(open box:Re=1.54×10^5; solid diamond:Re=5.16×10^5; solid box:Re=7.72×10^6).

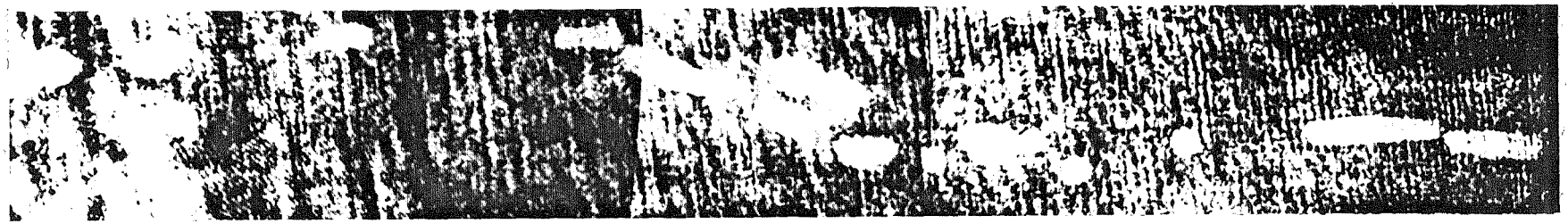

(a) x/c=2, $\alpha = 5°$, Re=1.03×10^6 (1cm in photo = 580μm in flow)

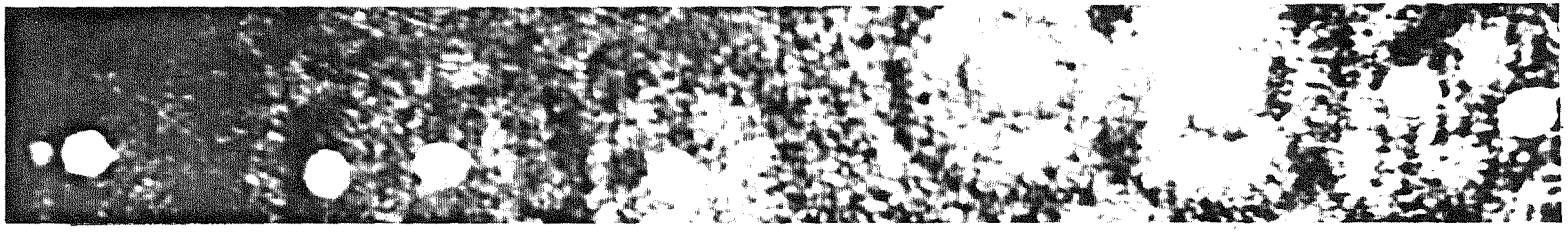

(b) x/c=2, $\alpha = 10°$, Re=7.72×10^5 (1cm in photo = 370μm in flow)

Figure IV.31 Double Pulsed Holograms of Vortex Kinks. Flow is left to right.

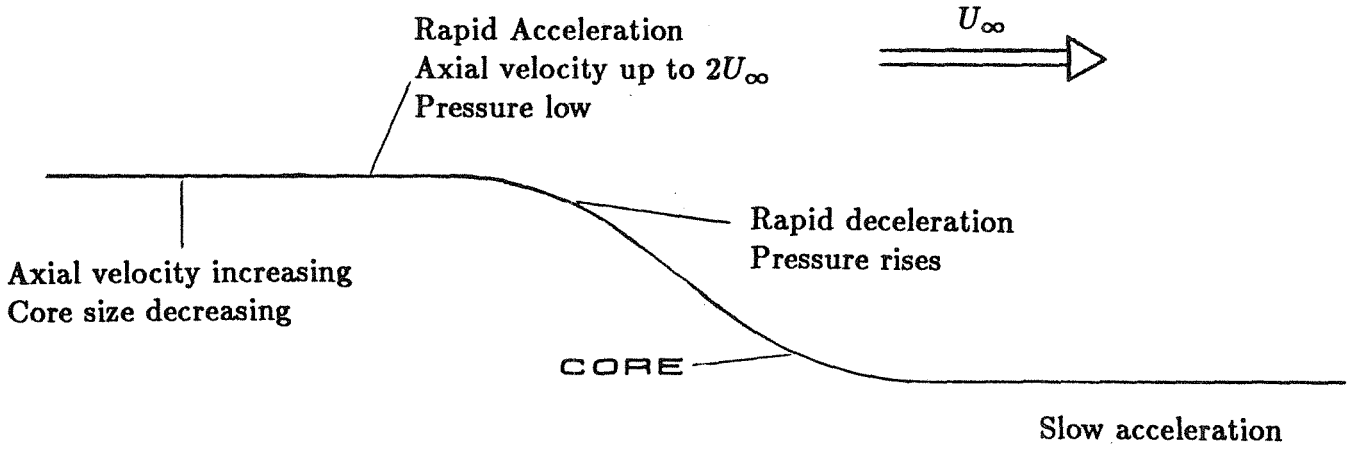

Figure IV.32 Schematic of a Vortex Kink.

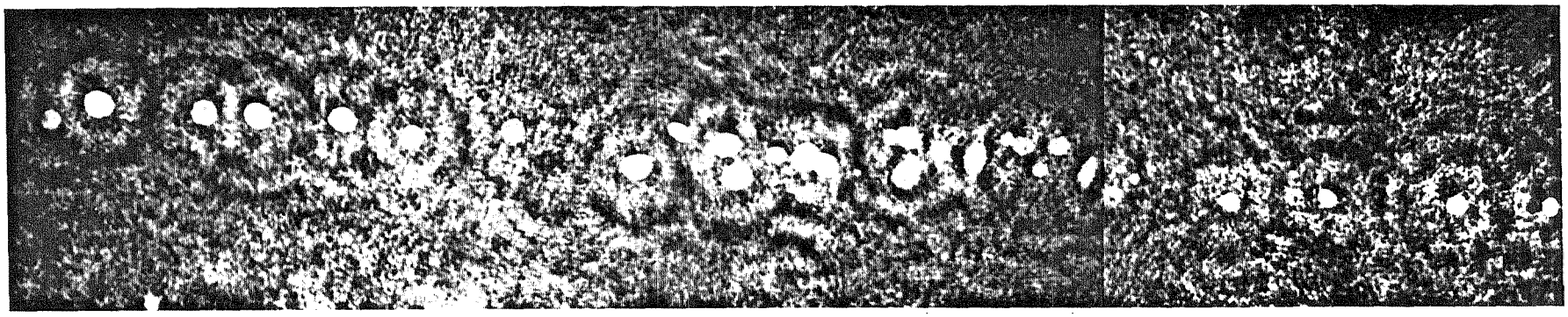

Figure IV.33 Vortex Stutter. Flow is left to right.
x/c=2, $\alpha = 10°$, Re=7.72×10^5 (1cm in photo = 960μm in flow)

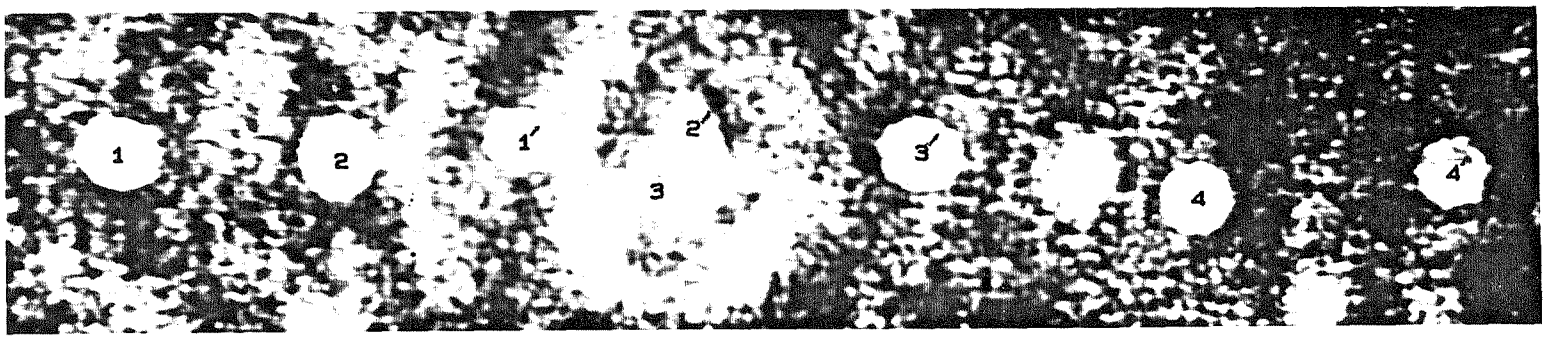

Figure IV.34 Rapid Deceleration of Core Fluid. Flow is left to right.
x/c=2, $\alpha = 10°$, Re=7.72×10^5. The two images of each
bubble are denoted by a number and the number primed.
(1cm in photo = 240μm in flow).

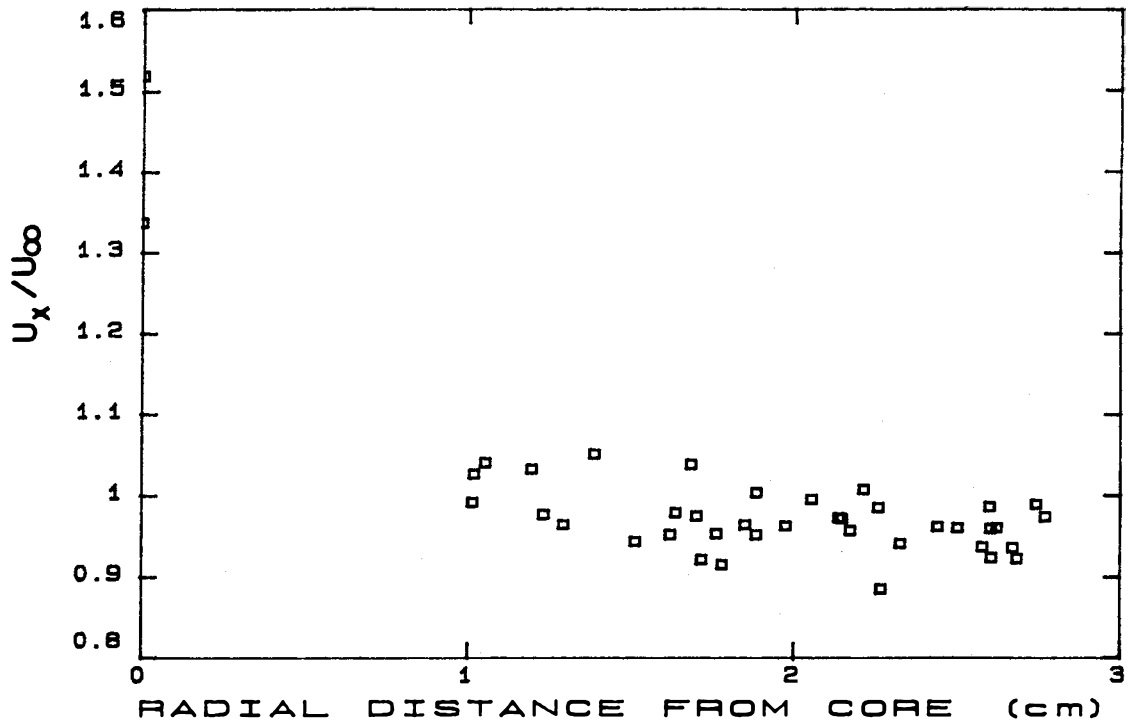

(a)Axial Velocity Distribution

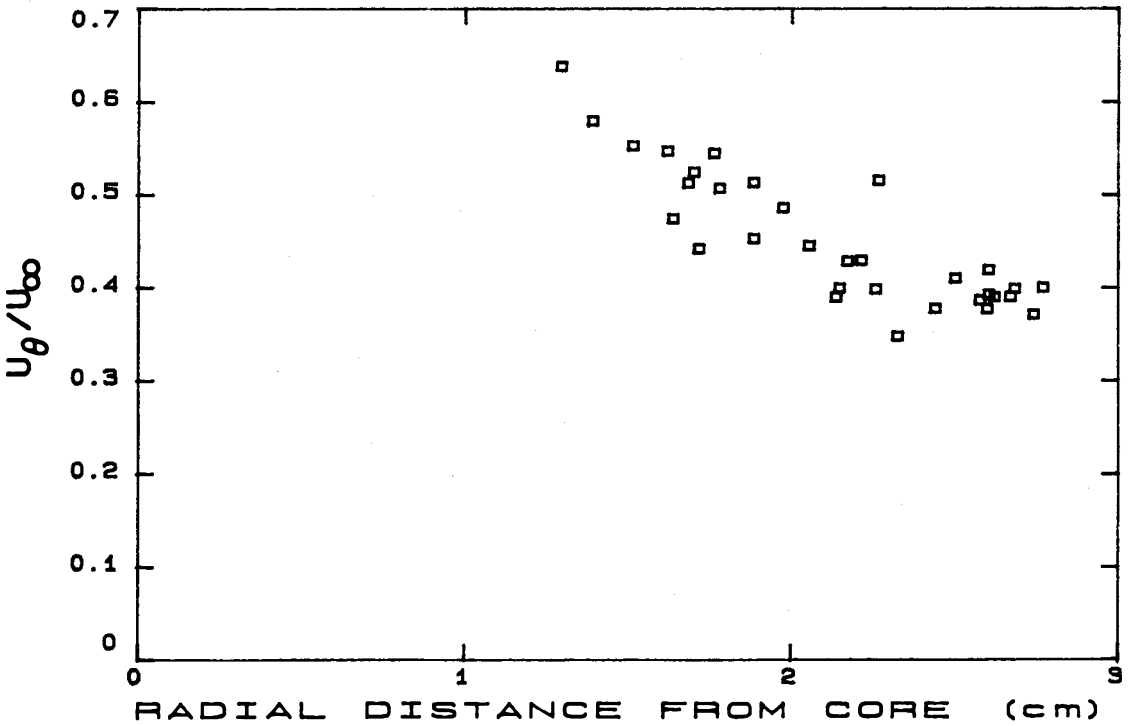

(b)Tangential Velocity Distribution

Figure IV.35(a,b) Vortex Velocity Distribution. x/c=1, $\alpha = 5°$, Re=1.86×10^5.

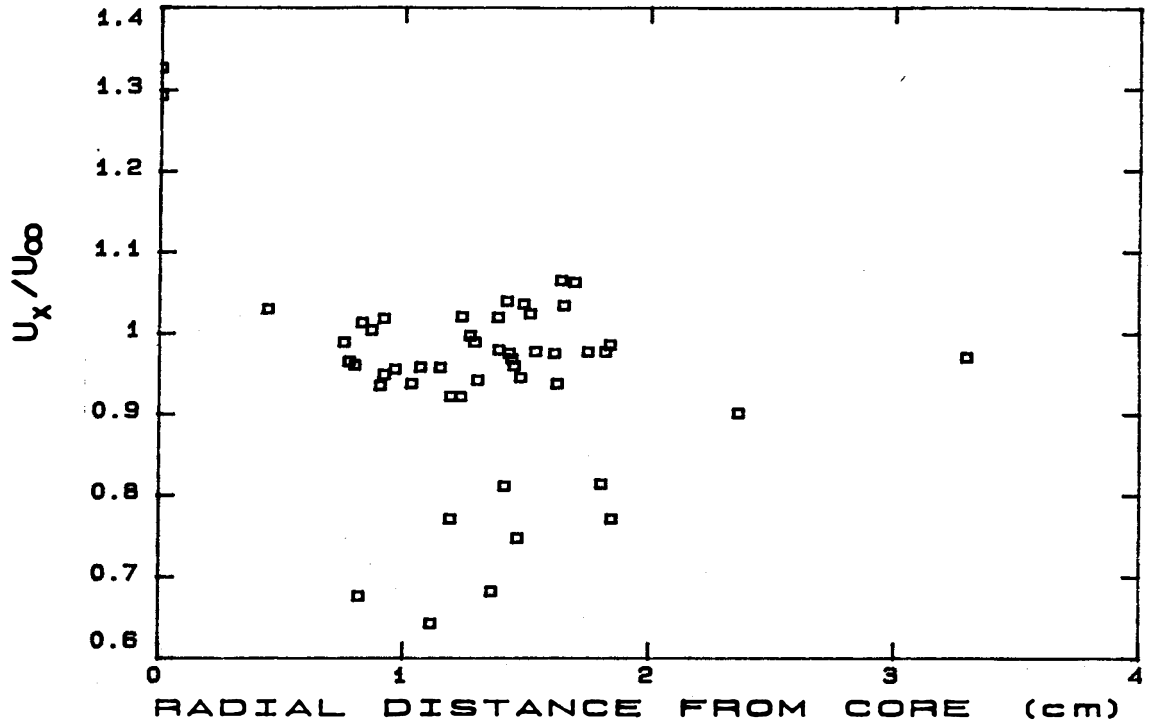

(a) Axial Velocity Distribution

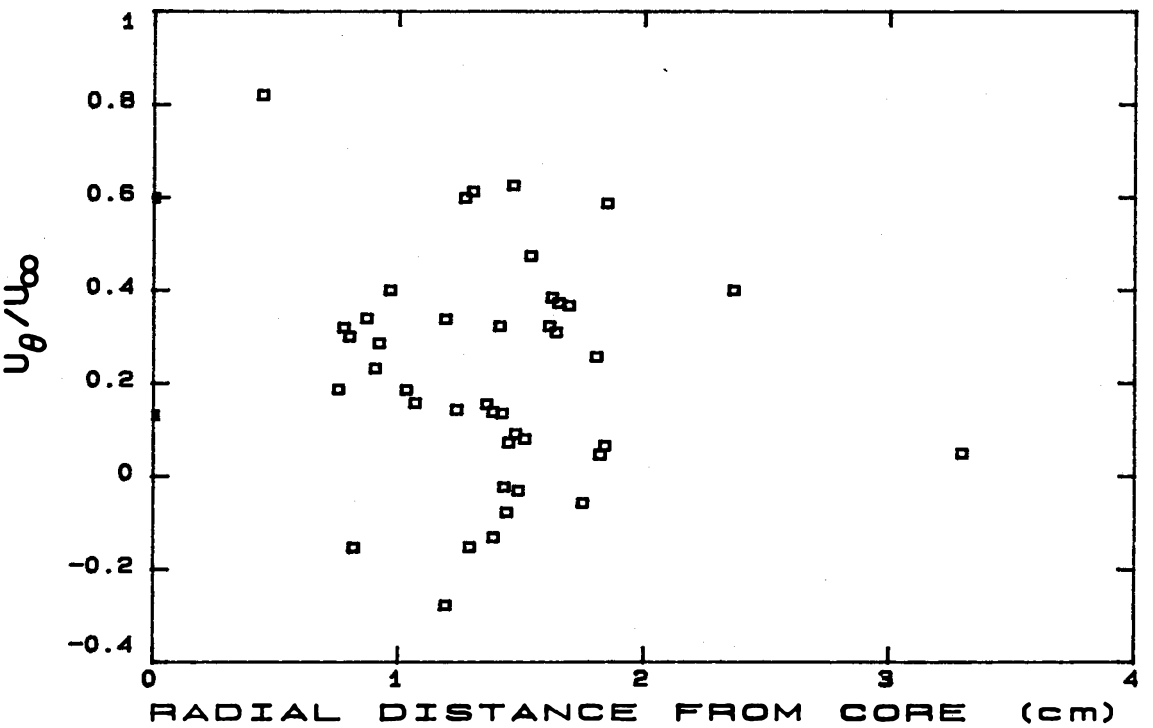

(b) Tangential Velocity Distribution

Figure IV.36(a,b) Vortex Velocity Distribution. x/c=1, $\alpha = 5°$, Re=8.06×10^6.

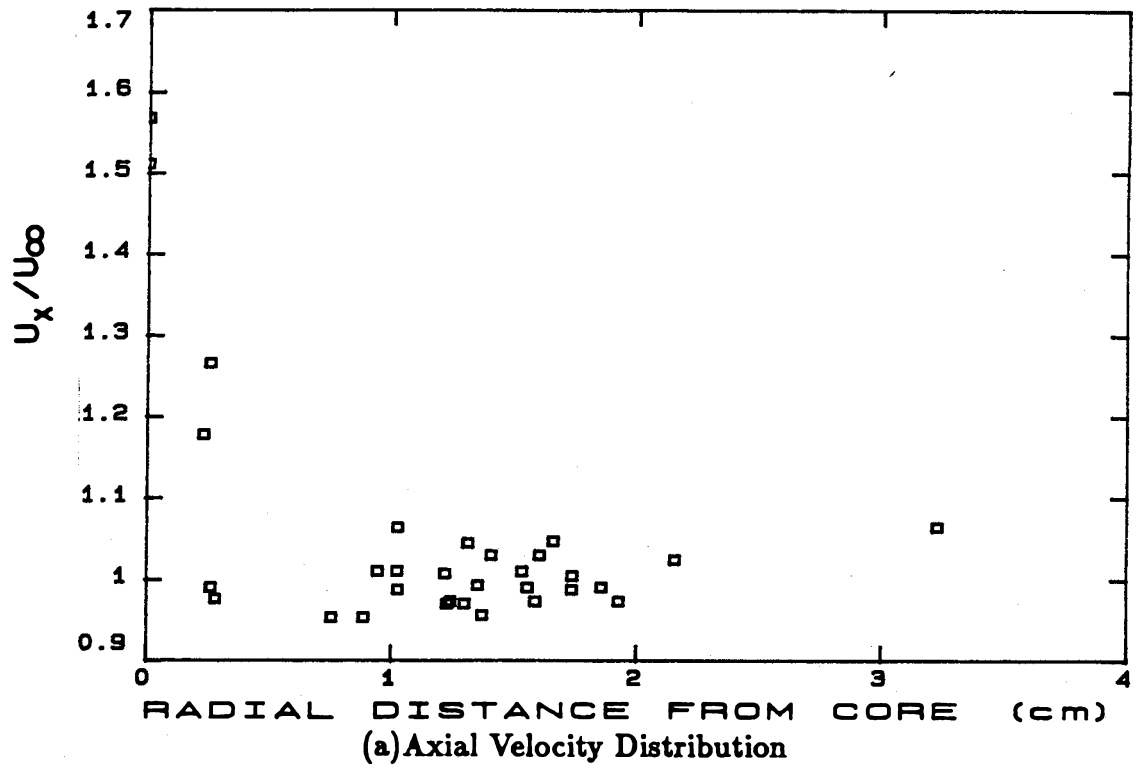

(a)Axial Velocity Distribution

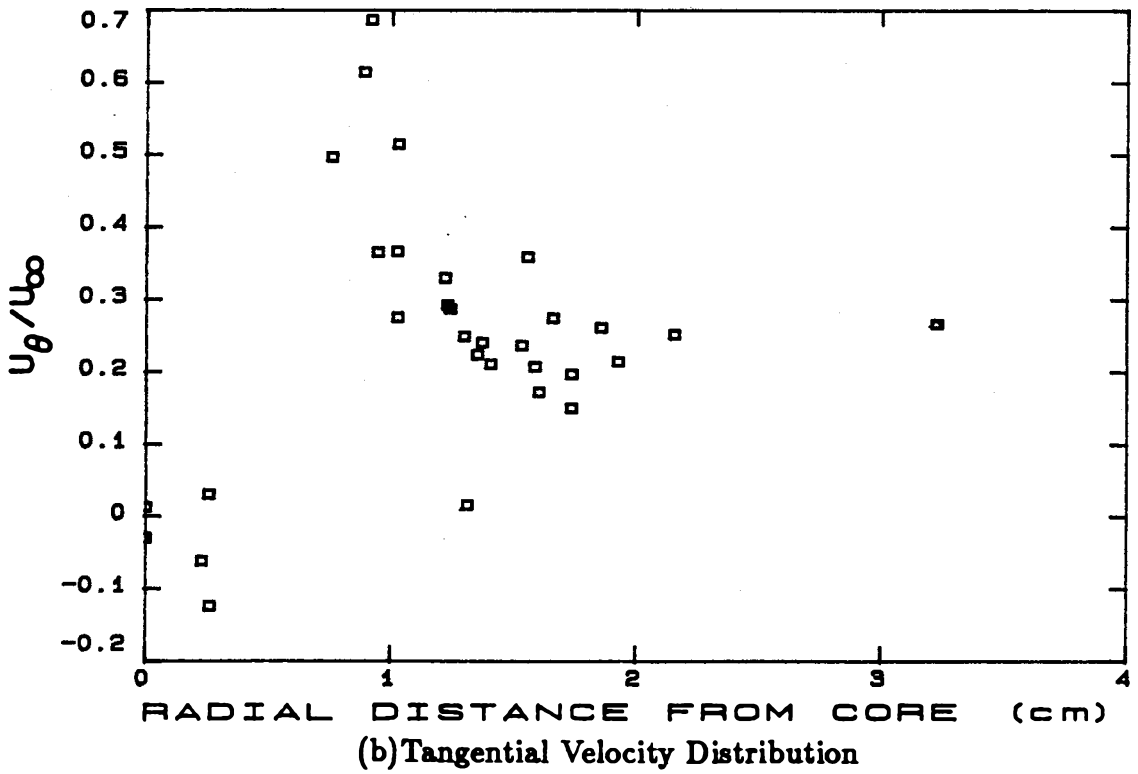

(b)Tangential Velocity Distribution

Figure IV.37(a,b) Vortex Velocity Distribution. x/c=1, $\alpha = 10°$, Re=1.86×10^5.

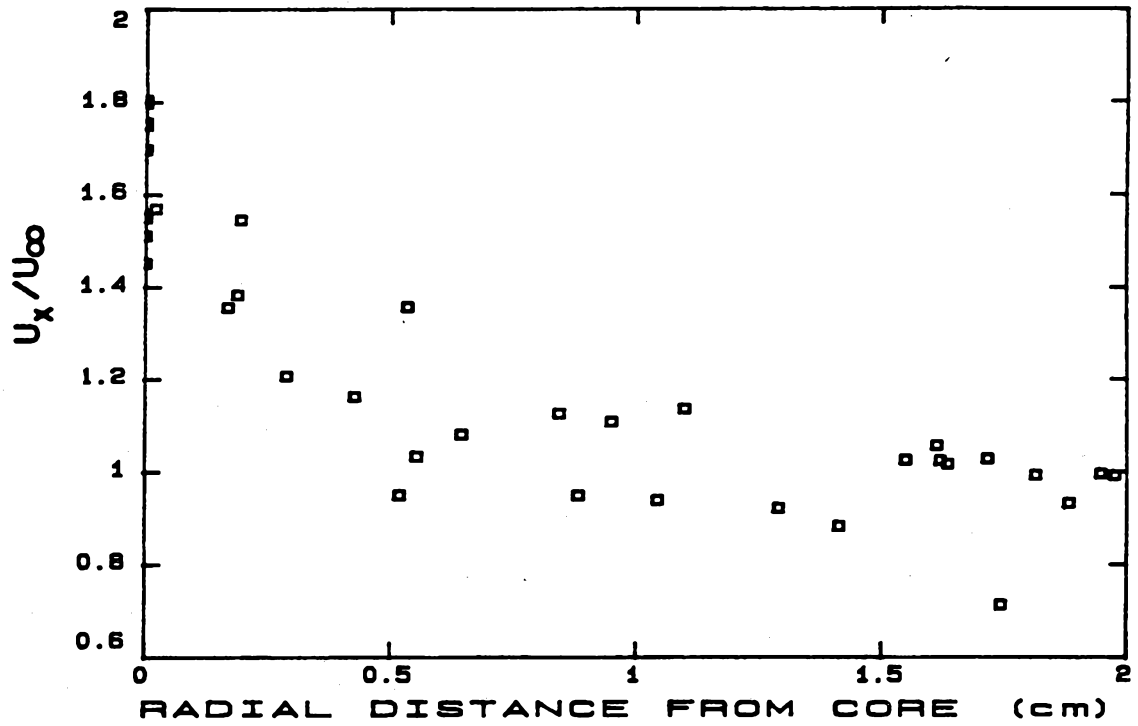

(a)Axial Velocity Distribution

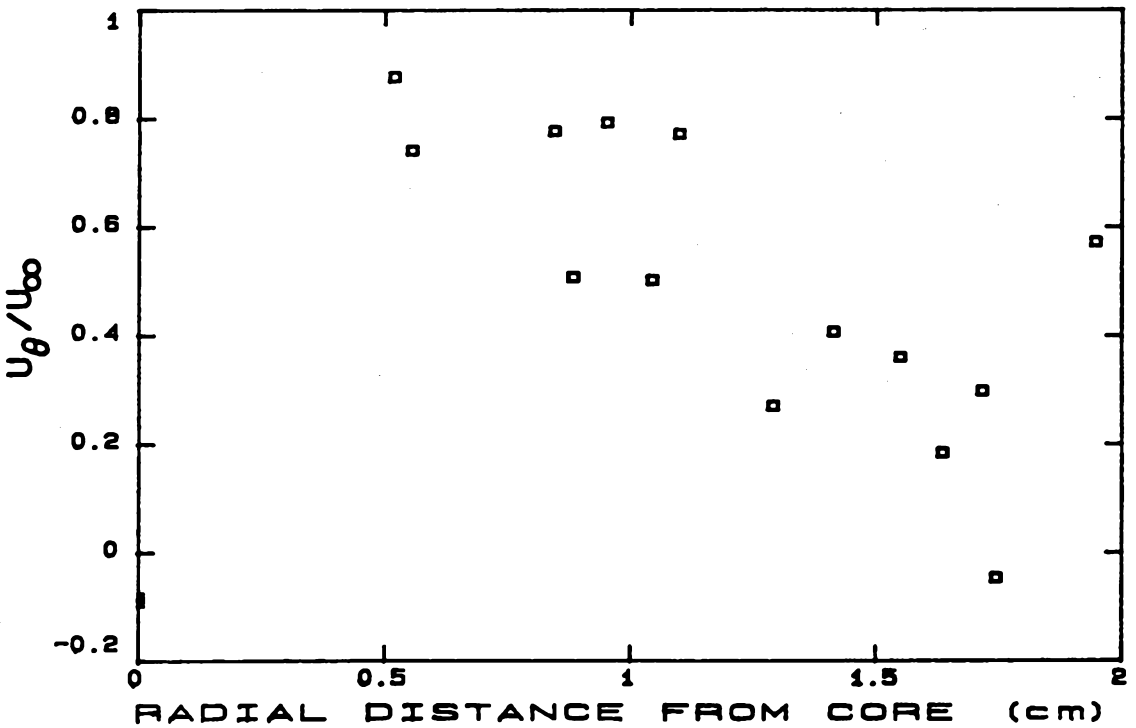

(b)Tangential Velocity Distribution

Figure IV.38(a,b) Vortex Velocity Distribution. x/c=1, $\alpha = 10°$, Re=8.06×10^5.

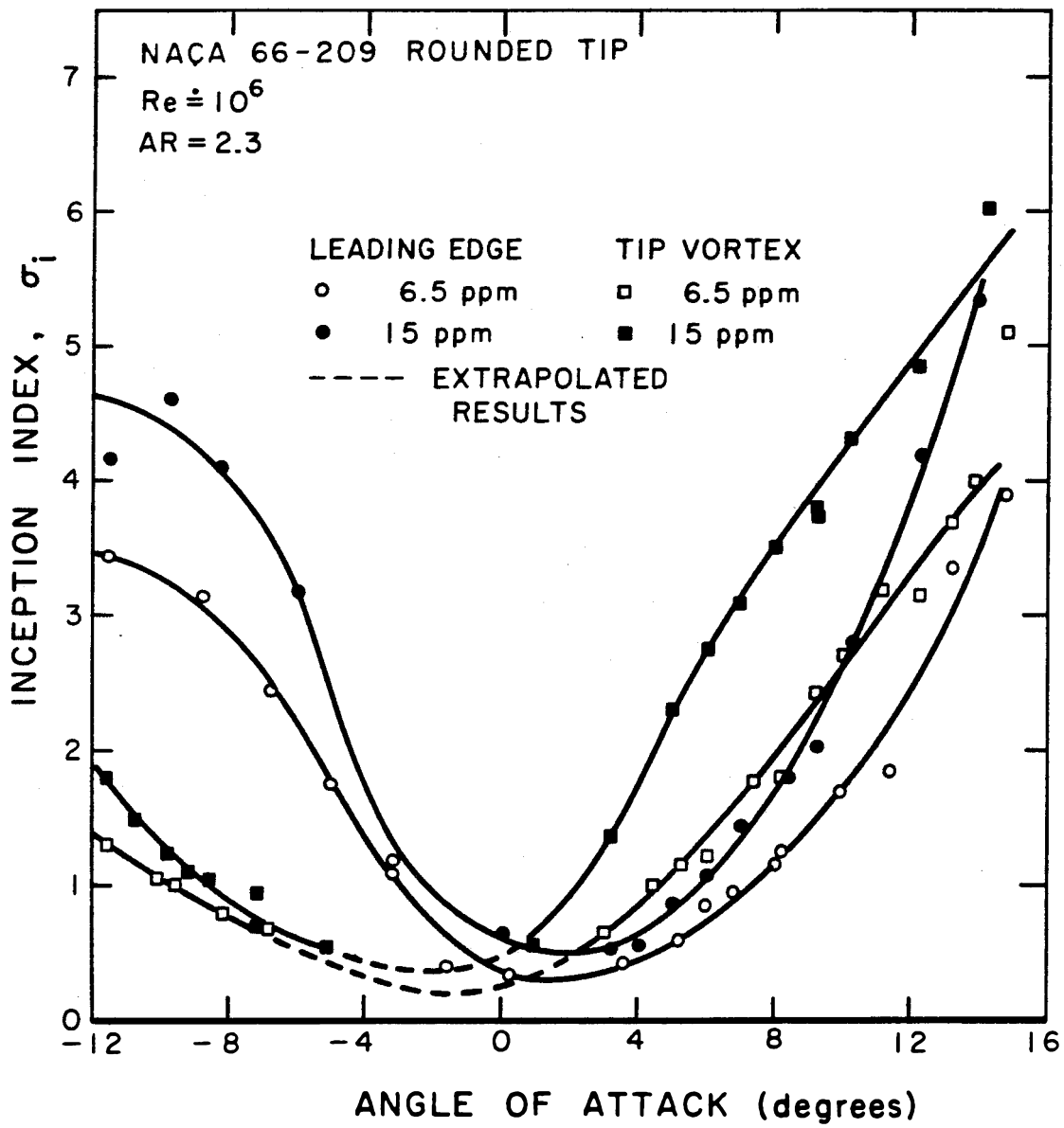

Figure IV.39 Inception Index versus Angle of Attack (NACA 66-209 rnd. tip foil).

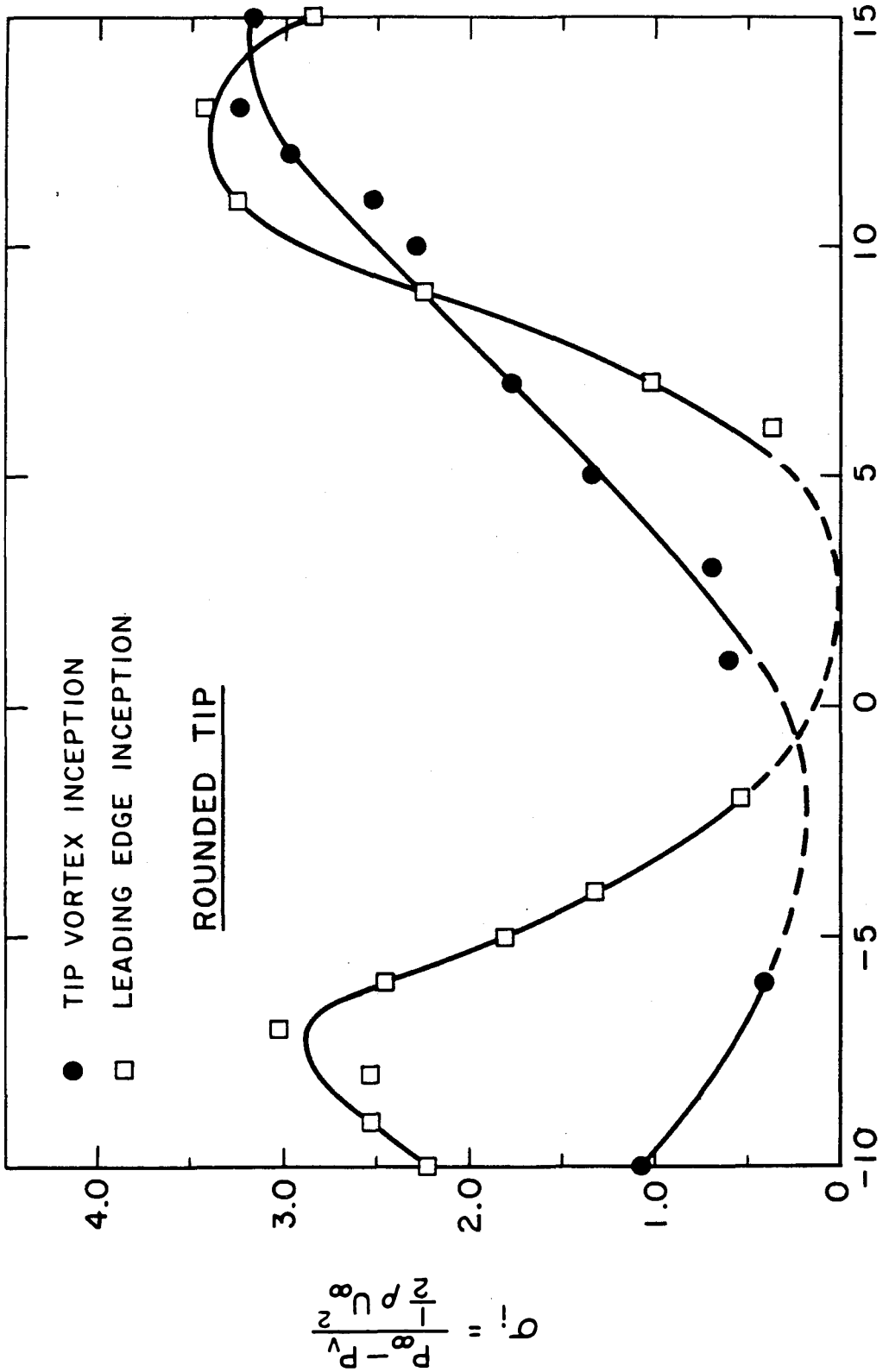

Figure IV.40 Inception Index versus Angle of Attack (NACA 64-309 rnd. tip foil).

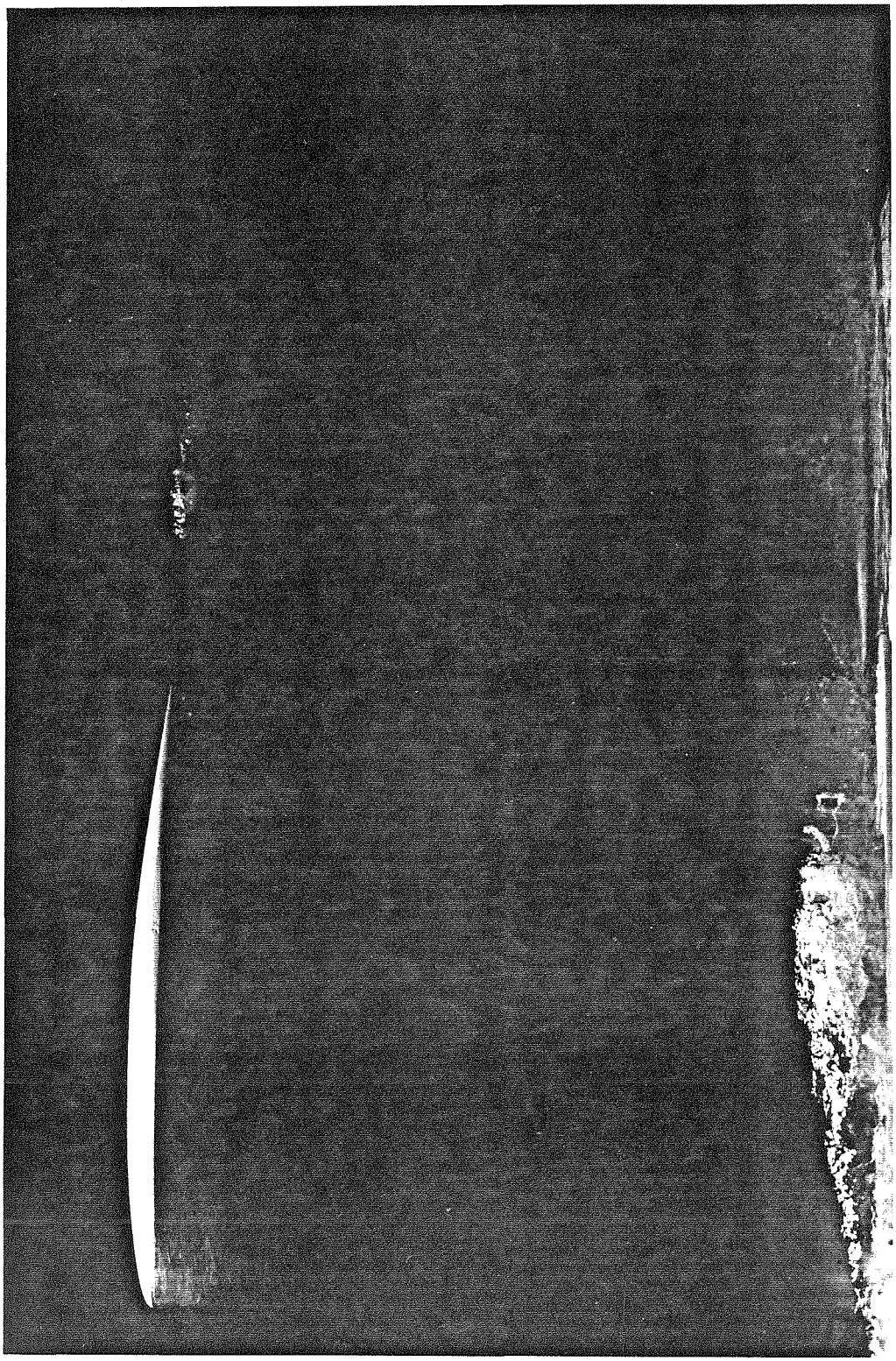

Figure IV.41 Trailing Vortex Cavitation Inception. Flow is left to right. $\alpha = 3°$, Re=1.5×10^6, DAC=5ppm, $\sigma = 0.62$ (NACA 64-309 rounded tip foil).

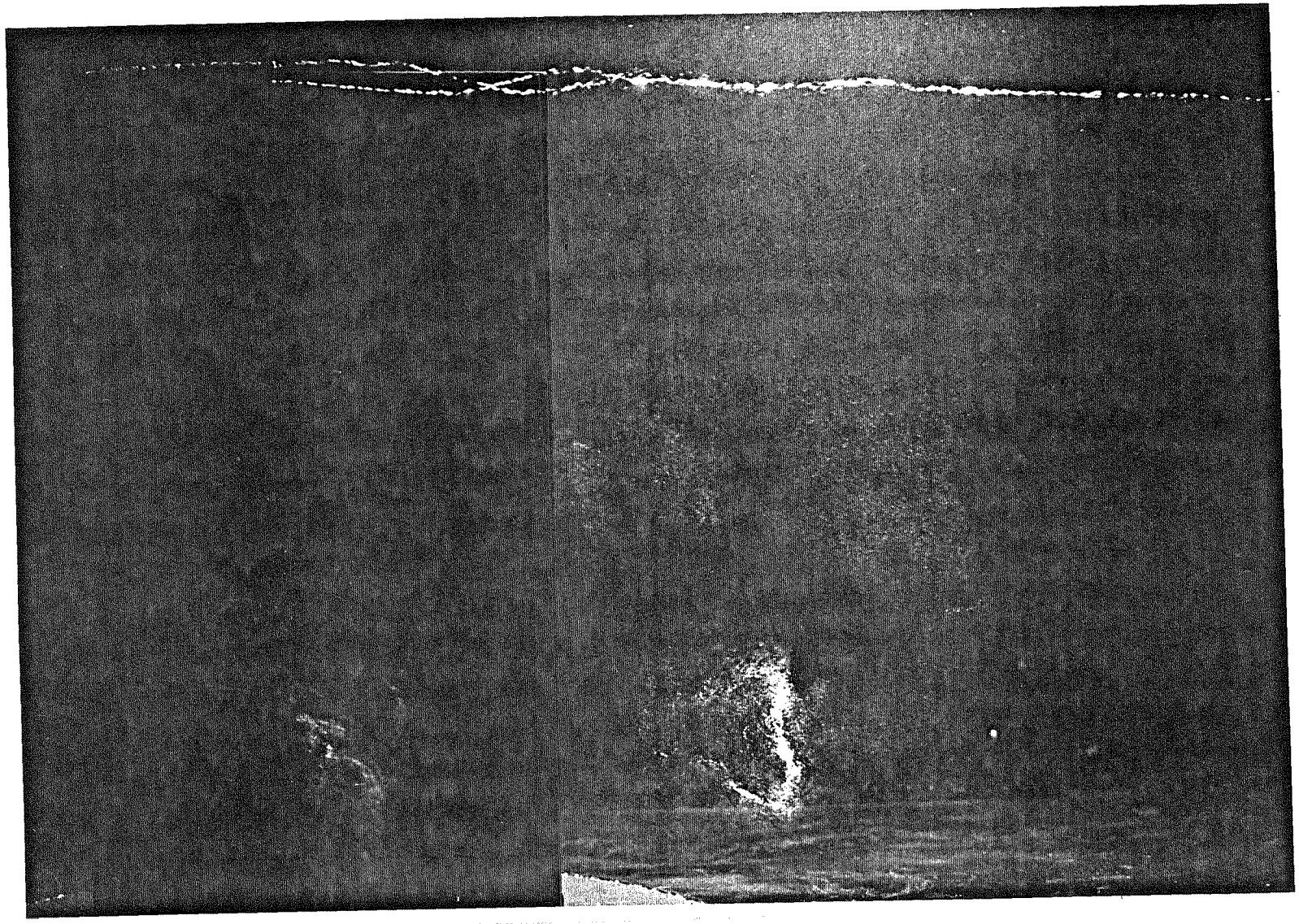

Figure IV.42 Trailing Vortex Cavitation. Flow is left to right. $\alpha = 7.5°$, Re=1.1×10^6, DAC=3.3ppm, $\sigma = 1.23$ (Joukowski).

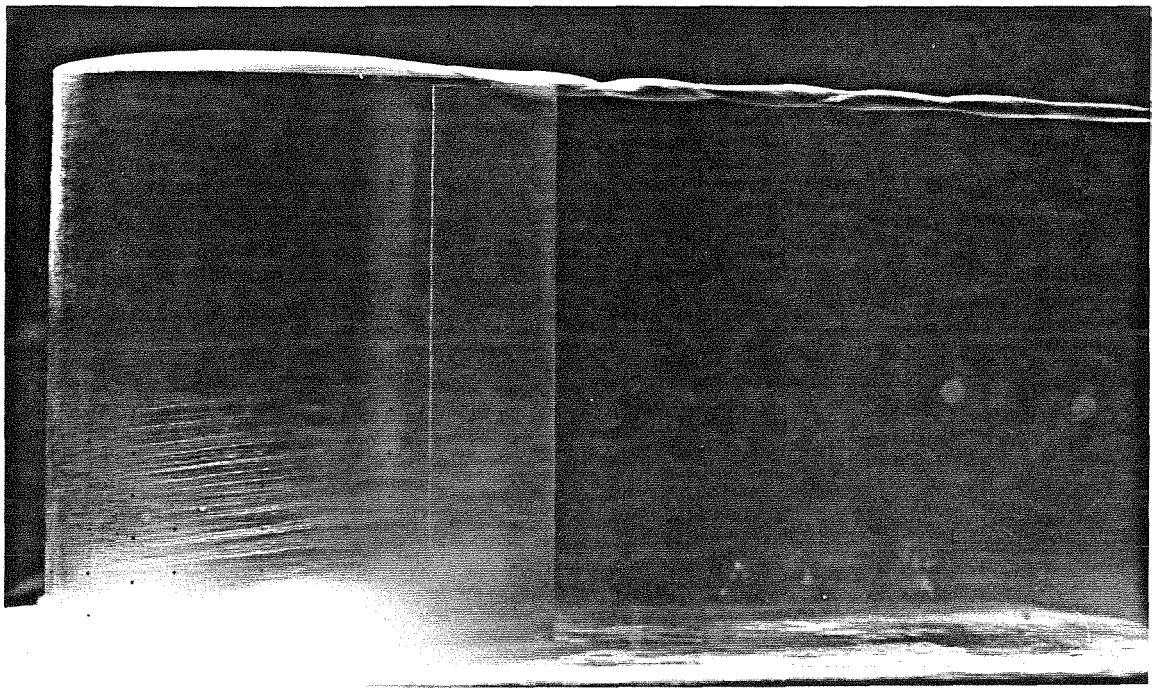

Figure IV.43 Developed Trailing Vortex Cavitation. Flow is left to right. $\alpha = 3°$, Re=1.5×10^6, DAC=5ppm, $\sigma = 0.44$ (NACA 64-309 rounded tip foil).

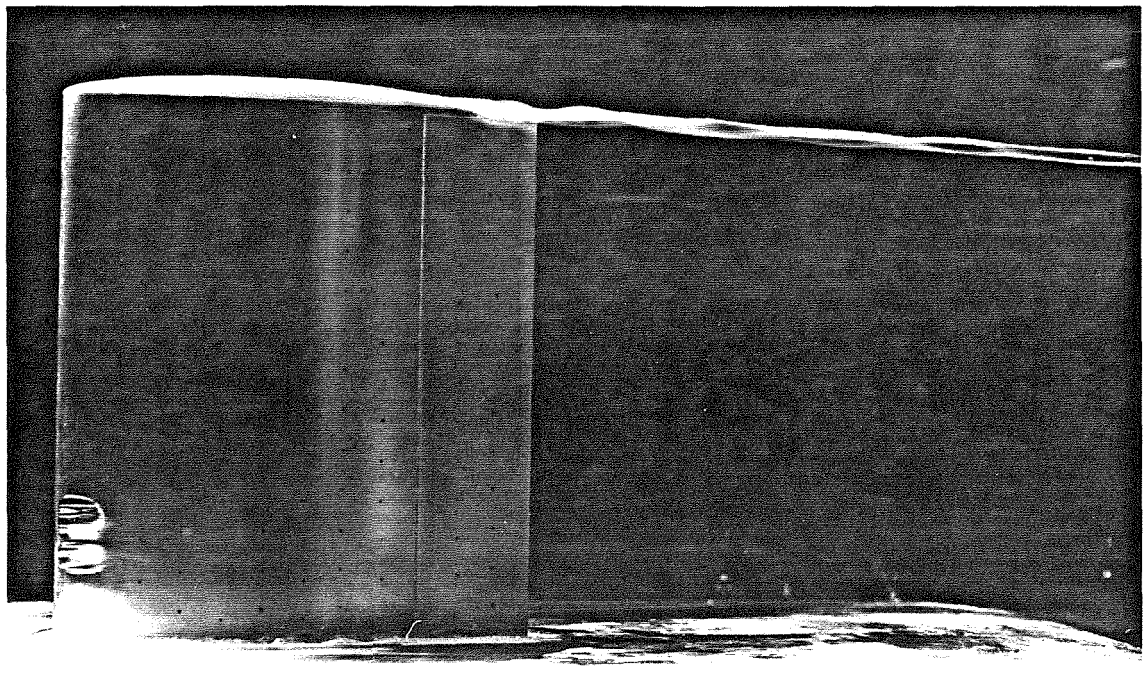

Figure IV.44 Developed Trailing Vortex Cavitation. Flow is left to right. $\alpha = 7°$, Re=1.4×10^6, DAC=5ppm, $\sigma = 1.33$ (NACA 64-309 rounded tip foil).

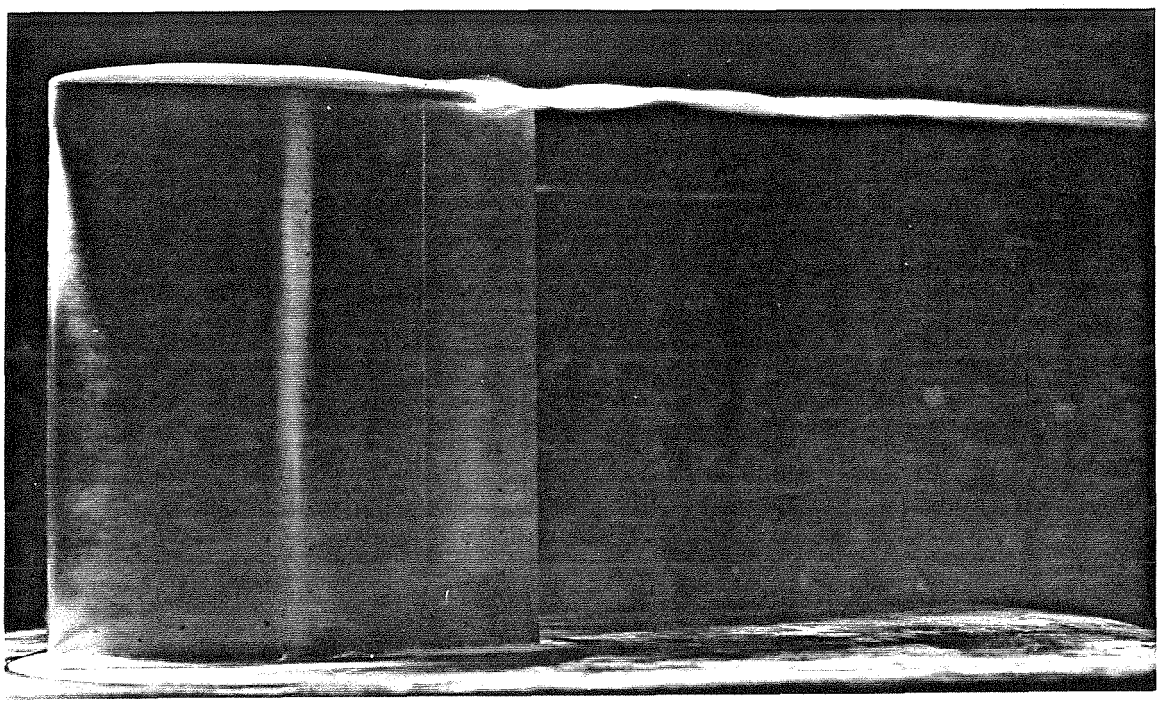

Figure IV.45 Developed Trailing Vortex Cavitation. Flow is left to right.
$\alpha = 15°$, Re=1.3×10^6, DAC=5ppm, $\sigma = 2.11$ (NACA 64-309 rounded tip foil).

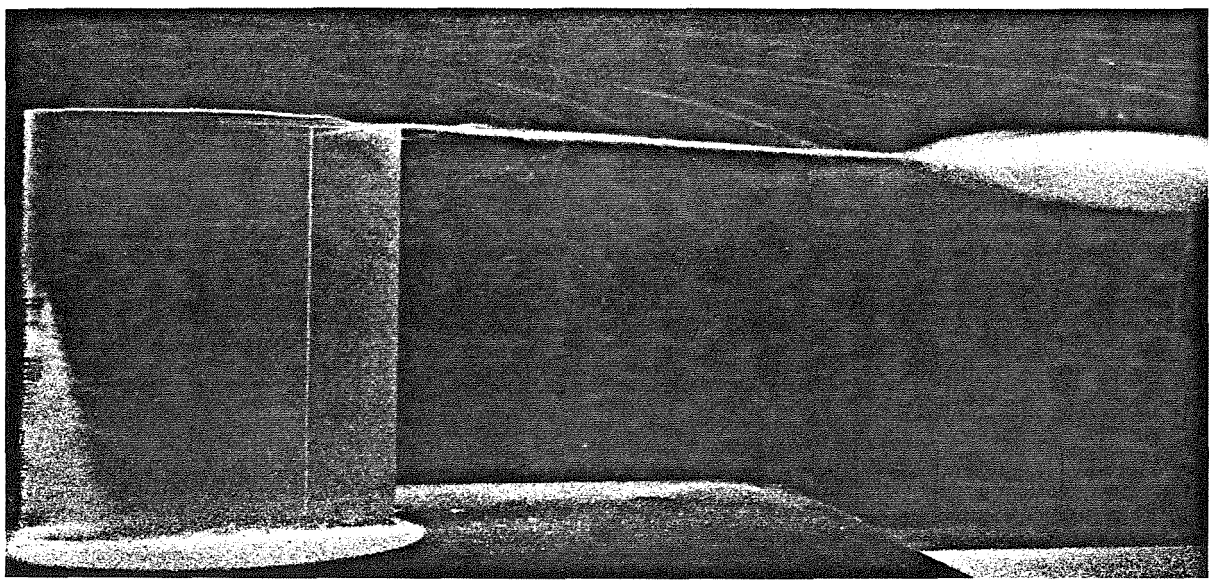

Figure IV.46 Two Phase Vortex Breakdown. Flow is left to right.
$\alpha = 8°$, Re=1.5×10^6, $\sigma = 0.50$ (NACA 64-309 rounded tip).

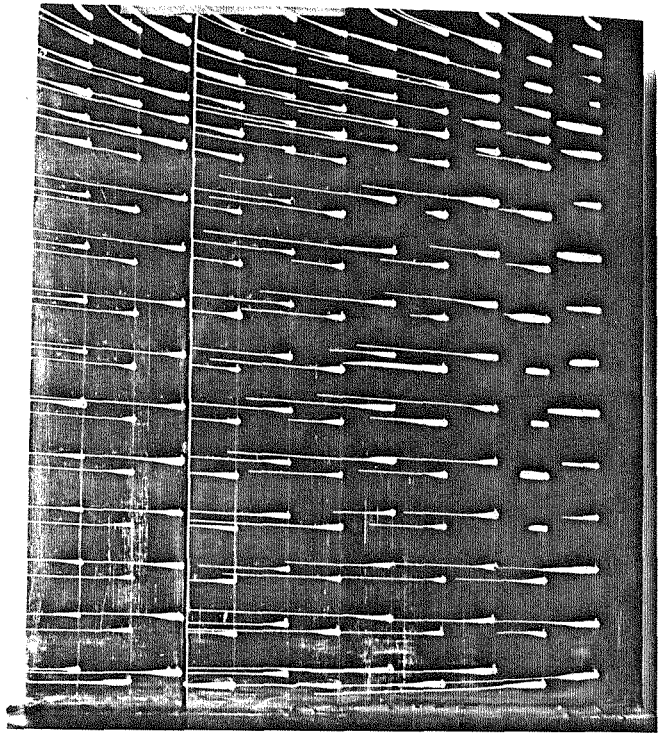

(a) pressure side

(b)suction side

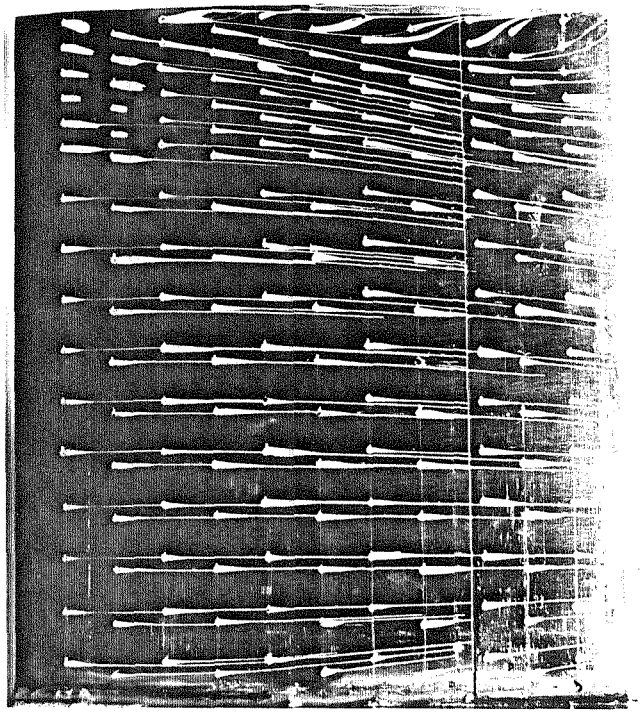

(c) inboard view

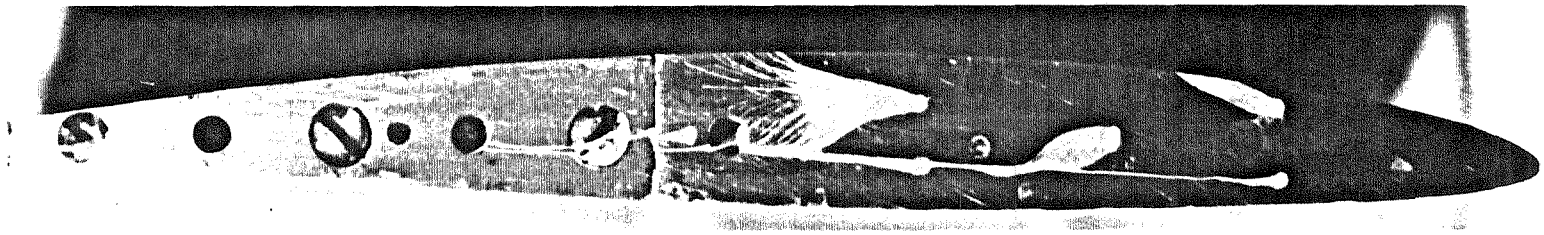

Figure IV.47(a,b,c) SFV of NACA 64-309 square tip foil at $\alpha = 7°$.

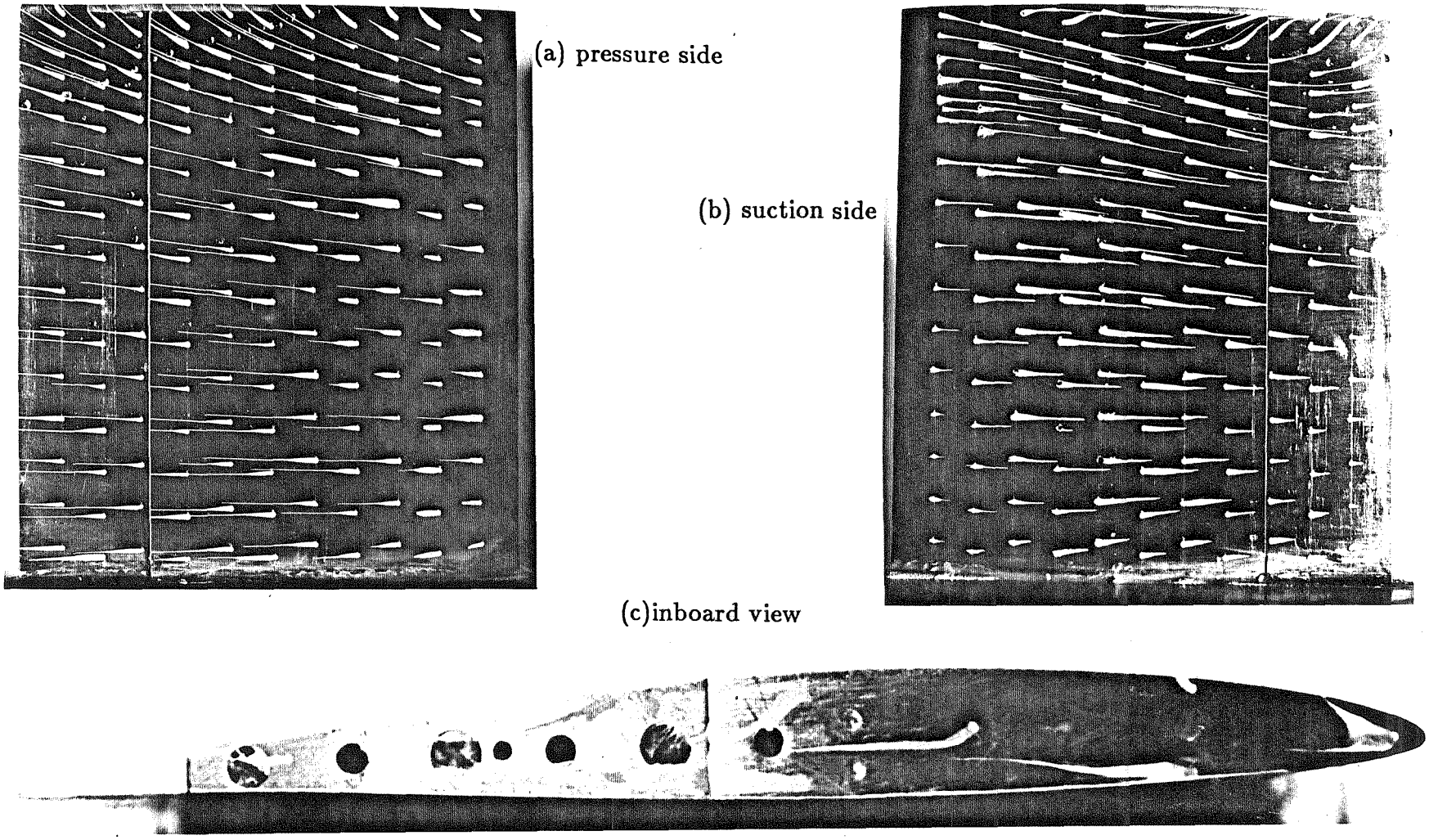

Figure IV.48(a,b,c) SFV of NACA 64-309 square tip foil at $\alpha = 12°$.

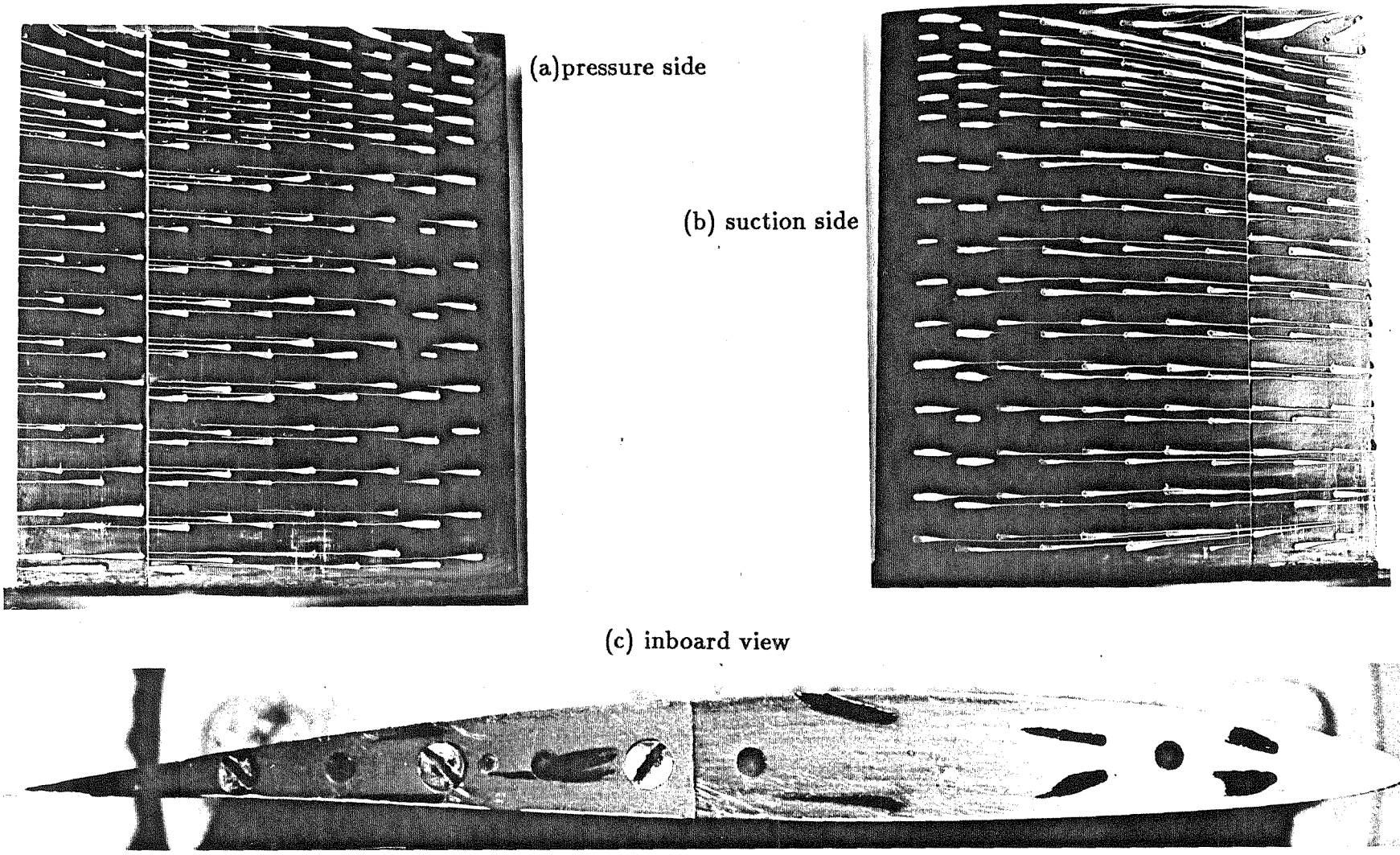

Figure IV.49(a,b,c) SFV of NACA 64-309 square tip foil at $\alpha = 3°$.

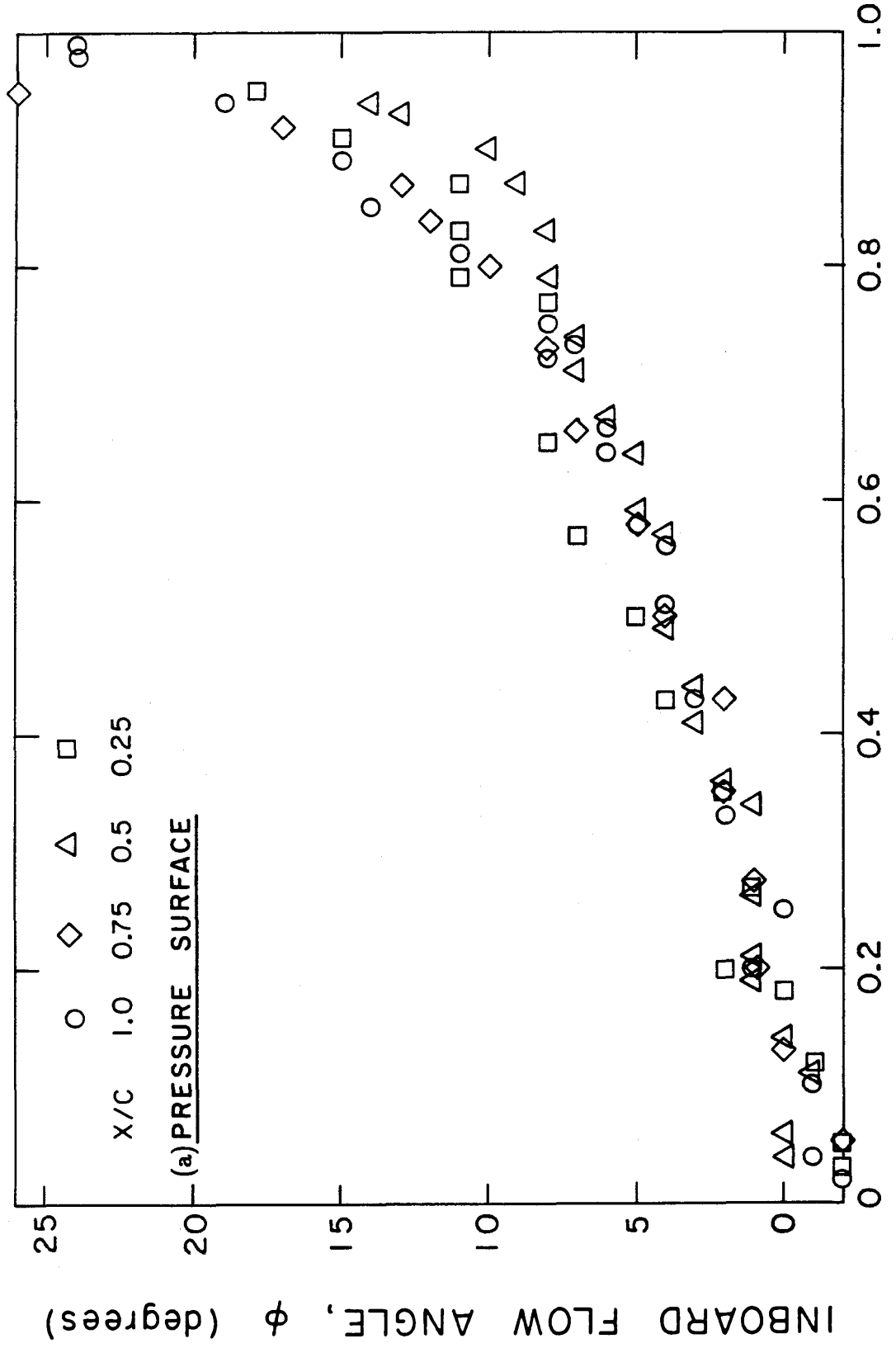

Figure IV.50(a,b) Inboard Flow Angles NACA 64-309 square tip, $\alpha = 7°$.

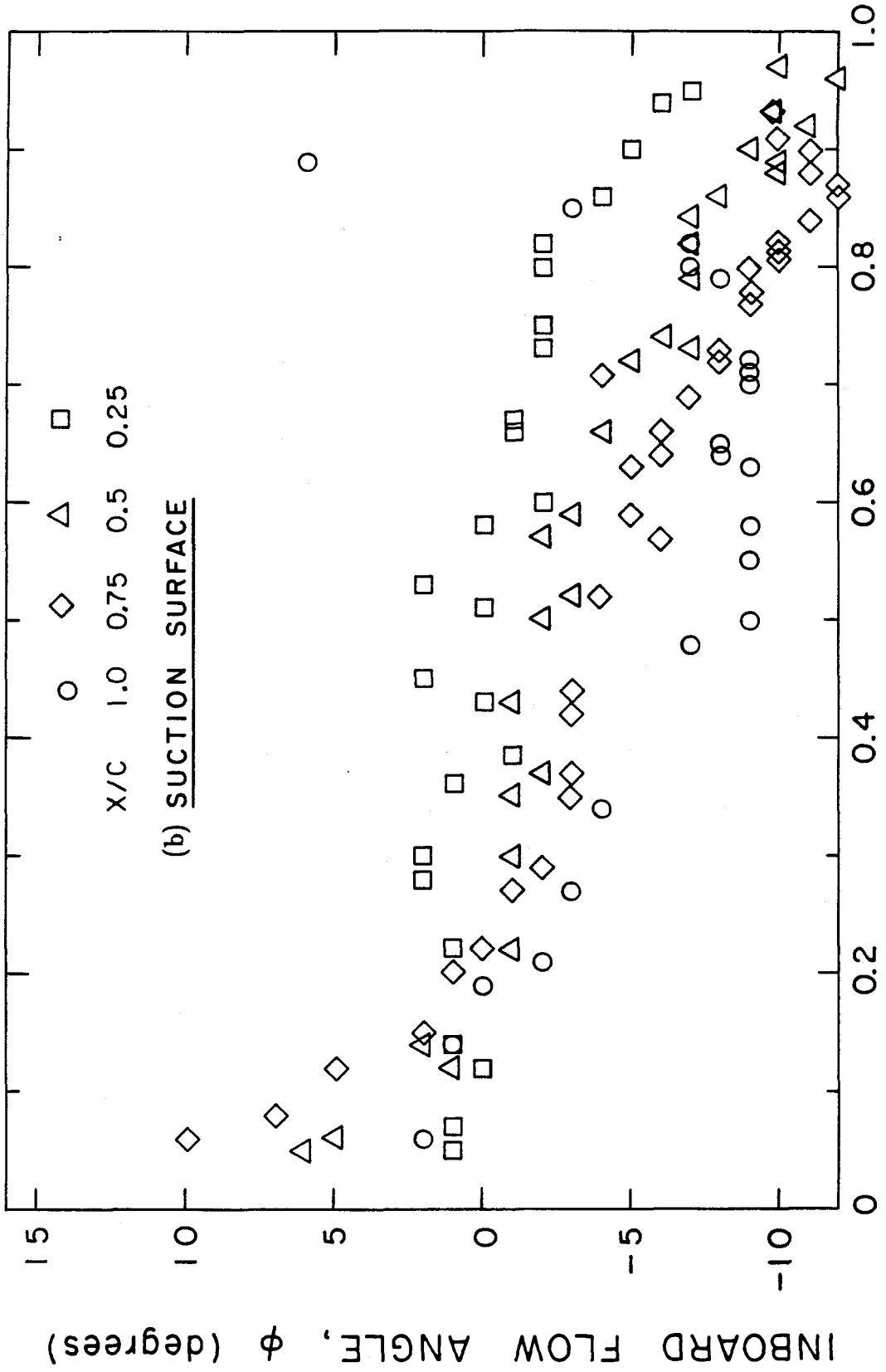

Figure IV.50(a,b) Inboard Flow Angles NACA 64-309 square tip, $\alpha = 7°$.

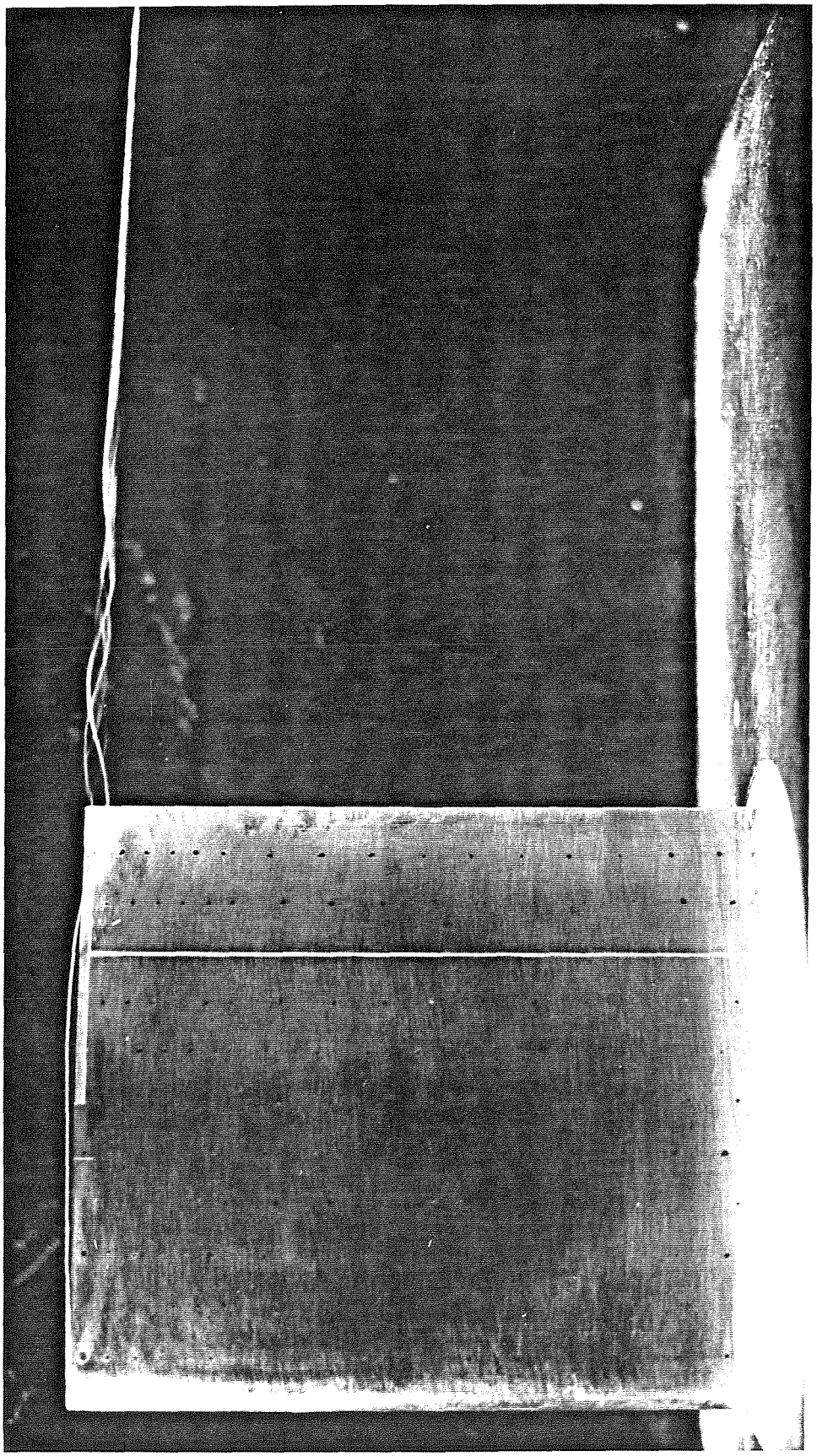

Figure IV.51 Trailing Vortex Cavitation. Flow is left to right. $\alpha = 6°$, $Re=1.4 \times 10^6$, $\sigma = 1.0$, DAC=6.0ppm (NACA 64-309 square tip).

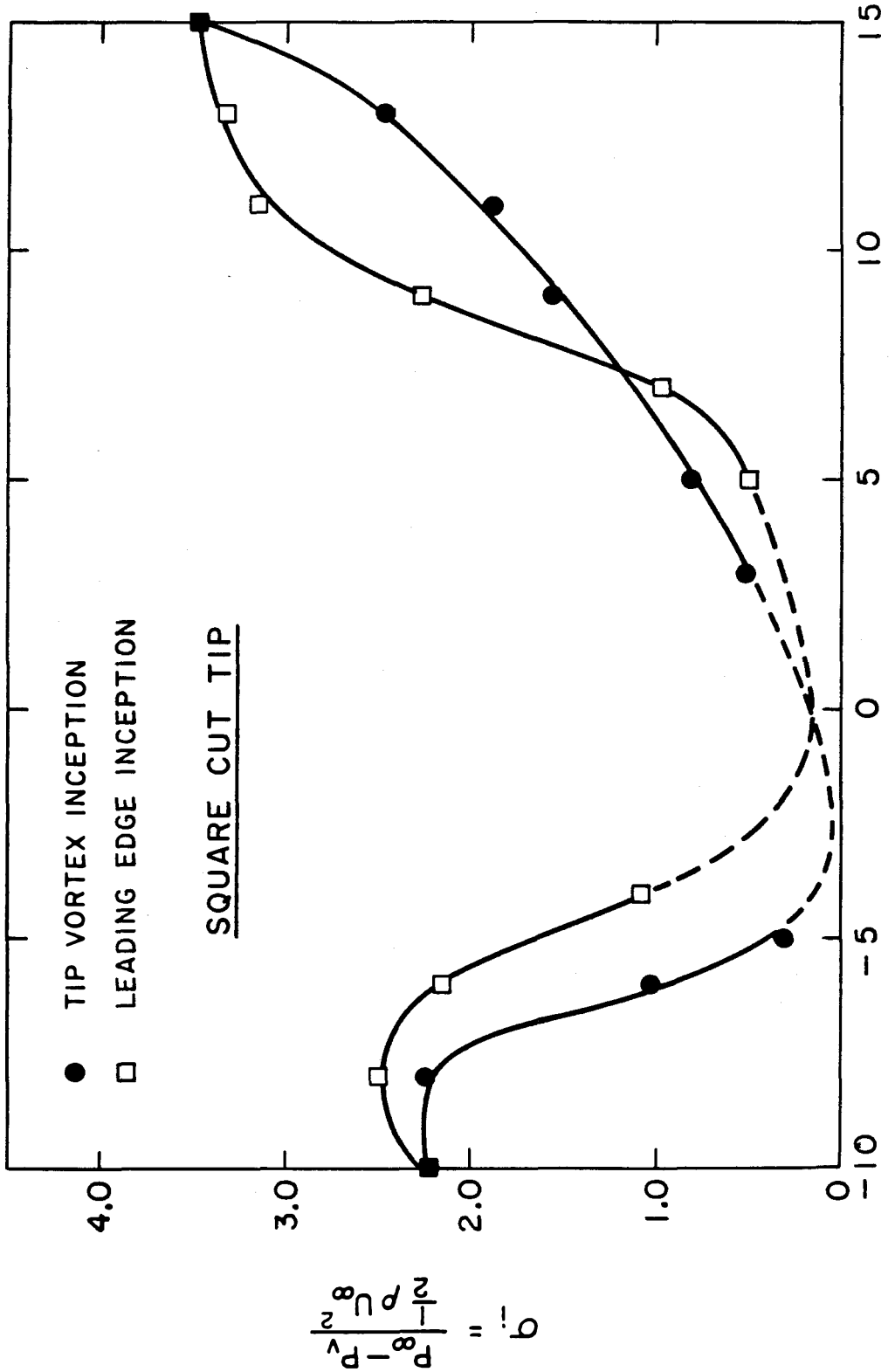

Figure IV.52 Inception Index versus Angle of Attack (NACA 64-309 square cut tip).

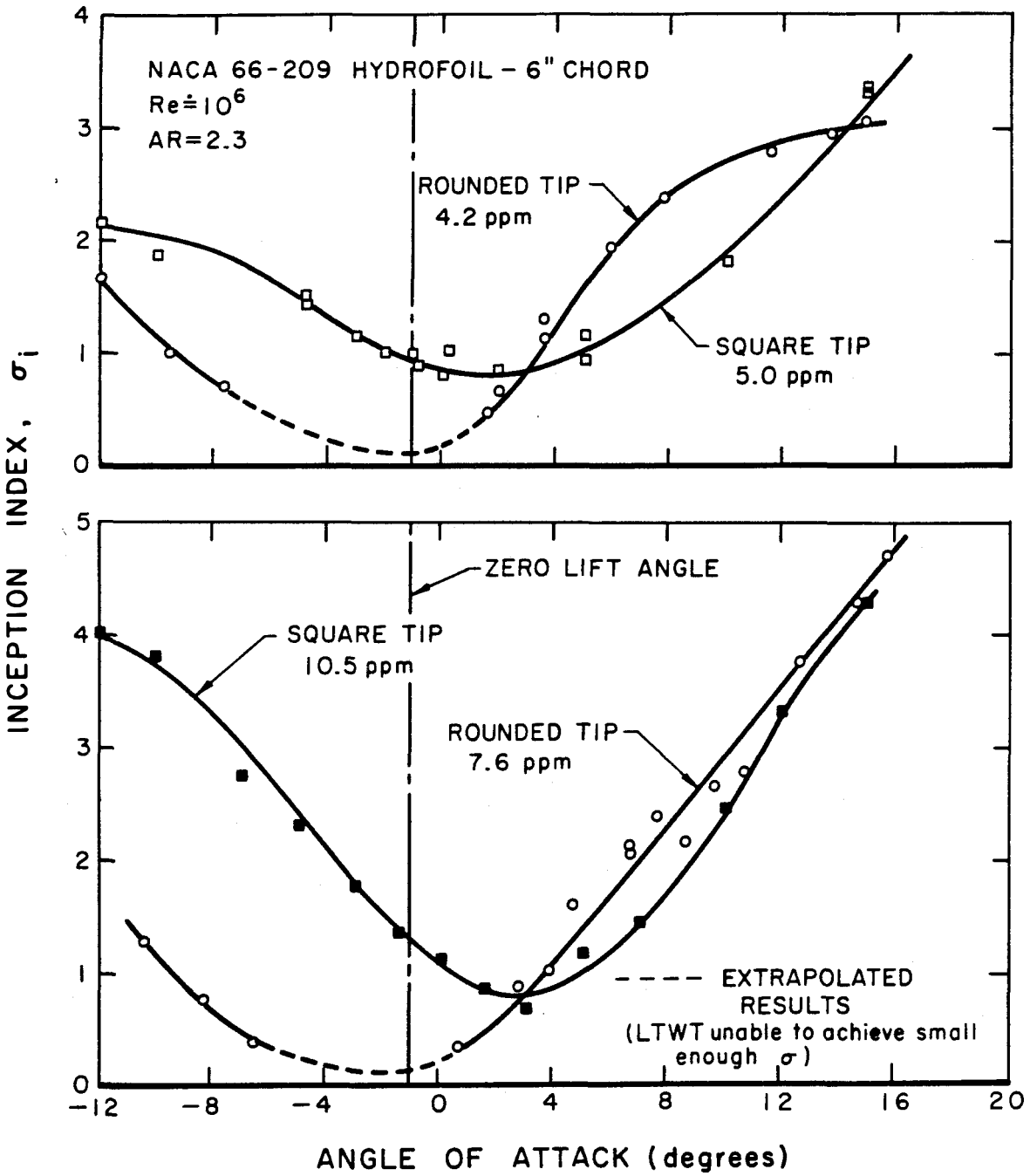

Figure IV.53 Comparison of Square and Rounded Tip Inception Indices (NACA 66-209 foil).

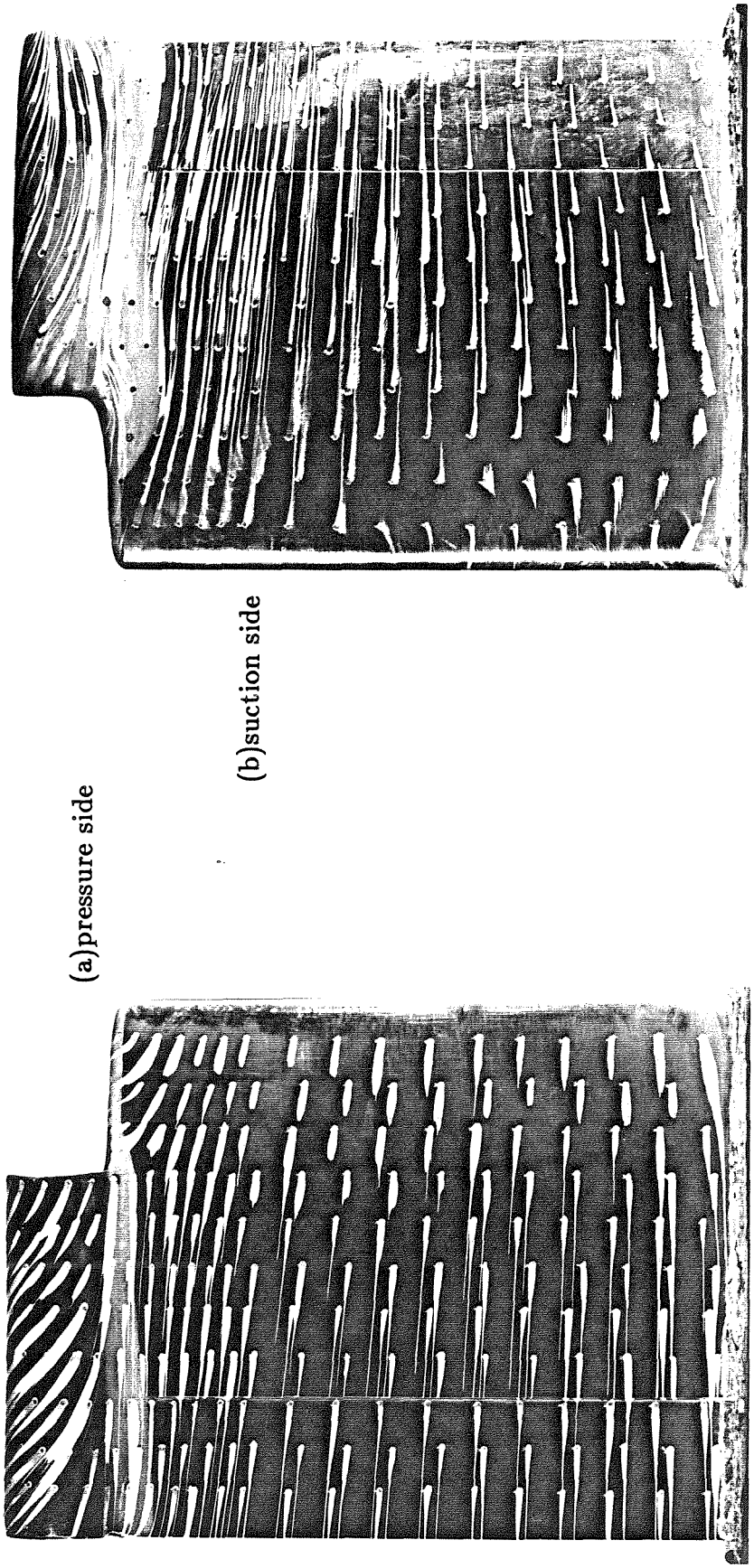

(a)pressure side

(b)suction side

Figure IV.54(a,b,c,d) SFV of NACA 64-309 ring wing tip foil at $\alpha = 12°$.

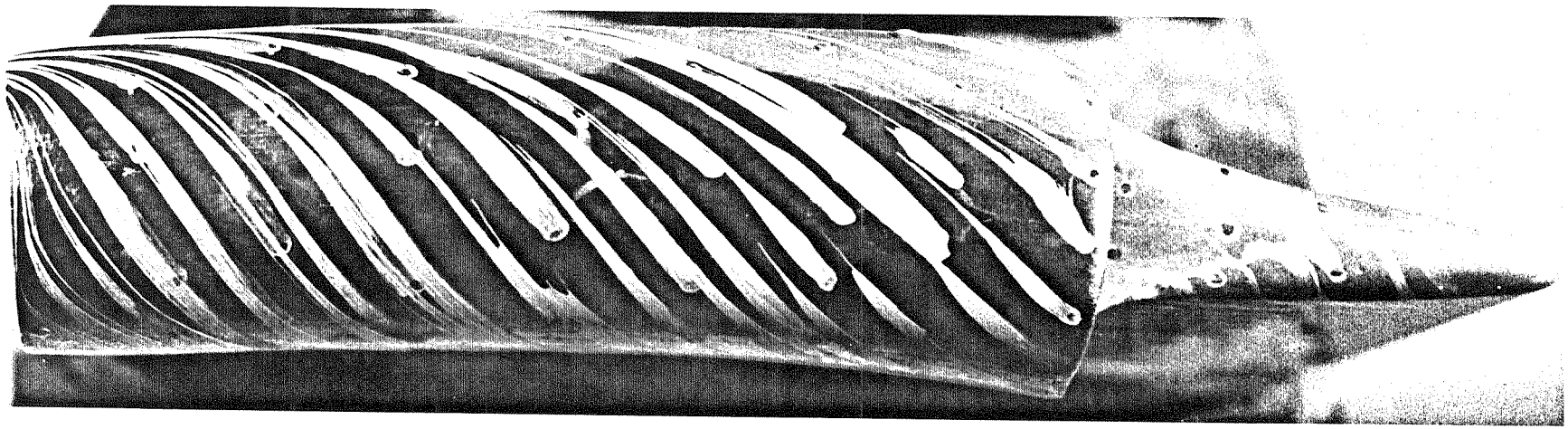

(c)inboard view

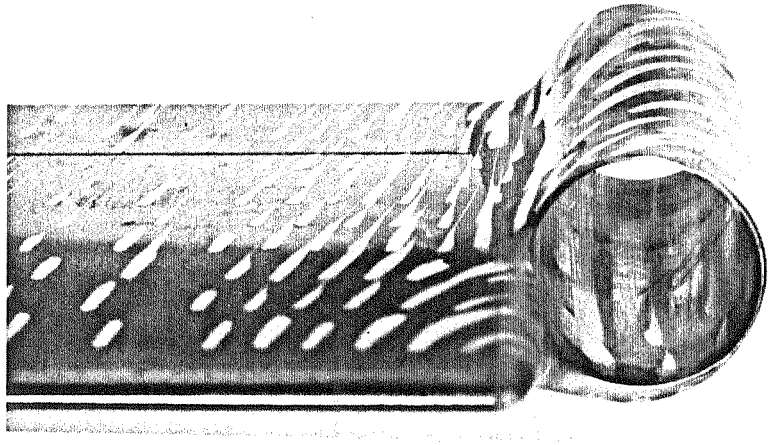

(d) downstream view through ring

Figure IV.54(a,b,c,d) SFV of NACA 64-309 ring wing tip foil at $\alpha = 12°$.

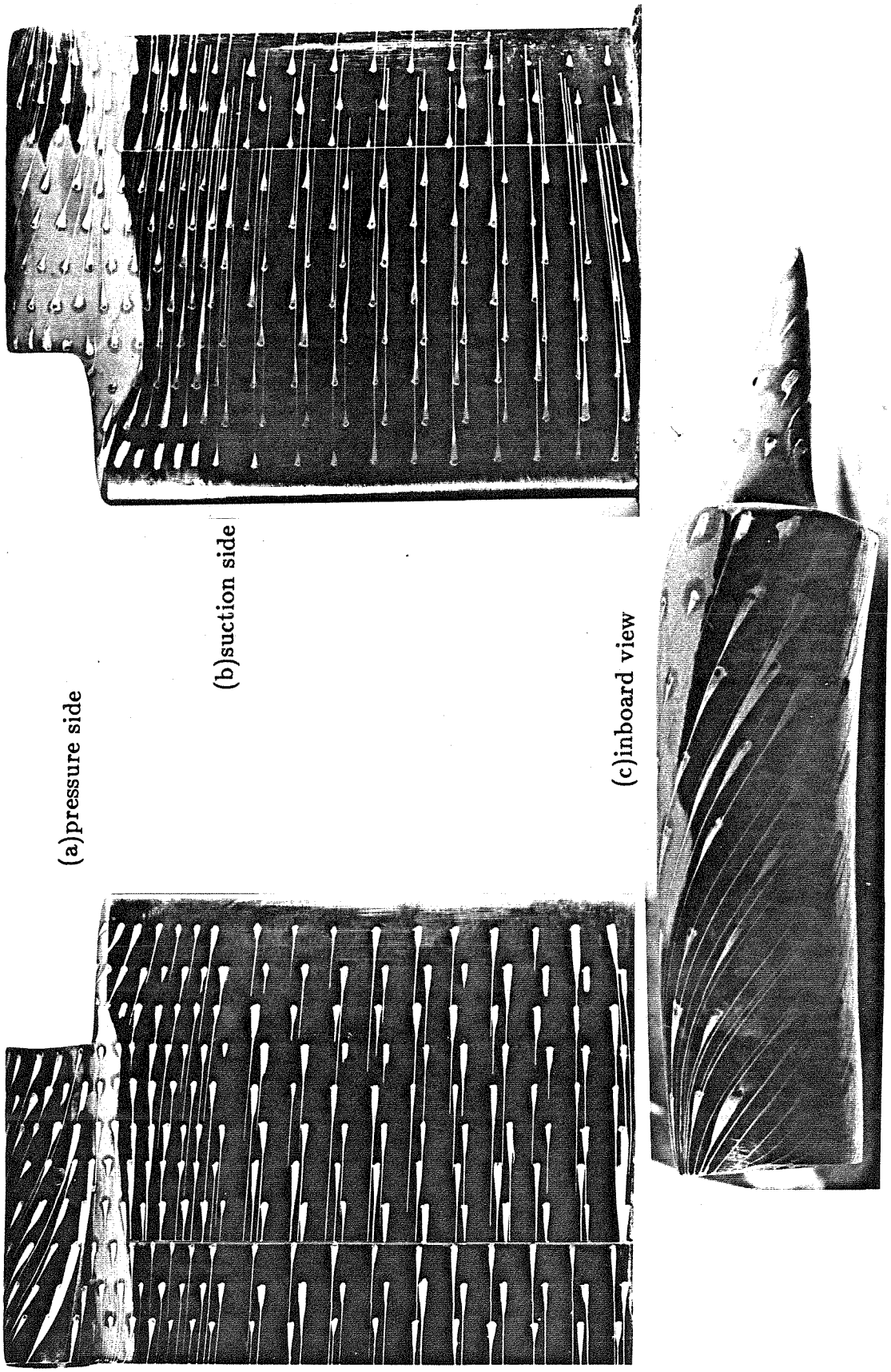

Figure IV.55(a,b,c) SFV of NACA 64-309 ring wing tip foil at $\alpha = 7°$.

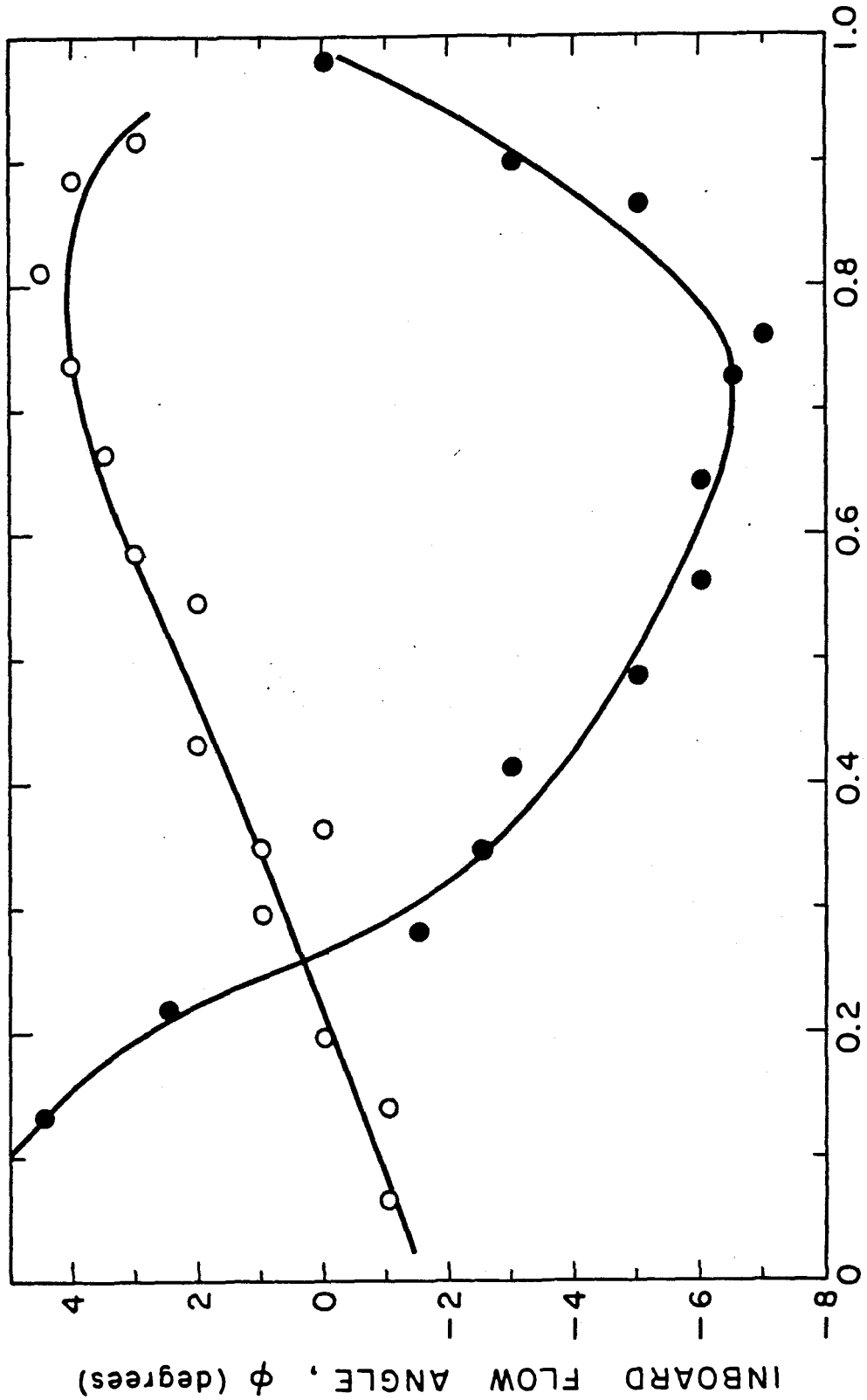

Figure IV.56 Inboard Flow Angles. 64-309 ring wing tip foil at $\alpha = 7°$.
(solid circles: suction side; open circles: pressure side).

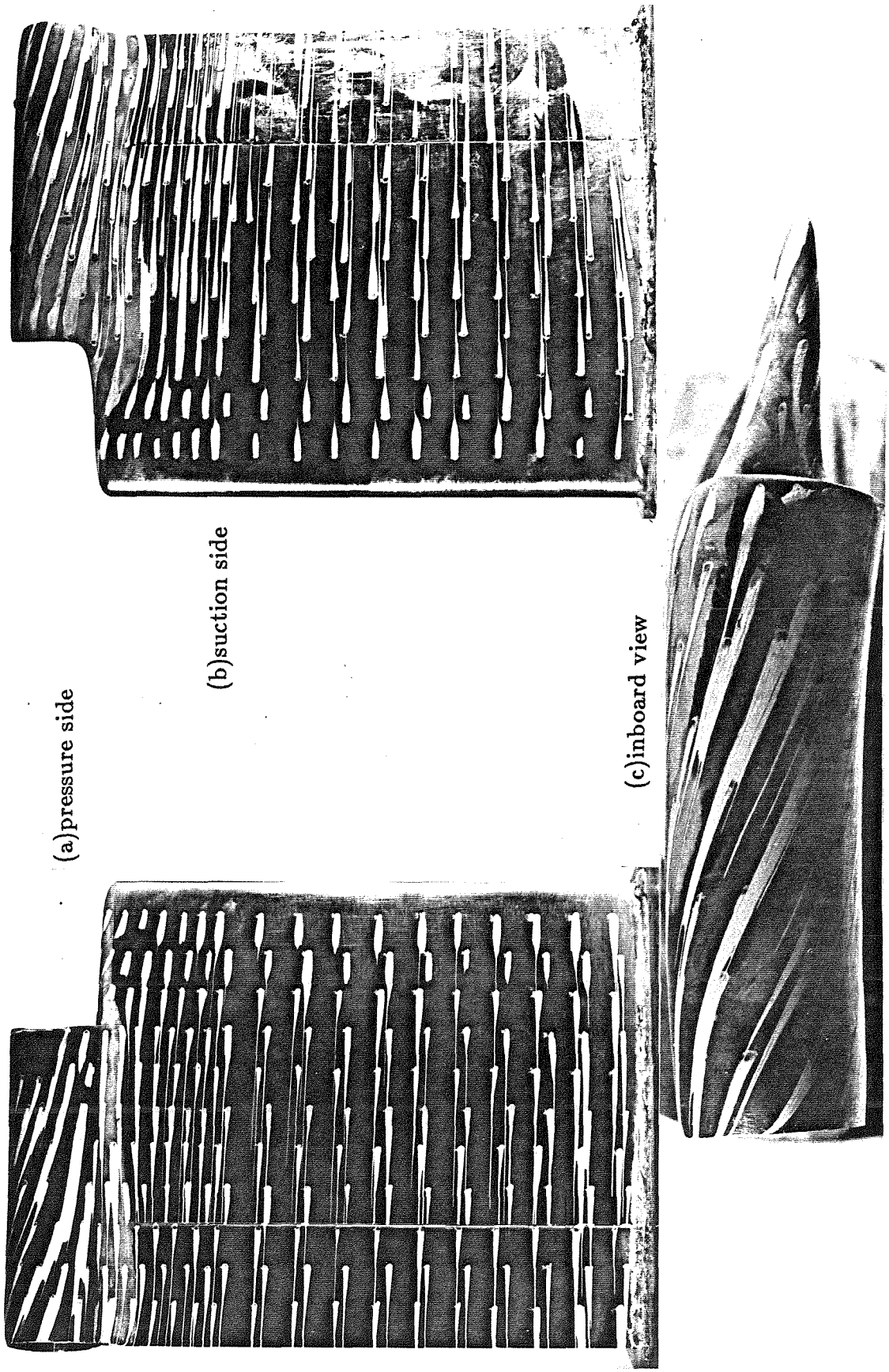

Figure IV.57(a,b,c) SFV of NACA 64-309 ring wing tip foil at $\alpha = 3°$.

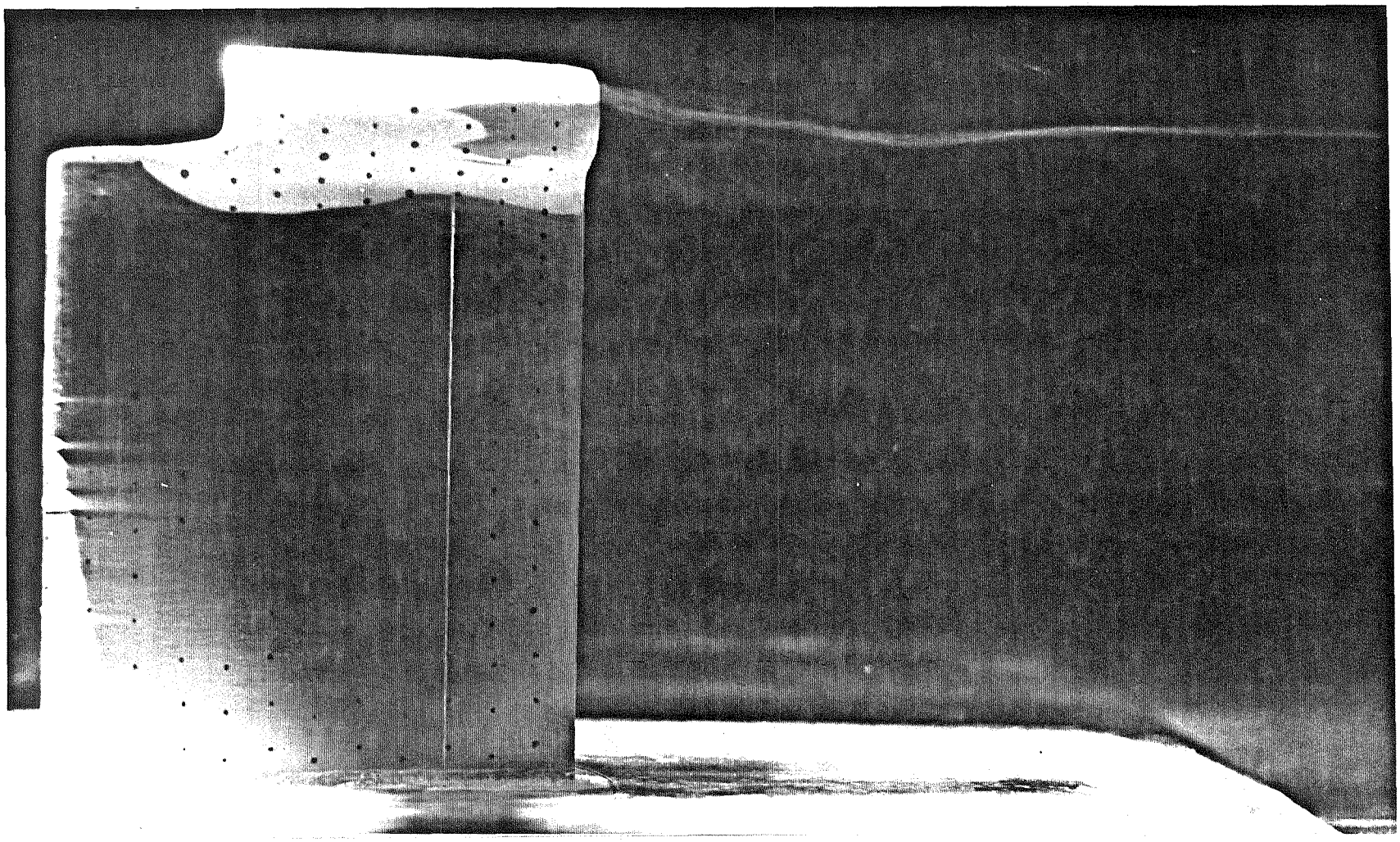

Figure IV.58 Trailing Vortex Visualization. Flow is left to right. NACA 64-309 ring wing tip. $\alpha = 7°$, Re=1.2×10^6, $\sigma = 1.5$, DAC=7.0ppm. Bubbles generated at the ring leading edge are forced into the trailing vortex core and serve to visualize the vortex.

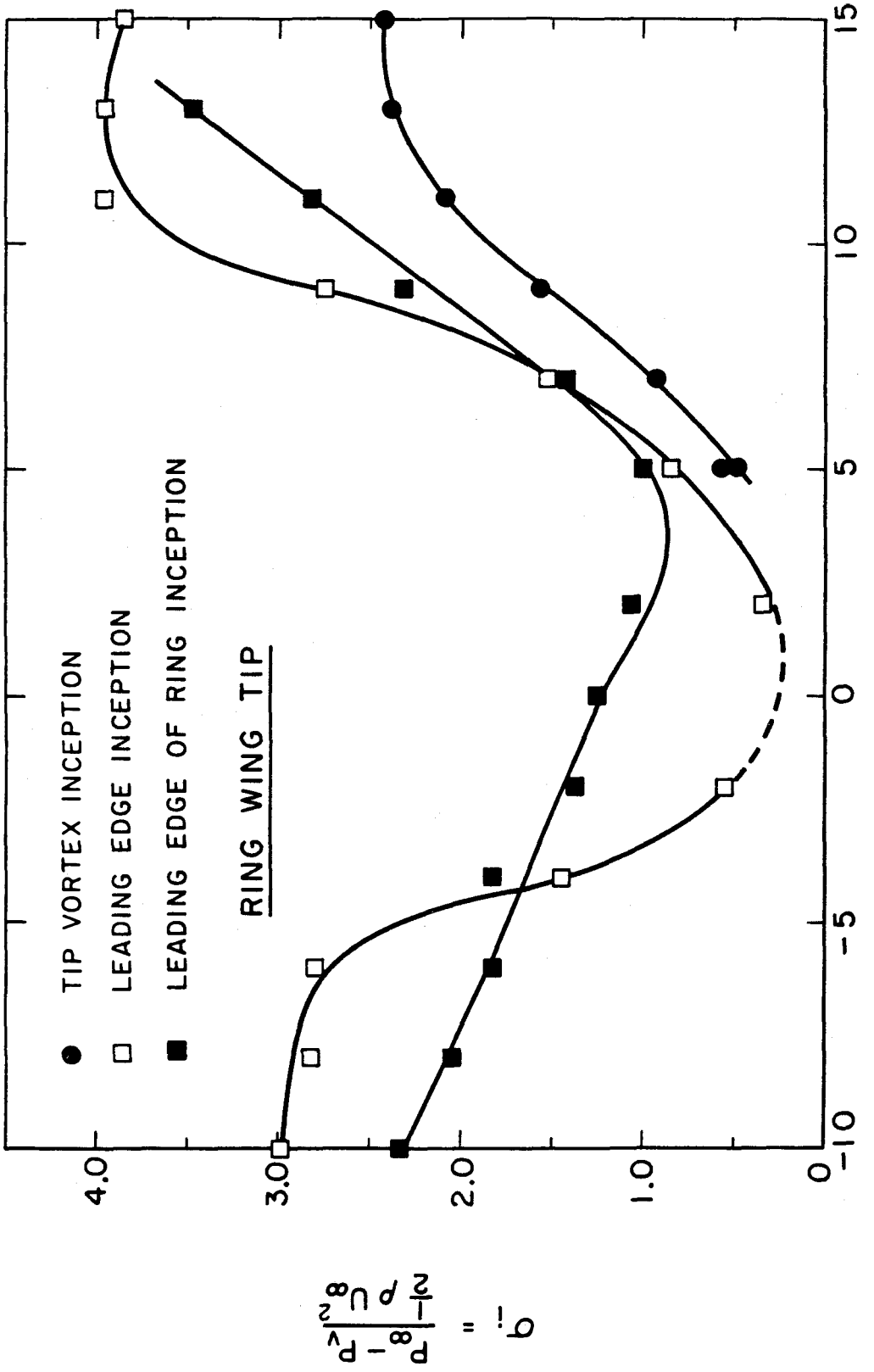

Figure IV.59 Inception Index versus Angle of Attack (NACA 64-309 ring wing tip).

CHAPTER V – DISCUSSION

The reader may feel, at this point, overwhelmed by a surfeit of data. An attempt will be made in this chapter to synthesize the multitudinous data into a coherent whole; to provide physical insight into the trailing vortex behaviour, both single phase and cavitating.

The trailing vortex has been shown in the present study to be an unsteady, viscous, 3D phenomenon, and as such is not readily amenable to analytic treatment. Perhaps, however, certain trailing vortex characteristics may be adequately explained using simple ideas, and other characteristics understood in terms of fundamental (though analytically elusive) variables. To wit, four independent variables describe the experiments of Chapter IV– α, x/c, U_∞, and the tip geometry. Seven different dependent variables (and two core phenomena) have been measured or observed– lift distribution (see V.1.1), U_θ, $\overline{p_c^*}$, $\overline{(p_c')^*}$, $\overline{U_{xc}}$, $\overline{U_{xc}'}$, R_c, core "kinking," and core "vortex stutter." These dependent variables/phenomena will be discussed in turn in the first section of this chapter. In section 2 the cavitation behaviour will be related to these variables.

V.1 Synthesizing the Single Phase Trailing Vortex Results

V.1.1 Wing Lift Distribution

The surface flow visualization photographs of Chapter IV can provide, remarkably, information on the lift distribution spanwise along the wing. From a two-dimensional potential flow analysis of the wing one may infer $U \approx U_\infty$ as the trailing edge is approached. Combining this with the definition of ϕ (the inboard flow angle) enables one to calculate V at the trailing edge ($= U_\infty \tan\phi$) on both the pressure and suction surfaces. It is then a straightforward matter to calculate the normalized shed circulation per unit length, $(d\Gamma/dy)/U_\infty \approx \tan\phi_{ps} - \tan\phi_{ss}$. This calculation is based on the assumption that the boundary layer flow matches the flow direction of the external inviscid flow. Quantifying the range of validity of this

assumption is virtually impossible. It is the best first order approximation. This result is plotted as Figure V.1 for the rounded tip foil (using the data of Figure IV.3(a)), as Figure V.2 for the square cut tip (data from Figure IV.50), and as Figure V.3 for the ring wing tip (Figure IV.56 has the raw data). Notice that the ring wing tip $(d\Gamma/dy)/U_\infty$ is only approximately half that of the rounded or square tips. The wing lift lost over the spanwise region (a,b) due to tip downwash is:

$$L_L = \rho U_\infty \int_a^b \int_0^h (d\Gamma/dy)dydh \qquad (V.1.1)$$

If the region (a,b)=(0.3s,0.8s) is considered (the region in which $d\Gamma/dy$ is fairly accurately known), one evaluates the ring wing tip lift loss to be only 60% of the square cut or rounded tip losses. Apparently the ring wing tip may be beneficial not only as a cavitation alleviation device, but also for increasing the lift of a fixed aspect ratio wing (though the drag cost is not known). The claim of increased lift for the ring wing tipped foil is bolstered by an examination of Figures IV.54 and IV.4. Note that flow separation on the ring wing tipped foil occurs over a larger region than for the rounded tip foil; additional evidence that the flow is closer to two dimensional over the former foil than the latter.

The only existing simple theory claiming to explain the variation of $d\Gamma/dy$ with y is lifting line theory. The Glauert series approximation (Milne-Thompson 1968) to lifting line theory is plotted in Figure V.2 . The agreement between the theory and the experimental results is very poor near y/s=0 where the wing/wall interaction is important, and near y/s=1, where tip vortex rollup causes both the theory, and the assumptions behind the interpretation of the experiment, to be invalid. The central portion of the curves provides strong evidence that lifting line theory does not accurately model the foil lift distribution. The plot of Figure V.4 indicates lifting line theory models the experimental results better at high angles of attack, possibly because stronger tip loading occurs as α increases. Lifting line theory cannot, of course, simulate the effect of different wing tips on the wing loading. The spanwise lift distribution, for this geometry, is thus a quantity which is not

readily describable analytically.†

V.1.2 Tangential Velocity Around the Core

Double pulsed holography and measurements of the SFV downwash angles at the tip both provide information on U_θ. A simple theoretical model will be developed in this subsection to predict the variation of U_θ with α, x/c, and Re.

Consider a two-dimensional wing at lift angle $(\alpha - \alpha_o)$ in a fluid moving at U_∞ in the far field. The lift per unit spanwise length of this wing is $L/l = \rho U_\infty \Gamma_B$. L/l may also be expressed by $c_L = 2\pi(\alpha - \alpha_o) = L/[l(0.5\rho U_\infty^2)c]$. Equating the two expressions gives $\Gamma_B/cU_\infty = \pi(\alpha - \alpha_o)$. Thus, if all of the bound vorticity of a two-dimensional foil rolls up into the trailing vortex, the trailing vortex circulation will also be $\Gamma_v = \pi c U_\infty(\alpha - \alpha_o)$.

This analysis may be repeated for a finite aspect ratio wing which has an assumed elliptical bound circulation distribution. It may be shown that (White 1979):

$$\Gamma_v = \frac{\pi c U_\infty(\alpha - \alpha_o)}{1 + 2/AR} \qquad (V.1.2)$$

for a wing in a freestream. For a wing mounted in the experimental configuration (Durand 1963), $c_L = 1.05 c_L$(no tunnel constraint).* Thus (V.1.2) becomes:

$$\Gamma_v = \frac{1.05\pi c U_\infty(\alpha - \alpha_o)}{1 + 2/AR} \qquad (V.1.3)$$

Equation V.1.3 is compared with the experimental results of Table IV.1 in Table V.1 (on the following page):

---

† The flow is tractable computationally, e.g. see Srinivasan 1986.

* This result is predicated on the assumption of bound vorticity shedding solely from the foil tip. Distributing the vorticity shedding over the span will tend to reduce the 1.05 coefficient to, perhaps, 1.04. No simple theory accounts for the effect of wing/wall interaction on c_L (Rae and Pope 1984).

α(deg)	x/c	Re	$\Gamma_{measured}(m^2/s)$	$\Gamma_{V.1.3}(m^2/s)$	% Difference
5	10	1.79×10^5	0.034	0.034	0
5	10	4.31×10^5	0.083	0.080	4
5	10	7.61×10^5	0.158	0.141	12
5	10	1.04×10^6	0.207	0.192	8
10	10	1.44×10^5	0.050	0.048	4
10	10	4.31×10^5	0.139	0.146	-5
10	10	7.76×10^5	0.283	0.262	8
5	4	2.14×10^5	0.040	0.040	0
5	4	8.19×10^5	0.133	0.151	-12
5	4	1.08×10^6	0.184	0.199	-7
5	2	5.79×10^5	0.110	0.107	3
5	2	7.85×10^5	0.140	0.145	-2
10	2	1.54×10^5	0.044	0.052	-15
10	2	5.16×10^5	0.168	0.174	-3
10	2	7.72×10^5	0.229	0.240	-5

Table V.1 Comparison of Theoretical and Experimental Γ_v

The theoretical circulation matches the measured circulation to within experimental error (recall that the error increases as Re decreases).

Several important conclusions may be drawn from the agreement between the theory of (V.1.3) and the experiment:

1. Even one chord downstream of the foil essentially all the bound vorticity has rolled up into the trailing vortex. One questions the usefulness of Moore's (1974) calculation that only 50% of an elliptically loaded foil's bound vorticity is contained in the trailing vortex at this value of x/c.

2. Spreiter and Sacks (1951) predict at $\alpha = 5°$, $(x/c)_{rolledup} = 2.4$ for a rectan-

gular wing. For $\alpha = 10°$ they predict $(x/c)_{rolledup} = 1.7$. Their theory is approximately supported by these data.

3. There is very little decay (or growth) of trailing vortex circulation with downstream distance.

4. The theory predicts Γ_v well. Orloff and Grant (1973) found similarly that (at x/c=7, $\alpha = 11°$) Γ_v is well predicted by theory. They also demonstrated that once Γ_v and R_c are known, the semi-analytical correlation of Nielson and Schwind (1971) accurately predicts the $U_\theta(R)$ distribution. Thus $U_\theta(R)$ may be determined *a priori* for any normal rectangular planform wing.

5. This theory also explains the observation (Figure IV.13) that ϵ' varies with $\alpha - \alpha_o$, and the further observation that ϵ' is almost independent of Reynolds number.

6. Phillips (1981) analytically predicted for an elliptically loaded wing that $(U_\theta)_{max}$ varies as $x^{-0.25}$. Between x/c=2 and 10, this analysis predicts $(U_\theta)_{max}$ should decrease by a factor of 0.67 . No such decrease is measured. However, $(U_\theta)_{max}$ does vary approximately as $x^{-0.25}$ (McCormick et al. 1968) for $x/c > 30$. The reason for this change in $(U_\theta)_{max}$ dependence with distance is not known, though perhaps the fact that McCormick's experiments were carried out on real aircraft in flight plays a role.

7. A few authors (e.g. Srinivasan 1986, Orloff and Grant 1973) have observed large scale vortex asymmetry many chords downstream of a foil. A statistical study of the present results was conducted, and no evidence of vortex asymmetry was found.

V.1.3 Core Mean Pressure

The steady radial momentum equation in cylindrical coordinates is:

$$\frac{\partial p}{\partial R} = \frac{\rho U_\infty^2}{R} \qquad \text{(V.1.4)}$$

This equation is readily integrated to yield:

$$p_c^* = \frac{p_\infty - p_c}{0.5\rho U_\infty^2} = \frac{1}{0.5\rho U_\infty^2}\left(\int_0^{0.025} \frac{\rho U_\theta^2}{R} dR + \int_{0.025}^{\infty} \frac{\rho U_\theta^2}{R} dR\right) \qquad (V.1.5)$$

The first integral, which must be evaluated numerically, represents the contribution to the radial pressure drop due to the fluid motion in R $\leq$ 2.5cm. The second integral is the contribution from the potential flow that exists outside R=2.5cm. This latter integral may be evaluated analytically. Γ_v from (V.1.3) with c=0.152 and AR=2.3 is substituted into the result yielding:

$$\frac{1}{0.5\rho U_\infty^2}\int_{0.025}^{\infty} \frac{\rho U_\theta^2 dR}{R} = 2.91(\alpha - \alpha_o)^2 \qquad (V.1.6)$$

For $\alpha = 10°$, (V.1.6) represents a contribution of 0.11 to p_c^*. For $\alpha = 5°$, (V.1.6) is an even more meagre 0.03.

The first integral has been determined numerically for four cases (the number in brackets is this integral, the second number is p_c^*):

x/c=2 $\alpha = 10°$: (2.3) 2.4

x/c=2 $\alpha = 5°$: (1.4) 1.4

x/c=2 $\alpha = 10°$: (2.3) 2.4

x/c=10 $\alpha = 5°$: (1.3) 1.3

The extremely limited data near the core causes the error in these results to be large, perhaps up to ± 0.4 in p_c^*. These results are nonetheless in excellent agreement with Dunham's (1979) semi-analytical correlation ($p_c^* = 1.7$ and 2.5, for $\alpha = 5°$ and 10° respectively), and in fair agreement with the tailored bubble measurements of mean core pressure. Thus, the mean core pressure is solely a function of U_θ, which is itself well understood (as noted in V.1.2).

V.1.4 Core Unsteady Pressure

In this subsection the unsteadiness in core pressure will be explained in terms of the fluctuating axial velocity. Consider core fluid being convected from a location where $U_{xc} = \overline{U_{xc}}, p_c = \overline{p_c}$ through a locally high axial velocity part of the core

(where the velocity and pressure are respectively U^+ and p^+). If the dynamics of the process are neglected, then a Bernoulli equation may be written to describe the pressure:

$$\overline{p_c} + 0.5\rho\overline{U}^2 = p_c^+ + 0.5\rho(U^+)^2 \qquad \text{(V.1.7)}$$

With some manipulation, (V.1.7) becomes:

$$(p_c^+)^* = \left(\frac{U^+}{U_\infty}\right)^2 - \left(\frac{\overline{U}}{U_\infty}\right)^2 \qquad \text{(V.1.8)}$$

Typical values from Figure IV.14 are $\overline{U}/U_\infty = 1.5$ and $U^+/U_\infty = 1.8$, for which $(p_c{}^+)^* = 1.0$. This value is within a factor of 2 of the measured $\overline{(p_c')^*}$ value. In light of the considerable experimental error in $\overline{(p_c')^*}$, this agreement should be viewed as satisfactory, i.e., the measured fluctuating core axial velocity adequately explains the fluctuating core pressure.

V.1.5 Mean and Fluctuating Core Axial Velocity

The first, and in retrospect still apparently the best, explanation of axial flow in trailing vortices is due to Batchelor (1964). As discussed in the Introduction, Batchelor's basic idea is that axial pressure gradients in the fluid either accelerate the core fluid to above U_∞ or decelerate the fluid to below U_∞.

In the near field, application of Bernoulli's equation from upstream of the foil where $U_x = U_\infty, p = p_\infty$ into the vortex core where $U_x = U_{xc}$, p=(evaluated using V.1.3 with an assumed Rankine vortex U_θ distribution*) gives:

$$U_{xc} = U_\infty\sqrt{1 + 2k^2} \qquad \text{(V.1.9)}$$

where $k=(U_\theta)_{max}/U_\infty$.

---

* Rankine vortex:

$$U_\theta = \begin{cases} (U_\theta)_{max}(R/R_c), & R \leq R_c \\ (U_\theta)_{max}(R_c/R), & R > R_c \end{cases}$$

For $\alpha = 5°$ at x/c=2 (refer to Figure IV.29) k $\approx$ 0.6, whence $U_{xc} = 1.31U_\infty$. This is in very good agreement with the measured value, $\overline{U_{xc}} \approx 1.25U_\infty$. Similarly, for $\alpha = 10°$ at x/c=2 (refer to Figure IV.30) k $\approx$ 0.8, whence $U_{xc} = 1.51U_\infty$. Once again, the agreement with the measured value, $\overline{U_{xc}} \approx 1.53U_\infty$, is excellent.

The near field mean core axial velocity is another phenomenon that may be understood simply on the basis of $U_\theta(R)$, which is itself well grounded theoretically.

In the far field, Batchelor argues, an adverse pressure gradient caused by viscous or turbulent diffusion of the core retards the axial velocity in the core. He then proceeds to calculate the asymptotic form of U_{xc} based on slow ($x^{0.5}$) diffusive growth of the core. Moore and Saffman (1973) have noted that Batchelor's solution is only valid thousands of chords downstream of a wing.

Moore and Saffman (1973) did a small perturbation study of the laminar trailing vortex, and analytically predict for a rectangular planform wing trailing vortex:

$$U_{xc} - U_\infty = -2.4 \times 10^{-5}(\alpha - \alpha_o/deg)^2 Re^{0.5}(x/c)^{-0.5} - 0.28(x/c)^{-0.5} \quad \text{(V.1.10)}$$

A few representative experimental values will be substituted into this expression:

x/c=2, Re=2.88×10^5, $\alpha - \alpha_o = 6°$: $U_{xc} - U_\infty = -0.53$ (c.f. 0.23 experimental)

x/c=10, Re=1.79×10^5, $\alpha - \alpha_o = 6°$: $U_{xc} - U_\infty = -0.20$ (c.f. -0.40 experimental)

Apparently equation (V.1.10) does not correctly model the trailing vortex core flow; it cannot predict axial velocity excesses in the core, and it predicts the wrong trend of U_{xc} with x/c and α. The failure of this theory to predict the experimental flow can be attributed to: $(\overline{U_{xc}}/U_\infty) - 1$ is large (the theory requires this quantity to be small), the flow is turbulent, and the foil lift distribution is different from the assumed lifting line distribution.

In summary, neither of the two leading theories which purport to elucidate the mean core axial flow behaviour passes the experimental litmus test.

One speculates that in the far field the mean axial velocity depends on the fluctuating core velocity (which is indicative of flow energy losses). No theory will

adequately exposit the behaviour of $\overline{U_{xc}}$ without simultaneously, at least approximately, predicting $\overline{U'_{xc}}$. Thompson's (1975) observation of pronounced tip geometry effects on $\overline{U_{xc}}$ in the far field suggests $\overline{U_{xc}}$ depends in addition on the original core radius.

The above remarks raise the question– What causes $\overline{U'_{xc}}$ to be so large? The author suggests the fluctuating core velocity is a manifestation of a non-linear core instability. This instability may be the vortex kinking seen when $\overline{U'_{xc}}$ is especially large.

Arguably the most perplexing observation related to axial flow is the strong dependence of U_{xc}/U_∞ on Re in the far field, despite the fact that U_θ/U_∞ and U_{xc}/U_∞ (near field) are Re independent. The author cannot explain this result, but puts forth the following suggestions:

1. Re effects associated with the fluid, perhaps with pertinent length scale=R_c, could cause this effect. 1. and 2. could be distinguished by varying the Re through changes in the foil chord. The author prefers this explanation.
2. The Re at which the measurements were taken is near the transition Re to turbulence on the foil. Transition could significantly affect the vortex core size, or fluctuating core velocity, and hence the downstream velocity distribution.
3. Freestream turbulence in the tunnel might have a velocity dependence which would cause the observed phenomena. This could be investigated by increasing the freestream turbulence through the use of flow conditioning grids.

V.1.6 Core Radius

It is now well established in the literature that the initial radius of a trailing vortex core depends on the pressure side boundary layer thickness near the tip (e.g. McCormick 1962, Moore and Saffman 1973). Analytical calculations of the boundary layer thickness in the complex three dimensional flow around the tip are extremely difficult, so the issue of initial core size will not be considered. The experimental techniques employed in this thesis were not suitable for accurate

determination of R_c, so a detailed experimental study of R_c also could not be made.

V.1.7 Core Structure

In order to simplify the analytical simulation of trailing vortices, theoreticians assume the vortex is axisymmetric. Often this is a reasonable approximation. However, two types of non-axisymmetric core structure, which may be of importance to an understanding of tip vortex flow, have been identified. In this subsection the author will cite other examples in the literature of these core structures.

Hopfinger et al.(1982) have published a paper describing the flow in a deep, rotating tank fitted with a bottom-mounted turbulence generation grid. An important feature of their flow is "concentrated vortices having axes approximately parallel to the rotation axis." These concentrated vortices

> "support waves consisting of helical distortions, which travel along the axes of individual vortices. Isolated, travelling waves seem well-described by the vortex-soliton theory of Hasimoto (1972). ... Interactions between waves, which are frequent occurrences, almost always result in a local breakdown of the vortex core, and small-scale turbulence production. Usually the portions of broken core reform within 1/2 - 1 rotation periods, but occasionally cores are destroyed and reformed on a much longer time scale." (Hopfinger et al. 1982)

The astonishing parallelism between this description, and the vortex kinking and breakdown observed in the present study, should be self-evident. This similarity of phenomena between two ostensibly very different vortical flows raises the possibility of **vortex kinking and breakdown occurring in all flows with concentrated vorticity.**

Proper study of this hypothesis is an excellent topic for future doctoral students. Perhaps, however, previous researchers have recorded vortex kinking without

recognizing its importance, and examples of vortex kinking may be found in the open literature.

In their pioneering studies of shear layer structure, Brown and Roshko (1974) speculated on the existence of streamwise vortices in the shear layer. Bernal (1986) demonstrated experimentally the existence of these vortices. O'Hern (1987) studied the cavitation in a shear flow (the flow behind a stream-normal plate) and discovered that inception occurs in the long concentrated streamwise vortices of the shear layer. Figure V.6 (reproduced with the permission of Dr. O'Hern) is a photograph of cavitating streamwise vortices. This author has marked onto the photograph the locations of three structures which appear to be vortex kinks. Additional examples of vortex kinks are visible in photographs taken under different flow conditions.

To summarize, vortex kinking has been observed in three different flows with regions of concentrated vorticity, an observation which suggests vortex kinking and the related phenomena may occur wherever concentrated vorticity exists in a fluid.

The author recommends that, in order to avoid confusion, the expression "vortex breakdown" be henceforth reserved to refer to classical, macroscopic trailing vortex breakdown. The author further recommends the expression "vortex stutter" be used for the type of core disruption observed in Hopfinger's and the present study.

V.1.8 Summary

This section may be readily summarized by dividing trailing vortex phenomena into those which are, and those which are not, understood on a simple analytical level. In the former category we may include U_θ, $\overline{p_c^*}$, and $\overline{U_{xc}}$ (in the near field). The "not understood" category includes $\overline{U_{xc}'}$ and $\overline{U_{xc}}$ (far field). Understanding of R_c, $\overline{(p_c')^*}$, and vortex kinking is limited to a qualitative level.

V.2 Relating Single Phase and Cavitating Flow Phenomena

Cavitation inception, as it is normally defined, occurs when a cavitation nucleus (typically a freestream microbubble) is exposed to reduced external pressure for

long enough to allow bubble growth to macroscopic size. This definition implies that cavitation inception depends on:

i/ the original size of the cavitation microbubble

ii/ the size to which the bubble must grow to be macroscopically observable

iii/ the time history of the external pressure

The detailed measurements performed in the present study fall far short of simultaneously providing all of the information deemed necessary for predicting inception. This statement begs the question– Is it possible to derive a *heuristic* model of inception based on single phase phenomena?

V.2.1 Relating σ_i to $\overline{p_c^*}$ and $\overline{(p_c')^*}$

A logical starting point in the consideration of this question is the measured values of $\overline{p_c^*}$ and $\overline{(p_c')^*}$, since to first order cavitation inception is determined by these quantities.

One may relate σ_i to p_c^*:

$$\sigma_i = \frac{p_\infty - p_v}{0.5\rho U_\infty^2} = p_c^* + \frac{p_c - p_v}{0.5\rho U_\infty^2} \qquad \text{(V.2.1)}$$

If one hypothesizes $p_c \approx p_v$ at inception (which should be true when there are many freestream nuclei, e.g. at high DAC), then one would anticipate $\sigma_i \approx p_c^*$. At $\alpha = 5°$, $\overline{p_c^*}$ was found to be (see section V.1.3) 1.3 . σ_i is 1.6 (Figure IV.53). At $\alpha = 10°$, $\overline{p_c^*}$ was found to be 2.4 . σ_i is 2.8 . The agreement between σ_i and $\overline{p_c^*}$ is in fact quite good in view of the uncertainty in both $\overline{p_c^*}$ and σ_i.

σ_i is in general elevated above $\overline{p_c^*}$ (and is even more so at higher DAC). At first this may seem counterintuitive because cavitation requires there be a small tension locally in the fluid. This would cause the discarded term in (V.2.1) to be negative, which implies $\sigma_i < \overline{p_c^*}$. A mitigating factor, however, is the unsteadiness of the core flow. The measured value of $\overline{(p_c')^*}(\approx 1.7)$ is more than sufficient to account for the observed $\sigma_i > \overline{p_c^*}$.

$\overline{p_c^*}$ is virtually independent of x/c, an observation which explains why trailing vortex cavitation appears as a very long core once σ is reduced below σ_i. Cavitation inception itself occurs in the region of the flow where $\overline{U'_{xc}}$ is largest, and hence where $\overline{(p'_c)^*}$ is large. It is logical to infer, then, that cavitation inception is dependent on the fluctuating pressure superimposed on the mean.

Ooi (1985) has shown that at high DAC there is a factor of 35 more 5-20μm radius ("large") microbubbles in the LTWT than at low DAC. As noted in Chapter IV, σ_i is reduced by 1.6 (at $\alpha = 7°$) when the DAC is reduced from saturation to 6.5ppm. One might reasonably pose the question – Can the DAC effect be explained solely in terms of a change in the bubble cavitation critical tension with bubble size?

Knapp et al. (1970) have derived the following expression for the critical tension of a gas bubble with respect to dynamic stability:

$$(p_v - p_\infty)_{critical} = \frac{4S}{3R_o}\left[3\left(1 + \frac{(p_\infty)_o - p_v}{2S/R_o}\right)\right]^{-0.5} \qquad (V.2.2)$$

Let us assume, at high DAC, R_o for typical large microbubbles is 20μm. Then, an applied tension of $(p_v - p_\infty)$ =740 Pa ($S=7.3\times10^{-2}$N/m, $(p_\infty)_o$=100kPa, p_v=2kPa) produces cavitation. If we assume at low DAC R_o (typical large microbubble) is an order of magnitude smaller (=2μm)*, then $p_v - p_\infty$ = 18kPa is necessary for cavitation. For the flow velocities employed experimentally, changing R_o by an order of magnitude has only changed σ_i by ≈ 0.5, much less than the 1.6 change in σ_i with DAC.

This brief analysis has demonstrated that different bubble size responses to a mean core pressure cannot account for the very significant DAC affect on σ_i, sup-

* Katz (1981) has compiled data from many different researchers, and found the bubble number density distribution ($n(R_B)$ in his terminology) varies as $R_B^{-(3or4)}$ for ocean and water tunnel water. Consider high DAC water for which the largest "typical" bubbles are 20μm. At lower DAC, for which the bubble concentration is reduced by a factor of 35, the concentration of the largest typical bubbles would be the same at $R_B \approx$ (6 or 8μm). The assumption of R_B = 2μm at low DAC *overestimates* the mean core pressure effect.

porting the author's contention that **bubble response to pressure fluctuations is an important aspect of inception.** To wit, large freestream microbubbles in the core grow to macroscopic size in the low pressure fluctuations at a high mean core pressure, whereas smaller microbubbles would only grow to visible size in the same fluctuations if the mean core pressure were lower. The task of proving the efficacy of pressure fluctuations in enhancing bubble size distribution inception effects is beyond the scope of the present study.

V.2.2 The Influence of Tip Geometry

The analysis just completed suggests two possible explanations for the measured strong variation of σ_i with tip configuration– $\overline{p_c^*}$ changes or changes in $\overline{(p_c')^*}$. The redistribution of wing loading that occurs with ring wing (and to a lesser extent with square cut) tip installation increases the trailing vortex radius, which certainly decreases $\overline{p_c^*}$. The effect of different wing tips on $\overline{(p_c')^*}$ is not known. One speculates that any measure that decreases $\overline{U_{xc}}$ (such as decreasing $(U_\theta)_{max}$, which also diminishes $\overline{p_c^*}$) will decrease $\overline{U_{xc}'}$ and thus $\overline{(p_c')^*}$. None of these ideas was tested experimentally. One suspects the first explication is closer to reality* in view of the reasonable agreement between σ_i and $\overline{p_c^*}$ for the low DAC at which σ_i was measured.

V.2.3 Developed Cavitation

In Chapter IV developed trailing vortex cavitation was seen to attach to the foil on the suction surface at x/c=0.8, independent of α. By way of contrast, SFV showed the vortex rollup location moves upstream on the foil from x/c=0.7 to 0.3 as α increases. This is concrete evidence that vapour-filled trailing vortices behave differently from single phase vortices. Distinctly two-phase characteristics were also the source of one type of cavitation hysteresis described in Chapter IV.

---

* "holds more water"!

V.2.4 Summary

Cavitation inception has been shown to be a phenomenon readily comprehensible in terms of the single phase flow mean and fluctuation core pressures. In general, at low DAC, σ_i takes on a value which is $\overline{p_c^*} + \kappa \left[\overline{(p_c')^*}\right]$, where $\kappa \approx 0.2$. At higher air contents κ is much larger, perhaps as great as 1. The DAC effect is attributed to the existence of large microbubbles in the liquid at high DAC, which respond readily to pressure fluctuations in the fluid.

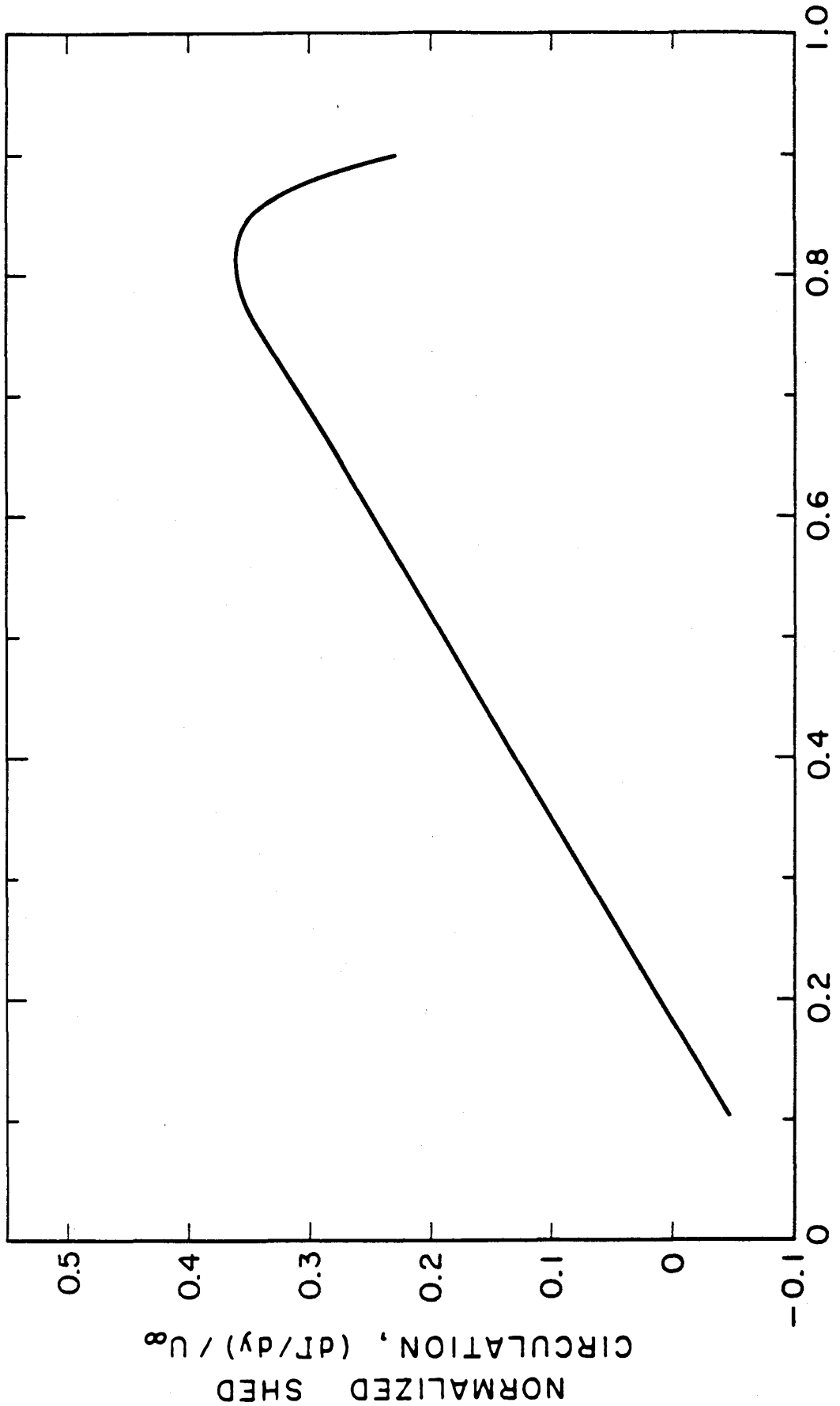

Figure V.1 Inferred Shed Circulation at the Trailing Edge. $\alpha = 7°$, Re=1.2×10^6, NACA 64-309 rounded tip.

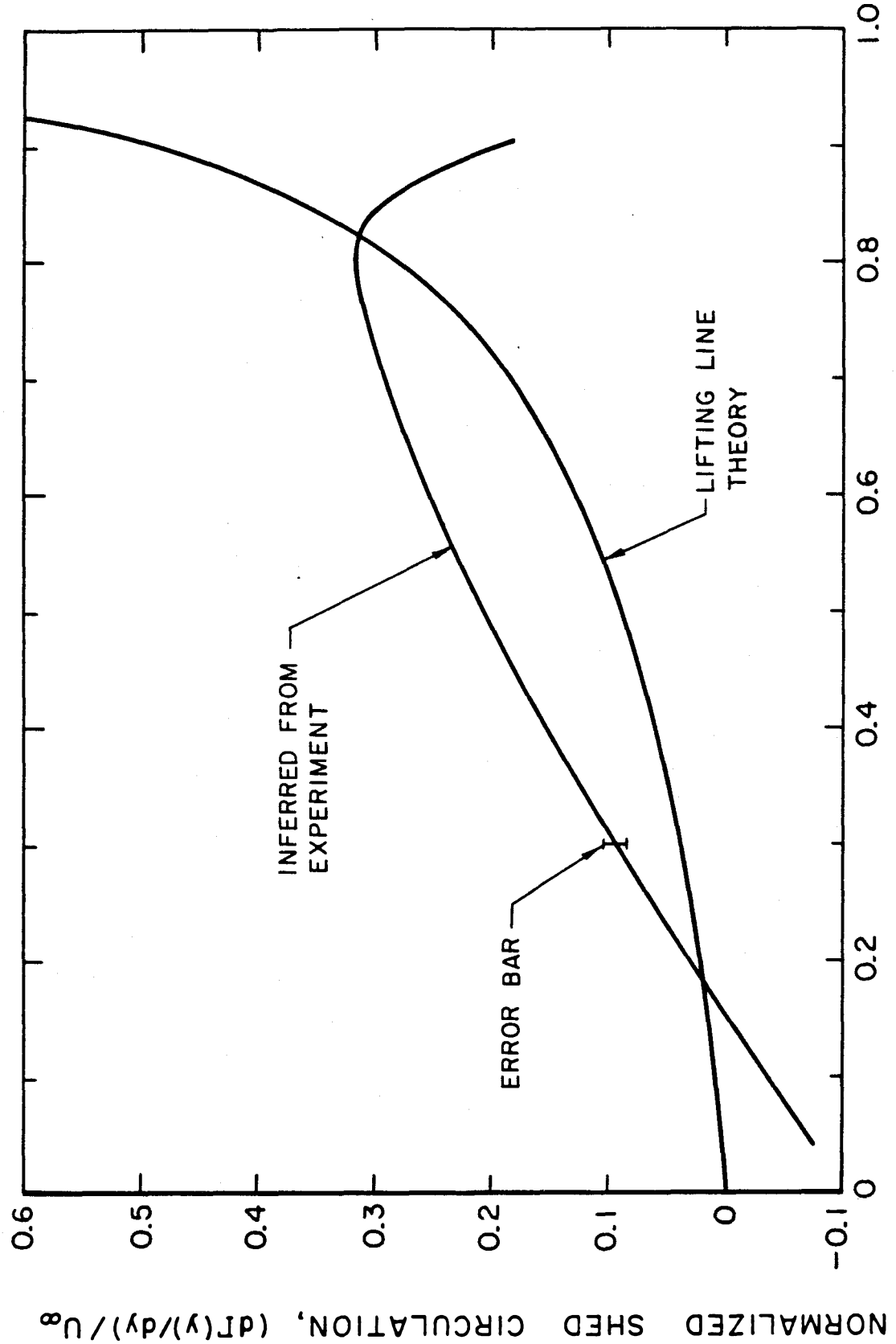

Figure V.2 Inferred Shed Circulation at the Trailing Edge. $\alpha = 7°$, $Re = 1.2 \times 10^6$, NACA 64-309 square cut tip.

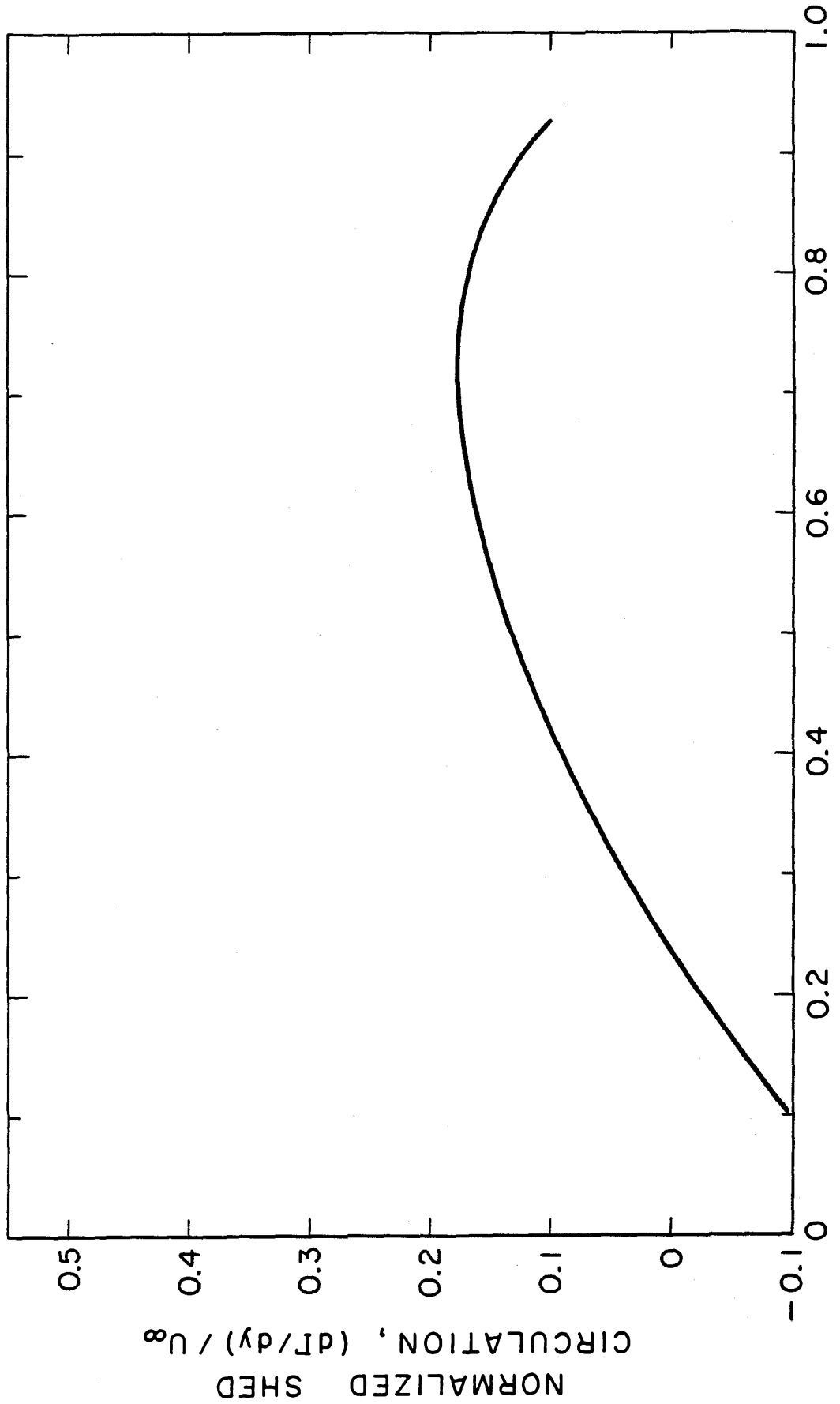

Figure V.3 Inferred Shed Circulation at the Trailing Edge. $\alpha = 7°$, Re=1.2×10^6, NACA 64-309 ring wing tip.

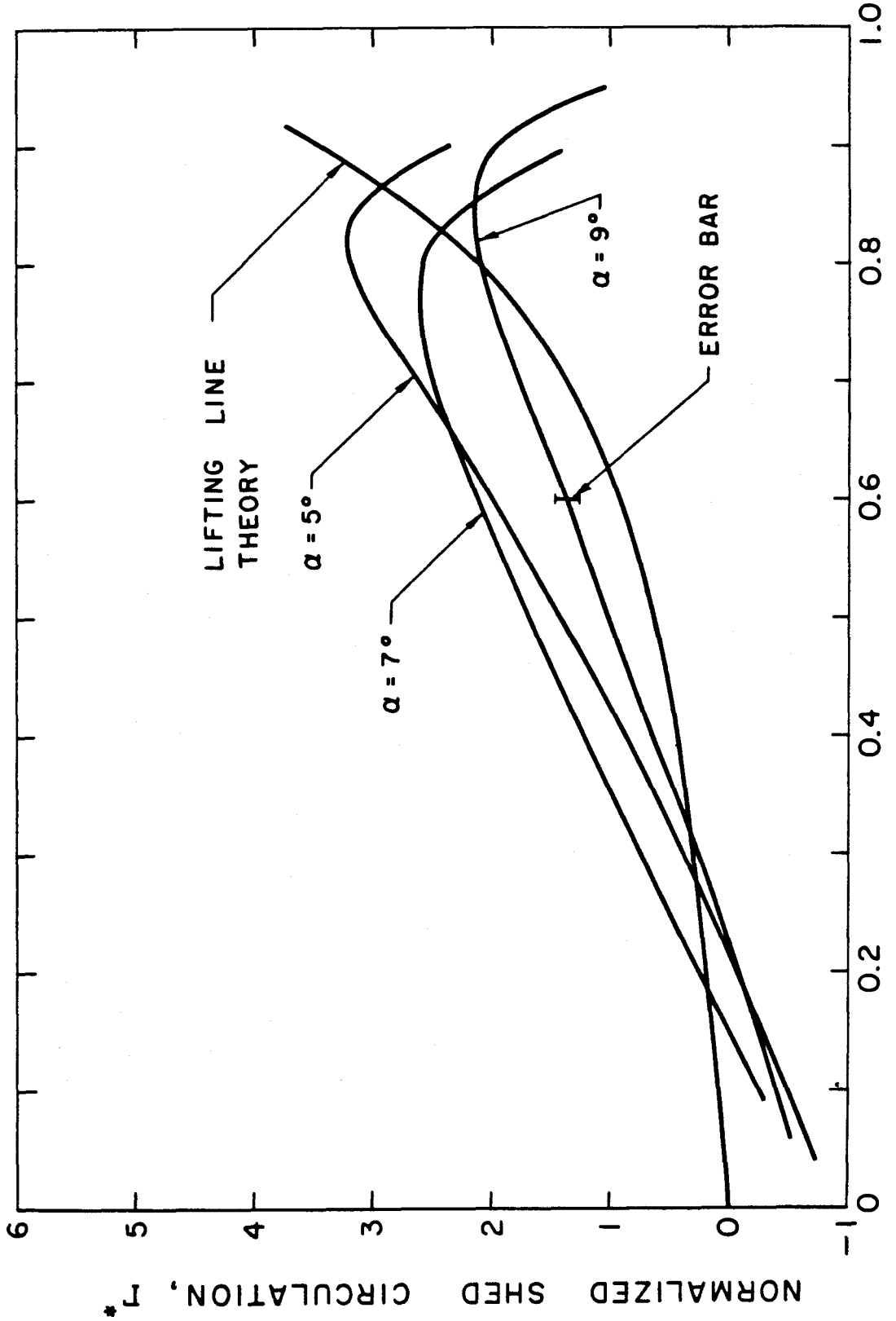

Figure V.4 Normalized Inferred Shed Circulation at the Trailing Edge. Re= 1.2×10^6, NACA 64-309 square cut tip.

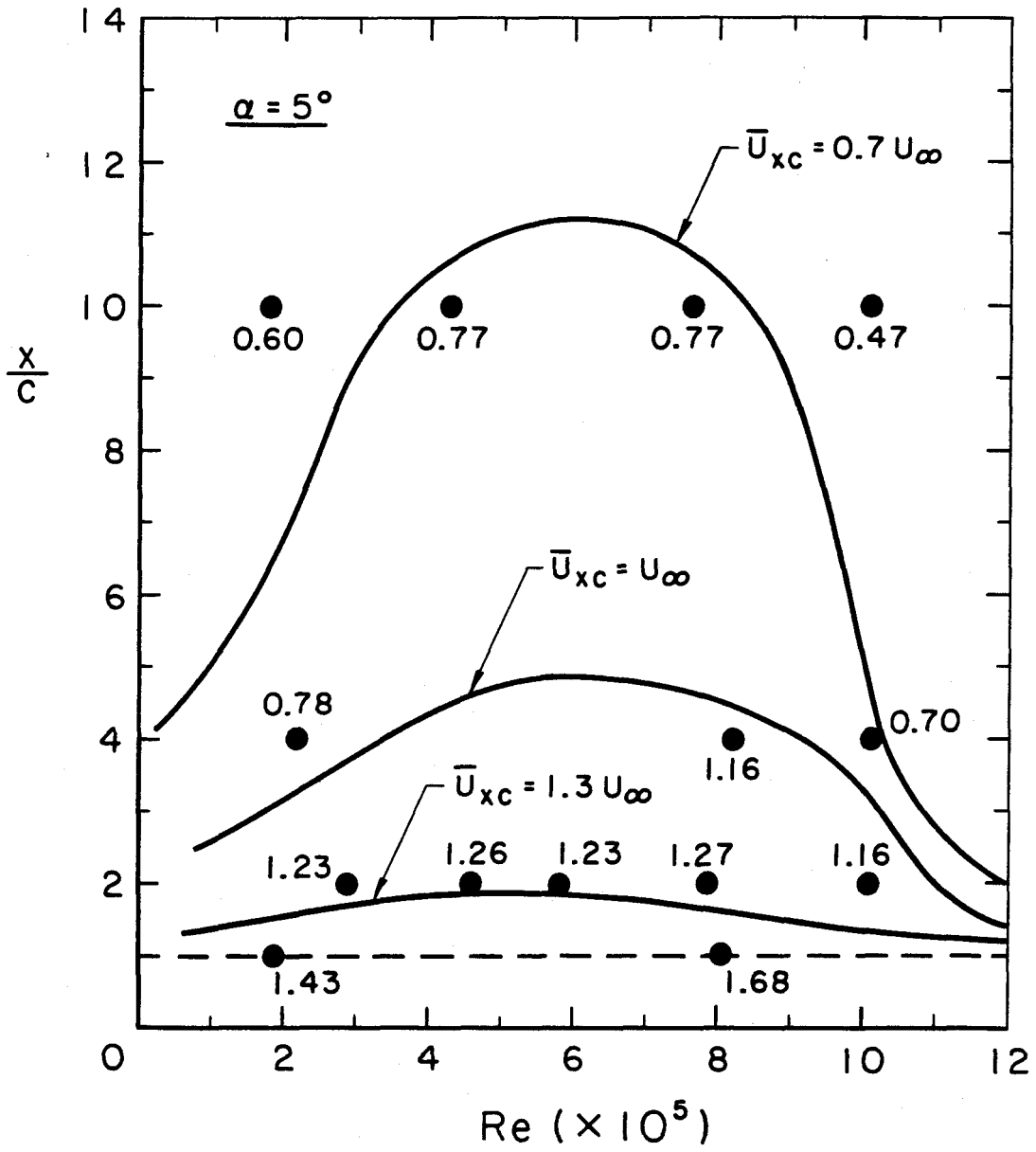

Figure V.5 Contour Plot of $\overline{U_{xc}}$ in x/c vs. Re Space.
($\alpha = 5°$, NACA 66-209 rounded tip).

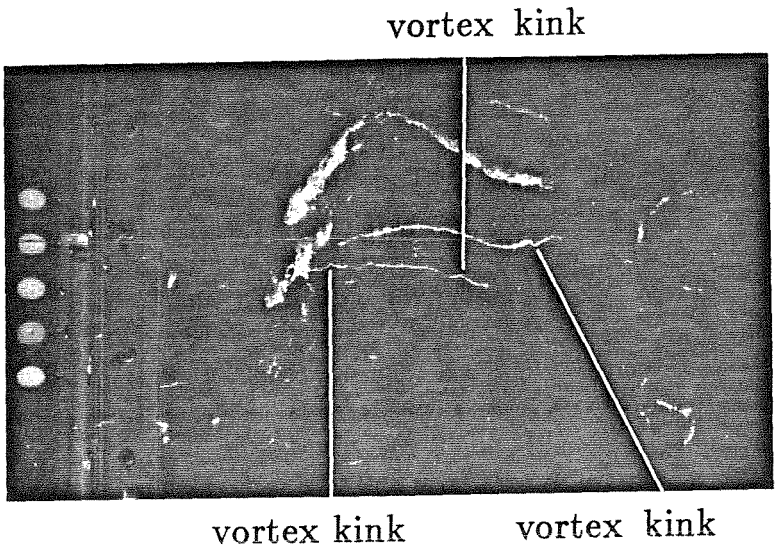

Figure V.6 Streamwise Vortex Cavitation. Flow is left to right.
Vortex kinks are marked. (U_L = 11.8m/s, σ = 0.62, DAC=4.2ppm).

Chapter VI–NUMERICAL SIMULATION

VI.1 Basic Considerations and Previous Efforts

The experimental results presented in Chapter IV have many consequences in terms of successful numerical modelling of the trailing vortex. The most obvious result of these experiments is that the trailing vortex may be highly unsteady, so that any tip vortex numerical scheme (TVNS) should model unsteadiness. Furthermore, typical time scales for this unsteadiness are on the order of $100\mu s$ (all physical quantities in this discussion refer to the experimental geometry described in Chapter II). Modelling the flow around the trailing vortex up to x/c=10 (for example) would require an unsteady simulation of the flow for at least a time, $t=10c/U_\infty$. This implies, with a typical time step $\Delta t = 100\mu s$, a total of $\approx$ 5000 time steps for the chord length and velocity used in this experiment. This analysis is based on the assumption that it is not possible to begin the computation with large time steps and then gradually reduce the time step as the solution converges. Allowing variable time steps reduces the time step requirement to perhaps 1000.

An additional and equally important constraint is that the small scales of the trailing vortex core must be resolved. Around the core itself the grid must be able to resolve a typical vortex kink, which is on the order of $300\mu m$ long. Since it is reasonable to anticipate that this resolution is necessary over the full 10c of the domain, this implies 5000 grid points in the axial direction. Orthogonal to the vortex, 200 grid points in each direction are likely to be required. As a rough estimate, then, $5000 \times 200 \times 200 = 2 \times 10^8$ grid points should suffice to define the flow.

It is helpful to reference these grid and time step requirements to present computer capacities. At present, the CRAY 2 supercomputer can handle on the order of 2×10^6 grid points (for a typical TVNS). This is fully two orders of magnitude smaller than the estimated number of grid points required. Approximately 5000 time steps on some 'normal' code (e.g. INS3D described in VI.3) for a 10^5

grid point system uses 5 hours of CPU time on the CRAY XM-P. Depending on the exact nature of the TVNS the CPU time varies as either N^2 or NlnN. Thus a 2×10^8 grid point simulation would require $\approx 10^4 - 10^7$ CPU hours. A machine at least 3 orders of magnitude faster than the CRAY XM-P would be required for this formidable task. It is highly unlikely that a computer of this power and storage capacity will be constructed for at least two decades.

A final consideration is the nature of the TVNS itself. In Chapter IV very large axial and tangential velocity gradients, and pressure gradients, were shown to exist near the core. Large flow parameter gradients are typically sources of numerical instability. Most numerical simulations combat instability through the introduction of artificial viscosity (e.g. numerical smoothing is a form of artificial viscosity). However, as demonstrated in Chapter V, viscosity plays only a small role downstream of the foil. Consequently, any artificial viscosity introduced to maintain numerical stability is unphysical, thus bringing into question the numerical results.

Many attempts have been made to numerically simulate the trailing vortex flow. Rossow (1975) has surveyed the literature, though that review is now considerably out of date. A brief listing of some of the relevant papers published since that time follows:

[i] Steger and Kutler (1977) – a fourth order accurate implicit finite difference procedure with clustering and a moveable grid to solve the incompressible (Reynolds averaged) Navier-Stokes equations with the Beam-Warming (1976) approximate factorization algorithm.

[ii] Raj and Gray (1979) – an iterative scheme of repeated invocation of the Biot-Savard law to relax the surface vorticity distribution on a wing to acheive self-consistent values, thus solving the 3D potential flow problem.

[iii] Lin et al. (1985, 1986) – a forward marching scheme on the parabolized Navier-Stokes equations (where the velocity field is described as the superposition of an *a priori* known potential flow solution and a secondary flow velocity).

[iv] Hoeijmakers (1985) represented the steady 3D trailing vortex by a transient 2D vortex development (where t $\mapsto$ axial distance). A second-order panel method computed the velocity induced by the wing vortex sheet, and integration in time was done using a modified Euler scheme.

[v] Srinivasan et al. (1986) and Holst et al. (1985) employed a zonal approach. Thin-layer Navier Stokes Equations were solved for the viscous flow near the wing surface, and this solution was coupled with the solution to Euler equations for the inviscid 3D flow away from the surface.

[vi] Sung et al. (1988) solved the 3D incompressible (Reynolds averaged) Navier-Stokes equations using a finite volume formulation and an explicit one-step multistage Runge-Kutta time step.

The author is not sufficiently well versed in the field to intelligently discuss the attributes and shortcomings of the various numerical schemes. Rather, the author merely notes that clear progress has been made in simulating tip vortex flows, but, as the preceding lucubration demonstrated, the existing computational capabilities are far from adequate to mimic the experimental results.

For this study, on the recommendation of several people, a 3D incompressible Navier-Stokes flow solver (INS3D) existing at NASA Ames was used to attempt to numerically model the flow around the rounded tip NACA 66-209 foil described in Chapter II. Section 2 of this chapter concerns the gridding of the experimental geometry. Section 3 is a brief description of the INS3D code. Section 4 is a listing of the boundary conditions employed. Finally, section 5 is a discussion of the results (or more appropriately, non-results) of the simulation.

VI.2 Selection of Domain and Gridding

The selection of a computational domain was constrained by an interest in simulating the experimental NACA 66-209 results. The domain normal to the flow direction was 2 chords on a side, in agreement with the experimental geometry. In order to obtain stable upstream boundary conditions, the inlet boundary was

chosen to be 0.5c upstream of the foil leading edge. In view of the stated interest in the cavitation characteristics of the trailing vortex, the downstream boundary was chosen to be at x/c=2.5.

Several flow features restrict the gridding scheme. Obviously, it is necessary to have a tight grid in the neighbourhood of the tip vortex to adequately resolve it. Similarly, a sufficiently dense grid must exist on the foil surface itself (to predict boundary layer effects), and on the lower plate boundary on which the foil sits (to allow for wing-wall interactions which the SFV in Chapter IV showed could be salient). Several different gridding schemes which fulfil these requirements were considered; the one ultimately chosen consisted of a stacked set of 50 2D grids, taken normal to the freestream flow direction, spaced with varying gaps. These planar grids were dense (as close as 0.01c apart) near the foil leading and trailing edges, and were less dense (up to 0.1c apart) away from the foil. Each 2D grid consisted of a c-grid – 61 grid points wrapped around the 'c' (the foil, or the slit which was its continuation beyond the foil edges) and 25 in the normal direction. The 61 points were clustered most densely near the foil tip and wall. The 25 normal grid points were packed most densely near the foil surface. The flow domain consisted of a total of $65 \times 61 \times 25 = 99,125$ grid points. 2D grids around the foil (refer to Figures VI.1 and VI.2) were generated using the GRAPE (Sorenson 1980) code, while the slit grids (e.g. Figure VI.3) were generated by appropriately stretching GRAPE grids at x/c=0.01 or 0.99 to a very small slit width. A perspective view of half the grid points which comprise the interior of the stacked c-grids is given as Figure VI.4. Careful inspection of the 3D grid revealed that mesh orthogonality was quite good. The major fault with the chosen gridding system was the existence of a singular line at the top of the c-grid slit, very close to the expected trailing vortex location.

VI.3 Description of the INS3D Code

The INS3D code has been described in detail previously (Rogers et al. 1987, Kwak et al. 1986, Chang et al. 1985, Kwak et al. 1984); the author will merely

summarize the basic features thereof.

The INS3D code was written at NASA Ames to solve 3D viscous, steady state, incompressible flow problems. In general, compressible flow is much easier to simulate than incompressible flow. The code takes advantage of this by formulating the continuity equation with the additional term $(1/\beta)(\partial p/\partial t)$ – a pseudocompressibility approach first proposed by Chorin (1967). The modified continuity equation together with the three momentum equations represent four equations in four unknowns (u,v,w,p). The code has the ability to handle arbitrary geometries by using coordinate transformations to map the domain onto a cartesian grid. The transformed equations are centrally finite-differenced and approximately factored (Beam and Warming 1976), and then solved implicitly. Computational efficiency is further enhanced by using a diagonal algorithm.

The code has been validated on certain 2D (channel, backward facing step, and circular cylinder) and 3D (ogive cylinder, rectangular duct, and cylinder-wall juncture) flows. It has never been tried on as complex a flow as the tip vortex.

VI.4 Boundary Conditions

The boundary conditions applied computationally over the flow domain were:

1. no slip on foil surface.
2. no slip on tunnel floor.
3. no flow through at the three other tunnel walls (viscous effects here are not relevant to the tip vortex).
4. linear flow parameter (u,v,w,p) extrapolation to the inner grid planes of the c-grid slit.
5. uniform freestream inlet conditions.
6. outlet boundary conditions extrapolated using the procedure recommended by Chang et al. (1985) to maintain stability.

VI.5 Results and Comparison with Experiment

Before attempting the $\alpha = 10°$ case (for which the gridding was shown in section 3), on the recommendation of the INS3D authors, an effort was made to simulate the $\alpha = 0°$, Re=1000 flow. Figure VI.5 is a typical result. The pressure field illustrated in this figure represents a converged solution based on the INS3D code authors' stipulation that "RMSDQ and DQMAX ... decrease by three or four orders of magnitude over their original values" (Rogers et al. 1987). Two basic problems are manifest. Computational instability is generated at the c-grid slit. The singularity at the top of the slit is a particularly strong noise generator because the Jacobian of the transformation is very large there. (This is comparable to the noise generated at the center of an o-grid; see Sobota 1987a.) Sawtooth solution behaviour due to the central differencing in the code is also evident. This undesirable behaviour would normally be eliminated by artificially smoothing the flow profile, but it was found that (see also Sobota 1987b) in order to obtain adequate convergence the smoothing parameters had to be reduced by 1.5 orders of magnitude below those recommended by the authors of the code.

In an effort to clarify the precise source of these difficulties, three tests were run. For the first test a 3D grid was made by stacking a set of identical 2D 'slit' grids. The code was run with all boundary conditions set to the freestream (i.e. allowing slip on the foil and the floor). The result was that freestream conditions were maintained for all time. The second test was similar to the first, with the modification that 2D grids identical with that at x/c=0.48 were stacked. Freestream conditions were again maintained. Finally, the proper 3D grid geometry was run with the same boundary conditions. Serious instabilities (negative pressures, wildly fluctuating velocities, etc.) were observed after only one timestep near the inner layer top of the c-grid where the grid varies rapidly in the streamwise direction (i.e. particularly severe problems were encountered near the leading edge tip and the trailing edge tip). The complete 3D grid was very carefully examined in these locations, but no flaws were discernible in it. The conclusion drawn is incontrovertible – the code as

it existed at the time of the tests could not handle the chosen grid.

This observation begs the question – "Why was a different grid not attempted?" In response, it is rather remarkable that no 3D grid generation program suitable for this application (Kwak 1987) exists, and all of the 3D grids produced by manipulating a set of 2D grids possessed unacceptable singularities not unlike the aforementioned singularity.

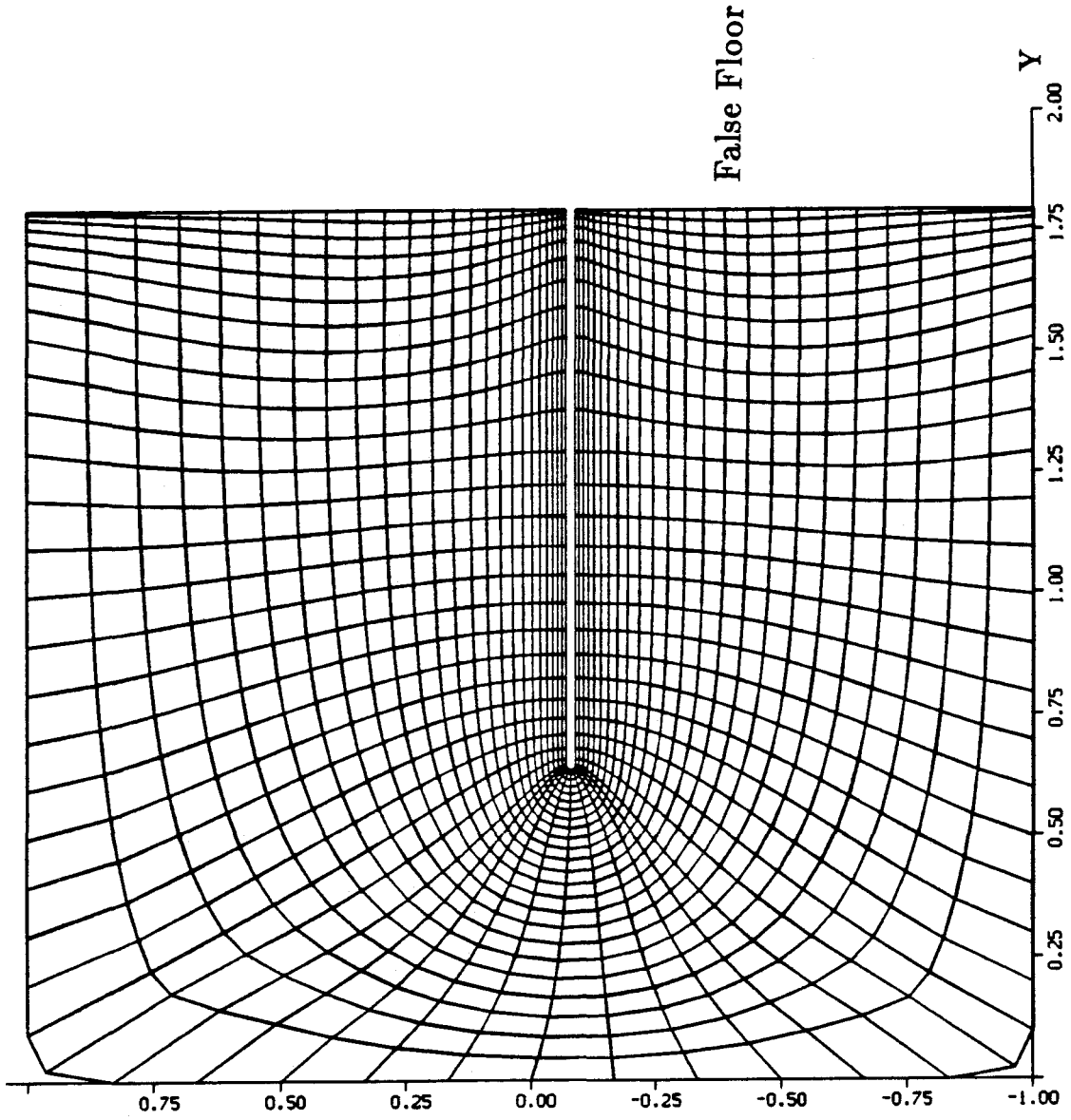

Figure VI.1 2D grid at x/c=0.01, $\alpha = 10°$.

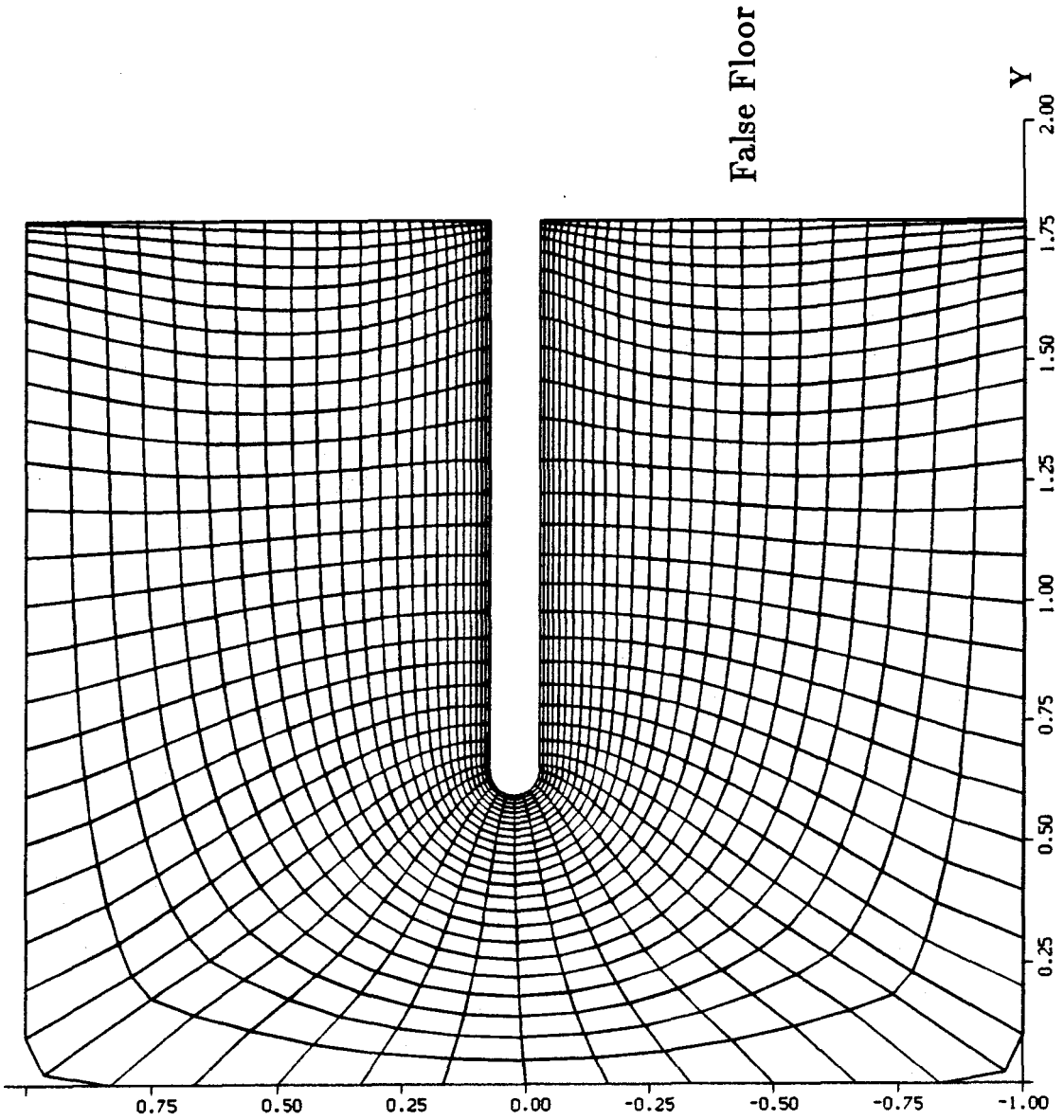

Figure VI.2 2D grid at x/c=0.48, $\alpha = 10°$.

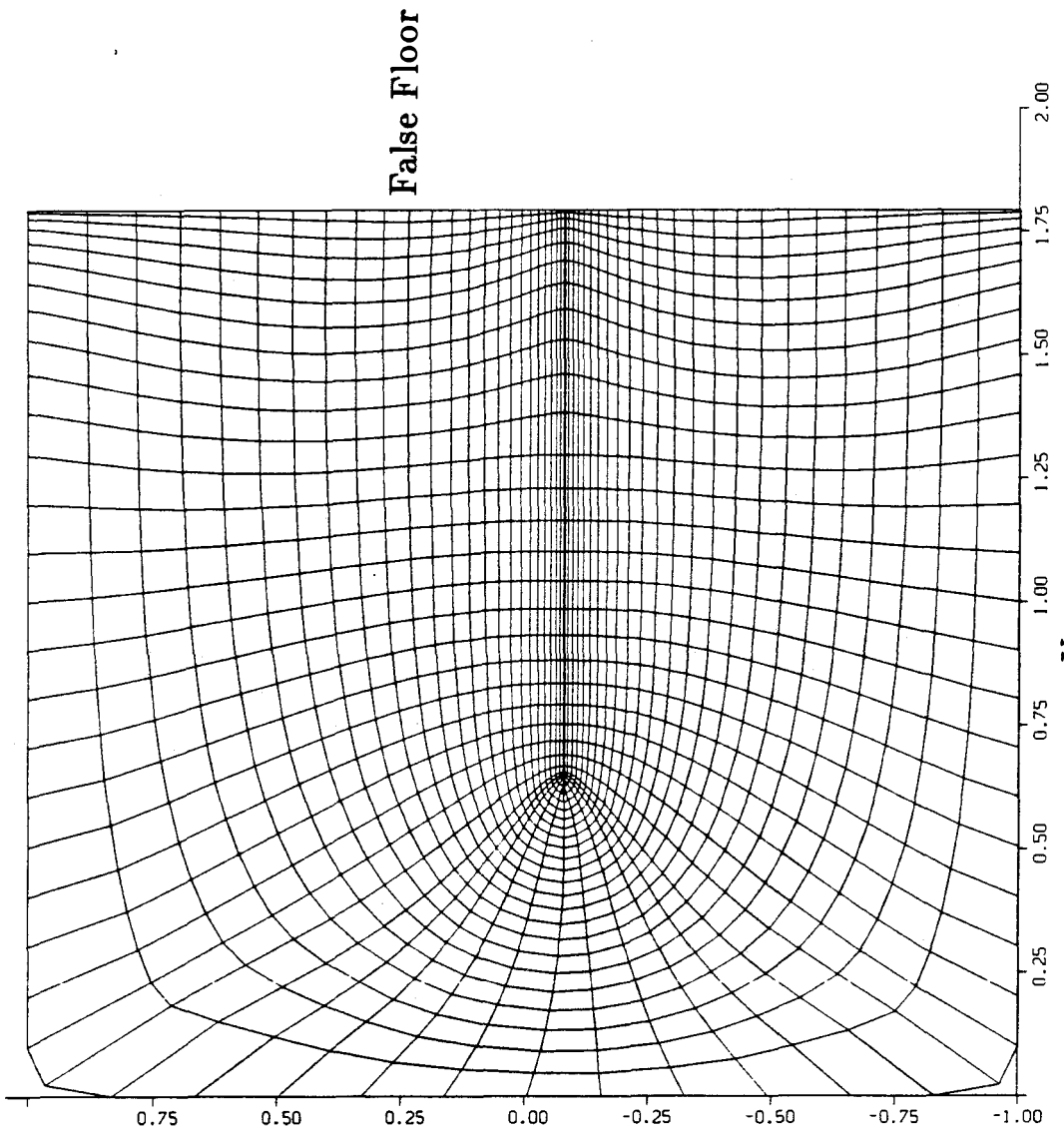

Figure VI.3 2D Slit Grid Which Occurs Upstream of the Foil.

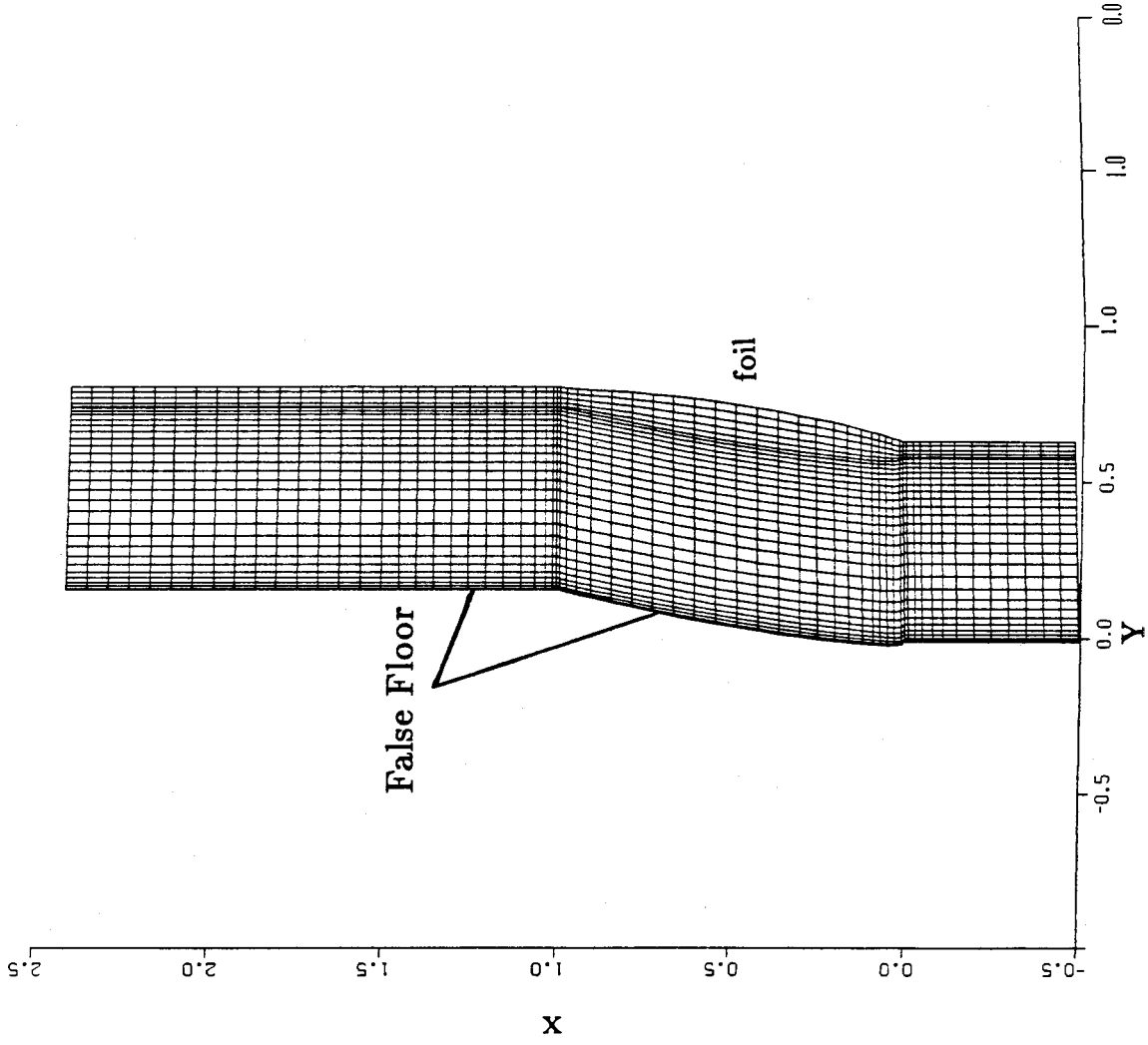

Figure VI.4 Perspective View of the Stacked Planar Grids "at the interior of the c."

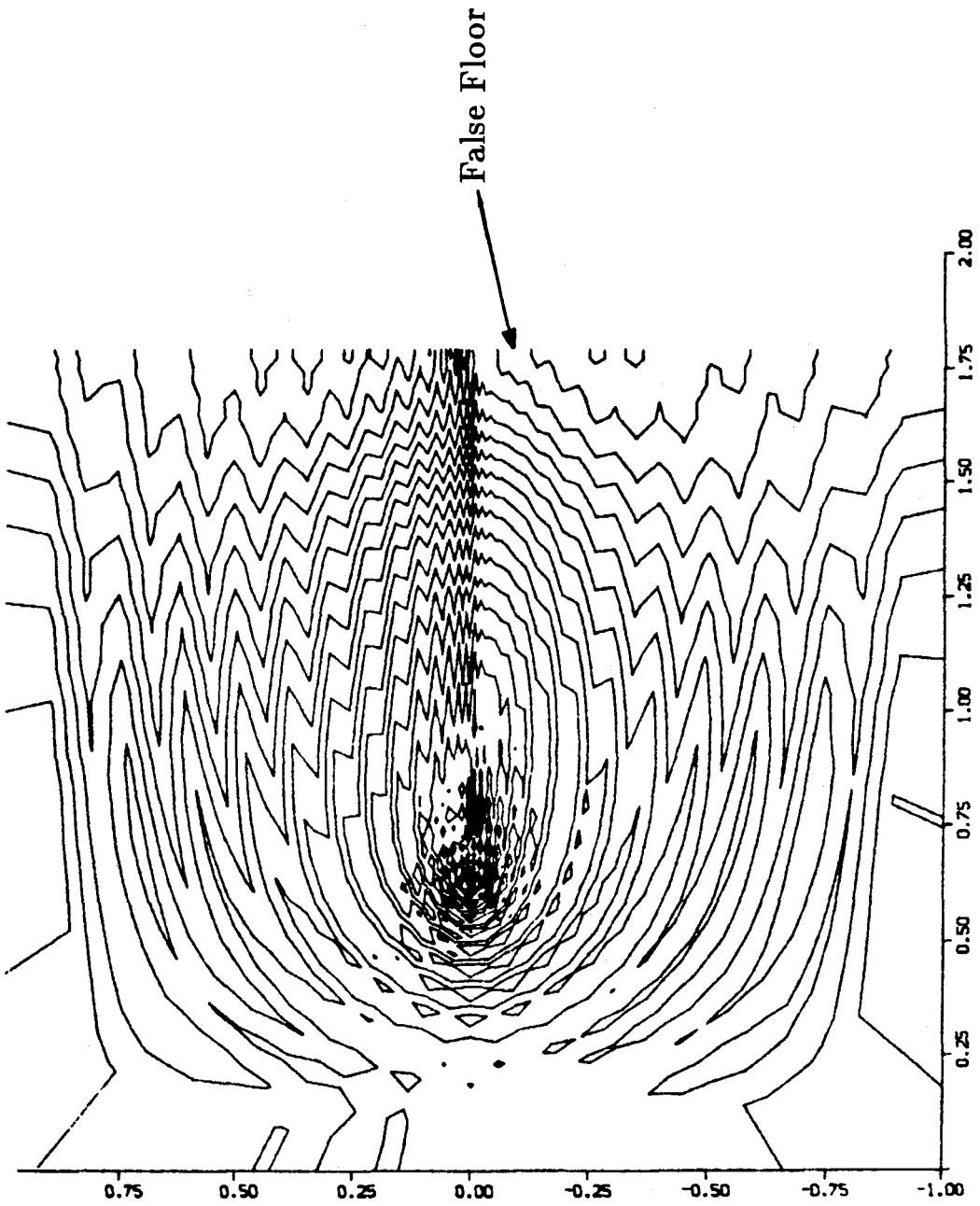

Figure VI.5 Upstream View of the Pressure Field at x/c=2, $\alpha = 10°$.

CHAPTER VII – SUMMARY AND CONCLUSIONS

This final chapter is divided into two parts– the first a summary of leading results and conclusions, and the second a free-ranging enumeration of other research topics spawned by the present work.

VII.1 Summary and Conclusions

The trailing vortex produced by a small aspect ratio wing was studied in the LTWT. Four different techniques– SFV, double pulsed holography of bubble tracers, single pulse holography of tailored air bubbles, and cavitation observation– were employed. These techniques allow for an examination of, respectively, the initial vortex rollup, the velocity distribution around the vortex, the vortex core pressure, and the cavitation behaviour. These observations have revealed facets of the trailing vortex flow unseen by previous investigators. This section is divided into summaries of three broad areas of research: single phase results, cavitating flow results, and tip geometry effects.

VII.1.1 Single Phase Results

Double pulsed holography of bubbles injected into and around the trailing vortex core allowed for **instantaneous** measurement of both the tangential and axial velocity.

These measurements revealed that the circulation around the trailing vortex is equal to the analytical bound wing circulation (White 1979) for $x/c \geq 2$. The normalized maximum tangential velocity, $(U_\theta)_{max}/U_\infty$, around the trailing vortex was virtually independent of x/c ($2 \leq x/c \leq 10$), and equal to 0.6 for $\alpha = 5°$, and 0.8 for $\alpha = 10°$. In the near field the core mean axial velocity, $\overline{U_{xc}}$, is elevated above the freestream velocity. Batchelor's (1964) theory yields accurate estimates of the extent to which $\overline{U_{xc}}$ is raised above U_∞. In the far field the core axial velocity tends to values less than the freestream velocity, U_∞, and is a non-monotonic function

of Re. Several possible explanations of the latter behaviour are listed in Chapter V.1.5 .

The core flow was found to be highly unsteady, particularly when $\overline{U_{xc}} > U_\infty$. The RMS core axial velocity has been measured to be as high as $0.2U_\infty$. Extremely unsteady core flow is often accompanied by vortical structures the author has labelled "vortex kinks." Vortex kinking is said to occur when a straight core undergoes an abrupt bend. After the bend the flow is locally at a large angle with respect to the freestream. A short distance farther downstream the flow rapidly turns to again be in the streamwise direction. A second vortical structure, labelled as "vortex stutter" (a linear core undergoes a rapid transition to a core in which the motion is not axially-directed and the core is spread laterally), has also been observed. These structures bear a striking resemblence to concentrated vortical structures in turbulent, rotating tank flows (Hopfinger et al. 1982), and to streamwise vortices in the free shear layer.

The core pressure was measured by introducing non-intrusive "tailored air bubbles" into the flow upstream of the foil. Their size when they lie in the core is related to the local, instantaneous, static pressure. The normalized core pressure, $\overline{p_c^*}$, determined using this technique is in fair agreement with an established correlation (Dunham 1979). The mean core pressure was also determined indirectly through integration of the radial momentum equation. This value of $\overline{p_c^*}$ was in much better agreement with the correlation. The normalized fluctuating pressure in the core, $\overline{(p_c')^*}$, is very high, perhaps as great as 2, albeit with a large error.

VII.1.2 Cavitating Flow Results

Cavitation inception was studied by examining the trailing vortex, under stroboscopic illumination, at different angles of attack. High speed flash photographs recorded the instantaneous appearance of both inception and developed cavitation.

Comparison between the measured core pressures and the inception index, $(\sigma_i)_{tv}$, supported the first order approximation that inception occurs when the

core pressure is reduced to the vapour pressure. The observed large value of the fluctuating core pressure explains both the appearance of inception prior to core pressure reduction to p_v, and the strong dependence of $(\sigma_i)_{tv}$ on the dissolved air content.

The mean core pressure was measured to be virtually independent of x/c. This fact elucidates the observation of long axial core cavitation when σ is reduced slightly below σ_i. The location of inception matches the location of maximum axial velocity fluctuation which, one speculates, should also be the location of maximum pressure fluctuation. It is apparent that the fluctuating core pressure is an important aspect of cavitation inception.

VII.1.3 Tip Geometry Effects

Two alternative tip geometries were compared with the basic rounded tip using surface flow visualization (which provides qualitative information about rollup and lift losses) and cavitation inception measurements.

Installation of a square cut tip reduced the tip inception index relative to that of the rounded tip. Flow separation from the sharp edge at the tip caused the shed vorticity to roll up into several vortices, rather than the single vortex characteristic of a rounded tip. The large core radius formed when these vortices wind together is a reasonable explanation of the decreased $(\sigma_i)_{tv}$.

Installation of a ring wing tip greatly reduced $(\sigma_i)_{tv}$. The reduction was caused primarily by redistributing, in the Trefftz plane, the shed vorticity about a line and circle, rather than the single line that characterizes rounded tips. Fortuitously, this redistribution caused most of the wing bound vorticity to be shed from the ring, decreasing the tip effect lift loss over the foil body.

VII.2 Suggestions for Future Work

Although the present work has clarified certain tip vortex phenomena, several require further investigation. This section is an enumeration of different areas of research one feels will be fruitful.

In the summary to Chapter V the author identified $\overline{U'_{xc}}$ and $\overline{U_{xc}}$(far field) as two "not understood" quantities. One suspects that both mean and fluctuating axial velocities could be explained analytically. An experimental study of Re effects on $\overline{U_{xc}}$ and $\overline{U'_{xc}}$ could be conducted by repeating the present work on similar, smaller chord, wings. The freestream turbulence explanation of Re effects could be conclusively ruled out by adjusting, or measuring, the freestream turbulence level in the tunnel.

Trailing vortices are the ideal settings in which to study vortex kinking. The advantages of trailing vortices over the other vortex kinking flows are threefold– the vortex position is known *a priori* (at x/c=2 the vortex barely meanders), the vortex circulation is known and readily adjusted, and (particularly in a towing tank) kink movement is easily followed in time. The author proposes that high speed photography be used to study vortex kink interactions. A criterion for the onset of vortex kinking could be established by careful adjustment of Γ_v, U_∞, and R_c. The role vortex kinks play in trailing vortex core unsteadiness might be better understood by such a study.

A great deal of additional work remains to be done with alternate tip geometries. The most obvious continuation of the present work would be to measure $U_\theta(R)$, $U_x(R)$, and p_c^* around the trailing vortex produced by different tips. Proper lift and drag measurements on the ring wing tip must be done. An attempt should be made to improve still further the ring wing tip performance by changing the length, diameter, cross-sectional shape, and camber of the ring. The optimization process would be greatly simplified if the local tip flow could be modelled numerically.

It has been seen that flow separation over the square cut tip causes shed vorticity to be rolled into several vortices. One suspects that judicious deployment of wing tip sails (e.g. between the vortices) could produce a larger R_c (by separating the vortices still further), thus diminishing σ_i.

REFERENCES

Abbot, I. H. and von Doenhoff, A. E. (1959), **Theory of Wing Sections**, Dover Publications Inc., New York.

Acosta, A. J. and Green, S. I. (1987), "Tip Vortex Suppression Device," patent action commenced.

Arakeri, V. H., Higuchi, H., and Arndt, R. E. A. (1986), "Analysis of Recent Tip Vortex Cavitation Inception Data," **21st ATTC**.

Arakeri, V. H. and Acosta, A. J. (1979), "Viscous Effects in the Inception of Cavitation," **ASME International Symposium on Cavitation Inception.**

Arndt, N. (1987), graduate student at the California Institute of Technology, personal communication.

Arndt, R. E. A., Higuchi, H., and Quadrelli, C. J. (1985), "Tip Vortex Cavitation," **ASME Cavitation and Multiphase Flow Forum**, pp. 61-64.

Arndt, R. E. A. (1981), "Cavitation in Fluid Machinery and Hydraulic Structures," **Ann. Rev. Fluid Mech.**, vol. 13, pp. 273-328.

Arndt, R. E. A. and George, W. K. (1979), "Pressure Fields and Cavitation in Turbulent Shear Flow," **12th Symp. on Naval Hydrodynamics**, pp. 327-339.

Arndt, R. E. A. (1976), "Cavitation on Model Propellors with Boundary Layer Trips," **ASME Cavitation and Multiphase Flow Forum**, pp. 30-32.

Baker, G. R., Barker, S. J., Bofah, K. K., and Saffman, P. G. (1974), "Laser Anemometer Measurements of Trailing Vortices in Water," **J. Fluid Mech.**, vol. 65, part 2, pp. 325-336.

Barber, M. R., et al. (1975), "Flight Test Investigation of the Vortex Wake Characteristics Behind a Boeing 727 During Two-Segment and Normal ILS Approaches," **NASA TM X-62,398.**

Batchelor, G. K. (1967), **An Introduction to Fluid Dynamics**, Cambridge University Press.

Batchelor, G. K. (1964), "Axial Flow in Trailing Line Vortices," **J. Fluid Mech.**, vol. 20, part 4, pp. 645-658.

Beam, R. M. and Warming, R. F. (1976), "An Implicit Finite Difference Algorithm for Hyperbolic Systems in Conservation-Law Form," **J. Comp. Phys.**, vol. 22, pp. 87-110.

Bernal, L. P. and Roshko, A. (1986), "Streamwise Vortex Structure in Plane Mixing Layers," **J. Fluid Mech.**, vol. 170, pp. 499-525.

Betz, A. (1933), "Behavior of Vortex Systems," **NACA TM 713.**

Billet, M. L. and Holl J. W. (1979), "Scale Effects on Various Types of Limited Cavitation," **Int. Symp. on Cavitation Inception**, pp. 11-23.

Brooks, T. F. and Marcolini, M. A. (1984), "Airfoil Tip Vortex Formation Noise," **AIAA #84-2308.**

Brown, G. L. (1988), Director of Aeronautical Research Laboratory, Melbourne, Australia, personal communication.

Brown, G. L. and Roshko, A. (1974), "On Density Effects and Large Structure in Turbulent Mixing Layers," **J. Fluid Mech.**, vol. 64, pp. 775-816.

Chang, J. L. C., Kwak, D., and Dao, S. C. (1985), "A Three Dimensional Incompressible Flow Simulation Method and its Application to the Space Shuttle Main Engine, Part 1, Laminar Flow," **AIAA #85-0175.**

Chigier, N. A. (1974), "Vortexes in Aircraft Wakes," **Scientific American**, March 1974, pp. 76-83.

Chigier, N. A. and Corsiglia, V. R. (1972), "Wind Tunnel Studies of Wing Wake Turbulence," **AIAA #72-41.**

Chigier, N. A. and Corsiglia, V. R. (1971), "Tip Vortices – Velocity Distributions," **NASA TM X-62,087.**

Chorin, A. J. (1967), "A Numerical Method for Solving Incompressible Viscous Flow Problems," **J. Comp. Physics**, vol. 2, pp. 12-26.

Corsiglia, V. R., Schwing, R. G., and Chigier, N. A. (1973), "Rapid Scanning, Three-Dimensional Hot-Wire Anemometer Surveys of Wing-Tip Vortices," **J. Aircraft**, vol. 10, no. 12, pp. 752-757.

Devoss, D. (1986), "The Race to Recover the Cup," **Los Angeles Times Magazine**, Aug. 31, pp. 9+.

Donaldson, C. and Bilanin, A. J. (1975), "Vortex Wakes of Conventional Aircraft," **AGARD-AG-204.**

Donaldson, C. (1971), "A Brief Review of the Aircraft Trailing Vortex Problem," **AFOSR TR-71-1910.**

Dunham, J. (1979), "The Static Pressure in a Vortex Core," **Aeronautical J.**, pp. 402-406.

Durand, W. F. (ed.) (1963), **Aerodynamic Theory**, Dover Publications, Inc., New York, vol. III, pp. 280-306.

Epstein, P. S. and Plesset, M. S. (1950), "On the Stability of Gas Bubbles in Liquid-Gas Solutions," **J. Chem. Phys.**, vol. 18, no. 11, pp. 1505-1509.

Flechner, S. G., Jacobs, P. F., and Whitcomb, R. T. (1976), "A High Subsonic Speed Wind Tunnel Investigation of Winglets on a Representative Second-Generation Jet Transport Wing," **NASA TN D-8264.**

Francis, M. S. and Kennedy, D. A. (1979), "Formation of a Trailing Vortex," **J. Aircraft**, vol. 16, no. 3, pp. 148-154.

Gates, E. M. and Acosta, A. J. (1978), "Some Effects of Several Free-stream Factors on Cavitation Inception on Axisymmetric Bodies," **12th Symposium on Naval Hydrodynamics**, Washington, D.C., pp. 86-108.

Gates, E. M. (1977), "The Influence of Freestream Turbulence, Freestream Nuclei Populations and a Drag-reducing Polymer on Cavitation Inception on Two Axisymmetric Bodies," Ph.D. thesis, California Institute of Technology.

George, A. R., Najjar, F. E., and Kim, Y. N. (1980), "Noise Due to Tip Vortex Formation on Lifting Rotors," **AIAA #80-1010.**

Gostelow, J. P. and Wong, K. K. (1985), "Observations of Impeller Tip Cavitation in an Axial Flow Pump," **ASME Cavitation and Multiphase Flow Forum.**

Green, S. I. (1988), "Trailing Vortex Core Unsteadiness – An Exploratory Study of Reynolds Number Effects," **National Fluid Dynamics Congress**, Cincinatti, Ohio.

Green, S. I., Acosta, A. J., and Akbar, R. (1988), "The Influence of Tip Geometry on Trailing Vortex Rollup and Cavitation," **ASME Cavitation and Multiphase Flow Forum.**

Green, S. I. (1987), "Three Tip Vortex Examination Techniques," **International Symposium on Cavitation Research and Techniques**, pp. 155-160.

Haberman, W. L. and Morton, R. K. (1953), Taylor Model Basin, Washington, Report #802.

Hackett, J. E. (1981), "Vortex Drag Reduction by Diffusing Vanes – Design for the 'Thrush' Agricultural Aircraft," **Society of Automotive Engineers**, Business Meeting and Exposition, Wichita, KS.

Hanson, D. B. (1986), "Propellor Noise Caused by Blade Tip Radial Forces," **AIAA #86-1892.**

Hasimoto, H. (1972), "A Soliton on a Vortex Filament," **J. Fluid Mech.**, vol. 51, part 3, pp. 477-485.

Hastings, E. C., Patterson, J. C., Shanks, R. E., Champine, R. A., Copeland, W. L., and Young, D. C. (1975), "Development and Flight Tests of Vortex Attenuating Splines," **NASA TN D-8083.**

Higuchi, H., Quadrelli, J. C., and Farell, C. (1986)a, "Vortex Roll-up from an Elliptical Wing at Moderately Low Reynolds Numbers," **AIAA #86-0562.**

Higuchi, H., Jiang, S. H., Rogers, M. F., and Arndt, R. E. A. (1986)b, "Cavitation Inception in Trailing Vortex from a Hydrofoil," **IAHR Symposium**, Montreal.

Hoeijmakers, H. W. M. (1983), " Computational Vortex Flow Aerodynamics," **AGARD Conference Proceedings #342**, pp. 18.1-18.35.

Holl, J. W., Arndt, R. E. A., Billet, M. L. (1972), "Limited Cavitation and the Related Scale Effects Problem," **JSME Proc. 2nd Int. Symp. Fluid Mechanics and Fluidics**, Tokyo, pp. 303-314.

Holl, J. W. (1970), "Nuclei and Cavitation," **ASME J. Basic Engg.**, pp. 681-688.

Holl, J. W. (1968), "Sources of Cavitation Nuclei," **15th American Towing Tank Conference**, Ottawa, Canada.

Holman, J. P. and Moore, G. D. (1961), "An Experimental Study of Vortex Chamber Flow," **ASME J. Basic Engg.**, pp. 632.

Holst, T. L., et al. (1985), " Numerical Solution of Transonic Wing Flows Using an Euler/ Navier-Stokes Zonal Approach," **AIAA #85-1640.**

Hopfinger, E. J., Browand, F. K., and Gagne, Y. (1982), "Turbulence and Waves in a Rotating Tank," **J. Fluid Mech.**, vol. 125, pp. 505-534.

Huang, T. (1987), David Taylor Naval Ship Research and Development Center, personal communication.

Jarvinen, P. O. (1973), "Aircraft Wing Tip Modification," **J. Aircraft**, vol. 10, no. 1, pp. 63-64.

Kantha, H. L., Lewellen, N. S., and Durgin, F. H. (1972), "Response of a Trailing Vortex to Axial Injection into the Core," **J. Aircraft**, vol. 9, no. 3, pp. 254-256.

Kantha, H. L., Lewellen, W. S., and Durgin, F. H. (1971), "Qualitative Responses of a Vortex Core to Tip Blowing and Intersecting Airfoils," **ASRL TR 153-4.**

Katz, J. (1984), "Cavitation Phenomena Within Regions of Flow Separation," **J. Fluid Mech.**, vol. 140, pp. 397-436.

Katz, J., O'Hern, T. J., and Acosta, A. J. (1984), "An Underwater Holographic Camera System for Detection of Microparticulates," **ASME Cavitation and Multiphase Flow Forum.**

Katz, J. (1981), "Cavitation Inception in Separated Flows," Ph.D. Thesis, California Institute of Technology, Report No. 183-5.

Katz, J. (1979), "Construction and Calibration of a Holographic Camera Designed for Microbubble Observation in Cavitation Research," California Institute of Technology, Report #183-4.

Kaul, U. (1987), NASA Ames Associate, personal communication.

Knapp, R. T., Daily, J. W., and Hammitt, F. G. (1970), **Cavitation**, McGraw-Hill Inc., New York.

Kreyszig, E. (1972), **Advanced Engineering Mathematics**, John Wiley and Sons Inc., New York.

Kuiper, G. (1985), "Reflections on Cavitation Inception," **ASME Cavitation and Multiphase Flow Forum**, pp. 1-13.

Kuiper, G. (1981), **Cavitation Inception on Ship Propellor Models**, H. Veenmanen Zonen B.V., Wageningen, pp. 130-159.

Kwak, D. (1987), NASA Ames, personal communication.

Kwak, D., Chang, J. L. C., Shanks, S. P., and Chakravarthy, S. (1986), "A Three-Dimensional Incompressible Navier-Stokes Flow Solver Using Primitive Variables," **AIAA J.**, vol.24, no.3, pp. 390-396.

Kwak, D., Chang, J. L. C., Shanks, S. P., and Chakravarthy, S. (1984), "An Incompressible Navier-Stokes Flow Solver in Three-Dimensional Curvilinear Coordinate Systems Using Primitive Variables," **AIAA #84-0253**.

Levich, V. G. (1962), **Physico-chemical Hydrodynamics**, Prentice-Hall, London.

Lewy, S. and Caplot, M. (1982), "Theoretical and Experimental Study of Helicopter Rotor Noise," **ONERA TP 1982-74**.

Lin, S.-J., Levy, R. and Shamroth, S. J. (1986), "A Three-Dimensional Viscous Flow Analysis for the Helicopter Tip Vortex Generation Process about Square and Round Tipped Blades," **AIAA #86-0560**.

Lin, S.-J., Levy, R., Shamroth, S. J., and Govindan, T. R. (1985), "A Three-Dimensional Viscous Flow Analysis for the Helicopter Tip Vortex Generation Problem," **NASA CR-3909**.

Logan, A. H. (1971), "Vortex Velocity Distributions at Large Downstream Distances," **J. Aircraft**, vol.8, no.11, pp. 930-932.

Maltby, R. L. (1962), "Flow Visualization in Wind Tunnels Using Indicators," **AGARDograph 70.**

Martin, R. M., Elliott, J. W., and Head, D. R. (1984), "Comparison of Experimental and Analytical Predictions of Rotor Blade Vortex Interactions Using Model Scale Acoustic Data," **AIAA #84-2269.**

Maskew, B. (1976), "A Quadrilateral Vortex Method Applied to Configurations with High Circulation," **NASA SP-405.**

Mason, W. H. and Marchman, J. F. (1972), "Far Field Structure of an Aircraft Trailing Vortex, Including Effects of Mass Injection," **NASA CR-62078.**

McCormick, B. W., Tangler, J. L., and Sherrieb, H. E. (1968), "Structure of Trailing Vortices," **J. Aircraft**, vol. 5, no. 3, pp. 260-267.

McCormick, B. W. (1962), "On Cavitation Produced by a Vortex Trailing from a Lifting Surface," **ASME, J. Basic Eng.**, vol. 84, pp. 369-379.

McInerny, S. A., Meecham, W. C., and Soderman, P. (1986), "An Experimental Investigation of Wing Tip Turbulence with Applications to Aerosound," **AIAA #86-1918.**

Milne-Thomson, L. M. (1968), **Theoretical Aerodynamics**, van Nostrand, New York, pp. 188-203.

Moore, D. W. (1974), "A Numerical Study of the Roll-up of a Finite Vortex Sheet," **J. Fluid Mech.**, vol. 63, part 2, pp. 225-235.

Moore, D. W. and Saffman, P. G. (1973), "Axial Flow in Laminar Trailing Vortices," **Proc. Roy. Soc. Lond. A**, vol. 333, pp. 225-235.

Moore, D. W. (1963), "The Boundary Layer on a Spherical Gas Bubble," **J. Fluid Mech.**, vol. 16, pp. 161-176.

Mosher, M. and Peterson, R. L. (1983), "Acoustic Measurements of a Full-Scale Coaxial Helicopter," **AIAA #83-0722.**

Nielsen, J. N. and Schwind, R. G. (1971), "Decay of a Vortex Pair Behind an Aircraft," in **Aircraft Wake Turbulence and its Detection**, Plenum Press, New York, pp. 413-454.

Noordzij, L. (1977), "A Note on the Scaling of Tip Vortex Cavitation Inception," **International Shipbuilding Progress**, no. 24, pp. 233-236.

O'Hern, T. J. (1987), "Cavitation Inception Scale Effects: I.Nuclei Distributions in Natural Waters; II. Cavitation Inception in a Turbulent Shear Flow," Ph.D. Thesis, California Institute of Technology, Report No. 183-15.

Ooi, K. K. (1985), "Scale Effects of Cavitation Inception in Submerged Water Jets: A New Look," **J. Fluid Mech.**, vol. 151, pp. 367-390.

Ooi, K. K. and Acosta, A. J. (1983), "The Utilization of Specially Tailored Air Bubbles as Static Pressure Sensors in a Jet," **ASME #83-FE-34.**

Ooi, K. K. (1981), "Scale Effects on Cavitation Inception in Submerged Jets," Ph.D. Thesis, California Institute of Technology, Report No. 183-6.

Orloff, K. L. and Grant, G. R. (1973), "The Application of a Scanning Laser Doppler Velocimeter to Trailing Vortex Definition and Alleviation," **AIAA #73-680.**

Pearson, H. A. (1937), "Empirical Corrections to the Span Load Distribution at the Tip," **NACA TN-606.**

Phillips, W. R. C. (1981), "The Turbulent Trailing Vortex During Roll-up," **J. Fluid Mech.**, vol. 105, pp. 451-467.

Platzer, G. P. and Sounders, W. G. (1979), "Tip Vortex Cavitation Delay with Application to Marine Lifting Surfaces, a Literature Survey," **DTNSRDC 79/051.**

Prandtl, L. (1920)a, "Theory of Lifting Surfaces Part I," **NACA TN #9.**

Prandtl, L. (1920)b, "Theory of Lifting Surfaces Part II," **NACA TN #10.**

Rae, W. D. and Pope, A. (1984), **Low Speed Wind Tunnel Testing**, John Wiley and Sons, New York.

Raines, D. A. (1954), "Tip Clearance Flows in Axial Compressors and Pumps," Report M.E.-5, Jet Propulsion Center, California Institute of Technology.

Raj, P. and Gray, R. B. (1979), "Computation of Three-Dimensional Potential Flow Using Surface Vorticity Distribution," **J. Aircraft**, vol.16, no.3, pp. 162-169.

Rogers, S. E., Kwak, D., and Chang, J. L. C. (1987), "INS3D–An Incompressible Navier-Stokes Code in Generalized Three-Dimensional Coordinates," **NASA TM-100012.**

Rogers, S. E., Chang, J. L. C., and Kwak, D. (1986), "A Diagonal Algorithm for the Method of Pseudocompressibility," **AIAA #86-1060.**

Rossow, V. J. (1975), "Survey of Computational Methods for Lift-Generated Wakes," **NASA SP-347**, pp. 897-923.

Ruden, P. (1947), "Investigation of a Single-Stage Axial Fan," **NACA TM-1062.**

Scheiman, J. and Shivers, J. (1971), "Exploratory Investigation of the Structure of the Tip Vortex of a Semispan Wing for Several Wing-Tip Modifications," **NASA TN D-6101.**

Schreier, J. (1982), "Fluctuating Forces and Rotor Noise Due to Main Rotor – Tail Rotor Interaction," **Association Aeronautique et Astronautique de France, 8th European Rotorcraft Forum.**

Snedeker, R. S. (1972), "Effect of Air Injection on the Torque Produced by a Trailing Vortex," **J. Aircraft**, vol. 9, no. 9, pp. 682-686.

Sobota, T. (1987)a, "An Experimental and Numerical Investigation of Swirling Flows in a Rectangular Nozzle," Ph.D. Thesis, California Institute of Technology.

Sobota, T. (1987)b, California Institute of Technology, personal communication.

Sorenson, R. L. (1980), "A Computer Program to Generate Two-Dimensional Grids About Airfoils and Other Shapes by the Use of Poisson's Equation," **NASA TM-81198.**

Spillman, J. J. (1978), "The Use of Wing Tip Sails to Reduce Vortex Drag," **Aeronautical J.**, pp. 387-395.

Sponagle, N. C. and Leggat, L. J. (1984), "The Spatial Distribution of Acoustic Sources at Propellor Vortex Cavitation Inception," **ASME International Symposium on Cavitation Inception**, pp. 191-198.

Spreiter, J. R. and Sacks, A. H. (1951), "The Rolling Up of the Trailing Vortex Sheet and its Effect on the Downwash Behind Wings," **J. Aero. Sciences**, pp. 21-32.

Srinivasan, G. R., McCroskey, W. J., Baeder, J. D., and Edwards, T. A. (1986), "Numerical Simulation of Tip Vortices of Wings in Subsonic and Transonic Flows," **AIAA 86-1095.**

Steger, J. L. and Kutler, P. (1977), "Implicit Finite-Difference Procedures for the Computation of Vortex Wakes," **AIAA Journal**, vol. 15, no. 4, pp. 581-590.

Summa, J. M. (1982), "Advanced Rotor Analysis Methods for the Aerodynamics of Vortex/Blade Interactions in Hover," **Association Aeronautique et Astronautique de France, 8th European Rotorcraft Forum.**

Sung, C.-H., Lin C.-W., and Hung, C. M. (1988), "An Explicit Runge-Kutta Method for 3D Turbulent Incompressible Flows," to be published.

Takami, H. (1964), "A Numerical Experiment with Discrete Vortex Approximation with Reference to the Rolling Up of a Vortex Sheet," Stanford University, **SUDAER 202.**

Thompson, D. H. (1975), "Experimental Study of Axial Flow in Wing Tip Vortices," **J. Aircraft**, vol. 12, no. 11, pp. 910-911.

Vaczy, C. M. and McCormick, D. C. (1987), "A Study of the Leading Edge Vortex and Tip Vortex on Prop-Fan Blades," **J. Turbomachinery**, vol. 109, pp. 325-331.

Vortex Wake Alleviation Workshop (1980), NASA Langley Research Center, Hampton, VA.

Webber, G. W. and Dansby, T. (1983), "Wing Tip Devices for Energy Conservation and Other Purposes – Experimental and Analytical Work in Progress at the Lockheed-Georgia Company," **Can. Aero. Space J.**, vol. 29, no. 2, pp. 105-120.

Westwater, F. L. (1935), "Rolling Up of the Surface Discontinuity Behind an Aerofoil of Finite Span," **Aero. Res. Counc. R. and M. #1962.**

Whitcomb, R. T. (1976), "A Design Approach and Selected Wind Tunnel Results at High Sub-sonic Speed for Wing-Tip Mounted Winglets," **NASA TN D-8260.**

Wickens, R. H. (1980), "Wake Vortex Trajectories of Low Flying Spray Aircraft," **Can. Aero. Space J.**, vol. 26, no. 1, pp. 41-45.

Widnall, S. E. and Wolf, T. L. (1980), "Effect of Tip Vortex Structure on Helicopter Noise Due to Blade-Vortex Interaction," **J. Aircraft**, vol. 17, pp. 705-711.

Zalay, A. D. (1976), "Hot-Wire and Vorticity Meter Wake Vortex Surveys," **AIAA J.**, vol. 15, no. 5, pp. 694-696.

APPENDIX A – CATALOGUE OF SFV PHOTOGRAPHS

This Appendix serves two purposes– as a reference for comparison with numerical simulations, and as an elaboration of the results described in Chapter IV.

Figure A.1.1 shows, at $\alpha = 15°$, a suction surface separated flow over the inboard 3/4 of the wing near the floor. The spanwise extent of separation agrees with the location of separated flow leading edge cavitation (refer to Chapter IV.4). The separated flow is highly three-dimensional, with flow reattachment not occurring until near the 3/4 chord point. The pressure surface flow is unaffected by the suction surface separation. The chordwise orientation of streaklines near the camberline in the inboard view provides additional support for the hypothesized streamline pattern of Figure IV.2 .

The orientation of "pressure side" streaklines in Figure A.2.5 suggests fluid entrainment from the separated flow region edges into the center. Notice again the inhibition of separation by the tip, and the unsteady appearance of the flow near reattachment. This latter is indicative of the unsteady wake shed at this angle of attack.

Figure A.3.1 provides evidence of a wing/wall interaction rôle in separation. In particular, observe the absence of separation in the middle (spanwise) of the foil where the tip effect is very small. Rather, separation occurs near the wall and disturbs the flow outboard from the wall.

Figures A.3.2 and A.3.3 confirm, for AR$\geq$ 2.3 at reasonable α, that the tip flow is independent of the aspect ratio. This result is in agreement with McCormick's (1962) study, wherein $(\sigma_i)_{tv}$ was found to be AR independent.

Figures A.4.1–A.4.4 should be very interesting to researchers involved in the modelling of separated flows. The flow has many fascinating features including: unsteadiness, three-dimensionality, strong dependence on α in terms of both spanwise and chordwise extent, tip separation suppression effect, and wall effect.

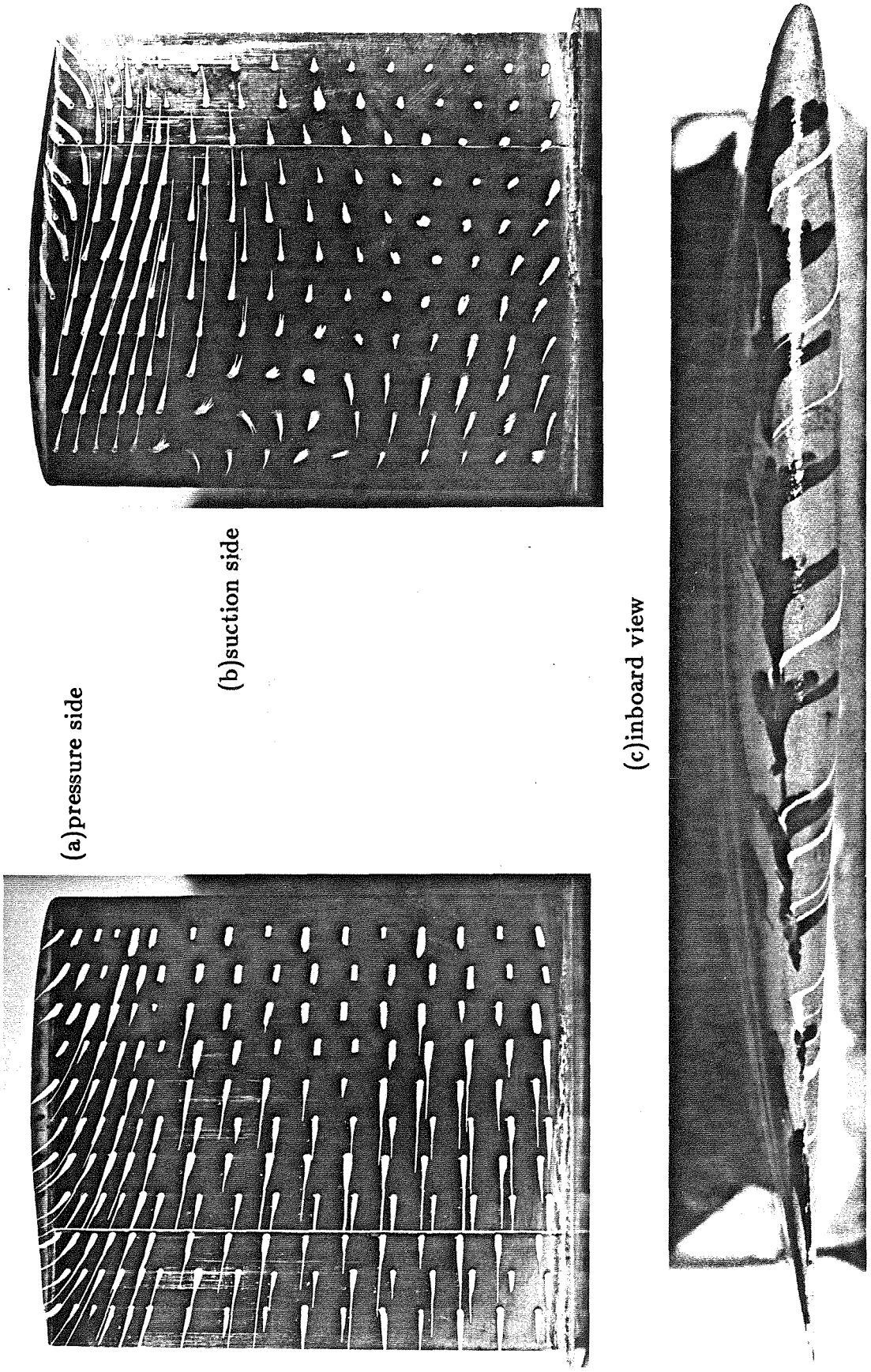

Figure A.1.1(a,b,c) SFV of 64-309 foil at $\alpha = 15°$.

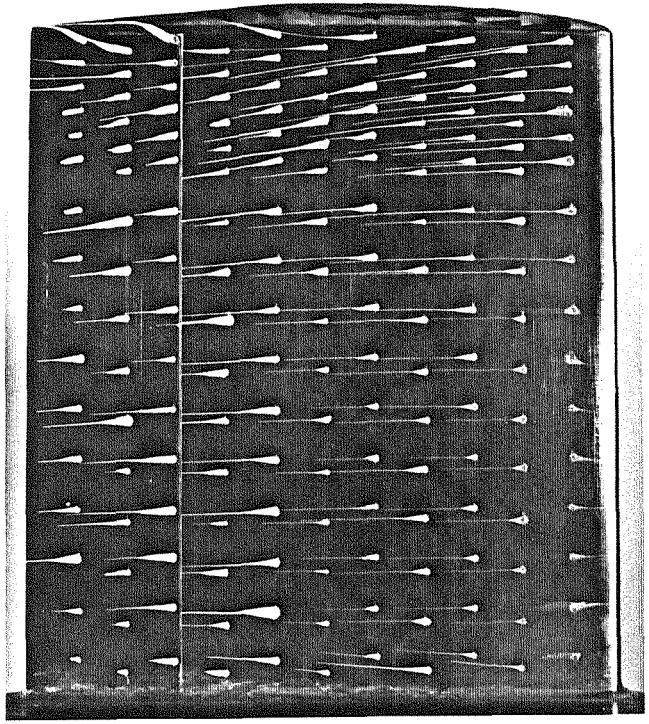

(a)pressure side

(b)suction side

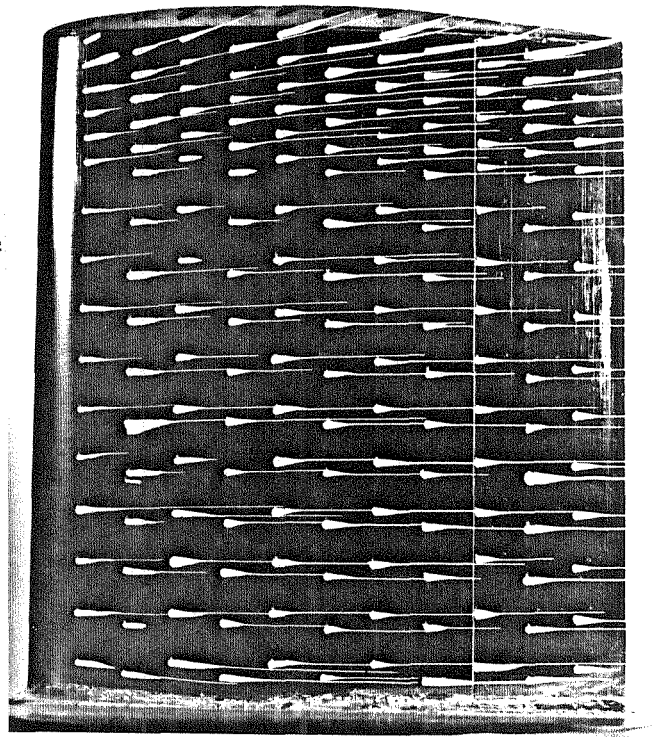

(c)inboard view

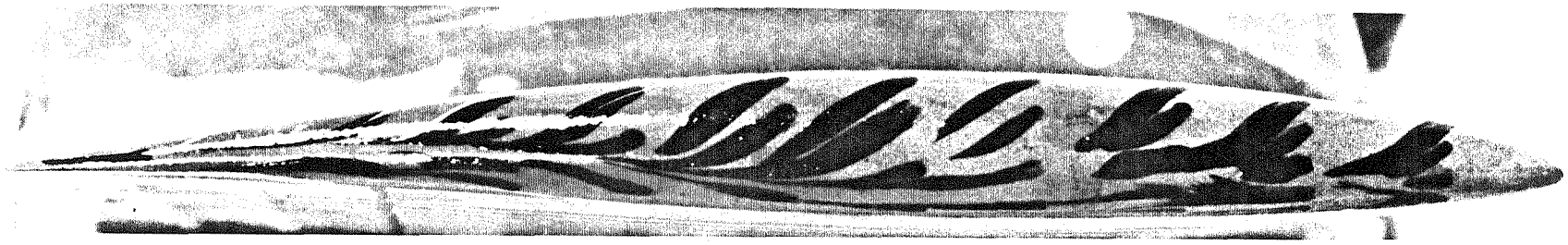

Figure A.1.2(a,b,c) SFV of 64-309 foil at $\alpha = -7°$.

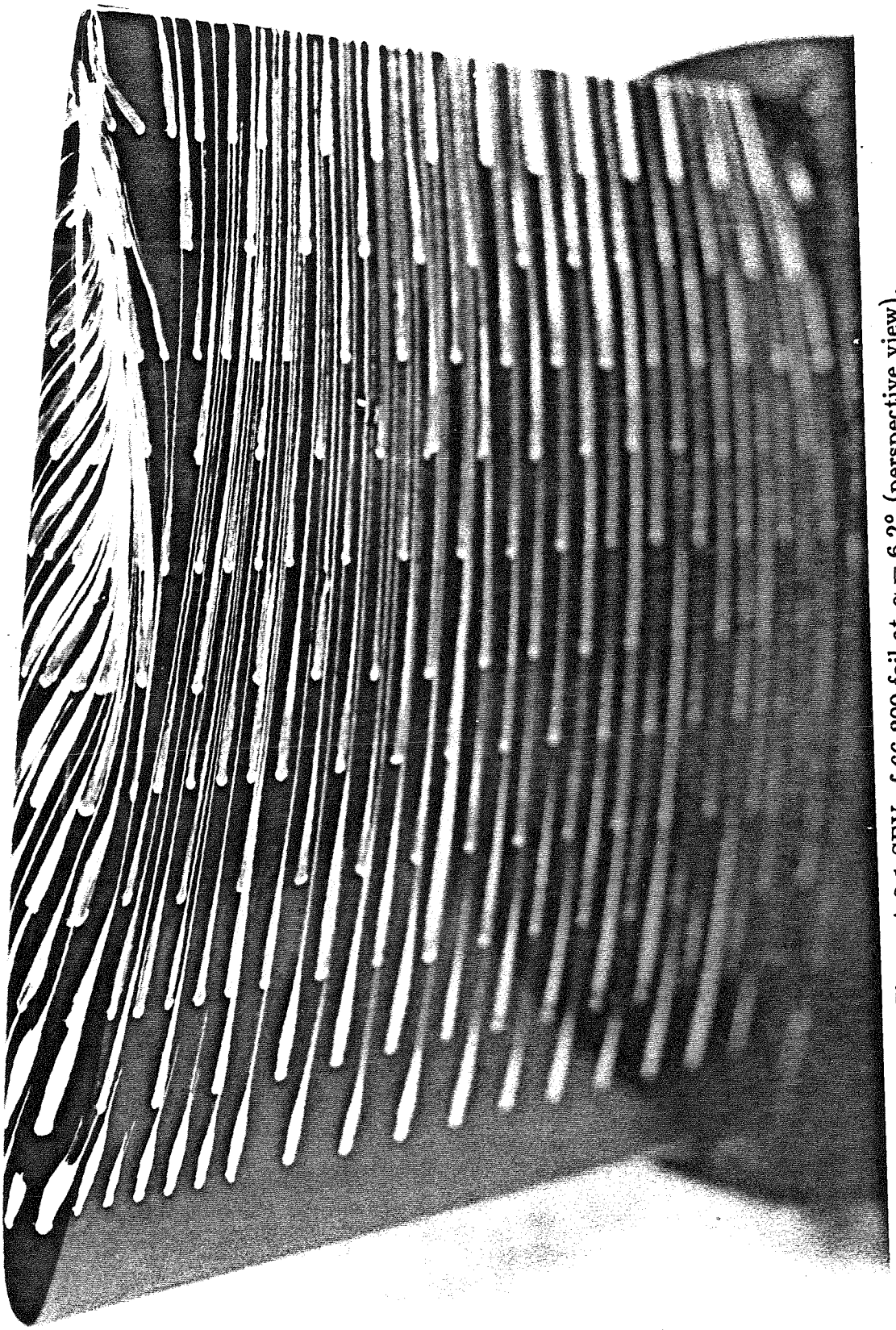

Figure A.2.1 SFV of 66-209 foil at $\alpha = 6.2°$ (perspective view).

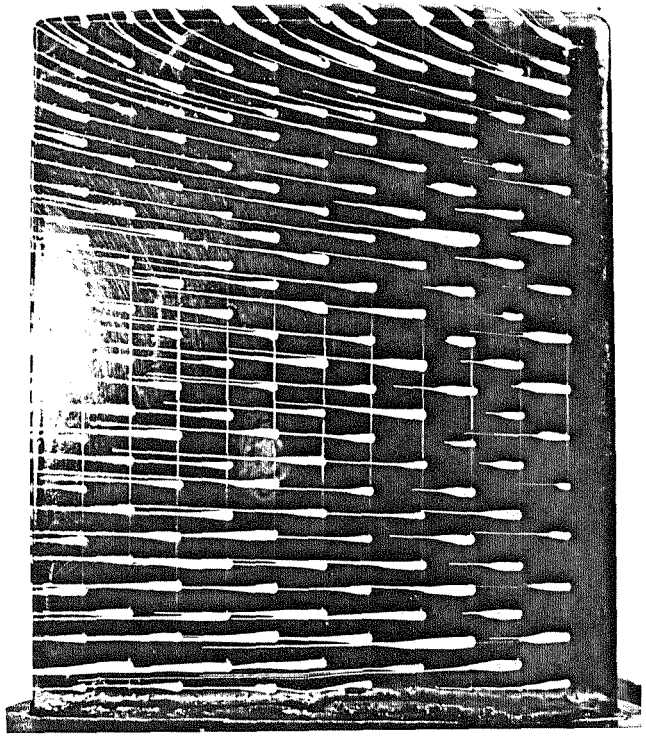

(a)pressure side

(b)suction side

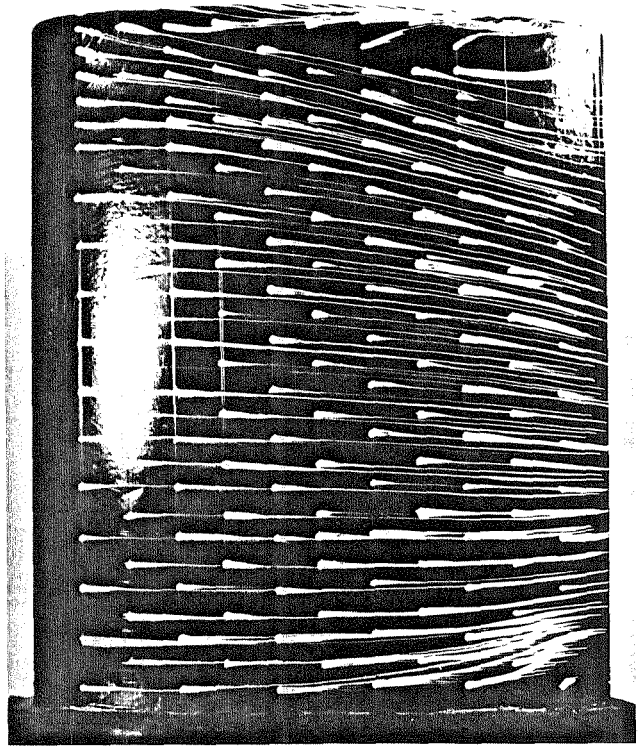

(c)inboard view

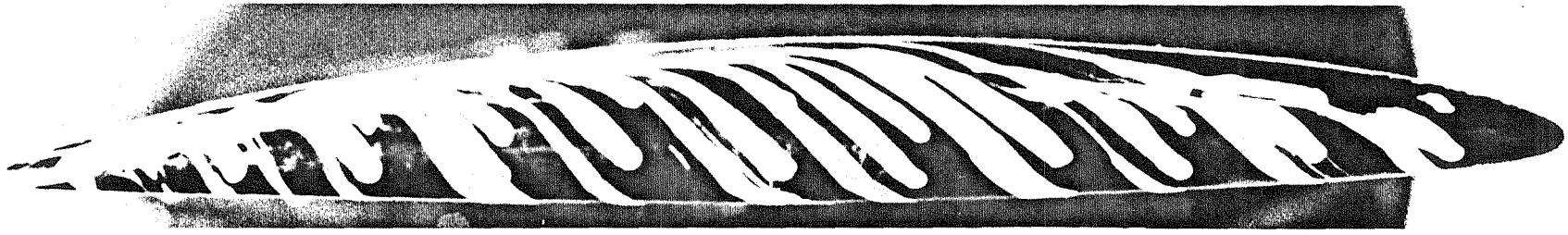

Figure A.2.2(a,b,c) SFV of 66-209 foil at $\alpha = 10.1°$.

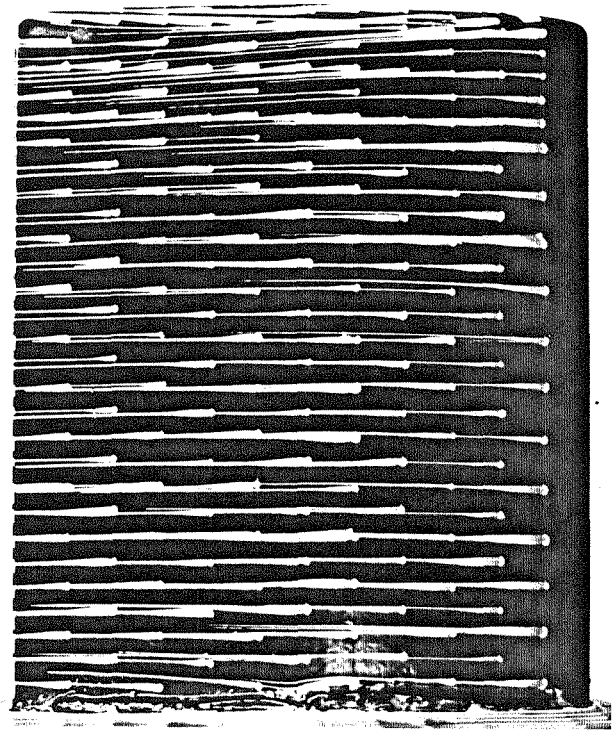

(a) pressure side

(b) suction side

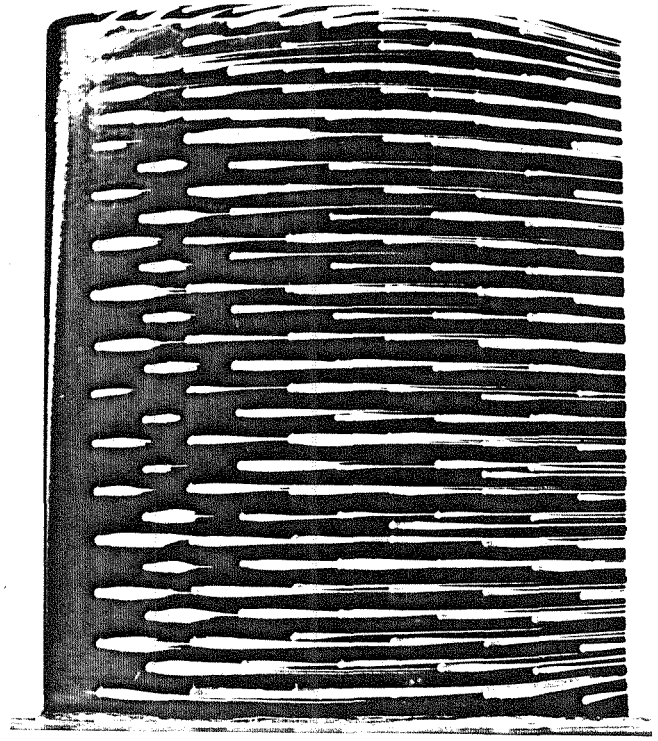

(c) inboard view

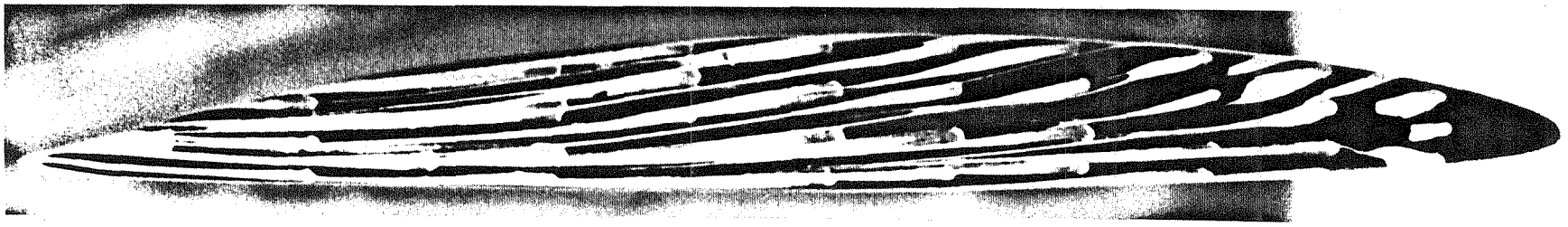

Figure A.2.3(a,b,c) SFV of 66-209 foil at $\alpha = -3°$.

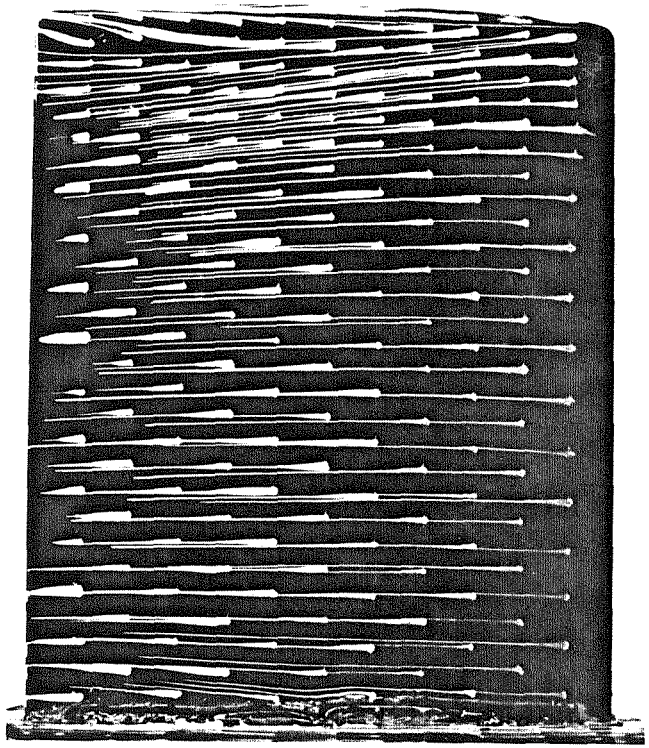

(a)pressure side

(b)suction side

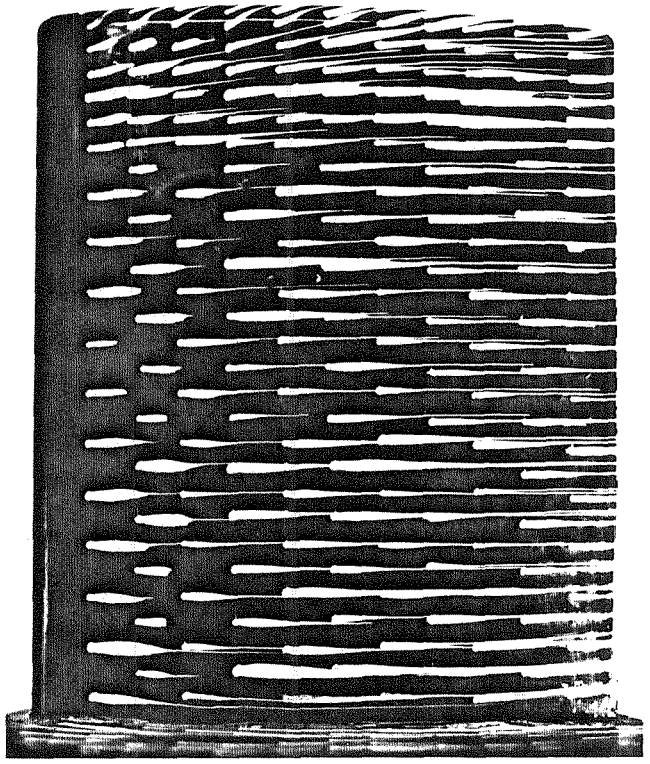

(c)inboard view

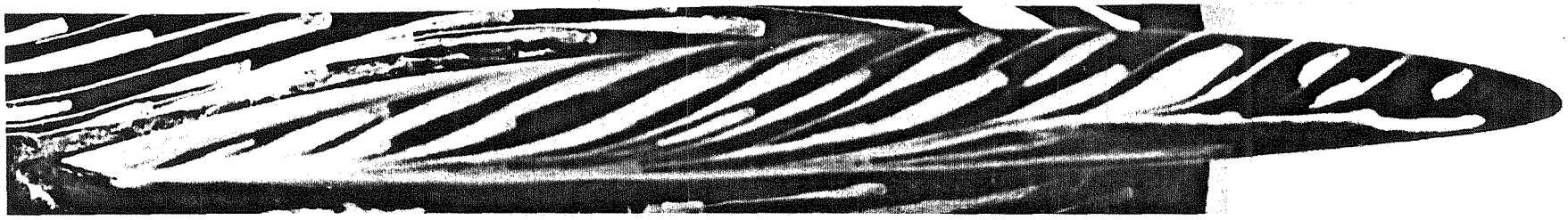

Figure A.2.4(a,b,c) SFV of 66-209 foil at $\alpha = -6°$.

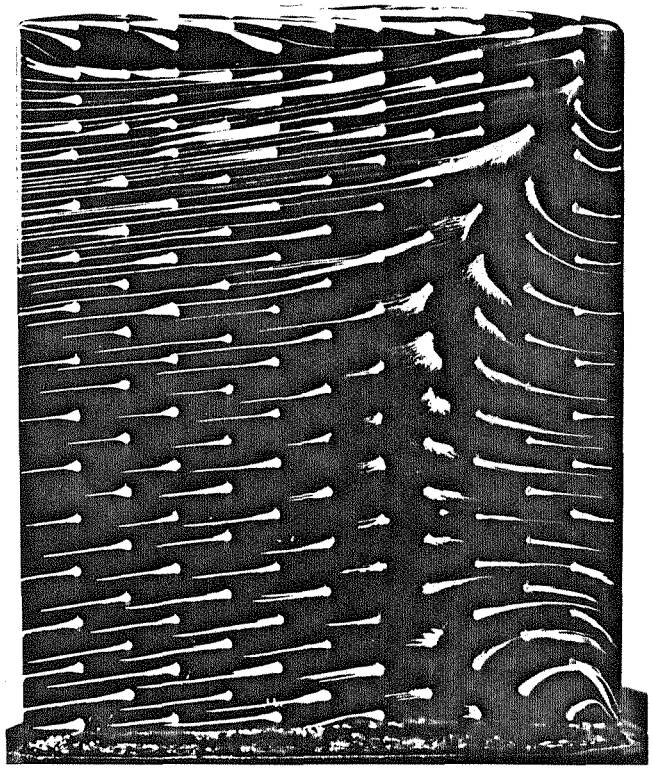

(a)pressure side

(b)suction side

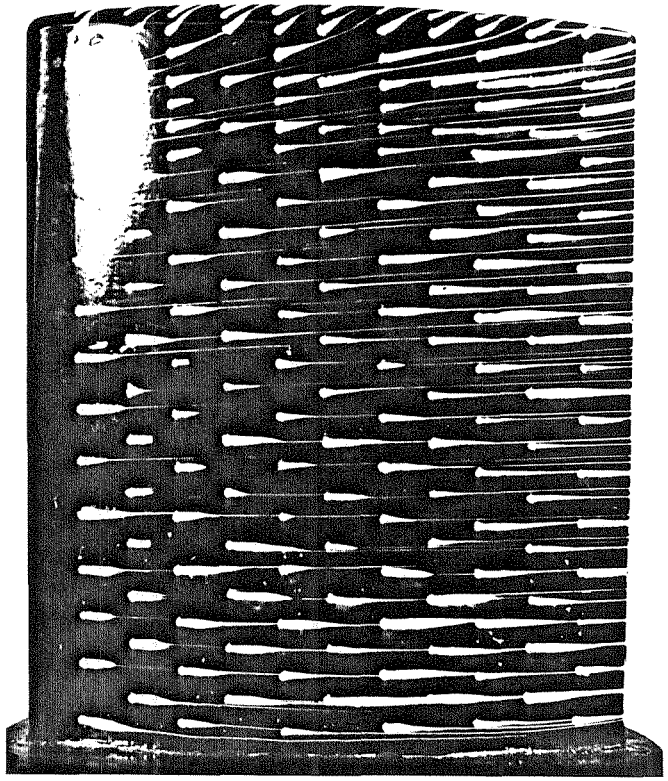

(c)inboard view

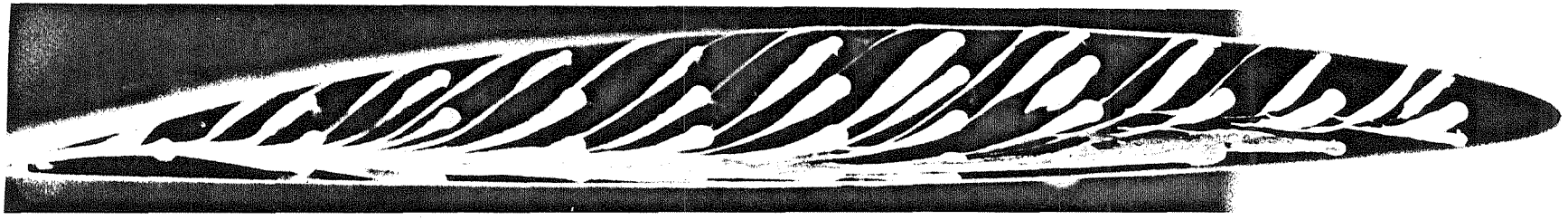

Figure A.2.5(a,b,c) SFV of 66-209 foil at $\alpha = -9°$.

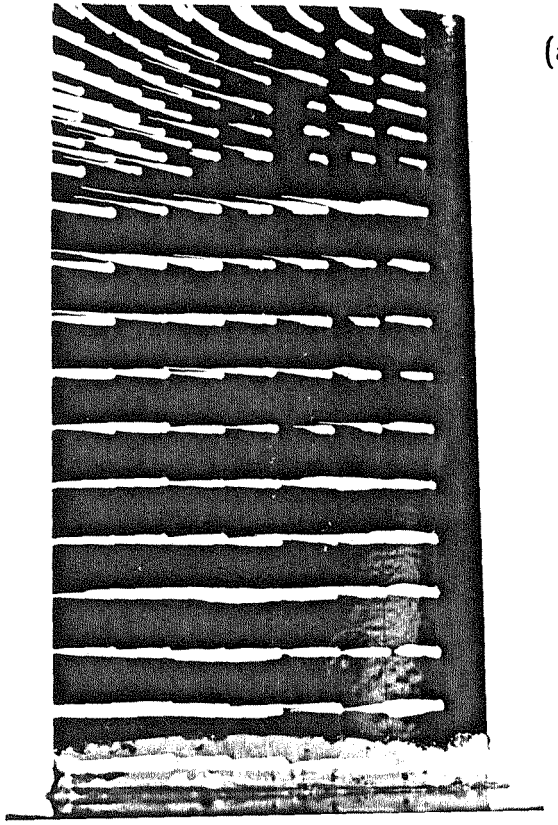

(a)pressure side

(b)suction side

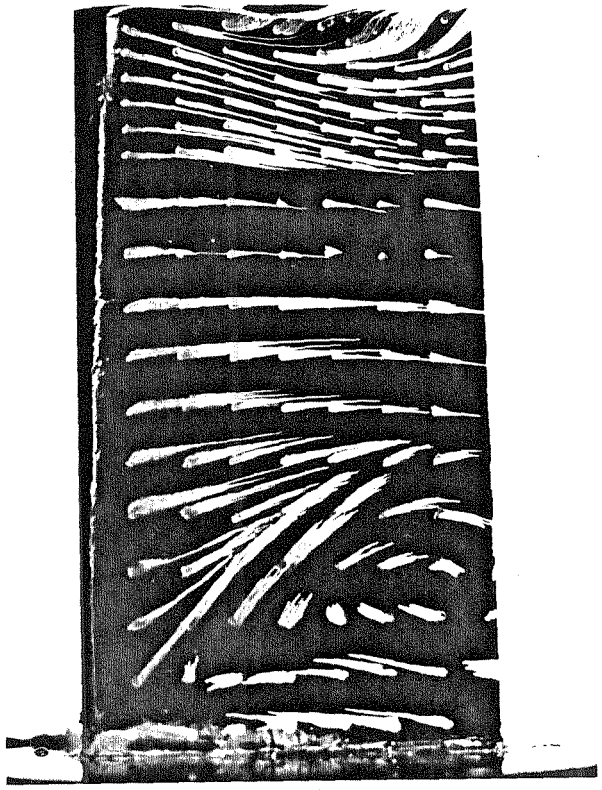

Figure A.3.1(a,b) SFV of Joukowski AR=3.8 foil at $\alpha = 14°$.

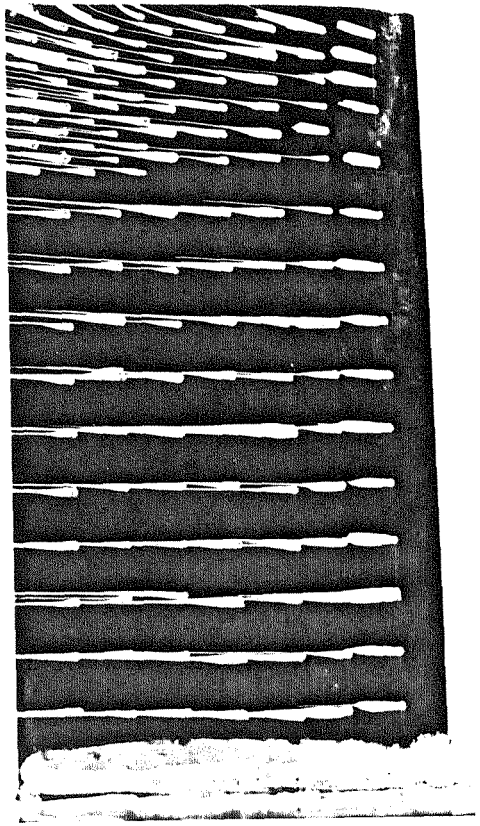

(a)pressure side

(b)suction side

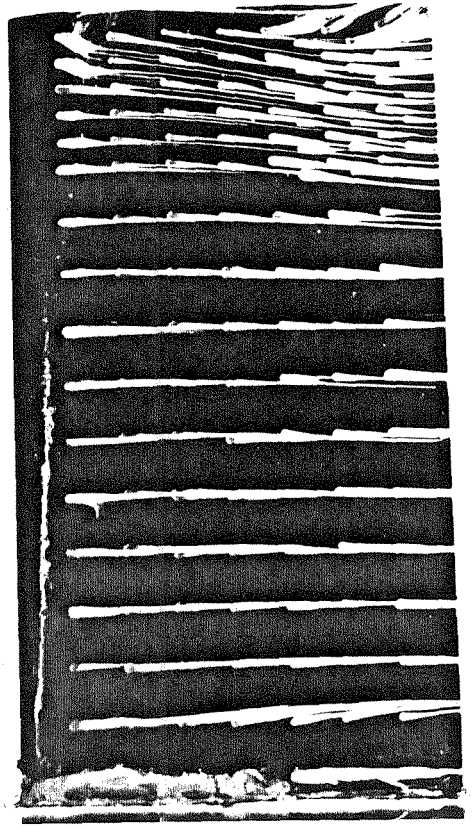

Figure A.3.2(a,b) SFV of Joukowski AR=3.8 foil at $\alpha = 6°$.

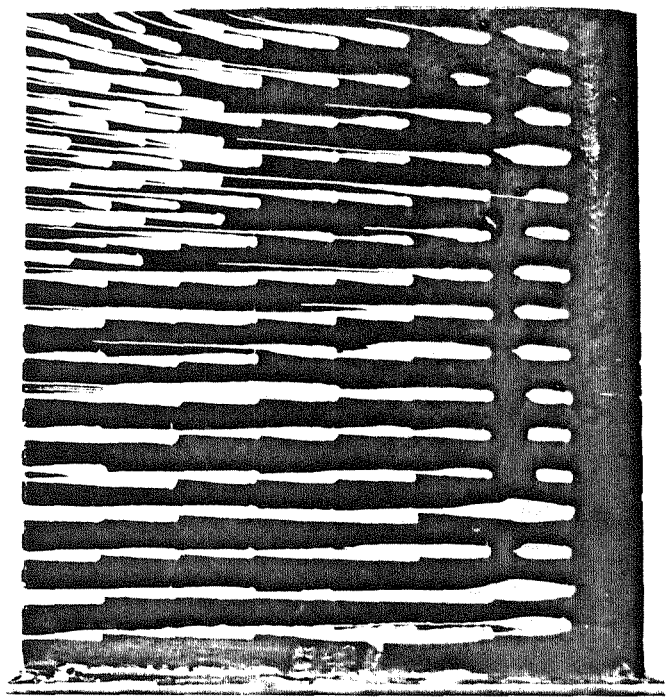

(a)pressure side

(b)suction side

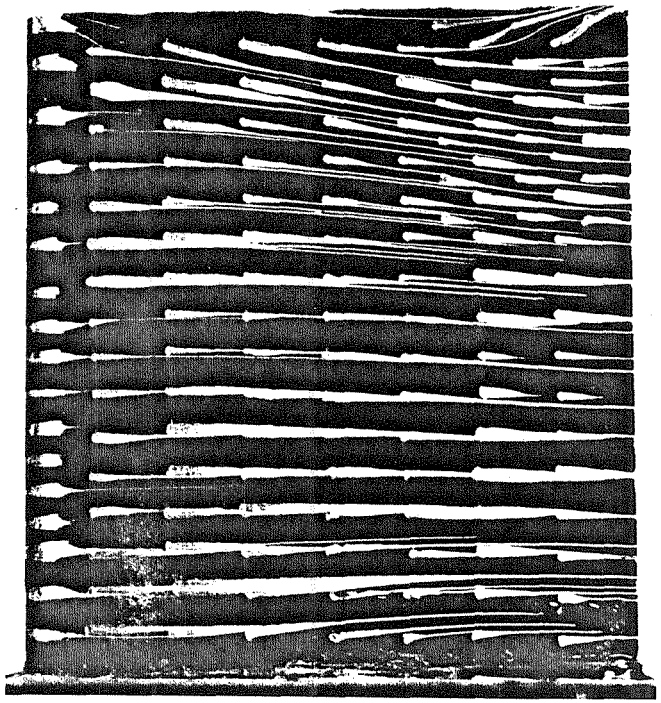

Figure A.3.3(a,b) SFV of Joukowski AR=2.3 foil at $\alpha = 6°$.

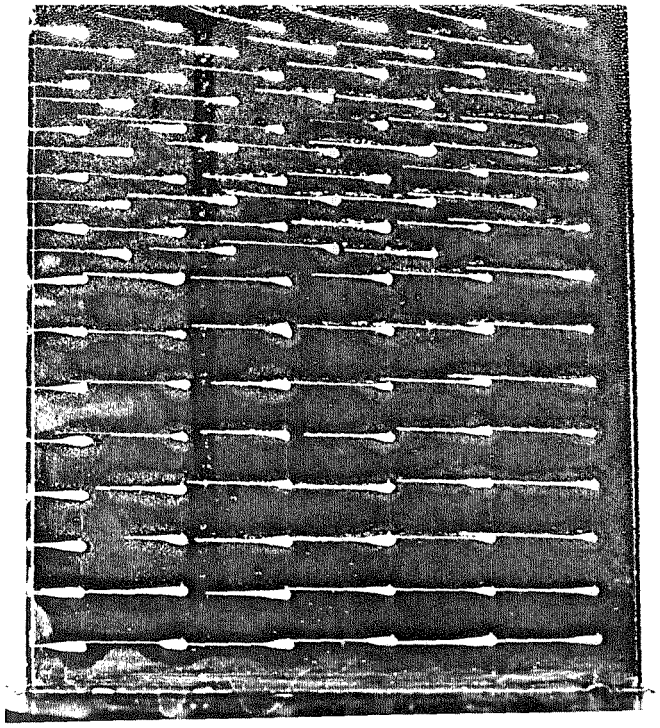

(a)pressure side

(b)suction side

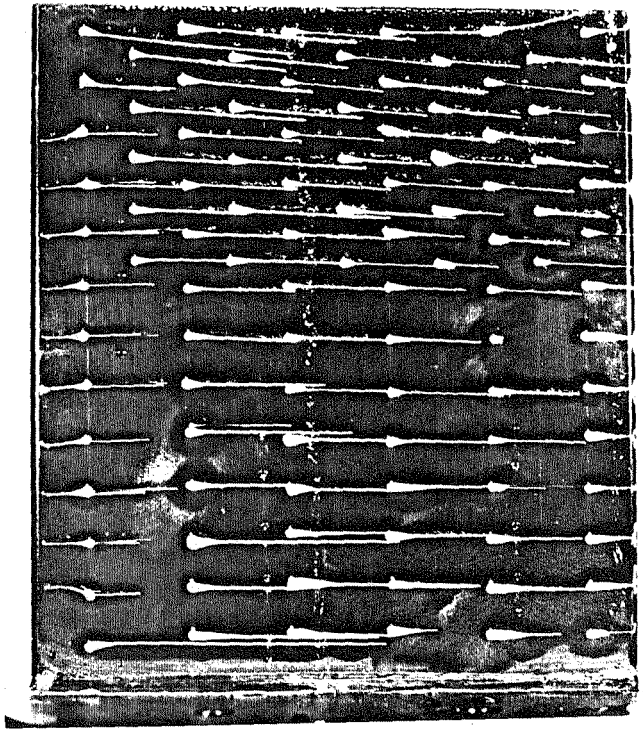

Figure A.4.1(a,b) SFV of Flat Plate foil at $\alpha = 3.3°$.

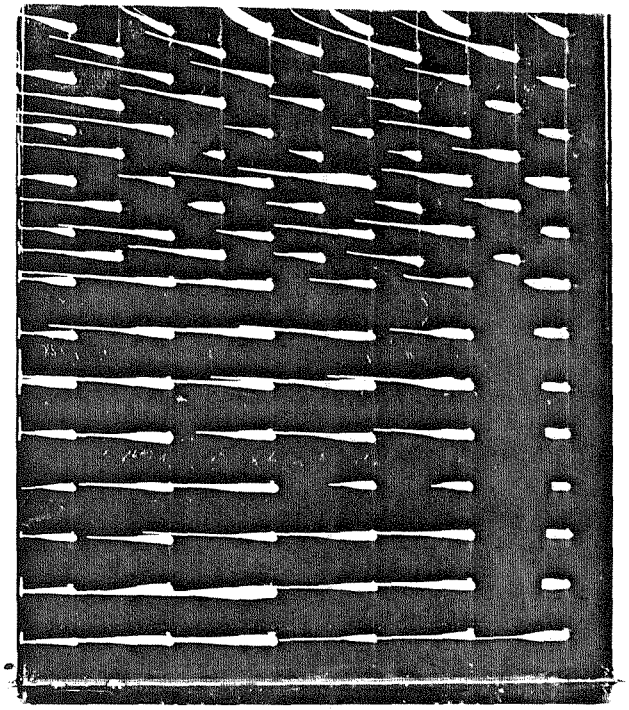

(a)pressure side

(b)suction side

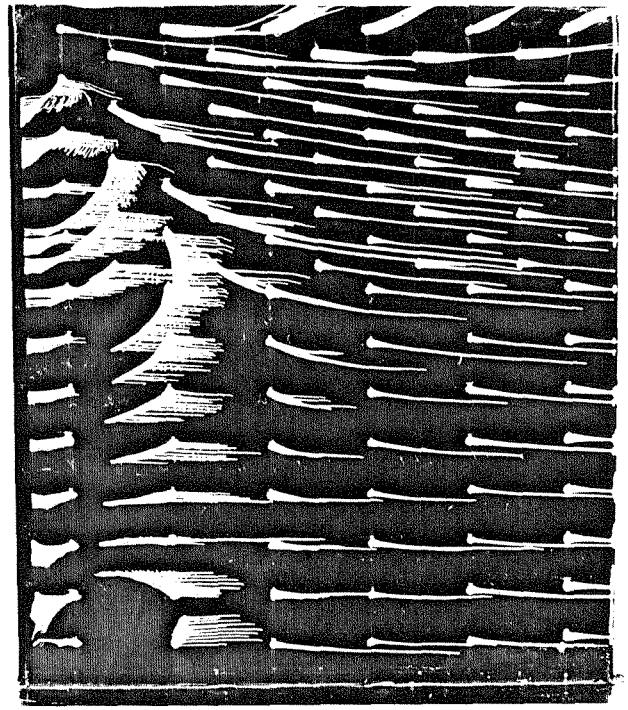

Figure A.4.2(a,b) SFV of Flat Plate foil at $\alpha = 6.9°$.

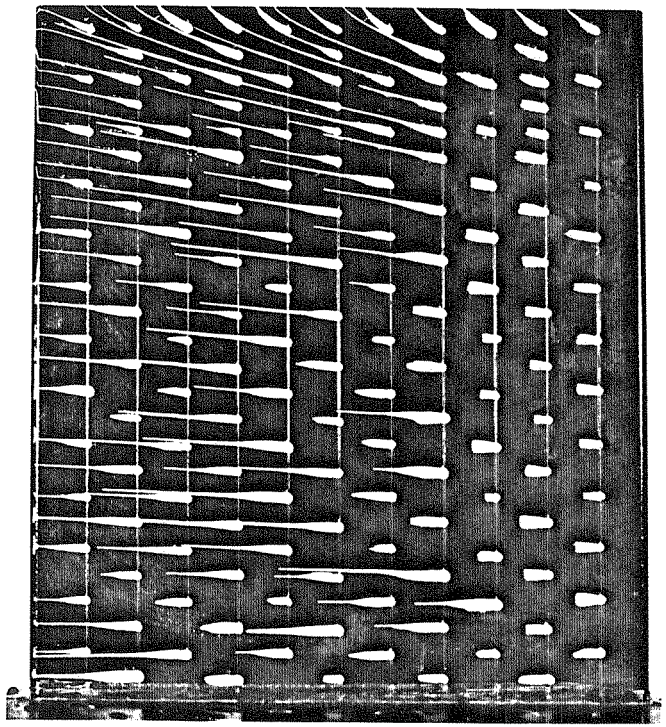

(a)pressure side

(b)suction side

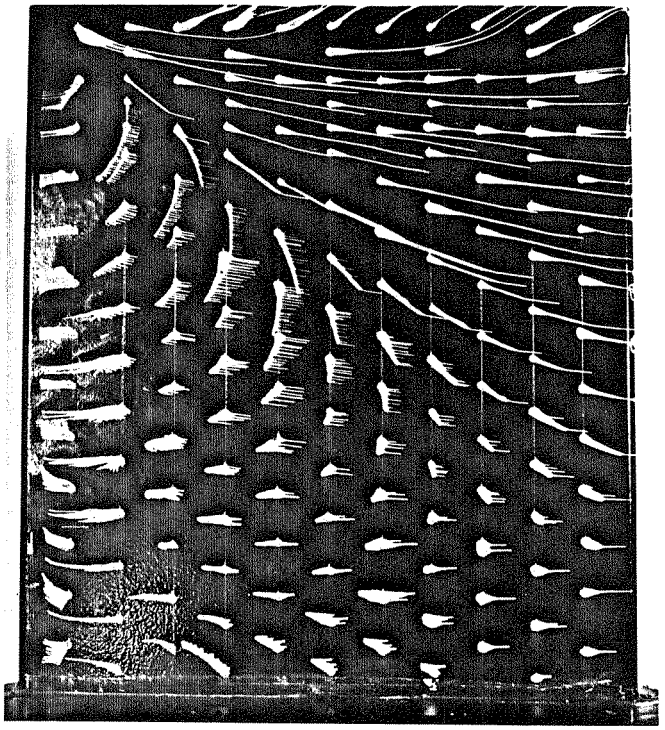

Figure A.4.3(a,b) SFV of Flat Plate foil at $\alpha = 10.1°$.

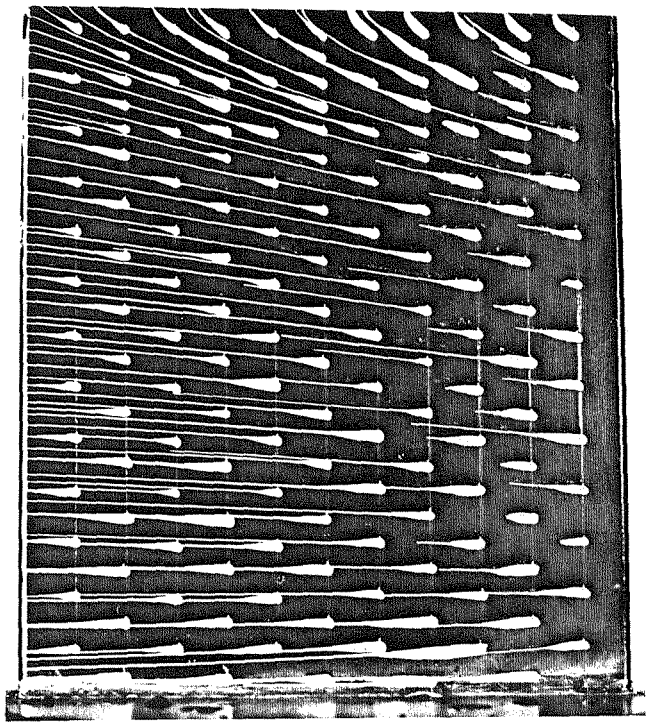

(a)pressure side

(b)suction side

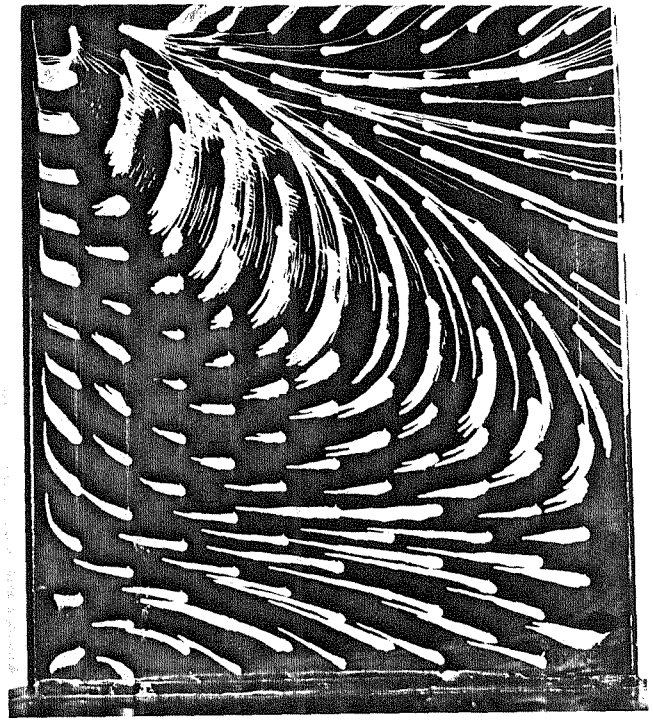

Figure A.4.4(a,b) SFV of Flat Plate foil at $\alpha = 13.7°$.

APPENDIX B – BUBBLE SLIP VELOCITY INTO A TRAILING VORTEX

Consider a bubble of radius R_B and density ρ_B travelling around a vortex core with velocity U_θ at a distance R. The fluid in which the bubble is embedded has density ρ and viscosity μ, and has a pressure field about the core p(r) (refer to Figure B.1). The aim of this discussion is to obtain a reasonable estimate of the maximum radial slip velocity, U_{rs}, of the bubble.

One first assumes that the presence of the bubble does not affect the pressure field in the fluid. Also, one assumes that the drag on the bubble is identical with that on a small spherical bubble in uniform flow. Finally, any bubble deformation or expansion in the pressure field, and acceleration of the bubble relative to the fluid, is neglected. The latter assumption is equivalent to supposing at each instant in time the bubble acheives its local terminal velocity. Then, the bubble reaches a slip velocity for which: (net pressure force) – (drag force)= mass × (centripetal acceleration).

It can be readily demonstrated that the right side of the equation is negligible, and hence:

$$F_p = F_D \tag{B.1}$$

The pressure force may be calculated exactly (subject to the aforementioned assumptions) by using:

$$F_p = \int_{surface} p(R + R_B \cos\phi) \sin 2\phi \pi R_B^2 \, d\phi \tag{B.2}$$

The location where the bubble slip is maximized is where dp/dr is a maximum. The radial momentum equation,

$$\frac{dp}{dr} = \frac{\rho U_\theta^2}{R} \tag{B.3}$$

implies this occurs where U_θ is a maximum in a Rankine vortex model. Because $R_B \ll R$ (in Chapter IV $(U_\theta)_{max}$ was found to occur at $R \approx 5 \times 10^{-3}$m;

$R_B \approx 8 \times 10^{-5}$m), it is an excellent approximation (especially in view of the other uncertainties) to set dp/dr=constant=$(\rho(U_\theta)^2_{max})/R$ in the neighbourhood of the bubble. Then, it can be shown that:

$$F_p = \frac{4}{3}\pi\rho {R_B}^3 \frac{(U_\theta)^2_{max}}{R} \tag{B.4}$$

Moore (1963) has analytically determined the drag coefficient on a spherical bubble to be $c_D = (48/Re)(1 - 2.2/Re^{0.5})$ where the Reynolds number is given by $Re=2R_B U_{rs}/\nu$. This drag coefficient fits the experimental measurements of Haberman and Morton (1953) well for $Re \approx 100$. In terms of a drag force, Moore's result is:

$$F_D = 12\pi\rho\nu U_{rs} R_B - 18.7\pi\rho\nu^{1.5} U_{rs}^{0.5} R_B^{0.5} \tag{B.5}$$

Equating (B.4) and (B.5) (denoting $\underline{U} = U_{rs}^{0.5}$):

$$12\pi\rho\nu R_B \underline{U}^2 - 18.7\pi\rho\nu^{1.5} {R_B}^{0.5} \underline{U} - \frac{4\pi\rho R_B^3 (U_\theta)^2_{max}}{3R} = 0 \tag{B.6}$$

which is trivially solved for U_{rs}.

Typical values from Chapter IV (with U_∞=6m/s, $\alpha = 10°$, x/c=2: $(U_\theta)_{max} =$ 5m/s, $R \approx 5 \times 10^{-3}$m, $R_B \approx 6 \times 10^{-5}$m, $\rho = 1000$kg/m^3, $\nu = 10^{-6}$m^2/s) one finds U_{rs}=1.7m/s (the second solution, U_{rs}=2.3m/s, would be presumably reached if the bubble were decelerating) and Re=200. Batchelor (1967) and Levich (1962) have pointed out that bubbles in liquids have surfactants which cause them to behave much as solid spheres. Consequently, it is instructive to recalculate the bubble slip velocity assuming the bubble acts as a solid. The solution is virtually the same: U_{rs}=1.66m/s. The slip velocity is sufficiently large to explain the nadir in the bubble density distribution in the region near $(U_\theta)_{max}$, but, because even at its maximum it is only $U_\theta/3$ (and of course due to the geometrical considerations discussed in Chapter III), its impact on the accuracy of the experimental results is small. The slip velocity should be less than $0.1U_\theta$ for $R > 1 \times 10^{-2}$m.

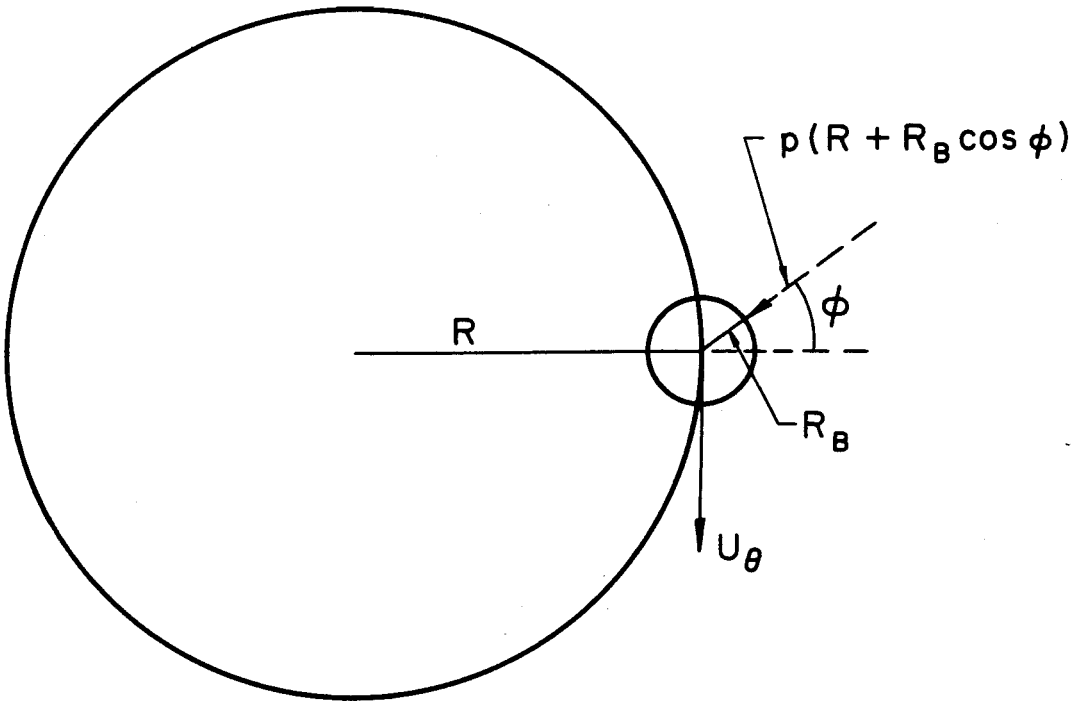

Figure B.1 Bubble Slip Analysis Geometry.